Design of novel nanostructured biosensing materials and their application in medical diagnostics

Fakhouri, Hussein

N°d'ordre NNT : xxx

THESE de DOCTORAT DE
L'UNIVERSITE CLAUDE BERNARD LYON 1
En cotutelle internationale avec
L'UNIVERSITE DE SPLIT, CROATIE

Ecole Doctorale N° 52
(Ecole Doctorale de Physique et d'Astrophysique de Lyon)
Et BIOPHYSICS PhD program at the University of Split

Spécialité de doctorat : Physique

Soutenue publiquement le 14/12/2022, par :
Hussein FAKHOURI

Design of novel nanostructured biosensing materials and their application in medical diagnostics

Devant le jury composé de :

MAYSINGER Dusica, Professeure, McGill University, Montréal, Canada	Rapporteur
SANCEY Lucie, Directrice de Recherche, CNRS	Rapporteur
BREVET Pierre-François, Professeur des Universités, Université Lyon 1	Examinateur
TRAJKOVIC Katarina, Chercheure, MEDILs, Split, Croatie	Examinatrice
ANTOINE Rodolphe, Directeur de Recherche, CNRS	Directeur de thèse
BONAČIĆ-KOUTECKÝ Vlasta, Professeure, Université de Split, Croatie	Co-directrice de thèse

Abstract

This doctoral thesis is focused on the rational design of novel nanostructured biosensing materials and their application in medical diagnostics, in the field of biological aging. Aging and age-related diseases are the consequences of the accumulation of oxidative damage to proteins. One way to measure protein oxidation is to determine levels of protein carbonyls. Currently, protein carbonylation is detected and quantified with 2D gel-based methods using specific fluorescent dyes coupled with hydrazide that reacts with protein carbonyls. However, commonly used dyes suffer from moderate biocompatibility, solubility and photostability. To improve the specificity and sensitivity necessary for diagnostics and prognostic purposes, there is room for advanced strategies. Luminescent ligated gold nanoclusters (AuNCs), composed of several to up to a few hundred Au atoms and protected by thiolated ligands, exhibit quantum confinement effects and molecule-like properties with tunable emission. Also, their impressive nonlinear optical properties make them promising candidates for various bio-imaging techniques such as multiphoton excited fluorescence microscopy. The main objective of this doctoral thesis was to detect protein carbonylation by optical methods using functionalized gold nanoclusters from 2D gels to in vitro.

Research presented in this thesis is organized in four chapters. In the first chapter, the current strategies used to analysis carbonylation in living materials will be briefly addressed as well as the potential of using nanoclusters obtained at the atomic precision for detection of carbonyl groups on proteins by optical methods. Experimental chapter describes in detail the techniques crucial to characterize nanoclusters specifying atomic precision by mass spectrometry, measurements of their optical properties (linear and nonlinear), and other characterization methods: sizing techniques, microscopies used to visualize signal from gels and the NCs inside the cells, chemical and biological protocols for carbonylation. The third chapter is devoted to describing the numerous synthesis approaches (most of them were unsuccessful) that have

conducted us to develop functionalized gold nanoclusters as luminescent probes for protein carbonylation detection. This research was done using the model lysozyme protein. This thesis outlines the development of glutathione gold NCs and its functionalization as efficient targets towards carbonylation, gels composition modification for studying both proteins and nanoclusters, proteomic approaches to understand the amount and the sites of carbonylation of the lysozyme, and the proof-of-principles of using NCs as luminescent probes for protein carbonylation detection with gels. Last chapter describes the strategies that were conducted to render nanoclusters appealing for cell bioimaging. For the first time, bioimaging measurements using multiphoton confocal microscopy were demonstrated in Lyon using silver based NCs internalized inside the cells. Thesis epilogue highlights the current stage of this project, the current limitations as well as some perspectives to render nanoclusters serviceable for biologists in particular in the context of biological aging.

Keywords : Nanocluster, carbonylation, bioimaging, post-functionalization, optical properties, in vitro, medical diagnostics.

Résumé:

Ce travail de doctorat porte sur la conception de nouveaux nanomatériaux et leur application au diagnostic médical, en particulier dans le domaine du vieillissement. Le vieillissement et les maladies liées à l'âge sont les conséquences de l'accumulation de dommages oxydatifs sur les protéines. Une façon de mesurer l'oxydation des protéines est de déterminer les niveaux de carbonyles des protéines. À l'heure actuelle, la carbonylation des protéines est détectée et quantifiée par des méthodes basées sur des gels 2D utilisant des colorants fluorescents spécifiques couplés à un réactif, e.g. l'hydrazide qui réagit avec les carbonyles des protéines. Cependant, les colorants souffrent de faible biocompatibilité, faible solubilité et d'une photostabilité modérée. Pour améliorer la spécificité et la sensibilité nécessaires aux dommages oxydatifs, des stratégies avancées sont nécessaires. Les nanoclusters d'or (AuNC), composés de plusieurs centaines d'atomes d'or et protégés par des ligands thiolés, présentent des effets de confinement quantique et des propriétés de type moléculaire avec propriétés de photoluminescence uniques. De plus, les propriétés optiques non linéaire impressionnante de ces nanoclusters en font des candidats prometteurs pour diverses techniques de bio-imagerie telles que la microscopie confocale multiphotonique. L'objectif principal de ce travail de doctorat était de détecter la carbonylation des protéines par des méthodes optiques en utilisant des nanoclusters d'or fonctionnalisés, en allant de gels 2D jusqu'à une exploration in vitro.

Ce manuscrit est organisé en quatre chapitres. Dans le premier chapitre, je passerai brièvement en revue les stratégies actuelles utilisées pour analyser la carbonylation dans le vivant et le potentiel de l'utilisation de nanoclusters obtenus à la précision atomique pour la détection des groupes carbonyles sur les protéines par des méthodes optiques. Dans le chapitre expérimental, je décrirai les techniques incontournables pour caractériser les nanoclusters et aborder la précision atomique par spectrométrie de masse, comment mesurer leurs propriétés optiques (linéaires et non linéaires), et d'autres méthodes de caractérisation en particulier les techniques

de mesure de taille, les microscopies utilisées pour visualiser le signal des gels et les NCs à l'intérieur des cellules, les protocoles chimiques et biologiques de carbonylation. Le troisième chapitre est consacré à la description des nombreuses approches de synthèse (dont la plupart ont été infructueuses) qui nous ont conduits à développer des nanoclusters d'or fonctionnalisés comme sondes luminescentes pour la détection de la carbonylation des protéines. Ce travail a été réalisé en utilisant la protéine modèle lysozyme. En particulier, je décrirai le développement de NCs d'or protégés par des molécules de glutathion et leur fonctionnalisation comme cibles efficaces de la carbonylation, la modification de la composition des gels pour étudier à la fois les protéines et les nanoclusters, les approches protéomiques pour comprendre la quantité et les sites de carbonylation du lysozyme, et la preuve de principe de l'utilisation des NCs comme sondes luminescentes pour la détection de la carbonylation des protéines avec les gels. Dans le dernier chapitre, je décrirai les stratégies que nous avons menées pour rendre les nanoclusters intéressants pour la bioimagerie cellulaire. Et pour la première fois, des mesures de bioimagerie par microscopie confocale multiphotonique ont été démontrées à Lyon en utilisant des NCs à base d'argent internalisées à l'intérieur des cellules. Je terminerai en résumant l'état d'avancement de ce projet, les limitations actuelles ainsi que quelques perspectives pour rendre les nanoclusters réellement utilisables pour les biologistes en particulier dans le contexte du vieillissement cellulaire.

Mots-clés : Nanocluster, carbonylation, bioimagerie, post-fonctionnalisation, propriétés optiques, in vitro, diagnostic médical.

Sažetak

Ovaj doktorski rad usmjeren je na dizajn novih nanostrukturiranih biosenzoričkih materijala za primjenu u medicinskoj dijagnostici, posebice u području biološkog starenja. Starenje i bolesti povezane sa starenjem posljedica su nakupljanja oksidativnog oštećenja proteina. Jedan od načina mjerenja oksidacije proteina jest određivanje razine karbonilacije proteina. Trenutačno se karbonilacija proteina detektira i kvantificira metodama koje se temelje na 2D gelovima uz korištenje specifičnih fluorescentnih boja vezanih na hidrazid, koji reagira s karbonilima proteina. Međutim, boje imaju nisku biokompatibilnost, nisku topljivost i umjerenu fotostabilnost. Kako bi se poboljšala potrebna specifičnost i osjetljivost na oksidativna oštećenja, potrebno je pronaći naprednije strategije. Nanoklastere zlata (AuNC), sastavljene od nekoliko do par stotina atoma zaštićenih tioliranim ligandima, karakteriziraju kvantni učinci te molekularna svojstva s kontroliranom fotoluminiscencijom. Štoviše, impresivna nelinearna optička svojstva ovih nanoklastera čine ih obećavajućim kandidatima za razne tehnike bio-oslikavanja kao što je multifotonska fluorescentna mikroskopija. Glavni cilj ovog doktorskog rada bio je identificirati karbonilaciju proteina optičkim metodama korištenjem funkcionaliziranih nanoklastera zlata, od 2D gelova do in vitro istraživanja.

Ovaj rad podijeljen je u četiri poglavlja. U prvom poglavlju ukratko su prikazane trenutne strategije koje se koriste za analizu karbonilacije u živim organizmima i potencijal korištenja nanoklastera dobivenih atomskom preciznošću, u svrhu detekcije karbonilnih skupina na proteinima optičkim metodama. U eksperimentalnom dijelu, opisane su osnovne tehnike za karakterizaciju nanoklastera kao i pojam atomske preciznosti masenom spektrometrijom, mjerenje optičkih svojstva (linearnih i nelinearnih) kao i druge metode karakterizacije: tehnike za modificiranje veličine, mikroskopije korištene za vizualizaciju signala gelova i nanoklastera unutar stanica, te kemijske i biološke protokole za karbonilaciju. Treće poglavlje posvećeno je opisu brojnih sintetskih pristupa (od kojih je većina bila neuspješna) koji su nas doveli do

razvoja funkcionaliziranih nanoklastera zlata kao luminiscentnih proba za detekciju karbonilacije proteina. U ovom radu korišten je model proteina lizozima. Posebice, opisan je razvoj zlatnih nanoklastera zaštićenih molekulama glutationa i njihova funkcionalizacija za učinkovito označavanje mjesta karbonilacije. Nadalje, pojašnjena je modifikacija sastava gelova za proučavanje proteina i nanoklastera, metoda proteomike za razumijevanje količine i mjesta karbonilacije lizozima te "dokaz principa" za upotrebu nanoklastera kao luminiscentnih probi za detekciju karbonilacije proteina na gelovima. Posljednje poglavlje opisuje strategije provedene kako bi nanoklasteri bili primjenjivi i učinkoviti u staničnom bio-oslikavanju. Po prvi puta, bio-oslikavanja multifotonskom konfokalnom mikroskopijom demonstrirana su u Lyonu korištenjem nanoklastera srebra unesenih unutar stanica. Epilog ovog doktorskog rada donosi pregled postignutog napretka istraživanja, trenutna ograničenja kao i neke nove perspektive koje bi nanoklastere usmjerilo većoj primjenjivosti za biologe, posebno u kontekstu staničnog starenja.

Ključne riječi: Nanoklaster, karbonilacija, bio-oslikavanje, postfunkcionalizacija, optička svojstva, in vitro, medicinska dijagnostika.

Acknowledgements

First and foremost, I would like to praise and thank God, the almighty, who has granted countless blessings, knowledge, and opportunities, so that I have been able to accomplish my thesis.

“If I have seen further, it is by standing on the shoulders of giants”, Sir Isaac Newton.

This quote touched me a lot, and it is true because all of scientific work conducted by researchers is now accessible to all seekers of science, this quote always motivated me to give my best during my PhD , hoping that my work can serve by any means the science and scientists.

This thesis is the fruit of my years of study, starting at the Lebanese University, and finishing at the University of Claude Bernard Lyon 1. It has allowed me to develop solid scientific knowledge, within a project that has always motivated me and held me at heart. I would like to express my gratitude to all those who helped me to complete my doctoral thesis.

First of all, this work wouldn’t have been as rich and could not have been accomplished without the help and supervision of Dr. Rodolphe ANTOINE (thesis director) and Prof. Vlasta BONAČIĆ-KOUTECKÝ (thesis co-director), who both saw the best in me and believed in my abilities. I would like to thank them, from all my heart, for the quality of their exceptional supervision, their patience and their rigor.

My sincere thanks go to Dr. Franck BERTORELLE for his precious help throughout my thesis. I was delighted to have the opportunity to work with you, thank you for your scientific support, you were always there to support me and advise me during the development of this thesis.

I would like to express my gratitude to the members of my thesis jury for carefully evaluating my thesis work. I thank you for your time, expertise, and advice.

I would like to thank both institute, ILM (Lyon, France) directed by Philippe DUGOURD and MEDILS (Split Croatia) directed by Miroslav RADMAN and all the team members who had supported me and helped me with their expertise. In particular Mrs. Isabelle RUSSIER-ANTOINE, Mr. Pierre-Francois BREVET, Mr. Christophe MOULIN, Mrs. Clothilde ZERBINO, Mr. Guillaume Fabien COMBES, Mrs. Katarina TRAJKOVIC... A special thanks go to Anita Rogošić from STIM-REI center of excellence for all the administrative procedure, without you it would have been impossible to accomplish everything.

I had the opportunity to meet Martina Perić Bakulić, Margarita Bužančić Milosavljević ,Antonija Mravak, thank you for the strong friendship that we had, and to share with me the culture of your city, and always helped me during my visits to Croatia, you took a special place in my heart.

I also wish to thank the doctoral school ED-PHAST in Lyon, and the doctoral school of biophysics in Split, for allowing me to carry out my thesis, especially Irena BITUNJAC.

To my parents "Nasser FAKHOURI" and "Rana ATWI", my angels, thank you for believing in me, you always pushed me to achieve my dreams, you stayed by my side during all my travails, my absences, my fits of anger and impatience. My brothers and sisters "Ali, Ahmad, Nadwa, Hassan and Fatima Al Zahraa", thank you for your support during my thesis, you were far from my eyes, but close to my heart.

During my thesis, I was not only searching for science and knowledge, I was also searching for my other half, the one that I want to spend my life with, start a family, share the moments of happiness and sadness. I address my thanks to my wife, the moon of my life, "Sara Natalie SOUEIDAN", for her unconditional love and support, and together, we were blessed with our first child "Ali" during my PhD. I shall carry both of you in my eyes, until infinity…

Table of Contents

General Introduction

Introduction

Science generates new knowledge, such as discoveries of new principles. Science and technology are supporting each other to advance. Scientific knowledge leads to the development of new technologies. Combining science, technology, engineering, and mathematics enhances interdisciplinary learning. The combination of mechanical and electrical engineers is named "mechatronics"; there is also "bioengineering," "bioprocessing" and other combinations. Such combinations allow for new ways in which materials and products are created. These last 30 years, the field of nanotechnology has resulted from the convergence of the traditional fields of chemistry, physics and biology. Nanotechnology is concerned with the fabrication and use of devices at dimensions between approximately 1 and 100 nanometers[1].

Nanoparticles have a special place in nanotechnology because they are building blocks for the development of nano-architectures with variable complexity. Among different elements used for these building blocks, noble metals display a wide range of material behavior along the atomic to bulk transition[2]. According to the number of metal atoms, metals at the nanoscale are roughly classified into three size domains: large nanoparticles, small nanoparticles, and clusters (or nanoclusters), corresponding to different characteristic length scales respectively. For large metal nanoparticles, with size in the range of the wavelength of light, the optical properties can be quantitatively described with Mie theory for small metallic spheres[3]. On the other hand, in this smallest size regime (with less than hundreds metal atoms), metal clusters become "molecular species", and discrete states with strong florescence can be observed. The understanding of their properties and in particular their optical properties has been dramatically deepened by quantum chemistry approaches. Recent progress in theory, in particular time-dependent density functional theory (TDDFT), allows the size range for the investigation of optical properties up to more than 100 atoms for the simplest transition metals to be extended[4].

Gold nanoclusters have received a lot of attention in nanotechnology compared with other materials due to their fascinating optical properties. Ligands play a very important role in the

formation of NCs as protectors, which can prevent the aggregation of metal clusters and thus retain the size-dependent fluorescence property. Fluorescent ligand-protected gold nanoclusters (AuNCs) have recently emerged as a novel kind of promising fluorescent probes for high-performance sensors and bioimaging because of their ultrasmall size, strong luminescence, good photostability, and excellent biocompatibility[5]. Thanks to ease of synthesis, AuNCs can be obtained at the atomic precision. Such NCs may display tunable fluorescent emission, that is size-dependent. In addition, the organic capping ligand and surface gold atoms are organized through surface staple-like bonding structure leading to unique structural and electronic properties and thus AuNCs are exciting nanomaterials for research. A large variety of ligands can be used to prepare AuNCs and surface functionalization of these conjugates permits to render them attractive for bioimaging and medical diagnostics.

My PhD work has focused on this last issue, e.g., preparing tailor-made ligand protected NCs with adequate surface functionalization to render them attractive for bioimaging and diagnostics. This PhD was conducted in "co-tutelle" between the University of Split and the University of Claude Bernard Lyon 1 and in co-direction between Rodolphe Antoine and Vlasta Bonačić-Koutecký. This PhD work was granted by the project STIM-REI, Contract Number: KK.01.1.1.01.0003, funded by the European Union through the European Regional Development Fund—the Operational Programme Competitiveness and Cohesion 2014–2020 (KK.01.1.1.01) and by the Mediterranean Institute for Life Sciences (MedILS). This PhD work was first discussed end of 2018 in Split with my co-directors and Miroslav Radman (Director of MedILS), and was focused on protein carbonylation, in the context of biological aging, through a multidisciplinary project that gathers expertise from different field of interest. During this first meeting, the overview and the aim of this project was clearly defined. The aim was to prepare ligand protected noble metal NCs and further surface functionalization permits to render them attractive as luminescent probes for protein carbonylation detection. This targeting was supposed to be conducted first with model proteins separated in gels and moving towards in vitro detection, see **Figure 0.1**. Different steps of validation (defined as GonoGo) were elaborated. The first GonoGo defined in the meeting was to develop gold, silver-based

nanoclusters presenting luminescent properties and specifically designed to target carbonylation. The second GoNoGo was the proof-of-concept, ability of functionalized nanoclusters to target carbonylated proteins in gels by fluorescent based methods (under linear and nonlinear optical characterization technique) and possibly to quantify the carbonylation with these techniques. The last GoNoGo was to bridge the gap to detect carbonylation in fixed and live cells by bioimaging.

The current challenges were clarified, and the project was conducted by three groups gathering complementary expertise: expertise in nanoclusters synthesis and characterization, expertise in biological tools and knowledge in the detection of carbonylation with conventional techniques, and expertise in quantum chemistry tools to understand the fundamentals and characteristics of the structure and interactions of gold nanoclusters with biomolecular systems. The expertise in nanoclusters synthesis was the result of the impressive work done by Franck Bertorelle (Research Engineer in organic-inorganic synthesis at ILM). I had the chance to be trained by him (before he left the lab in early 2021). All cluster synthesis done in the last part of my PhD work were done by myself. But I was also involved in the biological tools and knowledge in the detection of carbonylation in this project by travelling and meeting with biologists at MEDILS.

This manuscript is organized in four chapters. In the first chapter, I will review briefly the current strategies used to analysis carbonylation in living materials and the potential of using nanoclusters obtained at the atomic precision for detection of carbonyl groups on proteins by optical methods. In the experimental chapter, I will describe the most important techniques to characterize nanoclusters and address their atomic precision by mass spectrometry; how to measure their optical properties (linear and nonlinear); and other characterization methods in particular sizing techniques; microscopies used to visualize signal from gels and the NCs inside the cells; chemical and biological protocols for carbonylation. The third fourth chapter is the "central part" of my PhD work and is devoted to describing the numerous synthesis approaches (most of them were unsuccessful) that have conducted us to develop functionalized Au_{15}

nanoclusters as luminescent probes for protein carbonylation detection. This work was done using the model lysozyme protein. I will describe the development of glutathione gold NCs and its functionalization as efficient targets towards carbonylation, gels composition modification for studying both proteins and nanoclusters, proteomic approaches to understand the amount and the sites of carbonylation of the lysozyme, and the proof-of-principles of using NCs as luminescent probes for protein carbonylation detection with gels. We face most of the challenges in this period, but we successfully ended by publishing this work in Nature – Communications Chemistry[6]. Of note, due to the high impact of this paper in this journal, our contribution was selected in the collections "Celebrating Women in Chemistry" and "2021 Editors' Highlights". In the last chapter, which is the work I really did by myself, I will describe the strategies we conducted to render nanoclusters appealing for cell bioimaging. Since Au15 nanoclusters were not enough fluorescent for bio-imaging, we explored other routes to produce highly luminescent nanoclusters and in particular, I will introduce protein-templated gold NCs as starting candidates for in vitro application in different cells lines. The difficulties using such nanoclusters for a good internalization inside the cells conducted us to explore other strategies and at the end we found that only silver based NCs (AgNCs) show good internalization inside the cells. And for the first time, bioimaging measurements using multiphoton confocal microscopy were demonstrated in Lyon using AgNCs internalized inside the cells. I will then finish by summarizing the current stage in this project, the current limitations as well as some perspectives to render nanoclusters really usable for biologists in the context of biological aging.

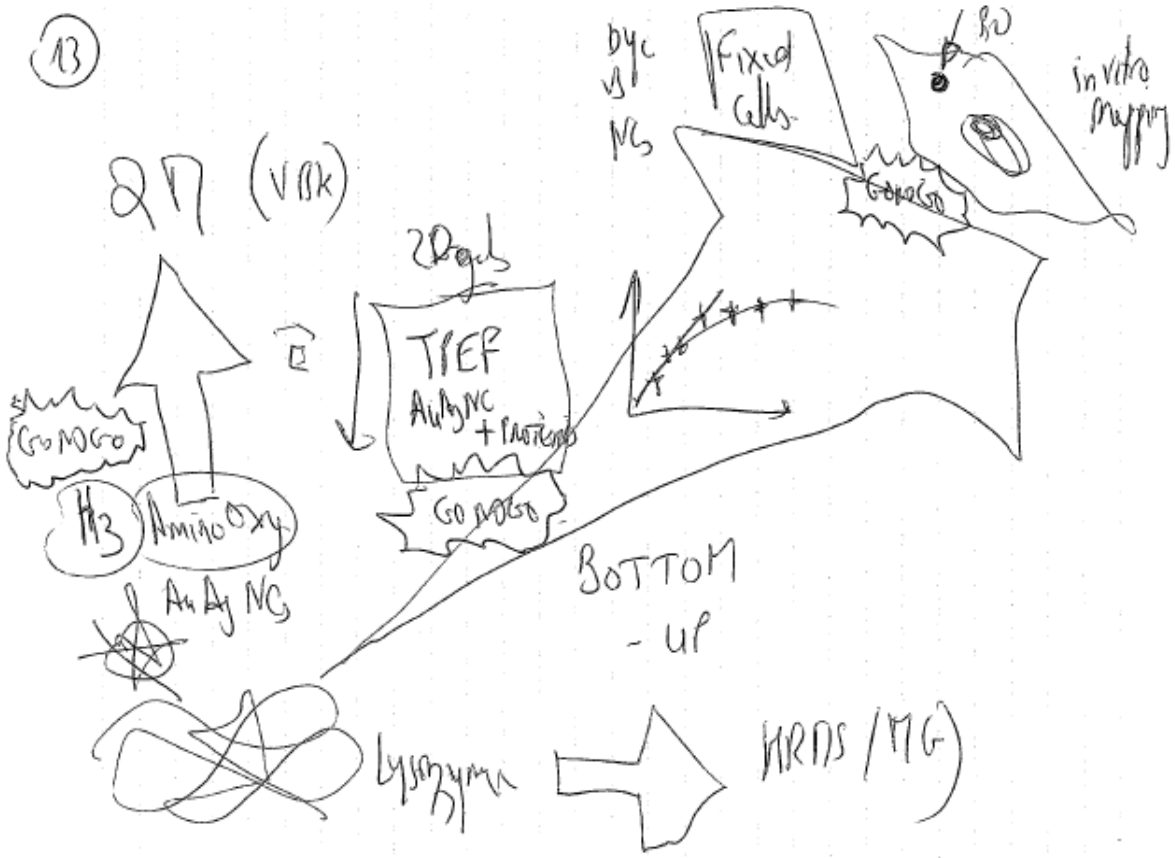

Figure 0.1 : Illustration of the general plan proposed in the first meeting in Split in December 2018, to define the steps of the multidisciplinary project.

References

[1] Bhushan B. Introduction to Nanotechnology. In: Bhushan B, ed. Springer Handbook of Nanotechnology. Springer Handbooks. Springer; 2017:1-19. doi:10.1007/978-3-662-54357-3_1

[2] Jennings T, Strouse G. Past, Present, and Future of Gold Nanoparticles. In: Chan WCW, ed. Bio-Applications of Nanoparticles. Advances in Experimental Medicine and Biology. Springer; 2007:34-47. doi:10.1007/978-0-387-76713-0_3

[3] Kreibig U, Vollmer M. Optical Properties of Metal Clusters. Vol 25. Springer; 1995. doi:10.1007/978-3-662-09109-8

[4] Antoine R, Bonačić-Koutecký V. Liganded Silver and Gold Quantum Clusters. Towards a New Class of Nonlinear Optical Nanomaterials. Springer International Publishing; 2018. doi:10.1007/978-3-319-64743-2

[5] Chen LY, Wang CW, Yuan Z, Chang HT. Fluorescent Gold Nanoclusters: Recent Advances in Sensing and Imaging. Anal Chem. 2015;87(1):216-229. doi:10.1021/ac503636j

[6] Combes GF, Fakhouri H, Moulin C, et al. Functionalized Au15 nanoclusters as luminescent probes for protein carbonylation detection. Commun Chem. 2021;4(1):1-11. doi:10.1038/s42004-021-00497-z

Chapter 1: A State-of-the-art Review

Strategies for the Analysis of Carbonyl Groups on Proteins and the Potential for Using Atomically Precise Nanoclusters

Introduction

Researchers are developing tools and method to visualize biomolecules and functional biological process in the cells, tissues, and organs. To this purpose, optical methods are often used and the bioimaging field has widely been developed during the last decades, introducing luminescent targets (often called fluorophores) as well as innovative imaging techniques to visualize the phenomenon of interest. The researchers are interested in developing fluorophores that give the better contrast for imaging. However, challenges regarding non-toxicity, biocompatibility, good photo-stability (avoiding photobleaching) of fluorophore must be considered.

Visible light is absorbed by a large biological functions in the body including blood cells, tissues and membranes, and reveal a new complication that limits conventional technique to low penetration[1], autofluorescence due to their absorption[2], and toxicology after the applied irradiation[3]. For deep-tissue optical imaging, the applied light is a key parameter to penetrate. And for instance, the best optical windows (for which attenuation and optical loss are the lowest) are NIR-I and NIR-II windows (emission in 700–950 nm NIR-I window and emission in the 1000–1700 nm NIR-II window). This requires special type of fluorophores that can absorb efficiently in these near infrared regions. Two strategies may be explored, (i) developing fluorophores with very low optical gap for which the absorption (and emission) may occur in NIR-I and NIR-II regions. Such fluorophores, generally are based on the concept of push-pull molecules for which specific functional groups allow to reach very low optical gaps[4], (ii) using nonlinear optical (NLO) process (in particular two-photon excited fluorescence). NLO strategies are extremely appealing because such processes convert two (or more) photons with low energy to a higher photon's energy that can be absorbed by any fluorophores. The initial photons used for NLO have wavelengths usually in the range of NIR-I (for two-photon excited fluorescence) or NIR-II (three-photon excited fluorescence).

The second aspect even more important is the ability of the fluorophore molecules to bear functional groups for be sensitive and specific to a given class of biomolecules. This is of paramount importance for fluorescent nanomaterials, including silver chalcogenide quantum dots, single-walled carbon nanotubes and polymer nanoparticles[5]. Atomically precise nanoclusters as we will see during this manuscript are a new class of nanomaterials able to match all the criteria mentioned above. And thus, the idea was to explore the possibility to use them for the analysis of carbonyl groups on proteins in the context of biological aging. Thus, this introduction chapter aims at reviewing the current state-of-the-art of techniques used to probe carbonyl groups on proteins. Then I will briefly present the potential of using nanoclusters for such bio-application.

1.1 Strategies for the Analysis of Carbonyl Groups on Proteins in the context of biological aging.

Oxidation as a definition is the process where an atom takes electron from another. It is accruing in all species and molecules. Oxidation in the body is an important phenomenon that accurate in macromolecules and serve for many physiological rules including cell signaling, cell communication and play a crucial rule for the immune system[6,7]. The main product of the oxidative stress know as ROS (reactive oxygen species) are mostly hydrogen peroxide (H_2O_2), hydroxyl radicals ($^{\cdot}OH$), superoxide radicals ($O2^{\cdot-}$), and singlet oxygen ($^1O_2$), they are the byproducts of oxygen metabolism in the cells[8]. Oxidative stress can also be triggered by heat, UV irradiation, and osmatic shock (change in salt composition outside the cells). These molecules are freely diffusing, small, they do not have specific targets and react with all molecules including lipids, sugar, and proteins. Unlike redox signaling, that require mostly one reaction and considered reversible, oxidative stress is irreversible in most of the times. Cell do not die after an oxidative stress; it will adapt and repair the damage with the help of antioxidants that play a crucial rule on repairing oxidative damage.

Between all carbonylated species, studies focused on protein carbonylation because it is related to diseases including Alzheimer, Parkinson, diabetes, and cancer[9,10]. Protein excites and participates in cellular functions, maintaining them, playing critical roles in the body, they are

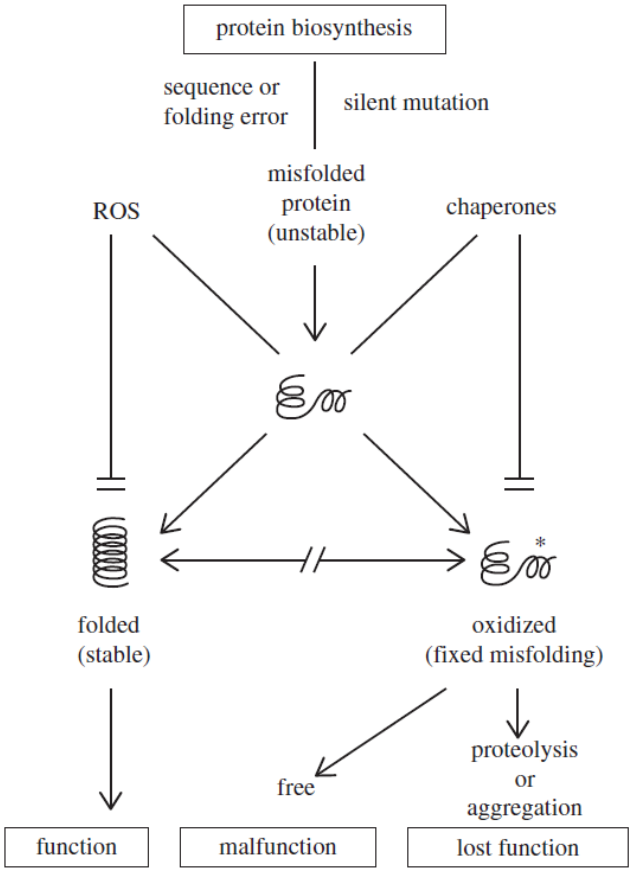

Figure 1.1 : Opposition between protein folding and oxidation, the imperfection in native folding arises from random biosynthetic and folding errors and from silent mutations, the native folding prevents oxidation and oxidation stop correct folding. After the oxidation, the protein will lose their function and aggregates or malfunction (change the initial function).

the basis of the biological system of the human body. In the last century, researchers were arguing that aging and age-related diseases (ARDs) are complex consequences of the cumulative oxidative damage to proteins and the oxidized protein accumulate with age and cause reversible ageing-like phenotypes with irreversible consequences like mutations and

aggregation. **Figure 1.1**[11,12] shows an example of protein oxidation, the worse scenario happen when the misfolded protein are oxidized, causing the loss of function or malfunction of proteins[10], chaperones can interfere before oxidation and fold the protein to give it her normal function, but when oxidation domain and overcome the antioxidant system, oxidative stress will accumulate, causing many damage in the biological system.

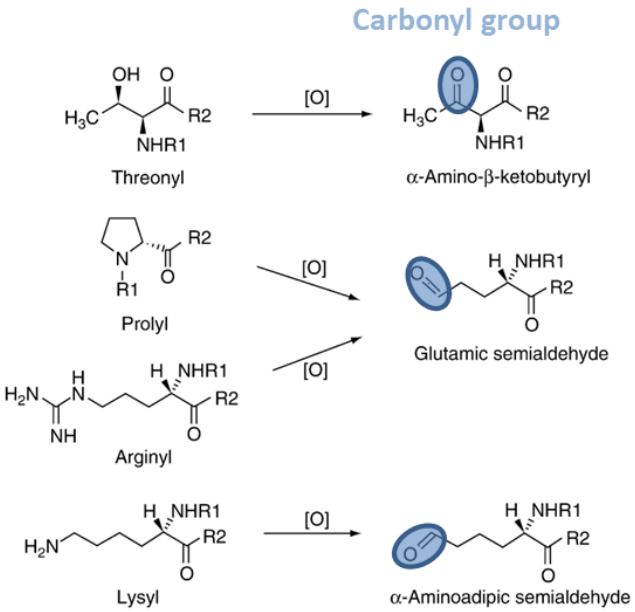

Figure 1.2 : Amino acids affected by the carbonylation, causing the change of their function and thus the function of protein.

Protein carbonylation is considered too be irreversible and unrepairable. Since the amino acid are the main components that make up proteins, they are the main target of carbonylation. Studies show that the common amino acids that are related to carbonylation are arginine, lysine, proline and threonine[13], see **Figure 1.2**[14]. Carbonyl group has no distinguished UV or visible optical properties and require specific chemical probes for their detection. Aldehydes, ketones, and lactams are the common carbonyl species. Many methods have been developed using markers to quantify and detect this phenomena[15 16 17], where this markers will bind covalently

to the carbonyl groups in the protein, while the other side of this markers is fluorescence, enabling the detection and quantification of carbonylation **Figure 1.3**.

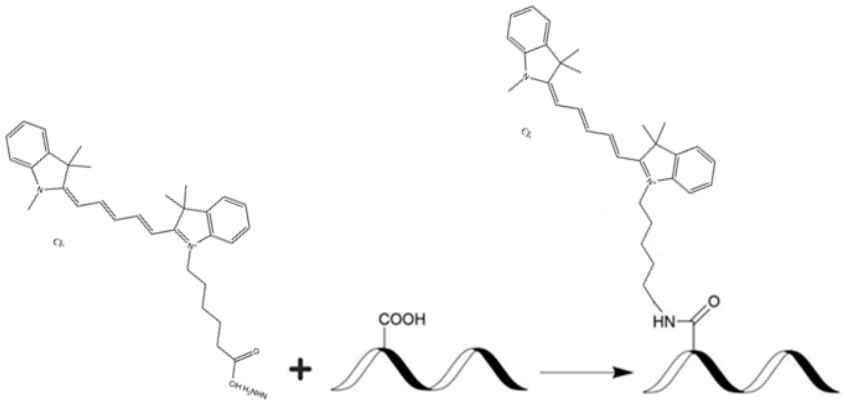

Figure 1.3 : General illustrations of how fluorophore with carbonyl detective group (CY5 dye in this example) will bind to carbonylated protein.

Carbonylated biomolecules cannot be specifically detected due to the absence of specific physico-chemical properties, such as absorbance or fluorescence. Most analytical techniques depend on specific chemical derivatization of carbonyl groups with hydrazines, hydrazides and hydroxyl amines. Derivatized compounds are detectable by absorbance[18], Western blot[19], chromatography[20], mass spectrometry[21], and fluorescence[22]. All protocols allow the detection or/and quantification of carbonyl compounds. However, the spatial location of carbonyls in cells and tissues remains less studied. Carbonylation is a dynamic process, tending to accumulate under oxidative stress, and the cellular spatial location of carbonyl species can change in time. It is therefore important to understand the spatial dynamics of carbonyls and to attribute carbonyl levels to specific molecular species.

One of the most widely used derivatization reagent is 2,4dinitrophenylhydrazine (DNPH), originally used for spectrophotometric detection and quantification of carbonylated proteins[18]. Venukumar Vemula et al. have presented a simple, fast and cost efficient microscopy imaging

of cellular carbonyls based on coumarin-hydrazide, providing spatial information on both protein and lipid carbonyls[23].

In addition, Tamarit et al. established a study for the detection of carbonylation based on fluorophores with carbonyl-reactive using cyanine dyes and BODIPY hydrazides allowing a direct detection and quantitation of carbonyls on the proteins in one and two-dimensional electrophoresis gels using fluorescence imaging scanner[24], see **Figure 1.4**.

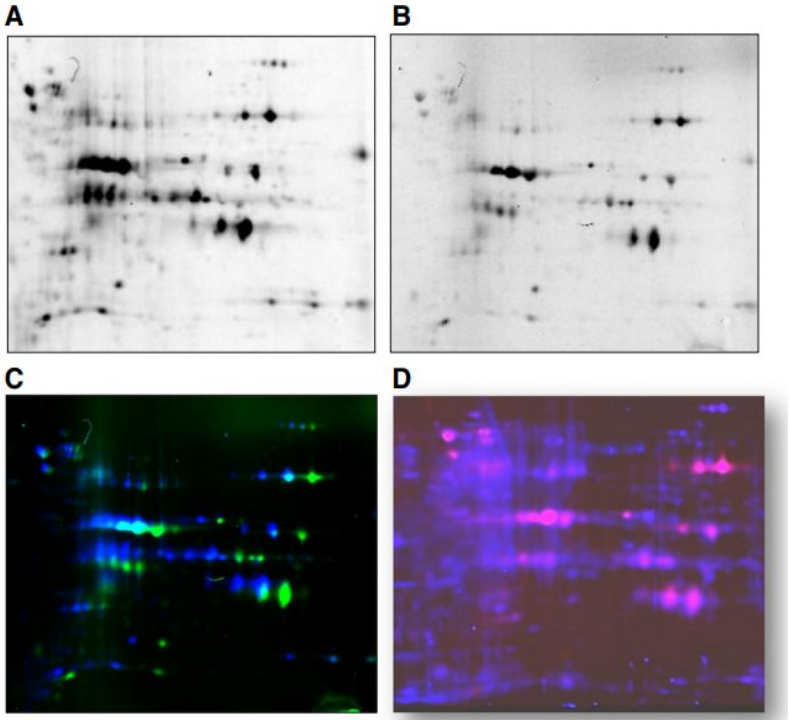

Figure 1.4 : Carbonylated protein derivatized with Cy5-Hz and Bodipy-Hz and migrated in 2D gel electrophoresis and visualized in different channels : A, Cy5 channel; B, Bodipy channel; C, superposition of images A and B. In D, the correspondence between the Bodipy signal and protein staining is shown[24].

As already mentioned, the carbonylation of proteins is irreversible. However, the damaged proteins can be removed by the cell as long as the degradation process of damaged proteins (protein complexes) is sufficiently active (Fig. 1). At high oxidative rates (for instance with high radiation doses (i.e., 200-1000 Gy)), in some cases there is a correlation between the

production of carbonylated proteins and a decrease in fecundity (e.g., in invertebrates, a decrease in the hatching rate of eggs laid and thus reproductive success) or even mortality. Thus, it is of paramount importance to establish correlations between the levels of carbonylated proteins, the nature of the damaged proteins, the degradation activity of the damaged proteins and, finally, "macroscopic" effects such as reproduction. Kuzmic et al developed a protocol to target carbonyl groups, and the carbonylation of the different biomolecules (protein, lipids, DNA)[25]. Two models of distinct radiosensitivity nematode Caenorhabditis elegans and the fish Danio rerio, were exposed to radiation exposed to radiation by external irradiation at low and high doses, in acute or chronic or chronically, for a comparative approach. In parallel, several parameters were monitored: DNA damage (single-strand and double-strand breaks) and double-strand breaks) and their repair mechanism; epigenetic processes (transmissible changes in gene function not resulting from DNA sequence changes); and cell death (apoptosis). Level of carbonylation has been shown to be a good biomarker of ageing biomarker of ageing, as older nematodes show a higher carbonylation than younger ones. The amount of lipids was studied and followed the same trends as carbonylation, i.e., increase with age, but decrease after irradiation (Figure 5). Lipids are very important signaling molecules that constitute the cell membrane and a storage membrane as well as an energy storage.

In this initial study conducted by Kuzmic et al. two different methods for measuring carbonylation have been developed. The first method counts and identifies carbonylated proteins in the sample of several individuals that have undergone the same treatment. This method is based on the extraction and chemical separation of proteins, whose carbonyls are specifically labeled. The second method measures the level of carbonylation of biomolecules (proteins, DNA, RNA and lipids) in the whole organism (**Figure 1.5**)[26]. It uses confocal imaging, and multiple labeling of biomolecules (carbonyl labeling and specific labeling identifying each biomolecule). This study represents one of the most advanced strategies to

study carbonylation in a multi-scale approach and demonstrates the importance of confocal imaging as well as functional fluorescent tragedies.

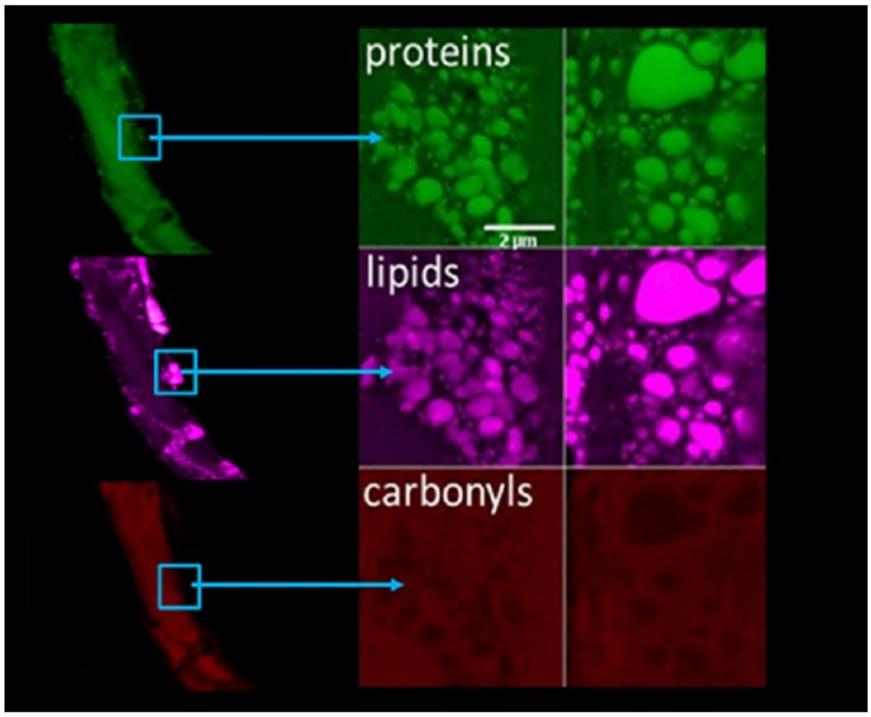

Figure 1.5 : Positive co-localization between proteins and lipids in the adult stage (10 d), irradiated 10 d with a dose rate of 52 mGy.h-1 (cumulative dose 12 Gy) and in the aged stage (19 d, not irradiated), excluding co-localization with carbonyls (Pearson's carbonyl coecient ~ 0.2) Thesis M. Kuzmic © IRSN.

1.2 Luminescent gold nanoclusters for applications in biomedical field.

Thiolated-protected gold nanoclusters are an important class of nanoclusters obtained at the atomic precision and stabilized with sulfur containing molecules (thiolates). Thiolates residues are naturally present in peptides and proteins (cysteine residue) and such thiolated-protected gold nanoclusters are suitable systems for bioimaging applications, with biocompatibility, interesting optical properties in terms of one photon and two photon absorption, surface modification and high stability. Gold is known for centuries to react with sulfured containing compounds. The interaction of sulfur with gold and the bond formed is still not clear nowadays, evidence show that the distance between sulfur and gold atom is shorter than the gold atoms distance, a weak bond but strong enough to prevent detachment[27].

Regarding optical properties, high-emissive nanoclusters are of great desirability. While gold NCs exhibit luminescent properties from near UV to IR, their PL quantum yield is low compared to organic dyes, lanthanide complexes, and quantum dot-based nanomaterials. To improve the quantum yield and PL, a variety of approaches were developed, including ligand engineering, selective doping with silver or other metal NCs, self-assembly induced emission by aggregation[28]. However, the origins of PL in nanoclusters are not completely understood yet. The ligand molecules, the geometric and electronic structures of the metal core play a major role in enhancing the emissive properties. Such nanoclusters can be considered as a "multi-shell system" (see **Figure 1.6**) composed by (1) a metallic core, (2) a metal-ligand interface, in particular with staple motifs leading to metal-sulfur bonds, and (3) the surface ligand molecules[29]. The communication between these three shells accurate in two different ways, from ligand to metal core (LMCT) or ligand to metal-metal charge transfer (LMMCT)

observed in metal complexes, due to direct bonding or the direct donation of delocalized electrons of electron-rich groups of the ligands.

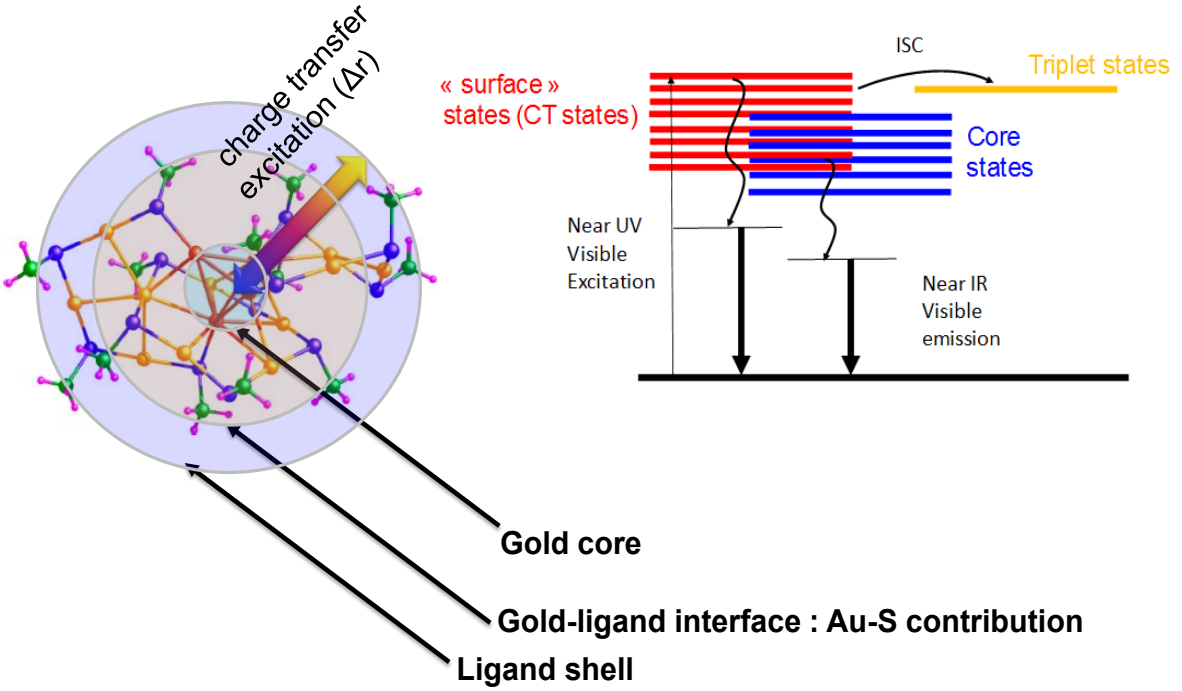

Figure 1.6 : Illustration showing the three shells of liganted gold nanoclusters that can be viewed as Au_nSR_m and the possible excitation and relaxation pathways of the system.

The last ten years, some general trends have been figured out concerning the de-excitation pathways following a visible or near-UV absorption[30]. The following experimental and theoretical findings were assembled from the present work and literature to derive the energy diagram in **Figure 1.6**. First, the local environment of gold nanoclusters can induce multiple energy transfers associated with intersystem crossings (ISC) which may explain the overall boost in PL emission and longer PL lifetimes. Upon visible excitation, the nature of states is both of "surface-like" and "core-like" (or combination of both) nature. Of course, the nature of ligands, and in particular their capability to interact through electron-rich donor groups with the surface of Au core may increase the number of "surface" states involved during excitation

(following one photon in visible or two-photon in IR) and can modulate the deexcitation pathways and thus the relative intensities in emission bands of gold nanoclusters (see **Figure 1.6**).

The non-linear optical properties of nanoclusters include two-photon absorption (TPA), two-photon fluorescence (TPF), and second- or third-harmonic generation (SHG/THG). Regarding the TPA properties, the TPA cross-sections of small thiolate-protected Au nanoclusters have been investigated to be much larger than that of typical small organic molecules; additionally, the TPA cross-sections per Au atom are also significantly larger than that of Au nanoparticles [29]. Goodson and co-workers firstly revealed the noticeable TPA properties of the Au25(SR)18 nanoclusters[31]. Antoine and co-workers allowed to gain fundamental knowledge on the mechanism involved in multiphoton processes in gold nanoclusters, at the basis of the design of efficient NLO-phores[32]. Elements that regulate the dipole moments and the nonlinear optical properties are the nanocluster size, its structure and the charge distribution on both the metal core and the bound ligands[33]. It is pertinent to draw some analogy between Au NCs and push-pull dipolar molecules, characterized by a low-lying, high-intensity absorption band, related to the intramolecular charge transfer (ICT) between the electron donor (D) and acceptor (A) groups **Figure 1.7**. The TPA cross section of such molecules (and therefore also of AuNCs) is considered to be governed by two factors: transition dipole moments and transition energies of the molecule. As seen below, the theoretical expression of TPA cross section ($\delta_{TPA}(\omega)$) based on the perturbation expansion is comprised of the numerator including transition dipole moments and the denominator including the transition energies and the incident photon energy. The energy term governs the wavelength dispersion of ($\delta_{TPA}(\omega)$) whereas the dipole moment term governs the overall magnitude of ($\delta_{TPA}(\omega)$). Thus, the structure–property relationship for the molecules with large ($\delta_{TPA}(\omega)$) can be reduced by optimizing the transition dipole moments and frequencies involved in the TPA process. As mentioned, atomically precise nanoclusters of silver or gold can be viewed as a "multi-shell system" composed by a metallic core, a metal-ligand interface and the surface ligand molecules. The "communications" between ligands and metal core may increase the transition dipole moments leading to enhanced $\delta_{TPA}(\omega)$. The

excitation energy of one photon absorption and two-photon absorption states are close for AuNCs, leading o large resonance enhancement after using near-IR excitation **Figure 1.7**.

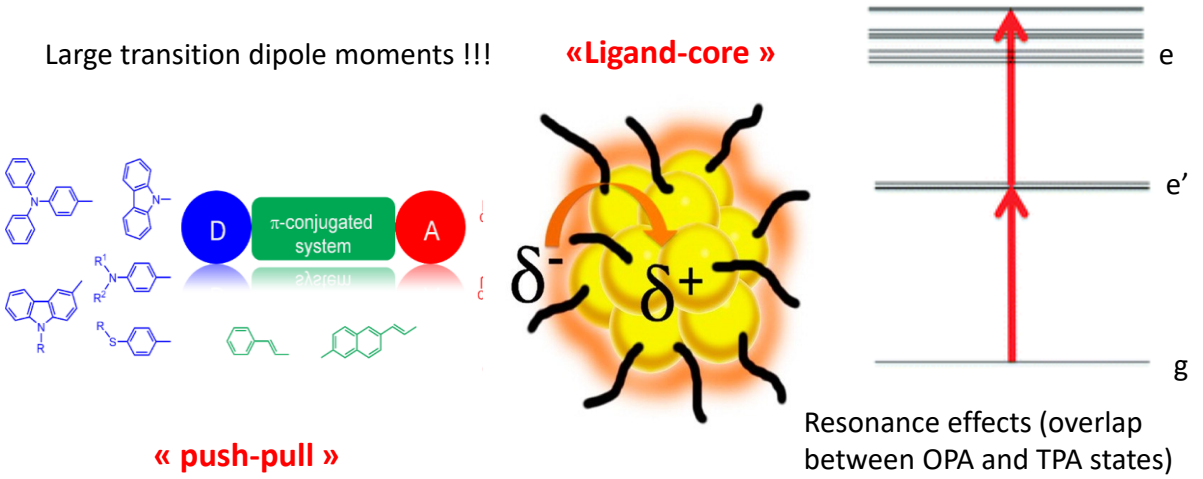

Figure 1.7: Left and middle, illustration showing push pull dipole molecule to compare it with the communication that occurs between the shells in gold NCs, and right side illustrate the similarity in terms of excitation energy between one photon absorption and two photon absorption states.

Beside optical properties, nanoclusters show their capability to be efficiently functionalized in a controlled manner. Small organic molecules and biomolecules are commonly used for functionalizing the NC surface as fluorophores to shift the optical properties of NCs toward the NIR region; drugs, photo or radiosensitizers for cancer therapy or as targeting molecules to specifically interact with receptors overexpressed at the surface of tumor cells. Two main techniques can be used to functionalize the NCs for specific molecules. The first technique involves directly synthesizing Au NCs with the molecule of interest, using a terminal thiol group that could bind to the metal surface. For instance, Le Guevel's group demonstrated that zwitterionic sulfobetaine stabilized AuNCs have the capacity to accumulate in brain tumors[34]. To further improve tumor uptake, they developed AuNCs functionalized with arginine (AuSG-2Arg), which demonstrated rapid accumulation in cancer cells, making them potentially interesting for radiotherapy enhancement[35]. A second approach is to post-functionalization of

NCs. Click chemistry and succinimidyl ester reactions have been used to covalently bind molecules of interest to the ligand stabilizing the NCs[36]. Oh et al showed a facile direct synthesis of highly luminescence water-soluble AuNCs, directly reduced in the presence of PEG dithiolane ligands in water at room temperature, the PEG can be terminated in a methoxy, amine, carboxy, leading to a QYs in the 4–8% range. The accessibility of the PEG ligand terminal groups was confirmed by DNA, dye and peptide modification[37].

Thanks to easiness of synthesis and functionalization, water solubility and biocompatibility, luminescent AuNCs have become attractive for biosensing applications. Luminescence signals of AuNCs is used to selectively and sensitively detect ions, small biomolecules, DNA/RNA, proteins and cells[38].The application of gold nanoclusters and their investigation was also reported in the last years for bio-applications, including intra-cellular signaling, nuclear localization, and biosensing of pathogens[39,40]. Compared to organic dyes, gold nanoclusters present lower toxicity and higher two photon absorption, this advantage allows to use the gold NCs to image live cells[41]. Surface functionalization of Au NCs can be rationally designed to produce their massive accumulation and to enhance selective binding toward cancerous cells. Precise medical diagnosis and treatment has triggered the development of various bioimaging techniques combining luminescence with X-ray computed tomography (CT), magnetic resonance imaging (MRI), positron emission tomography (PET), photoacoustic (PA) imaging, and ultrasound (US) imaging. CT shows the highest resolution of 3D structural details of hard tissues is obtained with CT technique, while MRI can provide high spatial resolution. On the other hand, PET has the highest detection sensitivity. Since, luminescence-based imaging technology has a limited penetration depth of light, the addition of other imaging techniques (e.g., CT, PET, MR and PA) can achieve high-resolution and sensitive bioimaging. As a first example, Le Guével and co-workers managed to produce dual-modal imaging targets with Au NCs stabilized by different shells of zwitterion ligands (with a fine control of the metal core size and the ligand coverage)[42].The higher ligand converge, the more intense fluorescence signal was reported, whereas photoacoustic signal is stronger for the largest metal core. The best compromise was obtained with Au NC candidate with an average molecular weight of 17

kDa that could be detected with high sensitivity on a 2D-near-infrared imaging instrument and by photoacoustic imaging. In vitro and in vivo experiments demonstrated an efficient cell uptake in U87 cell lines, a fast renal clearance, and a good correlation between near infrared fluorescence and photoacoustic measurements to monitor the uptake of Au NCs in the liver in the early phase[42]. Considering the advantages of MRI, the combination of AuNCs with magnetic agents, such as Gd-based compounds and Fe3O4 NPs allow for FL/MRI dual-modal imaging[43]. Also triple-modal imaging is usually more accurate in clinical diagnosis. In recent years, Gd2O3-AuNCs-ICG composites have been developed and can perform FL/CT/MRI triple-modal imaging and cancer therapy[44].

To summarize, luminescent Au-NCs have shown great potential in biosensing and bioimaging applications. Whereas they present some problem and challenges, experimental and theoretical scientist are working nowadays to address these challenges, a collective works aiming towards a luminescent Au-NCs with broad applications in biomedicine and many other fields. No studies have yet shown a liganted gold nanoclusters that present a carbonyl-reactive groups. It will be hard to compete with these methods using gold NCs, regarding the ability of targeting the carbonylation, with a high QY developed probes. Gold NCs will face different challenging in gels (composition), in cells (PH, degradation by thiolated species). Our work will introduce for the first time the application of gold nanoclusters as biomarkers to detect carbonylation in the bioimaging domain (see pictorial scheme).

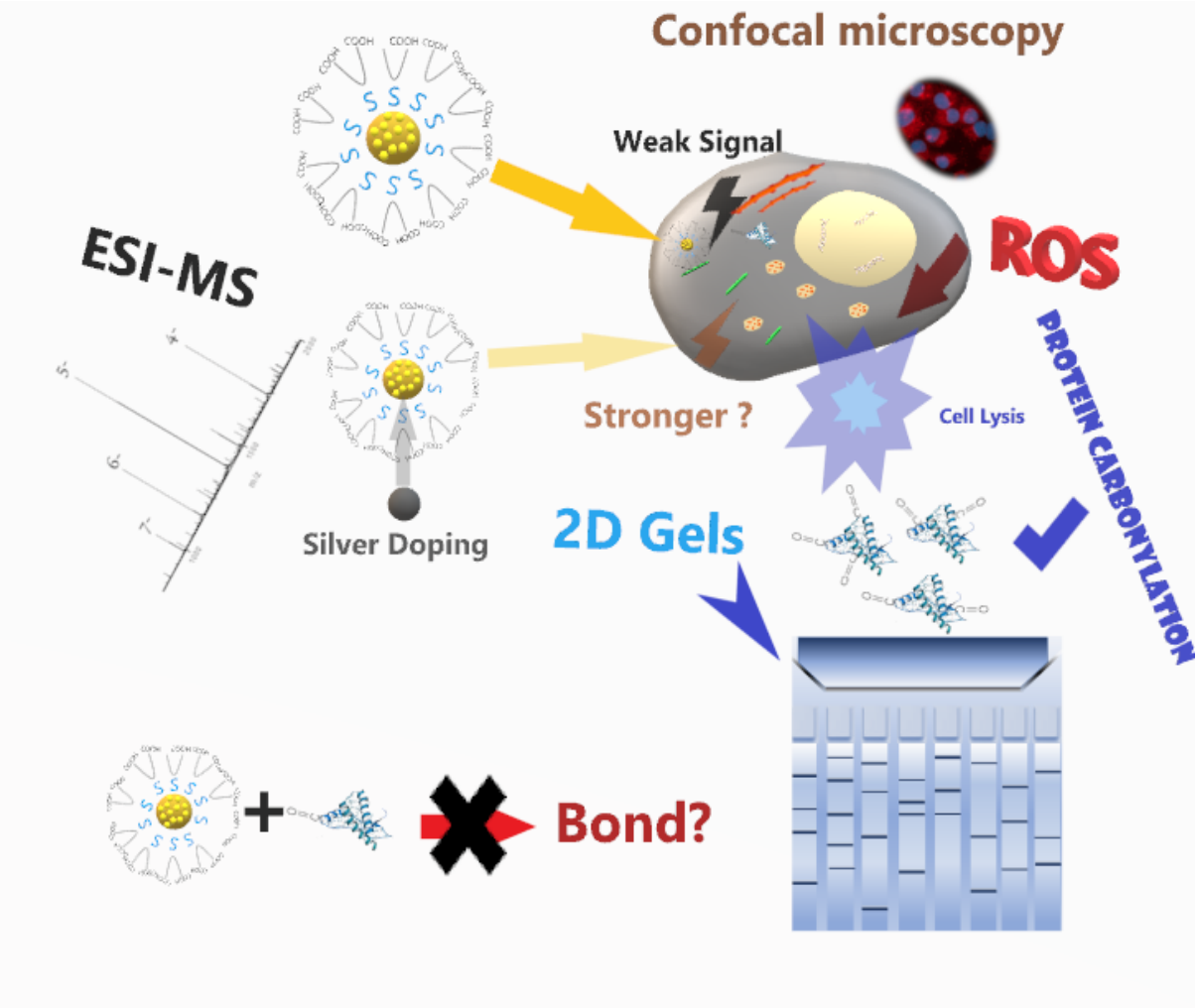

Figure 1.8 : Illustration showing a quick view of challenges and aim of the projects.

References

[1] Smith AM, Mancini MC, Nie S. Second window for in vivo imaging. Nature Nanotech. 2009;4(11):710-711. doi:10.1038/nnano.2009.326

[2] Li JB, Liu HW, Fu T, Wang R, Zhang XB, Tan W. Recent Progress in Small-Molecule Near-IR Probes for Bioimaging. TRECHEM. 2019;1(2):224-234. doi:10.1016/j.trechm.2019.03.002

[3] Golovynskyi S, Golovynska I, Stepanova LI, et al. Optical windows for head tissues in near-infrared and short-wave infrared regions: Approaching transcranial light applications. Journal of Biophotonics. 2018;11(12):e201800141. doi:10.1002/jbio.201800141

[4] Lei Z, Zhang F. Molecular Engineering of NIR-II Fluorophores for Improved Biomedical Detection. Angewandte Chemie International Edition. 2021;60(30):16294-16308. doi:10.1002/anie.202007040

[5] Zhao J, Zhong D, Zhou S. NIR-I-to-NIR-II fluorescent nanomaterials for biomedical imaging and cancer therapy. J Mater Chem B. 2018;6(3):349-365. doi:10.1039/C7TB02573D

[6] Dröge W. Free Radicals in the Physiological Control of Cell Function. Physiological Reviews. 2002;82(1):47-95. doi:10.1152/physrev.00018.2001

[7] Valko M, Leibfritz D, Moncol J, Cronin MTD, Mazur M, Telser J. Free radicals and antioxidants in normal physiological functions and human disease. The International Journal of Biochemistry & Cell Biology. 2007;39(1):44-84. doi:10.1016/j.biocel.2006.07.001

[8] Forman HJ, Fukuto JM, Torres M. Redox signaling: thiol chemistry defines which reactive oxygen and nitrogen species can act as second messengers. American Journal of Physiology-Cell Physiology. 2004;287(2):C246-C256. doi:10.1152/ajpcell.00516.2003

[9] Irvine GB, El-Agnaf OM, Shankar GM, Walsh DM. Protein Aggregation in the Brain: The Molecular Basis for Alzheimer's and Parkinson's Diseases. Mol Med. 2008;14(7):451-464. doi:10.2119/2007-00100.Irvine

[10] Krisko A, Radman M. Protein damage, ageing and age-related diseases. Open Biology. 9(3):180249. doi:10.1098/rsob.180249

[11] Krisko A, Radman M. Phenotypic and Genetic Consequences of Protein Damage. PLOS Genetics. 2013;9(9):e1003810. doi:10.1371/journal.pgen.1003810

[12] Dukan S, Farewell A, Ballesteros M, Taddei F, Radman M, Nyström T. Protein oxidation in response to increased transcriptional or translational errors. Proceedings of the National Academy of Sciences. 2000;97(11):5746-5749. doi:10.1073/pnas.100422497

[13] Role of oxidative carbonylation in protein quality control and senescence. The EMBO Journal. 2005;24(7):1311-1317. doi:10.1038/sj.emboj.7600599

[14] Bizzozero OA. Protein Carbonylation in Neurodegenerative and Demyelinating CNS Diseases. In: Lajtha A, Banik N, Ray SK, eds. Handbook of Neurochemistry and Molecular Neurobiology: Brain and Spinal Cord Trauma. Springer US; 2009:543-562. doi:10.1007/978-0-387-30375-8_23

[15] Baraibar MA, Ladouce R, Friguet B. Proteomic quantification and identification of carbonylated proteins upon oxidative stress and during cellular aging. J Proteomics. 2013;92:63-70. doi:10.1016/j.jprot.2013.05.008

[16] Hawkins CL, Davies MJ. Detection, identification, and quantification of oxidative protein modifications. J Biol Chem. 2019;294(51):19683-19708. doi:10.1074/jbc.REV119.006217

[17] Yan LJ, Forster MJ. Chemical probes for analysis of carbonylated proteins: a review. J Chromatogr B Analyt Technol Biomed Life Sci. 2011;879(17-18):1308-1315. doi:10.1016/j.jchromb.2010.08.004

[18] Levine RL, Garland D, Oliver CN, et al. [49] Determination of carbonyl content in oxidatively modified proteins. In: Methods in Enzymology. Vol 186. Oxygen Radicals in Biological Systems Part B: Oxygen Radicals and Antioxidants. Academic Press; 1990:464-478. doi:10.1016/0076-6879(90)86141-H

[19] Luo S, Wehr NB. Protein carbonylation: avoiding pitfalls in the 2,4-dinitrophenylhydrazine assay. Redox Report. 2009;14(4):159-166. doi:10.1179/135100009X392601

[20] Anderson JM. Fluorescent hydrazides for the high-performance liquid chromatographic determination of biological carbonyls. Analytical Biochemistry. 1986;152(1):146-153. doi:10.1016/0003-2697(86)90133-8

[21] Milic I, Hoffmann R, Fedorova M. Simultaneous Detection of Low and High Molecular Weight Carbonylated Compounds Derived from Lipid Peroxidation by Electrospray Ionization-Tandem Mass Spectrometry. Anal Chem. 2013;85(1):156-162. doi:10.1021/ac302356z

[22] Feng J, Navratil M, Thompson LV, Arriaga EA. Estimating relative carbonyl levels in muscle microstructures by fluorescence imaging. Anal Bioanal Chem. 2008;391(7):2591-2598. doi:10.1007/s00216-008-2187-5

[23] Vemula V, Ni Z, Fedorova M. Fluorescence labeling of carbonylated lipids and proteins in cells using coumarin-hydrazide. Redox Biology. 2015;5:195-204. doi:10.1016/j.redox.2015.04.006

[24] Tamarit J, de Hoogh A, Obis E, Alsina D, Cabiscol E, Ros J. Analysis of oxidative stress-induced protein carbonylation using fluorescent hydrazides. Journal of Proteomics. 2012;75(12):3778-3788. doi:10.1016/j.jprot.2012.04.046

[25] Kuzmic M, Javot H, Bonzom JM, et al. In situ visualization of carbonylation and its co-localization with proteins, lipids, DNA and RNA in Caenorhabditis elegans. Free Radical Biology and Medicine. 2016;101:465-474. doi:10.1016/j.freeradbiomed.2016.11.004

[26] Kuzmić M. UNIVERSITY OF SPLIT SCHOOL OF MEDICINE. :123.

[27] October 2007 SH. Nanoparticle reveals sulphur's Midas touch. Chemistry World. Accessed July 16, 2022. https://www.chemistryworld.com/news/nanoparticle-reveals-sulphurs-midas-touch/3002675.article

[28] Kang X, Zhu M. Tailoring the photoluminescence of atomically precise nanoclusters. Chem Soc Rev. 2019;48(8):2422-2457. doi:10.1039/C8CS00800K

[29] Antoine R, Bonačić-Koutecký V. Liganded Silver and Gold Quantum Clusters. Towards a New Class of Nonlinear Optical Nanomaterials. Springer International Publishing; 2018. doi:10.1007/978-3-319-64743-2

[30] Wei X, Kang X, Zhu M. Photoluminescence of metal nanoclusters. In: Reference Module in Materials Science and Materials Engineering. Elsevier; 2021. doi:10.1016/B978-0-12-822425-0.00043-9

[31] Ramakrishna G, Varnavski O, Kim J, Lee D, Goodson T. Quantum-Sized Gold Clusters as Efficient Two-Photon Absorbers. J Am Chem Soc. 2008;130(15):5032-5033. doi:10.1021/ja800341v

[32] Antoine R. Ligand-Core NLO-Phores. In: Koleżyński A, Król M, eds. Molecular Spectroscopy—Experiment and Theory: From Molecules to Functional Materials. Challenges and Advances in Computational Chemistry and Physics. Springer International Publishing; 2019:139-160. doi:10.1007/978-3-030-01355-4_5

[33] Russier-Antoine I, Bertorelle F, Calin N, et al. Ligand-core NLO-phores: a combined experimental and theoretical approach to the two-photon absorption and two-photon excited emission properties of small-ligated silver nanoclusters. Nanoscale. 2017;9(3):1221-1228. doi:10.1039/C6NR07989J

[34] Longo E, Bravin A, Brun F, et al. 3D map of theranostic nanoparticles distribution in mice brain and liver by means of X-ray Phase Contrast Tomography. J Inst. 2018;13(01):C01049-C01049. doi:10.1088/1748-0221/13/01/C01049

[35] Porret E. Applications des nanoclusters de métaux nobles pour lediagnostic et la thérapie ciblée du cancer. phdthesis. Université Grenoble Alpes; 2019. Accessed September 22, 2022. https://tel.archives-ouvertes.fr/tel-03175729

[36] Porret E, Guével XL, Coll JL. Gold nanoclusters for biomedical applications: toward in vivo studies. J Mater Chem B. 2020;8(11):2216-2232. doi:10.1039/C9TB02767J

[37] Oh E, Fatemi FK, Currie M, et al. PEGylated Luminescent Gold Nanoclusters: Synthesis, Characterization, Bioconjugation, and Application to One- and Two-Photon Cellular Imaging. Particle & Particle Systems Characterization. 2013;30(5):453-466. doi:10.1002/ppsc.201200140

[38] Chen LY, Wang CW, Yuan Z, Chang HT. Fluorescent Gold Nanoclusters: Recent Advances in Sensing and Imaging. Anal Chem. 2015;87(1):216-229. doi:10.1021/ac503636j

[39] Chan PH, Chen YC. Human Serum Albumin Stabilized Gold Nanoclusters as Selective Luminescent Probes for Staphylococcus aureus and Methicillin-Resistant Staphylococcus aureus. Anal Chem. 2012;84(21):8952-8956. doi:10.1021/ac302417k

[40] Lin SY, Chen NT, Sum SP, Lo LW, Yang CS. Ligand exchanged photoluminescentgold quantum dots functionalized with leading peptides for nuclear targeting and intracellular imaging. Chem Commun. 2008;(39):4762-4764. doi:10.1039/B808207C

[41] Olesiak-Banska J, Waszkielewicz M, Obstarczyk P, Samoc M. Two-photon absorption and photoluminescence of colloidal gold nanoparticles and nanoclusters. Chem Soc Rev. 2019;48(15):4087-4117. doi:10.1039/C8CS00849C

[42] Shen D, Henry M, Trouillet V, et al. Zwitterion functionalized gold nanoclusters for multimodal near infrared fluorescence and photoacoustic imaging. APL Materials. 2017;5(5):053404. doi:10.1063/1.4977203

[43] Yuan Y, Ding Z, Qian J, et al. Casp3/7-Instructed Intracellular Aggregation of Fe3O4 Nanoparticles Enhances T2 MR Imaging of Tumor Apoptosis. Nano Lett. 2016;16(4):2686-2691. doi:10.1021/acs.nanolett.6b00331

[44] Han L, Xia JM, Hai X, Shu Y, Chen XW, Wang JH. Protein-Stabilized Gadolinium Oxide-Gold Nanoclusters Hybrid for Multimodal Imaging and Drug Delivery. ACS Appl Mater Interfaces. 2017;9(8):6941-6949. doi:10.1021/acsami.7b00246

Chapter 2: Experimental Techniques

Introduction

Nanoclusters (NCs) are a specific class of nanomaterials, bridging the gap between molecules and nanoparticles. When such nanoclusters are protected by ligands (in particular thiolates), atomic precision can be raised. And such (thiolate) ligand protected nanoclusters typically consist of few gold or silver atoms and ligands, denoted as Mn(SR)m where SR is the thiolate ligand and M is the noble metal used, n and m the number of metal and ligands for the NC, respectively. In contrast to nanoparticles, their physical-chemical characteristics are not only determined by their size, structure, and surface area. But since atomic precision can be obtained, their characterization in terms of molecular formula and structure and their optical properties is crucial for fundamentals and applied research. For instance, during my PhD work, the quest for enhanced nonlinear optical targets has led us to explore their optical properties in the nonlinear optical regime for applications in bioimaging using multiphoton confocal microscopy.

Exhaustive characterization of nanoclusters allows us to figure out the structure-optical properties relationship. To this aim, we used diverse types of instrumentation combining (mainly) mass spectrometry characterization (electrospray time of flight mass spectrometry, ESI-TOF MS) and optical characterizations both using linear optics (UV-Vis absorption, photoluminescence, lifetime measurement) and non-linear optics (hyperpolarizabilities, two photon absorption and emission cross sections).

In this chapter, I will describe the main techniques I used during this PhD work aiming at figuring out the structure-optical properties relationship for the as-synthesized nanoclusters. Since this work was application oriented for using such nanoclusters as (nonlinear) optical targets for bioimaging using multiphoton confocal microscopy, the optical set-ups aiming at evaluating their photoluminescence properties will be thoroughly described and the last part of this chapter will be devoted to the description of in vitro bio-imaging set-ups and protocols.

2.1 Characterization of thiolate-protected gold nanoclusters with Time-of-flight mass spectrometry

2.1.1 Introduction

Mass spectrometry (MS), as a tool for characterization of nanomaterials, as regained new interests with the advancement of atomically precise nanoclusters (NCs) [1,2],which are materials that can produced at the atomic precision of general formula Au_xL_y (where L corresponds to different types of Ligands). In terms of size and mass, such nanoclusters range in the 2-3 nm diameter range and with molecular weights ranging between few dozen to few hundreds of kilodalton (10^3 g/mol) In the early 1990s, Whetten and Murray groups tried to determine the molecular formula of noble metal nanoclusters using electrospray ionization coupled to time of flight (TOF) mass spectrometry (ESI-MS). [3] [4] [5] ESI-MS take a lot of attention for many years and have been only recently developed for noble metal nanoclusters composition analysis. For these nanomaterials, due to their extremely small size, size determination by other techniques like transmission electronic microscopy (TEM) or dynamic light scattering (DLS), standard techniques for sizing nanoparticles, are usually not accurate or even not possible. On the other hand, with modern mass spectrometers (with extended mass range and high resolution and high accuracy), MS can accurately identify their compositions. Of course, if the nanoclusters are stable enough and if crystals can be produced at the gram-scale, powerful methods like single crystal Xray crystallography may be used for their structural characterization at the atomic precision. Even if more than hundred crystals structures are now available for nanoclusters, single crystal Xray crystallography is only applicable with particular ligands (mainly aromatic containing ligands) and failed to be applied with ligands using biomolecules (peptides, proteins, DNAs) or polymers. MS remains the most powerful characterization tools for such nanoclusters.

Electrospray ionization (ESI) has emerged as an important ionization technique for transferring large molecules in the gas phase [6]. ESI is a powerful, sensitive, and "soft" ionization technique that creates a minimum fragment in the ionization process. Coupled to mass spectrometry and in particular time-flight mass spectrometers (TOF-MS), ESI-TOF-MS is capable of quantitatively analyzing the molecular weight of analytes ranging from 100 Da to over 100 kDa at optimized operation conditions. This mass range is optimal for mass characterization of gold nanoclusters. Indeed, the mass of $Au_{10}(SG)_{10}$ (one of the smallest NCs) is 5333 Da and $Au_{144}(pMBA)_{60}$ (one of the largest NCs) is 34,662 kDa. Currently, by using ion mirrors like reflectors, the flight path of the ions could be extended by reflections or even multiple reflections and modern commercial TOF analyzers can reach a resolving power ($m/\Delta m$) of about 50,000 or more at m/z 20–16,000, with mass accuracy that can be as low as few tens of ppm. Such high resolving power allows for resolving isotopic pattern in atomically precise metal nanoclusters. Also of tremendous importance, mass accuracy reaching few tens of ppm, allows for unambiguous mass assignment.

During my PhD work, I have been using the ESI-TOF-MS instrumentation. MicrOTOF is an instrument developed by Brucker Daltonics® society. This mass spectrometry, based on the time-of-flight measurement where the ions are guided from the source to the mass analyzer then separated in m/z by the electric fields (time of flight is related to m/z ratio) and analyzed by the detector. The mass and charge of the species are the main parameters, smaller the m/z species, the faster it will arrive to the detector.

The entire system (presented in **Figure 2.1**) typically consists of an electro-spray-ionization Source known as ESI (Spray chamber and Desolvation assembly) transferring and ionizing analytes from the solution to the gas phase, an ion selection room (Transfer Optics) for guidance and focalization of ions flux and a detector based on time of flight TOF principle.

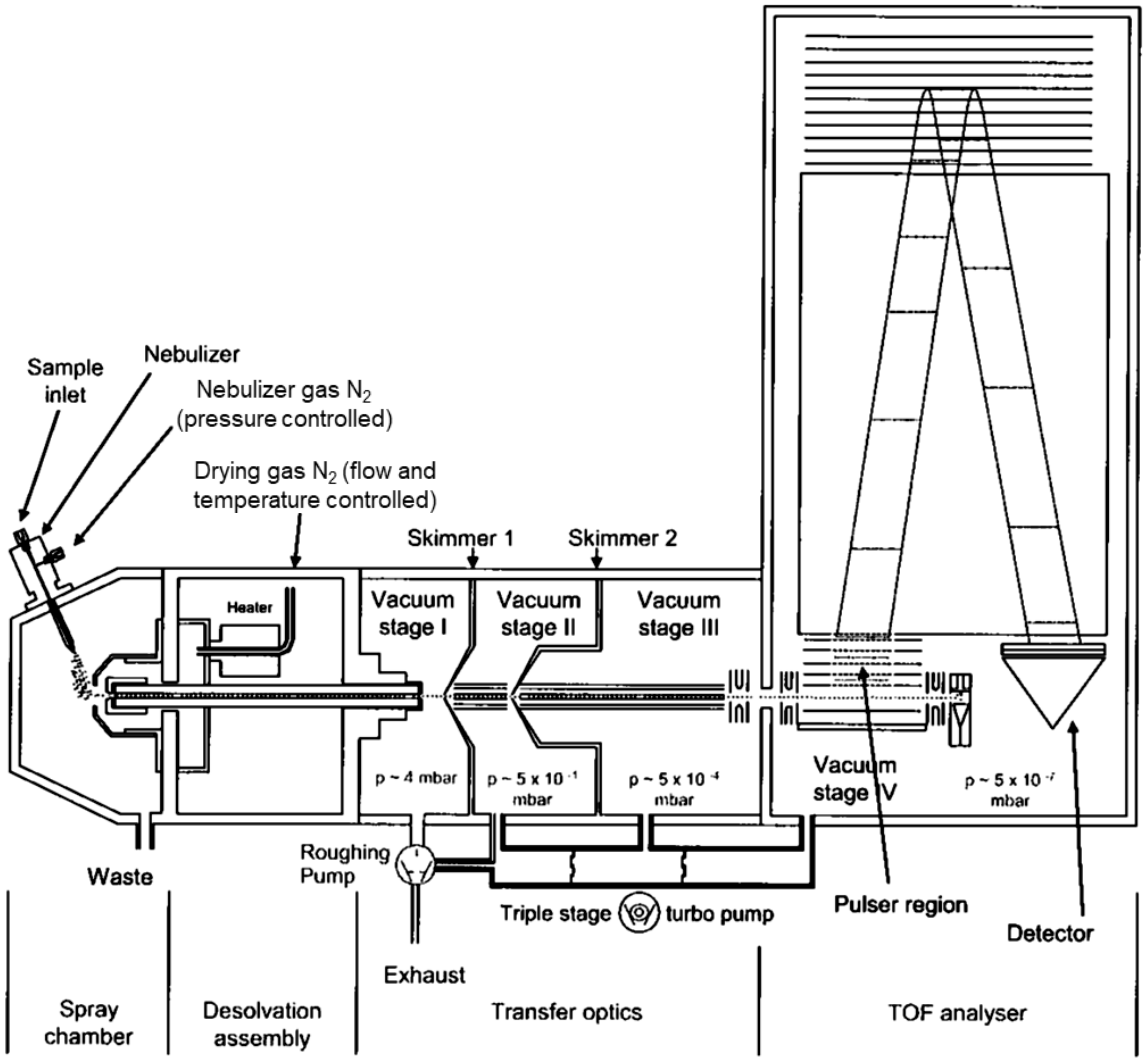

Figure 2.1 : Detailed parts of micrOTOF from Bruker.

2.1.2 ESI-TOF-MS : basic principles

2.1.2.1 ESI source : ions in the gas phase, from charged droplets formation and to desolvation process

A dilute (~10-100 µM in polar volatile solvent : water, water/methanol) analyte solution (containing NCs) is injected by a mechanical syringe pump through a stainless-steel capillary at low flow rate (typically 300µL/hour). A high voltage (2600 kV) is applied to the tip of the metal capillary relative to a heated capillary. This strong electric field causes the dispersion of the sample solution into an aerosol of highly charged electrospray droplets (see **Figure 2.2**). The charged droplets diminish in size by solvent evaporation. The droplets must be small enough to ensure the desolvation process (solvent removal). Charged droplets will get closer and closer, leading to increased Coulomb repulsion. When the coulomb repulsion is larger than the surface tension of droplets (Rayleigh instability), additional fissions of droplets lead to the formation of smaller and droplets up to complete desolvation and formation of gas phase ions. A coaxial sheath gas (dry N2) injected through two concentric tubes flow around the capillary results in better nebulization. This gas flow also helps to direct the spray emerging from the capillary tip towards the mass spectrometer. Also, a flow of nitrogen (heated drying gas) is

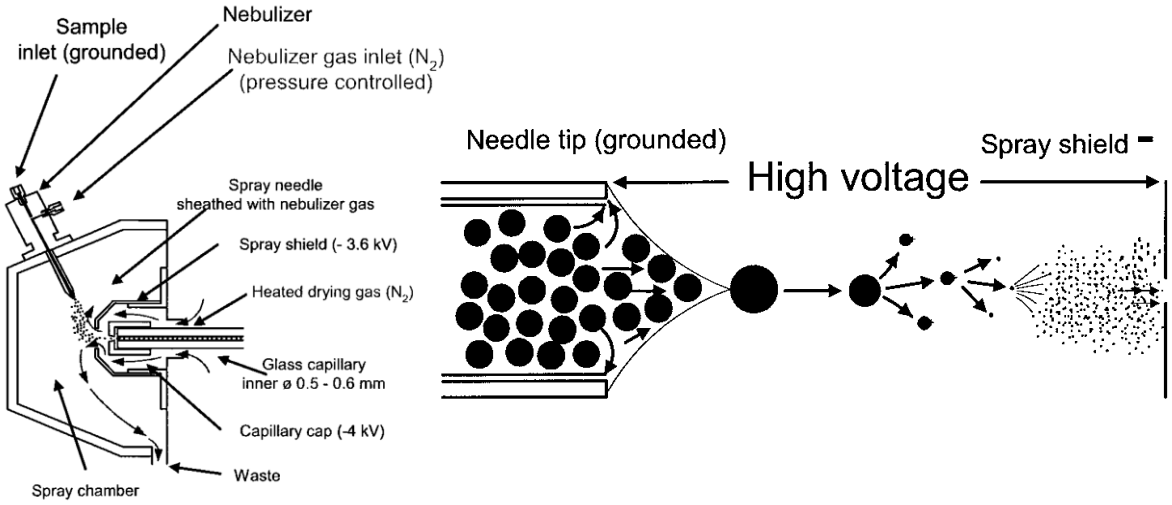

Figure 2.2 : Global view of the Bruker ESI system (Left) and the ESI process (Right).

added at the entrance of the glass capillary to complete desolvation and formation of gas phase ions.

2.1.2.2 Transfer optics

After the total desolvation of droplets, the gas phase ions will be transmitted into the Transfer optics (**Figure 2.3**) to focus them and maintain a uniform trajectory of ions (ion bunch with a well-defined spatial-temporal extension). The transfer optics consist of three vacuum stages separated by skimmers. The skimmers are small apertures , the central opening of skimmers is small enough to maintain the pressure difference between the vacuum stages.

The coated metal of the glass capillary ends with a potential of about +200 V. When the ions exit the capillary and go into the first stage vacuum, they will go from a steady steam beam to a subsonic jet due to the potential difference the capillary ends and the skimmers grounded potential. The potential of skimmers can be modified to control the potential difference and thus ions kinetic energy, especially between the first and second skimmers.

The first vacuum stage operates at pressure of about 4 mbar and directly connected to the roughing pump, the second and third vacuum is connected to one triple stage turbo-drag pump. The second and third vacuum stage will support the ion motion with a dragging force due to the difference of the pressure between each stage (5×10^{-1} and 5×10^{-4} mbar successively). A hexapole is seated in the second and third stage vacuum, to adjust a stable trajectory that will enter the TOF assembly system. The lens voltages at the end of the third stage are controlled by the PC software and are adjusted to ensure more ion stability at the exit.

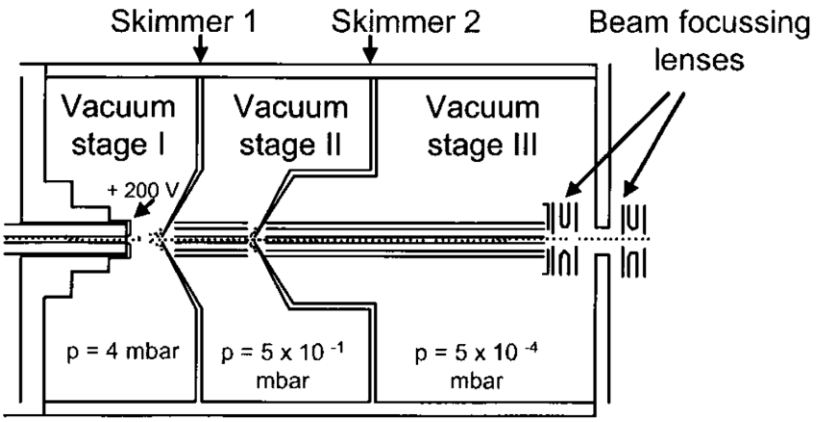

Figure 2.3 : Transfer optics system from micrOTOF Bruker

2.1.2.3 TOF assembly

This part consists of a fourth vacuum stage, operating at about 5×10^{-7} mbar, a quadrupole and a collision cell allowing the possibility to isolate and fragment the ions of interest. For fragmentation experiments, the quadrupole will filter the flux and isolate the ions with a fixed mass/charge ratio. The ions will enter the collision cell, facing a collision gas (Argon) to fragment them, some nanoclusters are highly stable such as Au10SG10 and a very high collision energy is required to fragment them, but for others like Au18SG14, a moderate collision energy is enough to induce fragmentation leading to small fragments like Au4SG4, so usually low collision energy should be set up to prevent the fragmentation of the samples. The transmitted energy to the ions due to the combination of the Quadrupole and collision cell system will define the settings of the lens in the entrance and exit of the chamber.

Ions then will enter to the TOF analyzer consisting of three main parts:

- Orthogonal accelerator
- Reflector
- Detector

The orthogonal accelerator consists of assemblies of electrodes on the top of each other, assembled towards the reflector and shaped like slot diaphragms. This stage represents the ion source acting in pulse mode. Acceleration electrodes with a high voltage will direct the ions to the first field free region and towards the reflector. The ions will then have a motion in a U shape in the ion reflector and then will be directed towards the second free flight region and then to the ion detector (see figure 4).

The fundamental equation for the determination of the mass/charge is related to the potential energy, kinetic energy, and time of flight of the ion inside the detection tube.

Let us suppose that all the ions are produced at the same time and position, each ion have the same total energy:

$$E_T = E_p + E_k \quad \textbf{(2.1.2.1)}$$

Where E_T is the total energy, E_p is the potential energy and E_k is the kinetic energy.

Once the ions leave the acceleration zone, the potential energy will be converted to kinetic energy:

$$E_p = E_c = zeU = \frac{1}{2}mv^2 \rightarrow v = \sqrt{\frac{2zeU}{m}} \quad \textbf{(2.1.2.2)}$$

Where v is the velocity, U is the potential difference, m is the mass of the ion and z is the charge.

The time of traveled of the ion is given by:

$$t = \frac{D}{v} \quad \textbf{(2.1.2.3)}$$

Where D is the tube length. Replacing v is this equation will give:

$$t = D\sqrt{\frac{m}{2zeV}} \rightarrow \frac{m}{z} = \frac{2eUt^2}{D^2} \qquad \textbf{(2.1.2.4)}$$

The main rule of the reflector is to normalize the energy difference between ions (due to different penetration of ions in the reflector) and to improve the resolution (due to the 2 field free regions) to obtain a high-quality mass spectrum. The ion detector will convert an ion signal into an electric signal. The signal from the detector is transmitted to a digitizer card, which is mounted in the PC. The detectors of micrOTOF are designed as micro channel plate detectors,

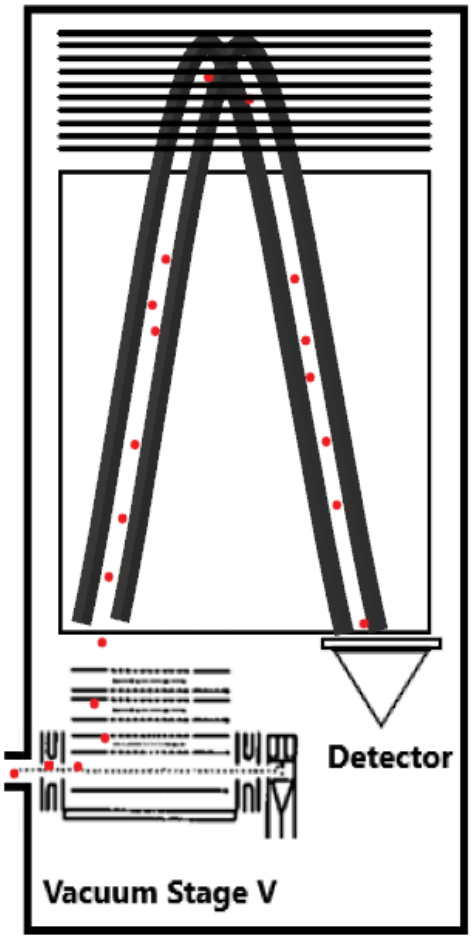

Figure 2.4 : TOF Assembly system from micrOTOF Bruker.

coated with a semi conductive layer, works as an electron multiplier, and mounted in parallel to obtain a maximum electron yield. The system is represented in.

2.1.3 Q-TOF for Nanoclusters

With the micrOTOF instrument, there are the positive-ion mode and the negative-ion mode for ESI-MS, which can detect positively charged species and negatively charged species, respectively. This mode of ionization is simply driven by the polarity of the electric fields in the ESI source and in the MS chambers (ion transfer and TOF voltages). Depending on the nature chemical groups of surface ligands either positive-ion mode or the negative-ion mode can be chosen to get optimal mass spectra and determine the composition of noble-metal NCs. In the positive-ion mode, the positive charges mostly come from the adsorption of protons and alkali cations to the noble-metal NCs. For example, noble-metal NCs may appear in the form of $[MnLm+x\ H]^{z+}$ (addition of protons) or $[MnLm+x\ alk]^{z+}$ (addition of other cations such as alkali ions) ions. On the other, the negative charges in negative-ion-mode ESI-MS, charges come from the intrinsic negative charges of the noble-metal or deprotonation of the chemical groups in ligands (as for example glutathione). Hence, in the negative-ion mode of ESI-MS, noble-metal NCs may appear in the form of $[MnLm-x\ H]^{z-}$ (removal of protons). Gold nanoclusters protected by acidic ligands are mostly presented as anions in the solution (at neutral pH), the ESI-MS will provide spectrum of the samples with different charge state, for example $Au_{15}SG_{13}$ have 4 charge state 4^-,5^-,6^- and 7^- and so 4 m/z peaks (see **Figure 2.5**).

As mentioned before, problems of fragmentation can appear due to high collision energy, especially for “fragile” nanoclusters such as $Au_{18}SG_{14}$ resulting in “typical” fragments like Au_4SG_4. We found soft optimized settings for all nanoclusters where we put the collision energy at zero but change some lens voltage in transfer optics, all parameters are controlled with Otof Control by Bruker Daltonik, where some was not modified after the calibration,

unlike lens 4,5,6 and collision energy in Collision cell, modified for each NCs for better spectrum, less fragments and more charge states **Table 2-1**.

	$Au_{15}SG_{13}$	$Au_{18}SG_{14}$
Capillary	2400 V	3100 V
Nebulizer	2.5 bar	2.5 bar
Lens 4	16V	21V
Lens 5	15V	15V
Lens 6	18V	21V
Collision energy	0.9 ev	0.5 ev
isCIS energy	1 ev	0 ev

Table 2-1 : Comparison of some parameters in the QTOF for two NCs to optimize the signal and prevent fragmentation of the cluster.

All chemical composition of nanoclusters is assigned by comparing the experimental isotope pattern for a given charge state of NCs with the simulated isotope pattern via TOF Bruker Daltonik Data Analysis, an example of $Au_{15}SG_{13}$ is shown in **Figure 2.5** where we used the following formula for the simulation isotopic pattern: $Au_{15}(C_{10}H_{16}N_3O_6S)_{13}$ (glutathione is a tripeptide with the following chemical formula $C_{10}H_{16}N_3O_6S$), **Figure 2.6**. The perfect

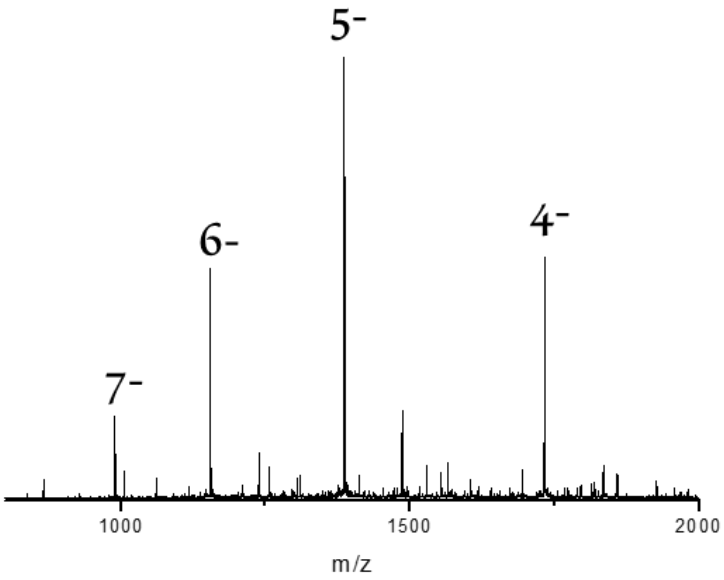

Figure 2.5 : ESI Mass spectrum for $Au_{15}SG_{13}$ operated in negative mode, a peak of $Au_{16}SG_{14}$ beside $[Au_{15}SG_{13}{}^{-H}]^{5-}$ is recorded due to some impurity of the synthesis, the negative charge comes from the deprotonation of the samples.

agreement between the experimental and simulated patterns allow for an unambiguous cluster composition assignment.

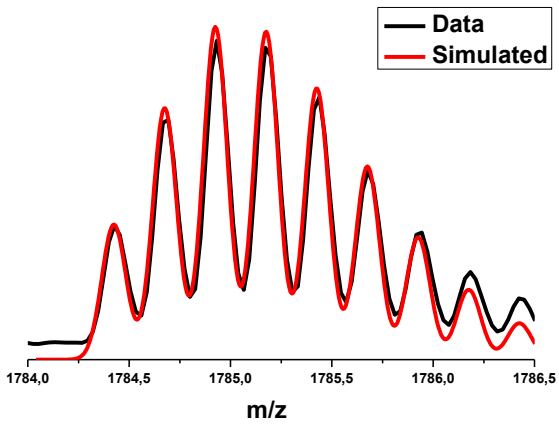

Figure 2.6 : Isotope pattern (black) and isotope pattern simulation (red) for $[Au_{15}SG_{13}{}^{-H}]^{4-}$ where we used the chemical formula of the molecule, and it is clear that it fits with the experimental results.

2.2 Sizing thiolate-protected gold nanoclusters by fluorescence anisotropy.

Due to their narrow width, sizing of fluorescent metal nanoclusters was and is an interesting type of characterization. Many analytical methods like DLS[7] , and TEM[8] are used as sizing methods. However, these traditional techniques used for the size characterization of large metal nanoparticles are not very applicable for nanoclusters. A complementary method for size determination is time-resolved fluorescence anisotropy TRFA and has been developed and applied for nanoclusters during the thesis of Antonin Soleilhac[9]. Time-resolved fluorescence anisotropy is widely used for many biological applications, including studying protein folding, to give information on the size and shape of proteins (in the size range 2-20 nm) to measure protein-protein interaction and binding conformational dynamics[10 11 12].

The absorption of the light in a luminescent material is related to its transition dipole moment, on other word, the coupling of the electromagnetic field with the dipole moment. When the sample is excited with a linearly polarized light, parallel to the transition dipole moment of the molecule, the absorption will be more efficient, and so its emission because both of photon absorption and emission have the same orientation, only the molecules that have a parallel transition dipole moment will be excited efficiently, this is called photo-selection **Figure 2.7**.

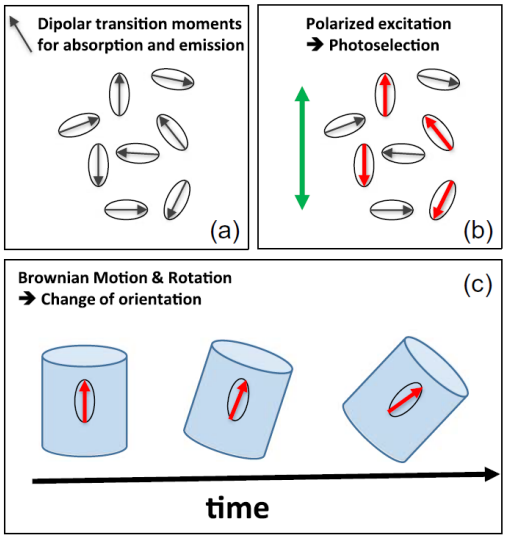

Figure 2.7 : (a) and (b) Illustration of the photo-selection process of a randomly oriented fluorophores by vertically polarized light followed by (c) rotational diffusion of a labelled protein with an intrinsic fluorophore.

This fluorescence anisotropy is based on the rotational Brownian motion of the molecule, once excited, the molecule moves during the life span of its excited state, the emission light will have a different direction, and hence a loss of fluorescence intensity (see figure 7). The loss of the fluorescence is quantified by the fluorescence anisotropy r(t) given by the following equation:

$$r(t) = \frac{I_{VV}(t) - \frac{I_{HV}(t) \times I_{VH}(t)}{I_{HH}(t)}}{I_{VV}(t) + \frac{I_{HV}(t) \times I_{VH}(t)}{I_{VH}(t)}} \qquad \textbf{(2.1.3.1)}$$

where I is the fluorescent intensity and for I_{XY}, X is direction of the excited polarized light and Y is the orientation of the collected emission light (V:Vertical H:Horizantal). We used a mono-exponential fitting to calculate the value of r(t):

$$r(t) = r_0 e^{-t/\theta} \quad \textbf{(2.1.3.2)}$$

where r_0 is the anisotropy at time t = 0 and θ is the rotational correlation time defined by the Stokes-Einstein relation:

$$\theta = \frac{\eta V}{kT} \quad \textbf{(2.1.3.3)}$$

where η is the viscosity of the solution, k the Boltzmann constant, T the temperature and V the volume of the rotating object. Once we know the volume, we can calculate the radius and hence its diameter (assuming a spherical object). The hydrodynamic size of clusters is then determined by the radius of a sphere with volume V. Here we would like to emphasize that the radius that is extracted from fluorescence anisotropy measurements is the hydrodynamic radius of nanoclusters, e.g., the radius of the nanoclusters with the addition the first shell of solvation.

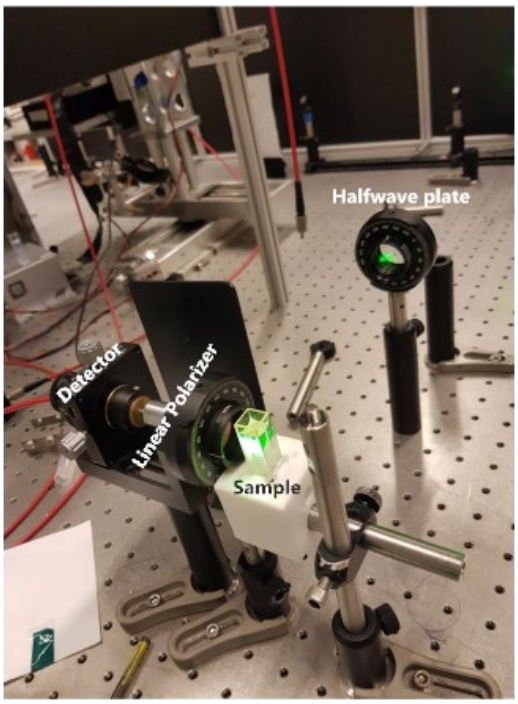

Figure 2.8 : Photograph of the instrumental set up.

This means that usually radius extracted from such sizing techniques are close to DLS measurements and higher than those extracted from TEM images analysis[13]. The measurement setup is given in **Figure 2.9** where a picosecond laser (PGx03 series Optical Parametric Generators (OPG) from EKSPLA) pumped by a 1 kHz mode-locked laser was used for excitation. The emission is collected using an optical fiber connected to a photomultiplier tube (R1463, Hamamatsu). The fluorescence decay signal was preamplified by a fast preamplifier (350 MHz Preamplifier SR445A, Stanford Research) and recorded as a function of time with a fast digital oscilloscope (Lecroy LT322). For time resolved fluorescence anisotropy measurements, a polarizing beam-splitter cube and a half-wave plate were used to tune the vertical or horizontal linear polarity of the light on the excitation line. A linear broadband polarizer in the range 500–720 nm was used for the collection according to the vertical or horizontal axis.

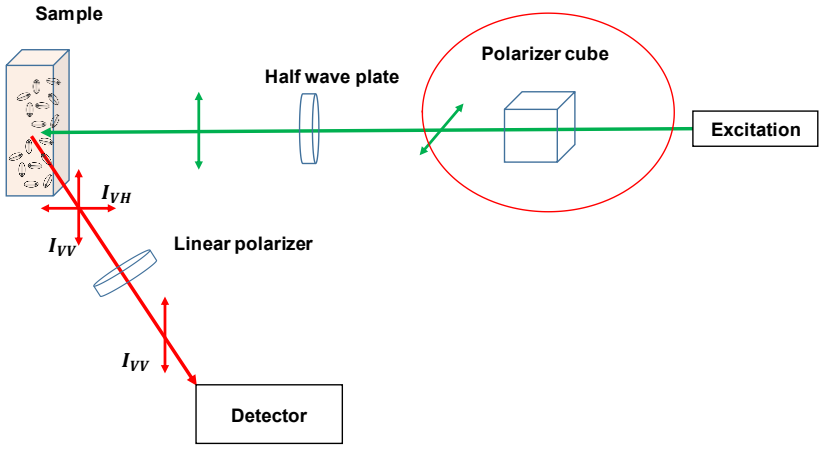

Figure 2.9 : Schematic view of the experimental setup to measure fluorescence anisotropy r.

Four replicates of measurement are usually conducted for the fluorescence anisotropy measurements as shown in **Figure 2.10**. Error bars are given by the standard error of the mean on the rotational correlation time measured on the four replicates individually **Figure 2.10**. The use of a high viscosity solvent (like glycerol) provides measurable anisotropy decay in the

nanocluster size range of 1−3 nm. Further cooling of the solvent temperature could help to further increase the sensitivity of this technique. In my PhD work, the limitation of this technique is given by the minimum decay time measured with enough precision in anisotropy decay curves which is ~100 ns, which corresponds to 0.8 nm for the smallest size.

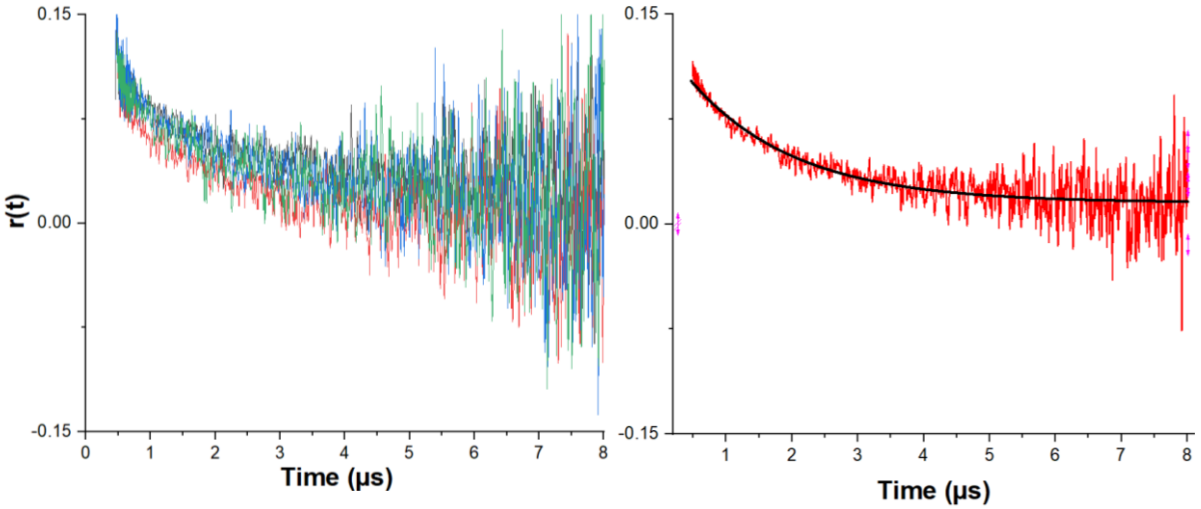

Figure 2.10 : Four replicate of measurement for the same species (On the left) and the average of the 4 (on the right).

Before any experiments, testing conditions are required. First, we need to check he alignment the laser polarization and the assembly of the half-wave plate and the linear broadband polarizer, we use a slightly diffusing solution of Polystyrene latex microsphere of 50 nm in ethanol the collected signal is the signal of diffused laser by the nanoparticles. We fix the value on the half plate and we modify the linear broadband polarizer from 0° to 180° and collect the intensity via ECONIC spectrometer, and then we obtain the polarization axe of the laser**,** **Figure 2.12**. Then, the value r(t) test to verify the polarizability of the system where we used a high diffusing nanoparticles of Polystyrene latex microsphere of 200 nm in ethanol, the value of r(t) should be between 0.98 and 1 for this kind of solution. These tests should be verified especially when we change the wavelength of the excited light. **Figure 2.11** shows the values of r(t) and the polar axe for different wavelength of the laser.

This technique is robust and able to measure the size of polymer liganted nanoclusters (Au_{15}PEG) from about 5 nm to protein gold nanoclusters Au-BSA about 9 nm[14]. This measurement for Au-BSA was in agreement with DLS with an uncertainty of about ±0.8 nm. For a small size nanocluster, this value of uncertainty is quite high ranging between 5-10 % referring to their size. Of note, during this work, some additional sizing measurements were performed using the DLS measurements using the Zetasizer (Malvern instruments) and some transmission electron microscopy with Nicola Blanchard available at the ILMTECH platforms.

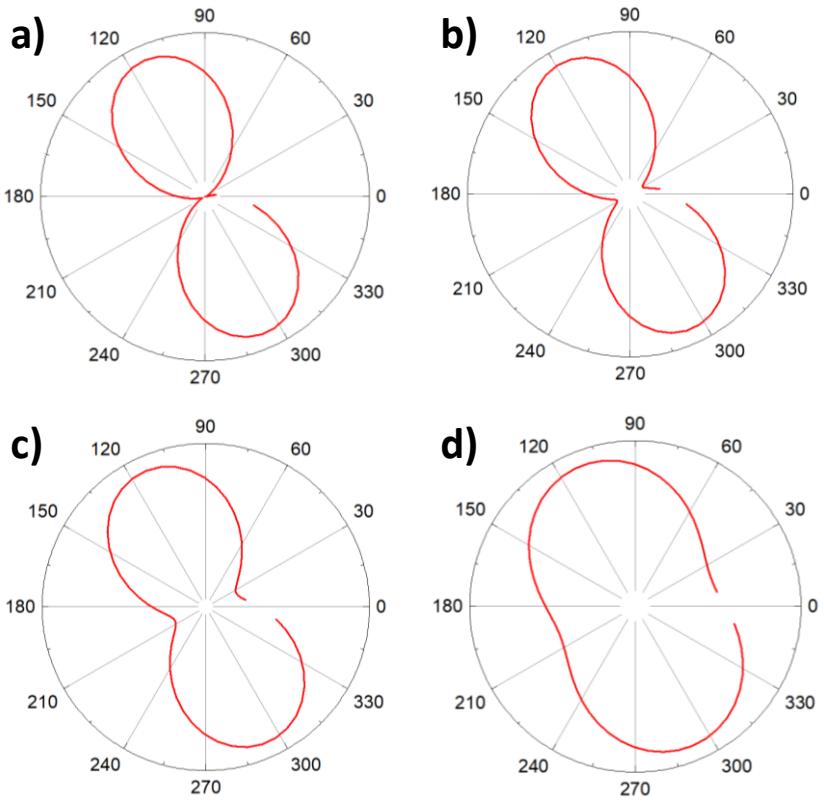

Figure 2.11 : Polarization axe for different wavelength of the laser a) 475nm r(t)=0.99 b) 465nm r(t)=0.98 c) 455nm r(t)=0.95 and d) 445nm r(t)=0.85, we can see that we lost the polarization of the laser under 465nm.

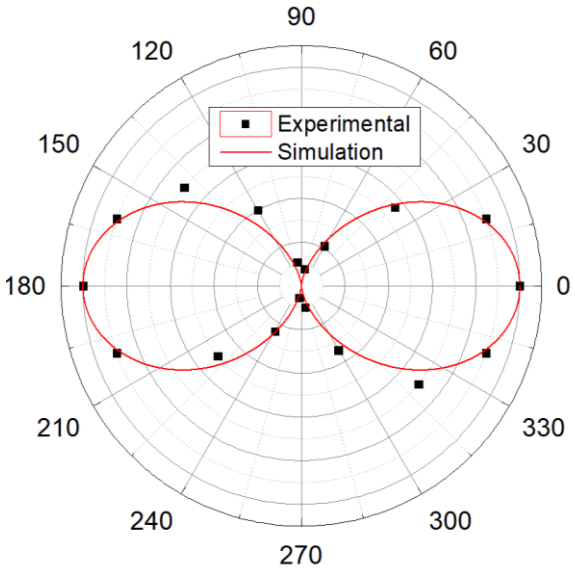

Figure 2.12 : Polarization axe of the laser with an excitation wavelength of 500nm vs incident polarization angle (in black) with the simulation (in red) using the following equation : $\cos(\alpha)^2$.

2.3 Linear optical properties

The previous sections have presented the main techniques we developed in Lyon for sizing and addressing the chemical composition of nanoclusters. Although their structures are not known at the atomic precision (as it is possible with single crystal XRD analysis for some specific ligand protected nanoclusters), their characterization allows for establishing (with the help of quantum chemistry investigations) the structure-optical properties relationships. These two next sections are devoted to describing the techniques I used for measuring linear and nonlinear optical properties of nanoclusters.

2.3.1 Absorption

Ultraviolet (UV) visible (Vis) absorption is an effective spectroscopy method that permits to identify specific chemical bounds in molecules. The sample (nanoclusters diluted in aqueous solution in a 1cm long quartz cuvette) is illuminated with a continuous spectrum using halogen lamp coupled to an AvaLight DH-S deuterium lamp, the transmitted light will be collected and analyzed with AvaSpec-2048FT spectrophotometer **Figure 2.13.**

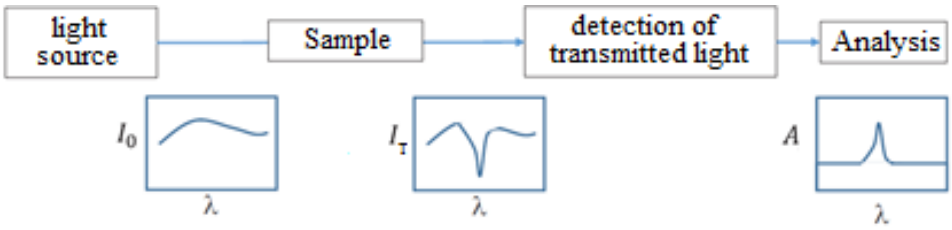

Figure 2.13: Principle of measurement of an absorption spectrum.

The absorption spectra depend on three factors: The optical path of the in the sample l, the solute concentration C, and the absorption coefficient ε. The absorption A is obtained using Beer-Lambert law:

$$\boldsymbol{I_T = I_0 e^{-A} = I_0 e^{-\varepsilon l C}} \qquad \textbf{(2.3.1.1)}$$

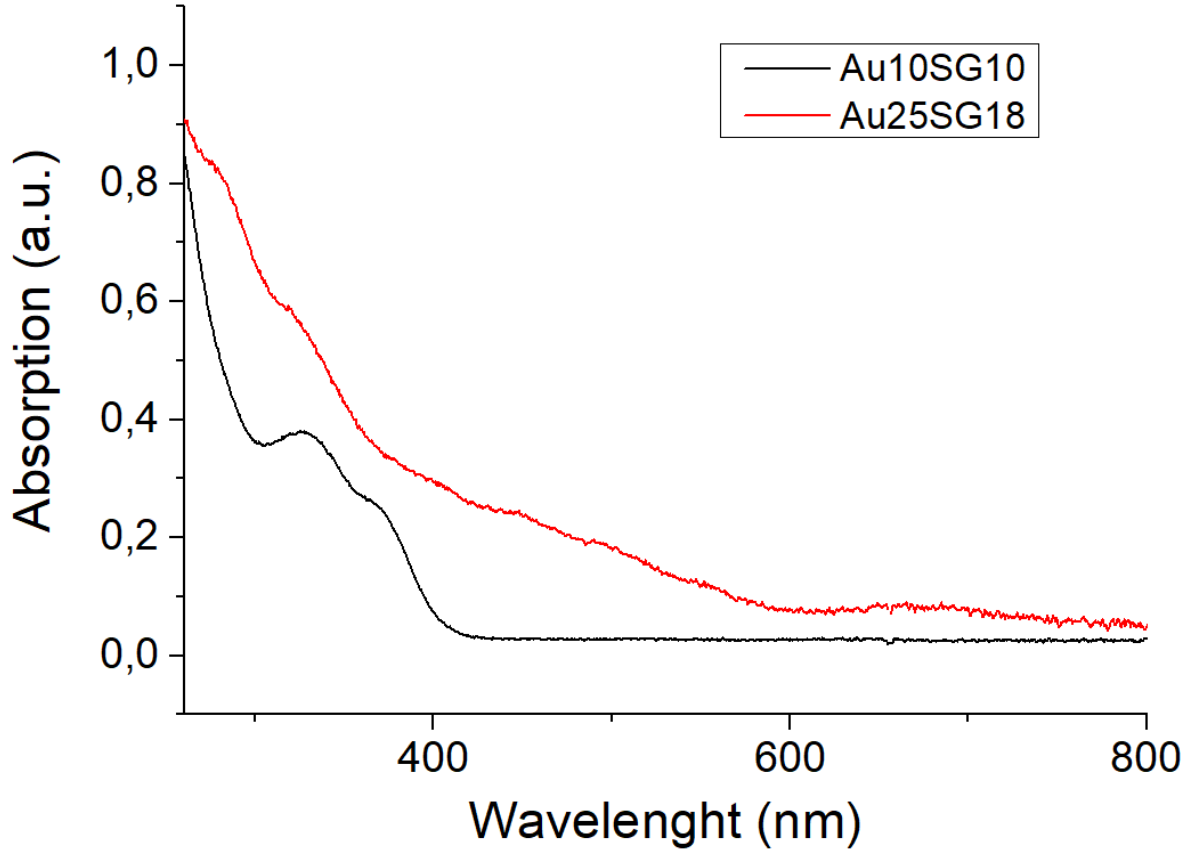

Figure 2.14: Absorption spectra of the $Au_{10}SG_{10}$ vs $Au_{25}SG_{18}$, we can see the differences in absorption spectrum between this two NCs.

Absorption spectra are important, since several absorption bands may be observed that can be used to identify the nanoclusters, In addition, he degradation of the nanoclusters will for instance lead to the disappearance or modification of some of the observed bands. Rongchao Jin for instance tried to establish some "benchmark" absorption spectra that could be used as fingerprint for characterization of nanoclusters, the most popular one is Au25SR18 with a unique and specific band at 670 nm. He has summarized the recent progress in the research of thiolate (SR)-protected gold nanoclusters with a focus on the reported stable sizes and their optical absorption spectra[15].

2.3.2 One photon emission fluorescence

2.3.2.1 Static and time-resolved Fluorescence

Luminescence properties, e.g., the ability of nanoclusters to emit light following photoexcitation is another important optical property to look at. A picosecond laser beam of tunable wavelength (Optical Parametric Oscillator (OPO) PGx03 series, EKSPLA) pumped by a mode-lock laser of frequency 1 kHz was used for the photoexcitation. The optical system is optimized to generate a laser pulse with a duration of around 20 ps with a small divergence The static fluorescence signal is recorded by an Ultracompact Econic spectro-fluorometer (B & WTek Inc., Newark, DE, U.S.A.) with a resolution of 1.5 nm.

Although static fluorescence spectra can be recorded with this set-up, it is mostly optimized for time resolved fluorescence. With the same laser OPO, the fluorescence signal is collected by the same objective and is then detected by a photomultiplier tube (PMT - R1463, Hamamatsu) supplied by a high voltage power supply box. The fluorescence decay signal is amplified by a fast preamplifier (350 MHz Preamplifier SR445A, Stanford Research) and recorded as a function of time by a digital oscilloscope (Lecroy LT 322) triggered by an ultra-fast photo detector (DET 10A / M, Thorlabs). In general, for the acquisition of a fluorescence decay curve, 400 scans are averaged. Even if the duration of the laser excitation allows on the principle of fluorescence lifetime measurements of the order of a nanosecond (the duration of the pulse is smaller (20 ps) as compared to the lifetime of the excited state of the chromophore), the instrumentation does not allow precise measurement for lifetimes close or shorter than the nanosecond (limited by the response of the of the photodetector). The system of detection is illustrated in **Figure 2.15**.

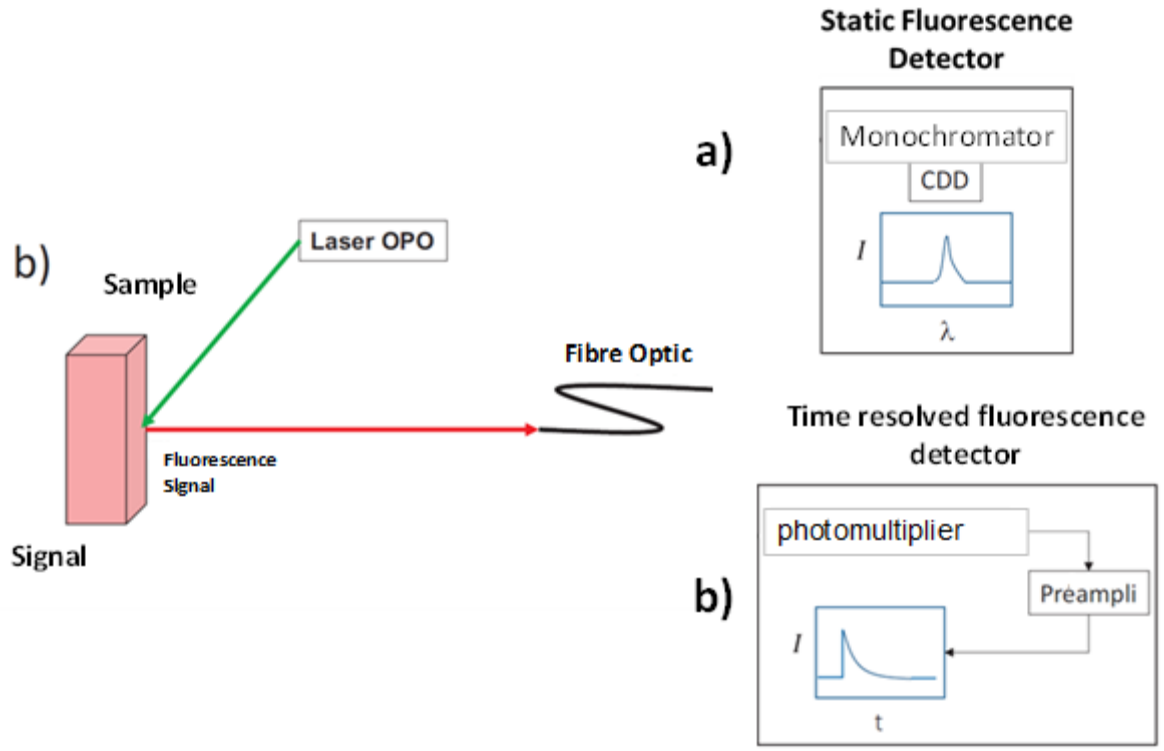

Figure 2.15: Schematic representation of fluorescence detection a) static, b) resolved in time.

2.3.2.2 Horiba Fluoromax-4 fluorescence spectrophotometer

The Fluoromax 4 spectrophotometer is a commercial spectrofluorometer from Horiba Jobin Yvon controlled by the FluorEssence software. This device allows the automatic acquisition of fluorescence spectra in emission (excitation at a given wavelength and observation over the entire visible spectrum), and in excitation (observation at a given wavelength and excitation over the entire visible spectrum). The light source is a Xenon arc lamp. An excitation monochromator allows the selection of the excitation wavelength. A second monochromator allows the selection of the emission wavelength. The emission is detected by a photon counter calibrated to optimize the signal to noise ratio. Finally, an additional module allows the

acquisition of a fluorescence decay curve. We can calculate the quantum yield ϕ with this instrument, the quantum yield is the ratio of the absorbed photon versus the emitted one. To calculate ϕ we need a reference substance, usually we use fluorescein, and using the following equation:

$$\emptyset_F = \emptyset_R \frac{I_F A_R}{I_R A_F} \qquad \textbf{(2.3.2.1)}$$

R stand to reference and F for the sample, I is the fluorescence intensity and A is the absorption at the excitation wavelength.

A nano-LED excitation at 370nm is used for pulsed excitation of a duration of the order of ten picoseconds. Detection by Time Correlated Single Photon Counting with a resolution of 7 ps / channel allows the measurement of lifetimes from 200 ps to 0.1 ms. With the custom-built and the Fluoromax 4 spectrophotometer, a large palette of lifetime measurements is possible ranging from sub-ps to milliseconds.

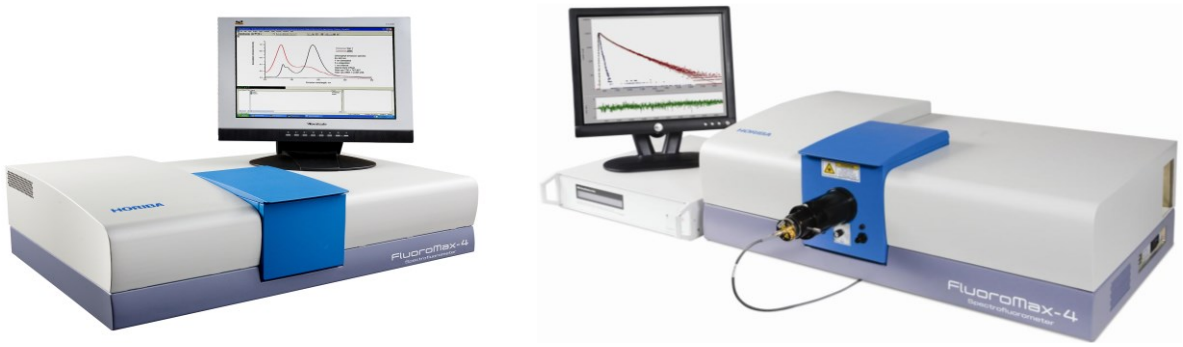

Figure 2.16 : Left, photograph of the Fluoromax 4 spectrophotometer in static configuration and right, in time-resolved configuration.

2.4 Non-linear optical characterization

As already mentioned in the introductive part of this chapter, we aim at using the ligand protected nanoclusters as nonlinear optical targets for bioimaging using multiphoton confocal microscopy. Thus, an exhaustive characterization of their NLO responses (Two-photon excited absorption and fluorescence cross sections and hyperpolarizability) is required. This will also permit to better address the structure-optical properties relationships in the nonlinear optical regime. The part of the experimental chapter deals with their experimental set-up allowing us to measure key NLO parameters.

2.4.1 General introduction

The field of non-linear optics developed very quickly after the discovery of lasers built by Theodore Maiman in 1960 [16], leading to a completely new approaches on optical physics. Indeed, in 1961, Franken already used a commercially available pulsed ruby laser! And harmonic light was observed after focusing red light into a quartz crystal[17]. The field of nonlinear optics continues to evolve and impact many fields and particularly has promising applications in 3D micro-fabrication[18], optical data storage[19] and two-photon fluorescence imaging[20]. Gold nanoclusters due to their quantum size regime (less than 2 nm), present unique nonlinear optical response which may lead to the creation of optical phenomena such as harmonic generations (second and third harmonic generation (SHG, THG) two photon absorption (TPA).

Lasers can generate high intensity of light with high electric field amplitude, close to those generated by the interaction of electrons with atomic nuclei. In this regime, the polarization of the material is no longer linear depending on the electric field, this will generate the non-linear dependency and thus the non-linear phenomena that can be expressed by the formula :

$$P_i = X_{ij}{}^{(1)}E_j + X_{ijk}^{(2)}E_jE_k + X_{ijkl}^{(3)}E_jE_kE_l + \ldots \quad (2.4.1.1)$$

Where Pi is the polarization, $X^{(n)}$ is n-th order susceptibility and E is the applied electric field. On the molecular level, we should introduce the power expansion of component of the dipole moment μ_i :

$$\mu_i = \alpha_{ij}^{(1)}E_j + \beta_{ijk}^{(2)}E_jE_k + \Upsilon_{ijkl}^{(3)}E_jE_kE_l + \ldots \quad (2.4.1.2)$$

Where $\alpha_{ij}^{(1)}$ is linear polarizability, $\beta_{ijk}^{(2)}E_jE_k$ and $\Upsilon_{ijkl}^{(3)}$ are the first and the second nonlinear polarizability, respectively. The second order susceptibility $X_{ijk}^{(2)}$ and first hyper-polarizability $\beta_{ijk}^{(2)}$ quantify the second-harmonic generation (SHG), sum and difference frequency generation (SFG) and (DFG), while the third order susceptibility $X_{ijkl}^{(3)}$ and second order hyper-polarizability $\Upsilon_{ijkl}^{(3)}$ are related to two-photon absorption (TPA), optical Kerr effect (non-linear refractive index) and third-harmonic generation (THG). The fundamental concepts and development of non-linear optical equations are introduced in [21,22].

Advances optical set-up and techniques have been developed to extract the different component of the non-linear phenomena's, leading to a wild field of research, challenges, and limitations. Since we are interested in light emission arising from nonlinear optical excitation in nanoclusters, a particular attention will be paid in the next section to describe the set-ups and techniques used for measuring first hyperpolarizability by hyper Rayleigh Scattering technique (HRS) and for evaluating, TPA and TFEF cross sections.

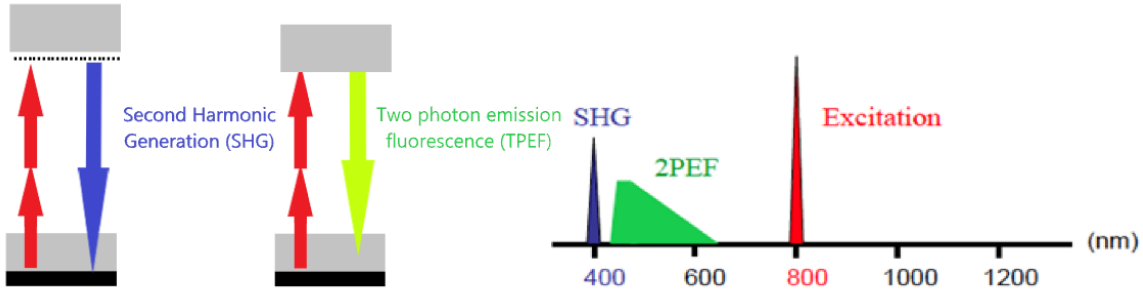

Figure 2.17 : General illustration of some nonlinear optics phenomena. While SHG convert two photons (coherent response), two photon emission fluorescence will create less energetic photons depending on the degeneration of the excited state of the fluorophore (non-coherent response).

2.4.2 HRS: set-up and equations

Second-order non-linear optical properties exhibit molecules with non-centrosymmetric structures, [23]. The non-linear susceptibility is considered as tensors because they connect different components of the electric field vector with the component of the induced polarization, for centrosymmetric molecules, all tensor components are null. The principle of Neumann (1988) states that the sign and magnitude of physical properties should be unchanged after a symmetry operation. For a centrosymmetric system, both electric field and polarization transform as $E \rightarrow -E$ and $P \rightarrow -P$, turning the equation $P^{(2)} = X^{(2)}EE$ to $-P^{(2)} = X^{(2)}(-E)(-E)$ and $X^{(2)}$ has to be zero.

Hyper Rayleigh scattering, HRS, is the nonlinear analogue of the Rayleigh scattering. Rayleigh scattering involves linear interaction of the incident radiation, without frequency change, for hyper Rayleigh scattering, one should introduce the generation of new frequency from the original frequencies of the incident radiation. HRS do not obey to Neumann principles, which

gives this technic an advantage on others technics like EFISHG (electric field induced second harmonic generation)[24], where in this technic the dipolar molecules in the solution are oriented in a static electric field to generate the macroscopic non-centrosymmetric. EFISHG technic is limited to molecules with dipolar symmetric, while HRS can be used to measure properties of all molecules. HRS is an important experimental tool that determine molecular and supramolecular symmetries. While EFISHG create a coherent response where all molecules are contributed coherently, HRS is a non-coherent technic, requesting a high-intense laser beam to increase the intensity to obtain a better ratio between signal and noise.

The experimental setup used for the HRS experiments is a classic right-angle scattering setup **Figure 2.19**. The light source used in this experimental set-up is a titanium-sapphire femtosecond laser delivering pulses with a duration of 180 fs with a repetition rate of 76 MHz

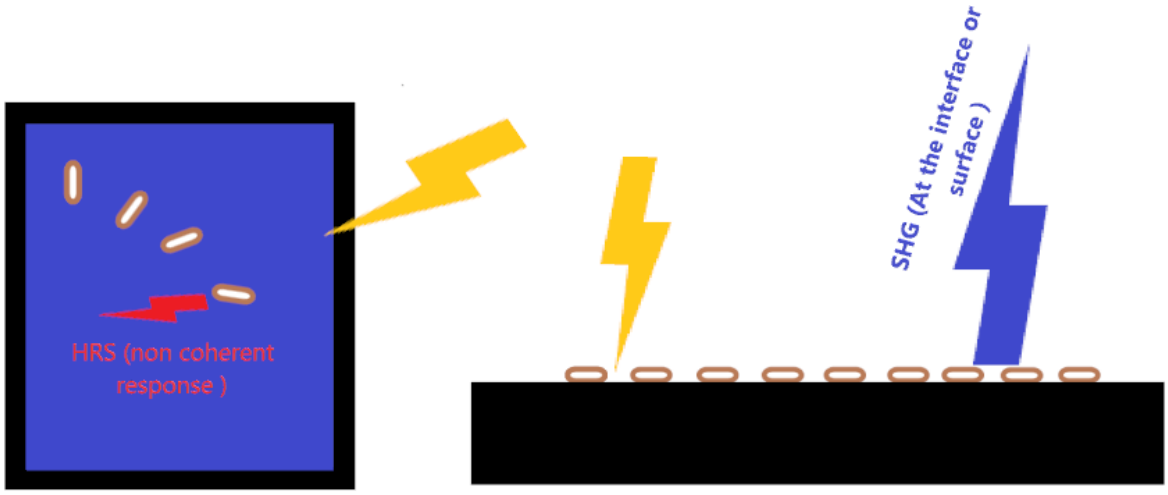

Figure 2.18 : Illustration showing the difference between coherent and non-coherent HRS response of fluorophores inside solvents (left) and the SHG at the interface or at the surfaces (right).

at the exit of this laser cavity, we placed an optical system composed of a half-wave plate, a polarizer cube allowing the control of the laser power delivered downstream at the level of the cell. The laser beam controlled in power is then directed towards a second half-wave plate allowing its control in polarization. A low-pass filter placed immediately after this second plate

eliminates the light generated at the harmonic frequency before the cell. The laser beam at the fundamental frequency is then focused on the cell whose walls are made of molten quartz to

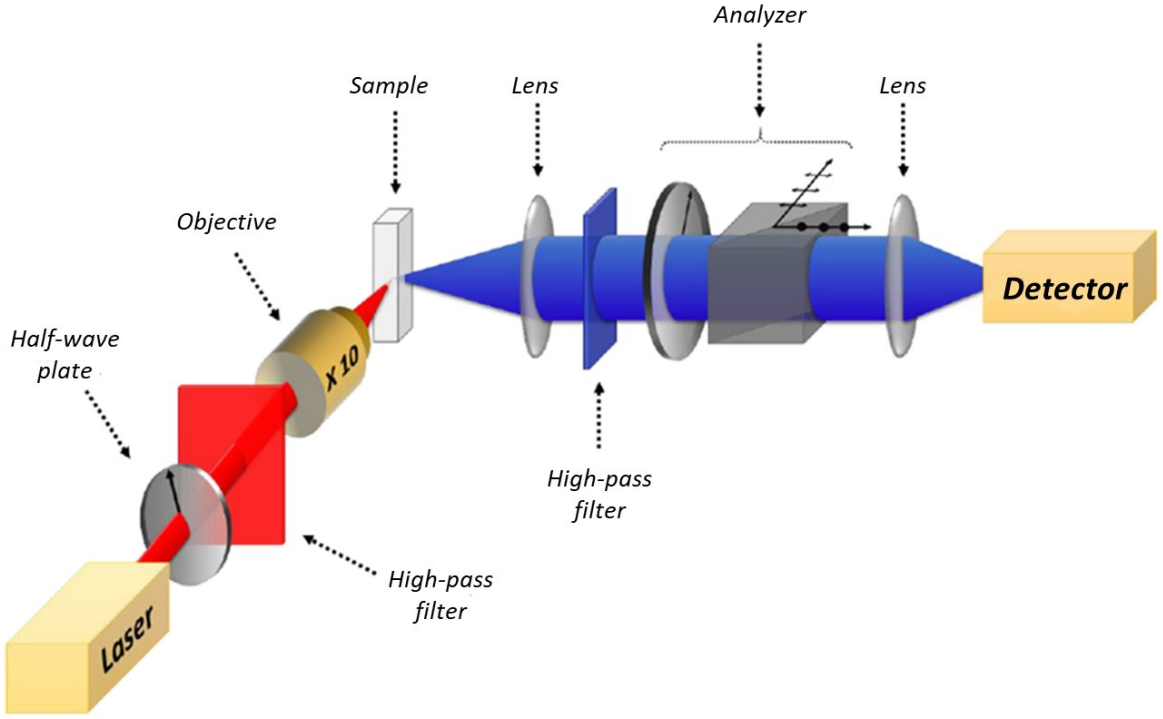

Figure 2.19 : General schematic diagram of the right-angle HRS assembly used in non-linear optical experiments.

obtain an excellent transmission at the harmonic frequency around 400 nm by an X10 microscope objective of numerical aperture NA = 0.25 (Thorlabs , LMH-10X-1064). The scattered SHG intensity is then collected at a right angle using a lens with a focal length of 50 mm and separated from the fundamental scattered intensity by a high pass filter. A polarization analysis system, composed of a half-wave plate and a polarizer cube adapted to the wavelength of 400 nm, is placed on the detection line to select a defined polarization state of the scattered harmonic wave.

First, we do the measurements for the solvent (often water) and after we do it for our sample for different concentrations to get a more precise value of our β. The HRS signal intensity I_{HRS}

values will be collected manually by subtracting from the fluorescence value of the curve (two photon emission signal), then the values found will be normalized against the linear absorption using this equation:

$$I_{HRS} = I_{HRSCollected,Normalised} \times 10^{0.5(Abs_{400}+2Abs_{800})} \quad (2.4.2.1)$$

After following these steps (1. Collected the values, 2. Normalized, 3. Correction with respect to the absorption) we draw the line of the intensities as a function of the concentration and then calculate the value of β using the equation (1) :

$$\frac{I_{HRS}}{I_{HRS}^{S}} = \frac{\langle N_S\beta_S^2 + N\beta^2\rangle}{\langle N_S\beta_S\rangle} = 1 + b' \; N\langle\beta^2\rangle \quad (2.4.2.2)$$

With I_{HRS} is the intensity at the excitation wavelength excluding total fluorescence, S indicates the solvent used, N is the sample particle concentration per m3, β is the hyperpolarizability value in esu. with βwater = 0.087 x 10-30 esu N water = 5. **Figure 2.20** shows the HRS signal and their plot versus different concentration for Au15SG13 published by our group[25].

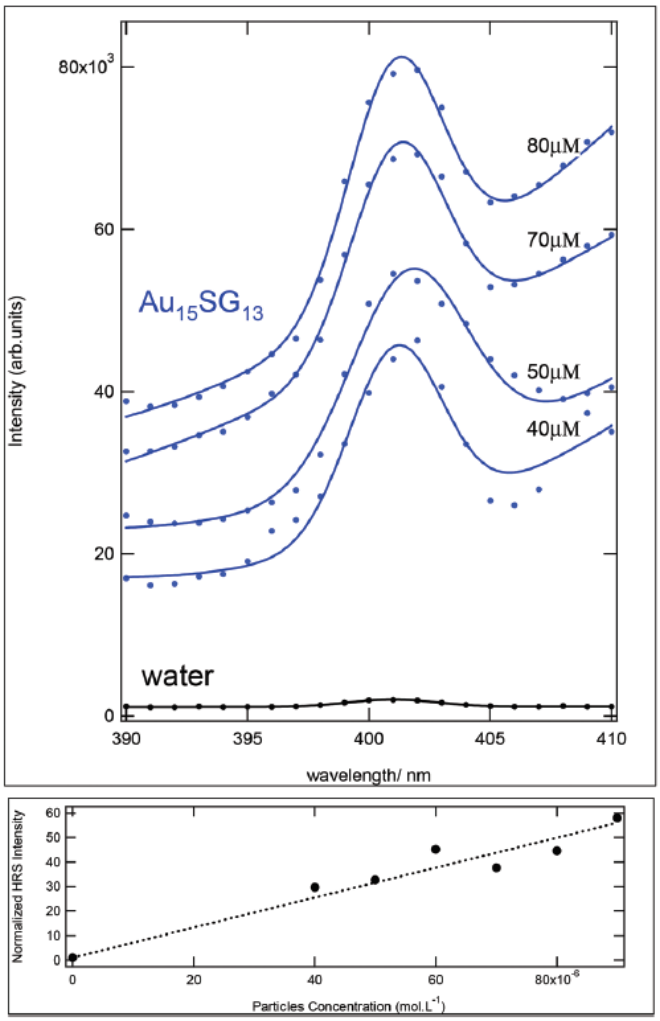

Figure 2.20 : (Top) HRS intensity versus wavelength for Au15SG13 solutions of different concentrations (blue circles). Lines: fit to a Gaussian function superposed on a linearly increasing function of the wavelength. (Bottom panel) Plot of the HRS intensity for Au15SG13 as a function of concentration.

2.4.3 Two photon emission fluorescence cross section

Two photon excitation fluorescence TPEF, is a nonlinear phenomenon that accurate when two photons arrive at the same time with a time window of an attosecond 10-18 s and excite the molecule. Usually the photons source used have the same photon energy (same wavelength) and they sum together to give double photon energy allowing the excitation from the ground state, and the double photon absorbed by the electron will share to the same process as for the electron who was excited at the half wavelength (laser at 800 nm will be the same as using a laser of 400nm). TPEF require high photon flux, about 10^{20} and 10^{30} per cm2s, thus only accessible with high laser fluence.

The TPEF cross section are extracted using the reference method and is calculated using fluorescein as a reference according to the equation:

$$\sigma_{TPEF} = \frac{\eta^{ref}\sigma_2^{ref}c^{ref}}{c}\frac{I}{I_{ref}} \qquad (2.4.3.1)$$

Where η is the quantum efficiency, σ2 is the two-photon absorption cross section, c is the particle concentration per m^3, and I is the fluorescence intensity. Here ref donates to the different coefficients of the reference used. The reference used for the experiments was the fluoresceine with a low concentration to obtain two-photon emission yields compatible with gold NCs yield. At 780nm, σ2 of the fluoresceine is 33 GM with a quantum yield of 0.9 and a two-photon absorption cross section of 37 GM[26]. **Figure 2.21** shows the TPEF signal for Au25SG18 NC[25], where we find a σ_{TPEF} value of 0.0022 GM referring to fluorescein.

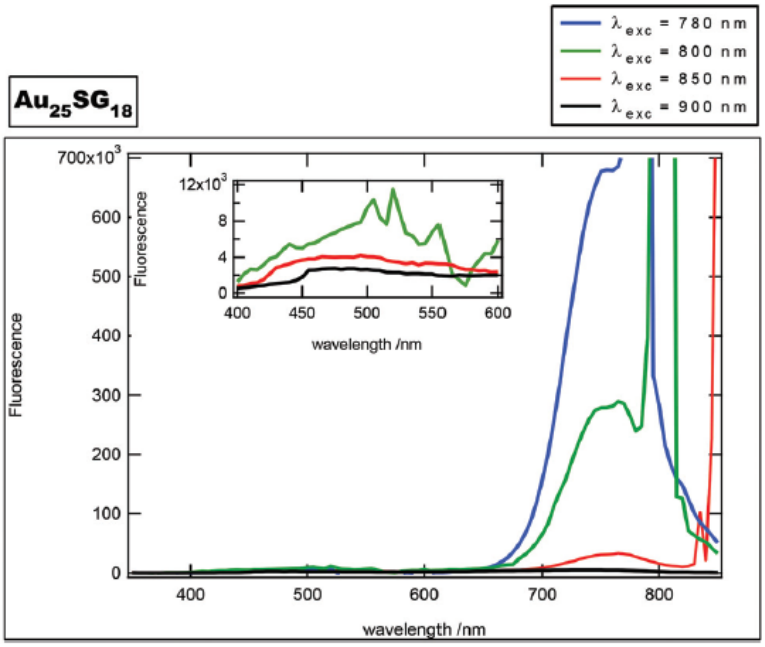

Figure 2.21 : Two-photon emission spectra for Au25SG18 as a function of wavelength for different excitation wavelengths (780, 800, 850 and 900 nm). The huge increase in the right part of the spectra is due to the excitation laser lines (780, 800, 850 and 900 nm).

2.4.4 Non-linear Absorption: TPA cross section: P-scan set-up

Two photon absorption TPA is a third order nonlinear optics, it can be measured by many technics such Z-scan[27], where the transmission of the sample is measured along z axis along the laser beam position. In our lab we used the P-scan technic to obtain the nonlinear absorption coefficient, in this technic we vary the power of the incident light and the change of the transmission is obtained[28].

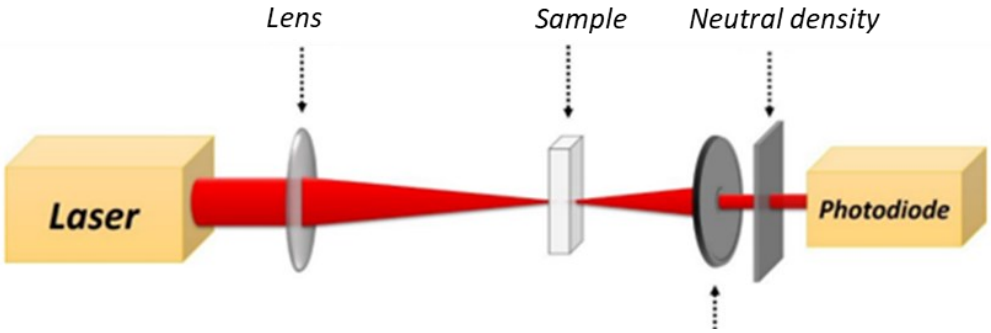

Figure 2.22 : P-scan experimental set-up used to calculate Two Photon Absorption.

The light source for the TPA experiments was a mode-locked femtosecond Ti:sapphire laser delivering at the fundamental wavelength of 780 nm pulses with a duration of about 140 femtoseconds at a repetition rate of 76 MHz . The beam was focused by a low NA microscope objective to a waist of 5.4 µm and sent in transmission into a 1 cm path length spectrophotometric cuvette. The transmitted light was detected with a large aperture photodiode. The incident power was controlled with a half-wave plate and a polarizing cube, **Figure 2.22** show the experimental set-up[29]. The calibration of the photodiode signal was obtained prior to the experiment by removing the cuvette and varying the incident power[25].

Theoretically, the Taylor expansion of Beer-Lambert equation is given by:

$$T = Ce^{-\alpha L} = Ce^{-(\alpha+\delta I)L} \qquad (2.4.4.1)$$

Where T is the transmission factor, α is the linear absorption, L is the path traversed by the laser beam in the cell, δ is the two-photon absorption cross section and I is the transmitted intensity. After that we develop by Taylor expansion:

$$T(I) = T(0)(1 - (\alpha + \delta I)L) \tag{2.4.4.2}$$

$$T(I) = T(0) - T(0)\delta L_{eff}\frac{(1-R)P_m}{\pi\, w_0^2} \tag{2.4.4.3}$$

With T (I) is the transmission measured by the photodiode, R is the reflection coefficient, Pm is the power measured before the cell and w0 is the laser waist. The power measurement is conducted with a wattmeter where it is fixed before the sample and therefore the measurement is made by changing the angle from 0 ° to 360 °. Then we measure the intensity transmitted by a photodiode for the water and then for the sample as a function of the polarization angle. We start by converting the values obtained by the photodiode into Watt, the values obtained by the wattmeter is plotted according to the values obtained by the cell of water, we fit the curve obtained by a linear equation in the form (y = Ax + B), we put these values for all the measurements obtained.

Finally, we plot the water result against the sample, and using the equation:

$$y = Data_{water} \times (1 - Data_{water} \times L \times \delta_{TPA}) \tag{2.4.4.4}$$

We made the straight line of the values obtained, L = 0.5cm is the length of the cell used, and δ_{TPA} is the two-photon cross section but not converted to GM, we must change the value of δ_{TPA} manually to adjust the fitting.

And we convert the value obtained to GM using the following equations:

$$K_1 = \frac{\lambda}{h \times c \times \pi \times Freq \times Dur \times waist^2} \tag{2.4.4.5}$$

$$K_1 = \frac{\lambda}{h \times c \times \pi \times Freq \times Dur \times waist^2} \quad (2.4.4.6)$$

$$K_2 = 10^{-3} \times N_{av} \times Conc \quad (2.4.4.7)$$

$$\delta_{TPA} = \frac{val \times 10^{50}}{K_1 \times K_2} \quad (2.4.4.8)$$

With λ is the excitation wavelength, h is Plank's constant, c is the speed of light, Freq is the frequency of laser used 76×10^6 Hz, Dur is the pulse duration 140×10^{-15} s, waist is the waist of the laser beam 9×10^{-4} m, Conc is the molar concentration of the analyte and val is the value of

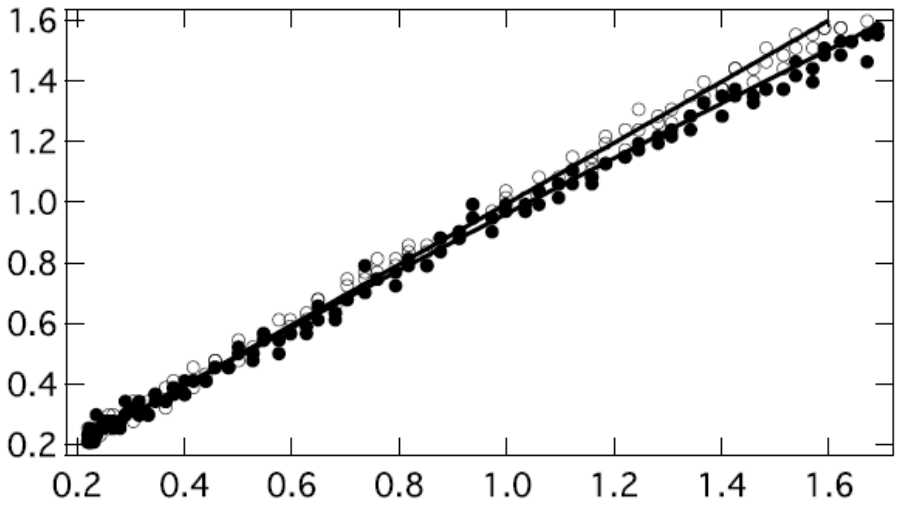

Figure 2.23 : Transmitted intensity recorded at 780 nm in the absence of the cell (empty circles) and with the cell (filled circles). Solid lines are fit using equation (2.4.4.4) to adjust the value of the TPA cross section. First the transmission power converted to watt for empty cell is plot against itself, them the transmitted power converted of the sample is plotted against the empty cell data.

δ_{TPA} obtained in equation (2.4.4.4). **Figure 2.23** shows the experimental results of the TPA cross section for $Au_{15}SG_{13}$ NC, we found $\delta(TPA, Au_{15}SG_{13})$ = 65 700 GM[25].

2.4.5 Multiphoton confocal microscopy

The section 4 described the set-ups used to measure nonlinear optical parameters (such as hyperpolarizabilities and TPA and TPEF cross sections). Clearly nanoclusters may present large TPEF and are thus interesting candidates for multiphoton confocal microscopy. In the last centuries, optical microscopy become one of the top biomedical research tools today. Confocal microscopy permits the acquisition of high-resolution three-dimensional (3-D) images, but this technics face limitation. In brain tissue, the average distance that a photon in the visible range travels between two scattering events is about 50–100 μm. Tissue is a hostile environment for light microscopy, due to the strong scattering of ultraviolet (UV) and visible light, and when referring to commercial fluorophores, they require excitation is the visible light around 600nm, leading to autofluorescence, because of some existed natural molecules like

hemoglobin and related molecules that will be excited in this range[30], therefore an optical windows in the near infrared is required for optimal tissue penetration see **Figure 2.24**.[31]

The main advantage of multiphoton confocal microscopy is to excite biomaterials with photons in the near-infrared window and thus to collect deeper signal in biological samples and to detect fluorescence in biological tissues. The excitation effective volume used in MCM is limited to

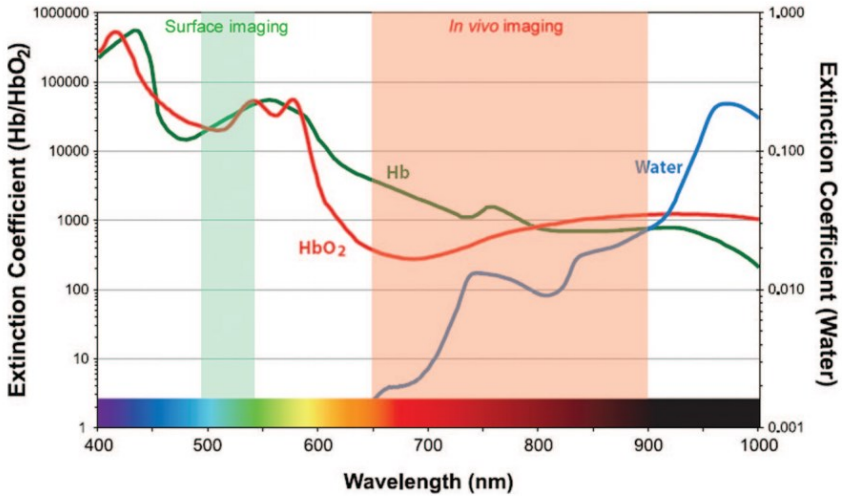

Figure 2.24 : Extinction coefficient value of water and oxy/deoxyhemoglobin plotted ranging from visible to near-infrared wavelength.

few femtoliter of volume. Compered to confocal microscopy, MCM imaging use near-infrared light, allowing a better collection for 3D images, more access to optical window and both scattering and the absorption will be reduced in the biological tissues and gives a deeper imaging[32]. The experiment conducted by Squirrell et al. conducted on hamsters to study the dynamics of mitochondrial distribution after using multiphoton microscopy (1047 nm) show no harm even on the fetal development of this hamsters, they found that two photon imaging do not cause any change in the production of H_2O_2 that increase oxidative stress, compared to an excitation at 514nm, which have an impact on the oxidative stress[33].

The MCM used for our experiments is a customized confocal microscopy (TE2000-U , Nikon Inc.) **Figure 2.25**. This instrument is located at the Nanoptec center (ILMTECH). The sample

was excited at 780nm with a mode-locked frequency-doubled femtosecond Er-doped fiber laser (C-Fiber 780, MenloSystems GmbH) with an output power of 62mW. The excitation light entrance was modified, the original optical-fiber light input was removed allowing free-space laser beam input. Two filters were used for delimiting the laser spectrum (FELH0750 and FESH0800, Thorlabs Inc.). The laser beam is focused with a Nikon Plan Fluor Ph1 DLL objective (10×/0.30 NA). The cartography in XY scale was performed using the inner microscope motorized stage and Galvano scanner (confocal C1 head, Nikon Inc.), the Z-scan was performed by the inner microscope motorized focus. The two-photon fluorescence emission was separated from the incident light through a dichroic mirror (NFD01-785, IDEX Health & Science LLC). A FESH0750 filter was employed to remove the photons from the excitation laser and collect in the visible range between 350 and 750 nm on the inner microscope photomultiplier tube. For gel imaging (see chapter 4), TPEF intensity raster scans performed at several Z positions of the gel (size of the gel image: 60 × 48 mm). Time per each point (0.25 mm×1 mm): (61 μs × 2 × 128 × 128 for averaging). For invitro bio-imaging of fixed cells (see chapter 5), TPEF intensity raster scans performed at several Z positions or fixed positions of the cells, depending on the purpose of the acquisition. For image acquisition the Z position was fixed, and the signal was collected on this position. Since the advantage of the multiphoton confocal is the Z-stack, where it enables to collect the signal on the desired Z position (one can imaging a 2D plan on the XY axes with a fixed Z position), it helps us to make sure that NCs are internalized inside the cells rather than nanoclusters stuck on the surface.

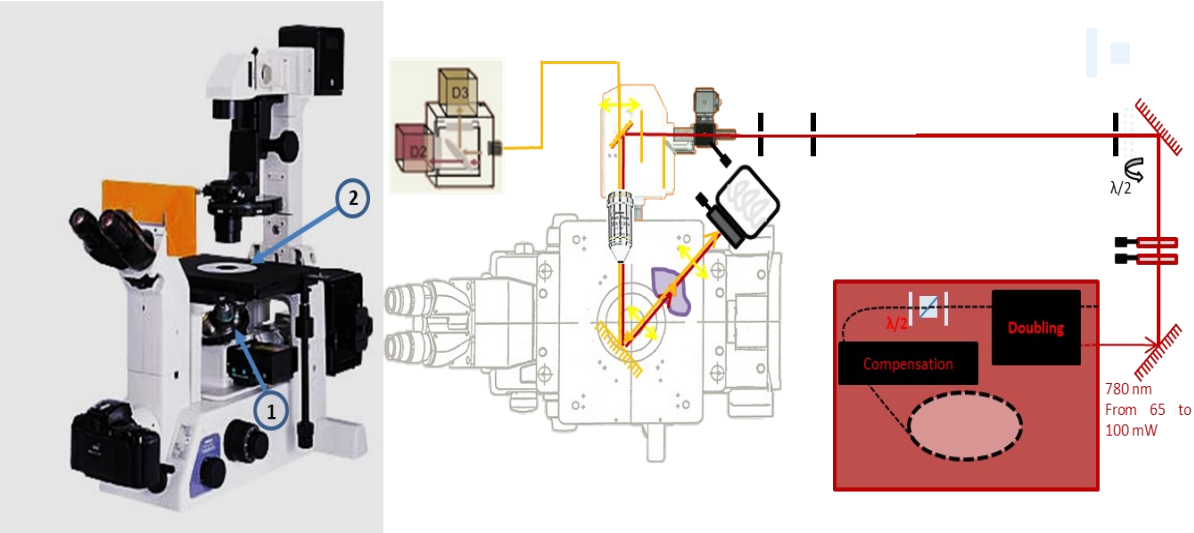

Figure 2.25 : Sheam representing the multiphoton confocal microscopy, where the sample is excited from blow and the fluorescence signal is collected with epic-collection method. 1 is the objective where is laser is focused to excite the specimen, and 2 is where the dried gel was placed for XY scanning, the fluorescence signal is then collected by an optical fiber and sent to the photomultiplier for analyzing.

2.5 Gold NCs synthesis

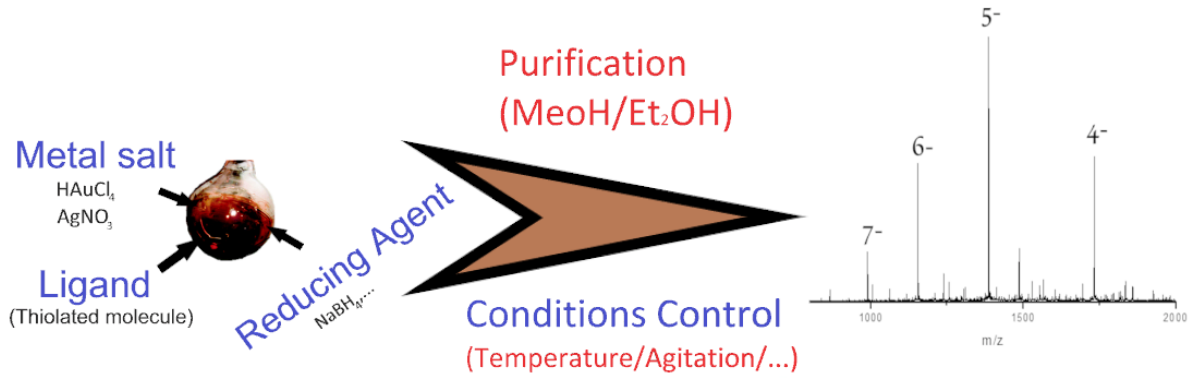

Figure 2.26 : Illustration showing a general step of the synthetic rote of gold NCs.

The route to make gold NCs smaller than 3 nm is principally by controlling the reduction phase during the synthesis and the use of thiolate ligands, because gold atoms will cluster faster in the presence of an excess of reducing reagents and form gold nanoparticles rather than small NCs. Today, there are two main approaches to form small NCs, "Atoms to clusters" and "Nanoparticles to clusters". In our work, we used the first method for thiolate-stabilized gold NCs, we follow a slow reduction phase due to the strong ligand stabilizer. The gold atoms will be reduced to the zerovalent state, leading to the nucleation of the gold atoms.

Controlling gold atoms number in the synthesis is challenging. Additional separation techniques like PAGE allows for spatial separation of nanoclusters on gels. Then interesting parts of gels (containing a specific nanocluster) are cut. Samples containing “atomically-precise NC” then can be further analyzed. This process is quite time consuming and the amount of samples is usually very low. By playing with the ratio of gold atoms to ligand, the temperature and by adding other stabilizing agents, synthesis may lead to the production of

nanoclusters at the atomic precision. This is true when glutathione is used as thiolated molecules to protect nanoclusters. Here are some syntheses that are now commonly used to produce atomically precise gold nanoclusters.

$Au_{10}SG_{10}$. This nanoclusters produced by adding 100mg of gold salt ($HAuCl_4$) to a solution containing 234 mg of GSH dissolved in 35mL of MeOH and 2mL of triethylamine in a 100ml balloon and mixed overnight, no reducer is added[34],

$Au_{15}SG_{13}$. The synthesis is similar to Au10SG10 but we added tetrabutylammonium borohydride to reduce overnight and the solution is kept overnight under stirring[25].

$Au_{18}SG_{14}$. The synthesis of $Au_{18}SG_{14}$ is different in term of the steps of adding reducer (2 reducer used for different time) and the ratio of gold atoms to ligand is modified, the reaction was performed in ice bath (our lab synthesis).

$Au_{25}SG_{18}$. This nanoclusters the largest cluster obtained at the atomic precision (in terms of gold atoms) that we produced in this project and demand 6 step of a adding reducer at room temperature[25].

All glutathione gold NCs was precipitated in powder and stored in freezer to later use and to prevent degradation. Adding of triethylamine and tributylamine in the first step will partially permit carboxylic acid to be solution in MeOH, at the end of the synthesis and during purification mode, different chemical reagents is added to precipitate the clusters, NaOH, excess of MeOH, and sometimes we used a rotary evaporator to minimize solvent and aid precipitation. After these 5 cycles of dissolution/precipitation/centrifugation using a minimum of Water/NH_4OH 10% in MeOH or diethyl ether to remove unwanted Au_xSG_x from the solution to have a pure synthesis. Finally, the powder is left in diethyl ether and left to dry under vacuum.

Surface modification of this NCs is now possible and depends on the purpose of use. For instance carboxylic acid can be easily grafted by peptide coupling using EDC as a coupling

agent (N-ethyl-N′-(3-(dimethyl amino)propyl)carbodiimide hydrochloride), we used this method to graft PEG_{5000}-NH_2 to the carboxylic acid of the glutathione[35].

2.5.1 Other NCs synthesis

Protein based gold NCs and silver NCs was synthesized in the next step of my PhD, the reason is explained in Advanced strategies to render metal NCs enough luminescent for in vitro imaging. section.

BSA-Au NCs. 5mL of $HAuCl_4$ (10mM) was added 250mg of BSA dissolved in 5ml of milliQ water and mixed by manually shaking, then 1mL of NaOH solution is added and the solution was put in the oven (37°C) for 16h. The solution was purified with dialysis membrane (3kDa) and the water was replaced two times. FA-BSA-Au follows the same synthetic protocol (just adding 20µl of ascorbic acid 1mM before adding the NaOH), and next 10mg of NHS and 20mg of EDC followed by adding 2ml of 0.1mM of folic acid and the solution was shacked at room temperature overnight.

Glucose-BSA-Au. 1ml of BSA (63mg/ml) was mixed with 1ml of Glucose (250mg/ml) under 60°C for 3 hours, after that 5ml of $HAuCl_4$ (10mM) was added under vigorous stirring at 45°C for 30 min followed by adding 0.5ml of NaOH (1M) and left for 12 hours. The solution was purified with dialysis membrane (3kDa) and the water was replaced two times.

Insulin-Au and lysozyme-Au. 5 mL of HAuCl4 solution (10 mM) was added to 4 mL of lysozyme solution (30mg/mL) / 5 ml of insulin solution (10 mg/ml at pH 10). 50mg of Gly-Trp dipeptide dissolved in 10ml milliQ water was added, the pH was adjusted to 11 by adding NaOH (1M) solution. After 24 h at 40°C (at the oven), the brown solutions were purified with (5 kDa or 10 kDa membrane).

Transferrin-Au. 1mL of $HAuCl_4$ (10mM) was added to 2ml human apo Transferrin (10mg/ml) at 37°C under vigorous stirring. 10µL of ascorbic acid (0.35mg/ml) was added dropwise in the

solution followed by adding 0.2ml of NaOH (1M), after 3 hours, the solution is washed with 5kDa membrane to purify the solution.

All protein based NCs was then stored in the fridge for later use.

$Ag_{29}DHLA_{12}$. As described in [36], 100 mg of (±)-α-lipoic acid was dissolved in 5ml of MeOH and 10 ml of water followed by the addition of 2 equivalent (in mol) of tetramethylammonium borohydride (NBH_4) for 30 minutes, then solution was ultrasonicated for 1 hour to remove the excess of reducer. 41 mg of silver nitrate was dissolved in 15 ml of milliQ water and added to the solution, 1ml of NH_4OH (10%) is added to the solution, followed by 85mg of NBH_4 and stirred at 50°C for 1 hour. Then, 1 equivalent of NBH_4 (42.5mg) is added and left for another 1 hour. The water quantity was reduced to 1ml using rotatory evaporator to help the precipitation with EtOH. 5ml of EtOH and 20ml of Et_2OH was added followed by 20µl of glacial acidic acid and centrifuged at 5000rpm for 5min. The precipitant was then dissolved in a minimum of water/NH_4OH (10%) followed by 5ml of ethanol and 20ml of diethyl ether (repeated 3 times). The last centrifugation is done by adding only diethyl ether and the precipitant was collected and dried under vacuum overnight and stored at the freezer for later use.

2.6 Gel preparation for targeting carbonylated proteins in electrophoresis gels with nanoclusters

We used Western Blot gel to quantify carbonylation with MCO and test method efficiency and reproducibility. Carbonylated protein is mixed with 10 mM EZ-Link™ Alkoxyamine-PEG4-Biotin (Thermofisher) for 3h hours to derivatize the carbonyl at room temperature. Samples were then subjected to gel electrophoresis by using the Mini-Protean® Tetra Cell system (Bio-Rad). Acrylamide/bisacrylamide (Fisher Bioreagent), PSA (Biosolve), TEMED (Sigma), and

Tris-glycine buffer are used to made gels. Linear gels (20%) are used for sample migration. Proteins were further transferred onto a PVDF membrane with the Trans-Blot Turbo Transfer System (BioRad) at constant 25 V (up to 1.0 A) during 30 min. Membranes were dyed with Red Ponceau dye (Sigma) to estimate transfer efficiency and total protein loading. Next, the membranes were blocked with 0.05% TBS-Tween buffer-5% milk for 30 min at room temperature with shaking. After that, the membranes were incubated for 1 h at room temperature with re-suspended Streptavidin-Alexa Fluor 700 probes (Invitrogen). Membranes is washed 3-4 times for 5 min with TBS-Tween 0.05% between each step after blocking. Lastly, the Typhoon™ FLA 9500 biomolecular imager (GE Healthcare) was utilized to measure fluorescence. We used ImageLab (Bio-rad) and GraphPad software for fluorescent quantifications and the statistical analysis.

To evaluate NCs targeting carbonylation in electrophoresis gels, carbonylated protein was first mix with NCs in PBS 1X. The time of incubation varied due the problems that we faced, discussed in the next chapter, same thing for protein and NCs concentration. Samples were then complemented with 10% glycerol, loaded into 15% or 20% Tris-Glycine gels, and then migrated with 1× Tris-Glycine buffer (25-192 mM). Before drying, the gels were equilibrated in a 20% ethanol and 5% glycerol solution for 20 minutes and then placed in a drying frame (Serva) for 48 hours. In-gel protein staining was performed using Coomassie staining solution (10% ammonium sulfate-10% phosphoric acid-0.12% Coomassie G250 and 20% ethanol) overnight under agitation at room temperature, followed by destaining with distilled water.

2.7 Cell culture. Protocols and incubation with nanoclusters for bio-imaging

We used different cell lines (A549 from Belgarde , HeLa, HEK from Gottingen and HDF), A549, HeLa and HEK were given as a gift for the institute, and we cannot know their origin and the ATCC numbers, HDF/TERT1 was purchased from EverCyte, cat no° CHT-008-0012. We used this different cell lines to assess the NC on cells with cancerous and non-cancerous cells with different size and shape of the cells and target them in the next step to detect carbonylation which considers all types of cells. The same incubation conditions were used for all cells, 37°C / 5% CO2 and 90% humidity. Before fixation of the cells, all materials used were sterilized. The culture medium, PBS 1x and trypsin were pre-warmed before use. The amount of trypsin added depended on the flask or dish of the culture used.

All steps and experiments were done in a cell culture hood (except after incubation with Nano Clusters,). We used flasks (T-25 / T-75 ...) depending on the number of cells we have or the number of cells per experiment, for 2M cells per experiment we used the T-75, we also used culture dishes (35mm, 60mm ...) adapted, likewise, to the number of cells per experiment. Flasks and dishes were purchased from Dutscher (in ILM institute in France) and TPP Techno Plastic Products AG (in MEDILS institute in Croatia)

We purchased Dulbecco's Modified Eagle Medium from Capricorn Scientific GmbH, DAPI (4′,6-diamidino-2-phenylindole) is a blue-fluorescent molecules that binds to the DNA inside nucleus, mounting medium for immunofluorescence are both purchased from Thermofisher. The first cell culture facility is located at Mediterranean institute for life science (MEDILS) in Split Croatia, the second located at the institute of light and matter (ILM), in the university of Lyon1 (Biophysics team).

2.7.1 Cell passage

- Wash with 1x PBS
- Aspirate the PBS

- Apply trypsin to detach the cells (about 5-10 min)
- Add culture medium (DMEM with 10%FBS)
- Take a sum of 100µL to count the cells and mix with trypan blue
- Put the flask containing the cells in a centrifuge (1000rpm 5 min)
- At the same time count the cells (automated cell counter or hemocytometer, I can do both)
- Aspirate the medium from the tube and re-dilute the cells with DMEM with 10%FBS to reach the desired cell concentration (1M cells/ml)
- Put in the flasks the number of cells desired by adding medium and put back in the incubator

2.7.2 Cell division for in vitro experiments

- Repeat the same steps above, but instead of putting the cells in the flask, make a concentration of cells depending on the type of cells and the multi-well boxes used for the experiment, we used 24well plates.
- Before putting them in the multi-well dish, we put the glass coverslips in the wells (sometimes glued with 2% gelatin) for the microscopy studies.
- Leave overnight, so that the cells can attach themselves to the coverslips.
- Aspirate the medium
- Dissolve the gold nanoclusters in DMEM without FBS
- Incubate (from 2h to 24h) depending on the NC used
- Remove from the incubator and take the dishes to the chemistry room
- Remove medium, wash 3 times with 1x PBS (5min each time)
- Fixation with 4% formaldehyde (16% formaldehyde stock solution, mix with PBS x10 1.6ml:1.5ml then continue to 15ml with milliQ water) for 10 min

- Wash 3 times with 1x PBS
- Stain the nucleus with DAPI (1 :2000) 10µl DAPI in 20ml milliQ water for 5min
- Wash 3 times with 1x PBS
- Rinse the slides in milliQ water with a forceps and dry them with paper towels then put them in an A4 paper to complete the drying
- Put mounting medium in the glass slides
- Put the slides in the glass slides with forceps and let dry overnight

2.7.3 MTT essay

The MTT assay is used for measuring cellular metabolic activity as an indicator of cell viability, proliferation, and cytotoxicity. This colorimetric assay is based on the reduction of a yellow tetrazolium salt (3-(4,5-dimethylthiazol-2-yl)-2,5-diphenyltetrazolium bromide or MTT) to purple formazan crystals by metabolically active cells. Viable cells contain NAD(P)H-dependent oxidoreductase enzymes that reduce MTT into formazan. DMSO (Dimethyl sulfoxide) is added to dissolve formazan crystals and the resulting purple solution is quantified by measuring the absorbance at 590nm using a multi-well spectrophotometer (for 96 well plate). The darker the solution, the higher the number of viable metabolically active cells.

- Prepare the solution: complete DMEM (DMEM + 10% FBS) + MTT (e.g., 30 mL of complete DMEM + 3 mL of MTT (5 mg/mL))
- Aspirate the cell culture medium. For adherent cells, carefully aspirate the medium.
- Wash one time with PBS 1x
- Add MTT solution, 100µL to each well.
- Incubate at 37C (cell incubator), 3-4 hours.

- Add DMSO to solubilize the formazan and pipette up and down, put the plate in the dark and wait 1h
- Read the absorbance at OD = 590 nm with the multi-well spectrophotometer.

2.8 Confocal and conventional microscope

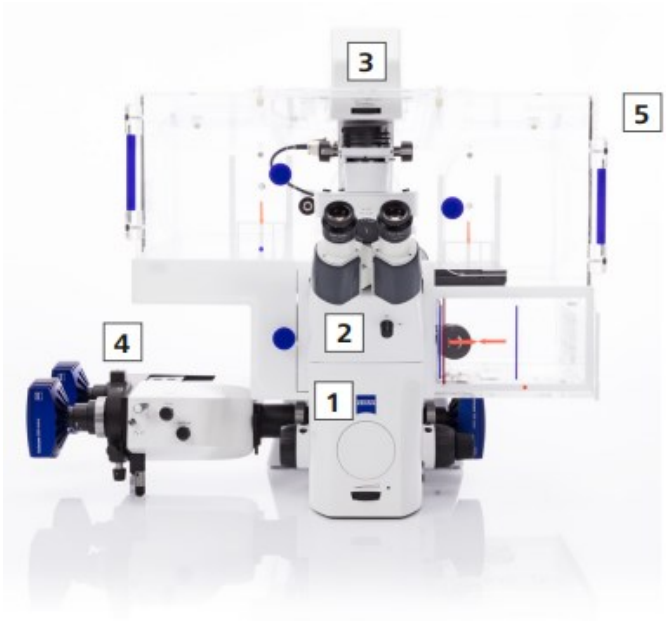

Figure 2.27: Axio Observer microscope 7 by Zeiss showing 1) the microscope 2) Objectives are within the microscope 3) Illumination 4) imaging system and 5) Accessories if live cell imaging is needed.

Axio Observer microscopes 7 by Zeiss inverted light microscope see **Figure 2.27** was used for in vitro experiment to study cellular uptake of gold and silver NCs. This instrument is located at Mediterranean institute for life science (MEDILS) in Split Croatia . The sample is excited with microLED illuminations, the plate is motorized in the XYZ direction for better focus. The system is fully controlled by Zen software. The system uses different reflector to select desired

fluorophore emission peak, for DAPI we use the reflector 90 at 385nm and for silver and gold NCs a reflector 56 at 475nm is used to visualize their range of emission.

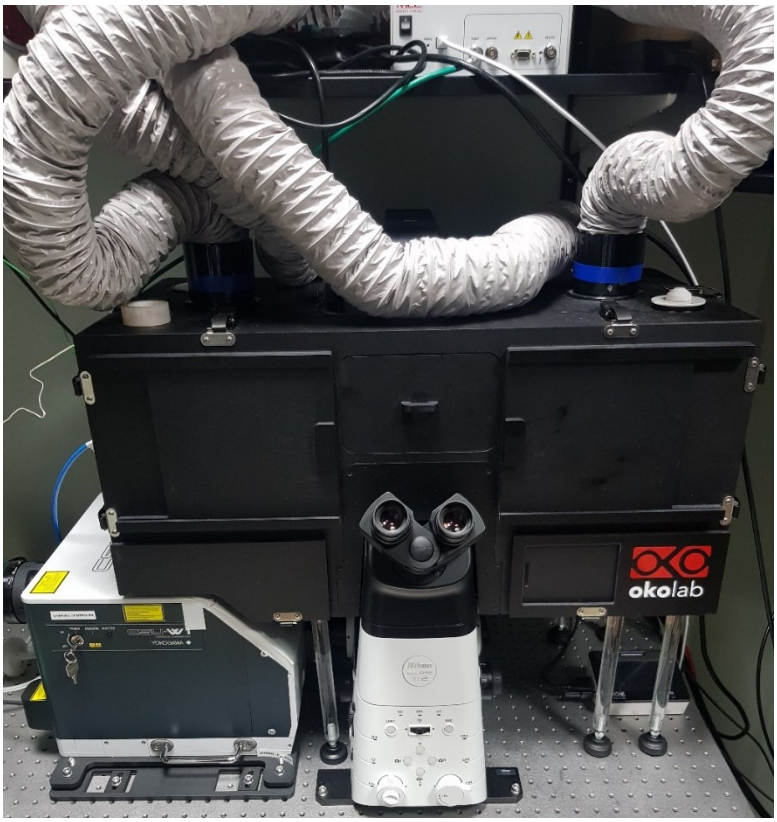

Figure 2.28 : Image showing a general picture of ECLIPSE Ti2-E/Ti2-E/B confocal microscope.

Yokogawa spinning disk inverted confocal microscope ECLIPSE Ti2-E/Ti2-E/B from Nikon located at the institute of light and matter (ILM), in the university of Lyon1 (Nanoptec team), is used to record high resolution images for cells, see **Figure 2.28**. The sample is excited using LightHUBplus N laser for different wavelengths. The emission signal is collected using ORCA-fusion BT digital camera C15440. Fluorophores (including NCs) was excited with different wavelengths (405nm for DAPI and 488nm for gold and silver NCs) with different emission filter. All the system is controlled with NIS-Elements software. This system includes

incubator with temperature controller and CO_2 flux to image live cell. This system is motorized with Ti2-S-SS-E joystick.

Conclusion

In this chapter, I have fully described the main techniques I used during this PhD work aiming at figuring out the structure-optical properties relationship for the as-synthesized nanoclusters. To this purpose, an impressive amount of work aiming at characterizing functionalized nanoclusters was conducted using high-resolution mass spectrometry, UV-Vis spectroscopy, fluorescence-based techniques for sizing, electron microscopy…

In addition, cutting-edge nonlinear optical set-ups and general concepts were described since this work was application oriented for using such nanoclusters as nonlinear optical targets for bioimaging using multiphoton confocal microscopy. The last part of this chapter was devoted to the description of in vitro bio-imaging set-ups and protocols (Nanoptec center (ILMTECH), microscopy in Croatia and cell culture facilities in Lyon and Split). Of note this chapter was intentionally written for future students working in the field of nanoclusters and their bio-applications, that's why, both synthesis protocols, and cell culture incubation were thoroughly and technically described.

References

[1] Lu, Y.; Chen, W. Application of Mass Spectrometry in the Synthesis and Characterization of Metal Nanoclusters. Anal. Chem. **2015**, 87 (21), 10659–10667. https://doi.org/10.1021/acs.analchem.5b00848.

[2] Comby-Zerbino, C.; Dagany, X.; Chirot, F.; Dugourd, P.; Antoine, R. The Emergence of Mass Spectrometry for Characterizing Nanomaterials. Atomically Precise Nanoclusters and Beyond. Mater. Adv. **2021**, 2 (15), 4896–4913. https://doi.org/10.1039/D1MA00261A.

[3] Grayson, M. A. John Bennett Fenn: A Curious Road to the Prize. J. Am. Soc. Mass Spectrom. **2011**, 22 (8), 1301–1308. https://doi.org/10.1007/s13361-011-0136-6.

[4] Ingram, R. S.; Hostetler, M. J.; Murray, R. W.; Schaaff, T. G.; Khoury, J. T.; Whetten, R. L.; Bigioni, T. P.; Guthrie, D. K.; First, P. N. 28 KDa Alkanethiolate-Protected Au Clusters Give Analogous Solution Electrochemistry and STM Coulomb Staircases. J. Am. Chem. Soc. **1997**, 119 (39), 9279–9280. https://doi.org/10.1021/ja972319y.

[5] Tracy, J. B.; Crowe, M. C.; Parker, J. F.; Hampe, O.; Fields-Zinna, C. A.; Dass, A.; Murray, R. W. Electrospray Ionization Mass Spectrometry of Uniform and Mixed Monolayer Nanoparticles: Au25[S(CH2)2Ph]18 and Au25[S(CH2)2Ph]18-x(SR)x. J. Am. Chem. Soc. **2007**, 129 (51), 16209–16215. https://doi.org/10.1021/ja076621a.

[6] Fenn, J. B. Electrospray Wings for Molecular Elephants (Nobel Lecture). Angew. Chem. Int. Ed Engl. **2003**, 42 (33), 3871–3894. https://doi.org/10.1002/anie.200300605.

[7] Carpenter, D. K. Dynamic Light Scattering with Applications to Chemistry, Biology, and Physics (Berne, Bruce J.; Pecora, Robert). J. Chem. Educ. **1977**, 54 (10), A430. https://doi.org/10.1021/ed054pA430.1.

[8] Li, Z. Y.; Young, N. P.; Di Vece, M.; Palomba, S.; Palmer, R. E.; Bleloch, A. L.; Curley, B. C.; Johnston, R. L.; Jiang, J.; Yuan, J. Three-Dimensional Atomic-Scale Structure of

Size-Selected Gold Nanoclusters. Nature **2008**, 451 (7174), 46–48. https://doi.org/10.1038/nature06470.

[9] Soleilhac, A. Thermographie Multi-Échelle Par Méthodes Optiques Sur Gouttelettes et Bulles Micrométriques : Applications Aux Nanoparticules Irradiées Par Laser Ultra-Intense et Aux Édifices Biomoléculaires En Cours de Déshydratation. These de doctorat, Lyon, 2017.

[10] Canet, D.; Doering, K.; Dobson, C. M.; Dupont, Y. High-Sensitivity Fluorescence Anisotropy Detection of Protein-Folding Events: Application to α-Lactalbumin. Biophys. J. **2001**, 80 (4), 1996–2003. https://doi.org/10.1016/S0006-3495(01)76169-3.

[11] LeTilly, V.; Royer, C. A. Fluorescence Anisotropy Assays Implicate Protein-Protein Interactions in Regulating Trp Repressor DNA Binding. Biochemistry **1993**, 32 (30), 7753–7758. https://doi.org/10.1021/bi00081a021.

[12] Weiss, S. Measuring Conformational Dynamics of Biomolecules by Single Molecule Fluorescence Spectroscopy. Nat. Struct. Biol. **2000**, 7 (9), 724–729. https://doi.org/10.1038/78941.

[13] Soleilhac, A.; Bertorelle, F.; Comby-Zerbino, C.; Chirot, F.; Calin, N.; Dugourd, P.; Antoine, R. Size Characterization of Glutathione-Protected Gold Nanoclusters in the Solid, Liquid and Gas Phases. J. Phys. Chem. C **2017**, 121 (49), 27733–27740. https://doi.org/10.1021/acs.jpcc.7b09500.

[14] Size Evolution of Protein-Protected Gold Clusters in Solution: A Combined SAXS–MS Investigation | The Journal of Physical Chemistry C. https://pubs.acs.org/doi/abs/10.1021/jp509332j (accessed 2021-07-22).

[15] Jin, R. Atomically Precise Metal Nanoclusters: Stable Sizes and Optical Properties. Nanoscale **2015**, 7 (5), 1549–1565. https://doi.org/10.1039/C4NR05794E.

[16] Maiman, T. H. Optical and Microwave-Optical Experiments in Ruby. Phys Rev Lett **1960**, 4 (11), 564–566. https://doi.org/10.1103/PhysRevLett.4.564.

[17] Franken, P. A.; Hill, A. E.; Peters, C. W.; Weinreich, G. Generation of Optical Harmonics. Phys. Rev. Lett. **1961**, 7 (4), 118–119. https://doi.org/10.1103/PhysRevLett.7.118.

[18] Three-dimensional micro-fabrication by femtosecond laser--《Opto-electronic Engineering》2005年04期. https://en.cnki.com.cn/Article_en/CJFDTotal-GDGC200504027.htm (accessed 2021-07-14).

[19] Castet, F.; Rodriguez, V.; Pozzo, J.-L.; Ducasse, L.; Plaquet, A.; Champagne, B. Design and Characterization of Molecular Nonlinear Optical Switches. Acc. Chem. Res. **2013**, 46 (11), 2656–2665. https://doi.org/10.1021/ar4000955.

[20] Mulligan, S. J.; Macvicar, B. A. Two-Photon Fluorescence Microscopy: Basic Principles, Advantages and Risks.

[21] Liganded Silver and Gold Quantum Clusters. Towards a New Class of Nonlinear Optical Nanomaterials.

[22] Non-Linear Optical Properties of Matter: From Molecules to Condensed Phases; Papadopoulos, M. G., Sadlej, A. J., Leszczynski, J., Eds.; Challenges and advances in computational chemistry and physics; Springer: Dordrecht, 2006.

[23] Verbiest, T.; Clays, K.; Rodriguez, V. Second-Order Nonlinear Optical Characterization Techniques: An Introduction; CRC Press, 2009.

[24] Rao, D. N.; Naga Srinivas, N. K. M.; Gangopadhyay, P.; Radhakrishnan, T. P. Internal Cancellation of Electric Field Induced Second Harmonic Generation in Solvent Mixtures and Solutions: An Efficient Protocol for the Determination of Molecular Hyperpolarizability. J. Phys. Chem. A **2004**, 108 (24), 5213–5219. https://doi.org/10.1021/jp037635f.

[25] Russier-Antoine, I.; Bertorelle, F.; Vojkovic, M.; Rayane, D.; Salmon, E.; Jonin, C.; Dugourd, P.; Antoine, R.; Brevet, P.-F. Non-Linear Optical Properties of Gold Quantum Clusters. The Smaller the Better. Nanoscale **2014**, 6 (22), 13572–13578. https://doi.org/10.1039/C4NR03782K.

[26] Albota, M. A.; Xu, C.; Webb, W. W. Two-Photon Fluorescence Excitation Cross Sections of Biomolecular Probes from 690 to 960 Nm. Appl. Opt. **1998**, 37 (31), 7352–7356. https://doi.org/10.1364/AO.37.007352.

[27] Sheik-Bahae, M.; Said, A. A.; Wei, T.-H.; Hagan, D. J.; Van Stryland, E. W. Sensitive Measurement of Optical Nonlinearities Using a Single Beam. IEEE J. Quantum Electron. **1990**, 26 (4), 760–769. https://doi.org/10.1109/3.53394.

[28] Lamarre, J.-M.; Billard, F.; Kerboua, C. H.; Lequime, M.; Roorda, S.; Martinu, L. Anisotropic Nonlinear Optical Absorption of Gold Nanorods in a Silica Matrix. Opt. Commun. **2008**, 281 (2), 331–340. https://doi.org/10.1016/j.optcom.2007.09.018.

[29] Maurice, A. Diffusion de Second Harmonique En Milieux Liquides : Approche Comparée Des Réponses de Volume et de Surface. These de doctorat, Lyon, 2016.

[30] Schaeffter, T. Imaging Modalities: Principles and Information Content. In Imaging in Drug Discovery and Early Clinical Trials; Herrling, P. L., Matter, A., Rudin, M., Eds.; Progress in Drug Research; Birkhäuser: Basel, 2005; pp 15–81. https://doi.org/10.1007/3-7643-7426-8_2.

[31] Kobayashi, H.; Ogawa, M.; Alford, R.; Choyke, P. L.; Urano, Y. New Strategies for Fluorescent Probe Design in Medical Diagnostic Imaging. Chem. Rev. **2010**, 110 (5), 2620–2640. https://doi.org/10.1021/cr900263j.

[32] Centonze, V. E.; White, J. G. Multiphoton Excitation Provides Optical Sections from Deeper within Scattering Specimens than Confocal Imaging. Biophys. J. **1998**, 75 (4), 2015–2024.

[33] Squirrell, J. M.; Wokosin, D. L.; White, J. G.; Bavister, B. D. Long-Term Two-Photon Fluorescence Imaging of Mammalian Embryos without Compromising Viability. Nat. Biotechnol. **1999**, 17 (8), 763–767. https://doi.org/10.1038/11698.

[34] Basu, S.; Bakulić, M. P.; Fakhouri, H.; Russier-Antoine, I.; Moulin, C.; Brevet, P.-F.; Bonačić-Koutecký, V.; Antoine, R. Rationale Strategy to Tune the Optical Properties of Gold Catenane Nanoclusters by Doping with Silver Atoms. J. Phys. Chem. C **2020**. https://doi.org/10.1021/acs.jpcc.0c05402.

[35] Maysinger, D.; Gran, E. R.; Bertorelle, F.; Fakhouri, H.; Antoine, R.; Kaul, E. S.; Samhadaneh, D. M.; Stochaj, U. Gold Nanoclusters Elicit Homeostatic Perturbations in Glioblastoma Cells and Adaptive Changes of Lysosomes. Theranostics **2020**, 10 (4), 1633–1648. https://doi.org/10.7150/thno.37674.

[36] Russier-Antoine, I.; Bertorelle, F.; Hamouda, R.; Rayane, D.; Dugourd, P.; Sanader, Ž.; Bonačić-Koutecký, V.; Brevet, P.-F.; Antoine, R. Tuning Ag29 Nanocluster Light Emission from Red to Blue with One and Two-Photon Excitation. Nanoscale **2016**, 8 (5), 2892–2898. https://doi.org/10.1039/C5NR08122J.

Chapter 3: Design of novel functionalized nanoclusters for application in biological aging

Introduction

This chapter is the centerpiece of my doctoral work. The work described in this chapter led to a paper published in 2021 in Communications Chemistry[1]. In addition, this paper, already cited 12 times, was selected for the collections "Celebrating Women in Chemistry" and "2021 Editors' Highlights". The aim of this present chapter is not to "copy-paste" the published paper, but more to explain how the paper (and the strategy to design novel functionalized nanoclusters) was built all avenues explored that have worked or not ! Thus, a lot of details will be paid to describe the experimental trials at the beginning of the project to find the best candidates based on nanoclusters to detect carbonylation. For this purpose, a significant number of months was spent to exploring silver-doping strategies ! The final goal was to give a "proof of concept" using functionalized gold nanoclusters to detect protein carbonylation in 2D electrophoresis gel. Finally, $Au_{15}SG_{13}$ was found to be the best compromise as nanoclusters in terms of optical properties, stability and ability to be functionalized.

Due to the pluridisciplinary nature of this collaborative work mixing biologists, physical, theoretical and analytical chemists (involving mainly the Center of Excellence for Science and Technology-Integration of Mediterranean Region (STIM), Faculty of Science, University of Split, the Mediterranean Institute for Life Sciences (MedILS), Split, and Institut Lumière Matière, Villeurbanne), the approaches in the project was divided in two major features, the first was the synthesis, functionalization and structural and (nonlinear) optical characterizations of gold NCs where I was mostly involved, the second was to adapt biological tools, in particular gels and biochemicals reagents and quantification methods with biologist where mostly Guillaume Combes (Post-doc STIM) was involved.

This work was started in early 2019 exploring first the potential candidate for gold –based NCs for this approach in terms of stability, optical properties, and surface modifiable ligand. I will thus describe strategies that was used for manipulating photoluminescence properties and stability issues of gold clusters ($Au_{18}SG_{14}$) via silver doping strategy. Next, the goal was to

render NCs specific to carbonyls. Thus, surface functionalization (either with surface post-modification or ligand exchange) was explored to target efficiently carbonylation with functionalized nanoclusters. Biological essays and approaches in parallel were adapted for the use of nanoclusters (instead of standard organic dyes) and conducted by the biological team in STIM-MedILS, at Split. Due to the complication and nature of gold NCs migration inside the cells, gels protocols were modified to adapt to both gold NCs and proteins migrations inside gels. The aim of this chapter is also to highlight the fruitful collaborative work in this multidisciplinary project.

3.1 The quest for the best nanocluster candidates for optical detection by photoluminescence.

Optical properties depend on NCs structures, ligand and gold atoms number. Absorption spectra are very specific in this size regime where "each atom counts". Rongchao Jin for instance tried to establish some "benchmark" absorption spectra that could be used as fingerprint for characterization of nanoclusters.[2]

Using glutathione as ligand, we have been able to produce at the "gram scale" and at atomic precision, 4 cluster sizes, $Au_{10}SG_{10}$, $Au_{15}SG_{13}$, $Au_{18}SG_{14}$, and $Au_{25}SG_{18}$, The atomic precision of these nanoclusters was confirmed by ESI-MS analysis (see **Figure 3.1)**. Au10SG10 is the smallest nanoclusters (in terms of number of gold atoms). It is an interesting cluster with a very particular structure, a chiral gold catenane structure, this nanocluster has no metal with zero confined electrons[3]. Although very interesting chiroptical applications, this nanocluster presents a very weak fluorescence (less than 0.01% quantum yield). At this stage, we knew that

$Au_{10}SG_{10}$ NC is not fluorescence, but we believed that silver doping strategy may enhance the optical properties for NCs that I will talk about it later in this section.

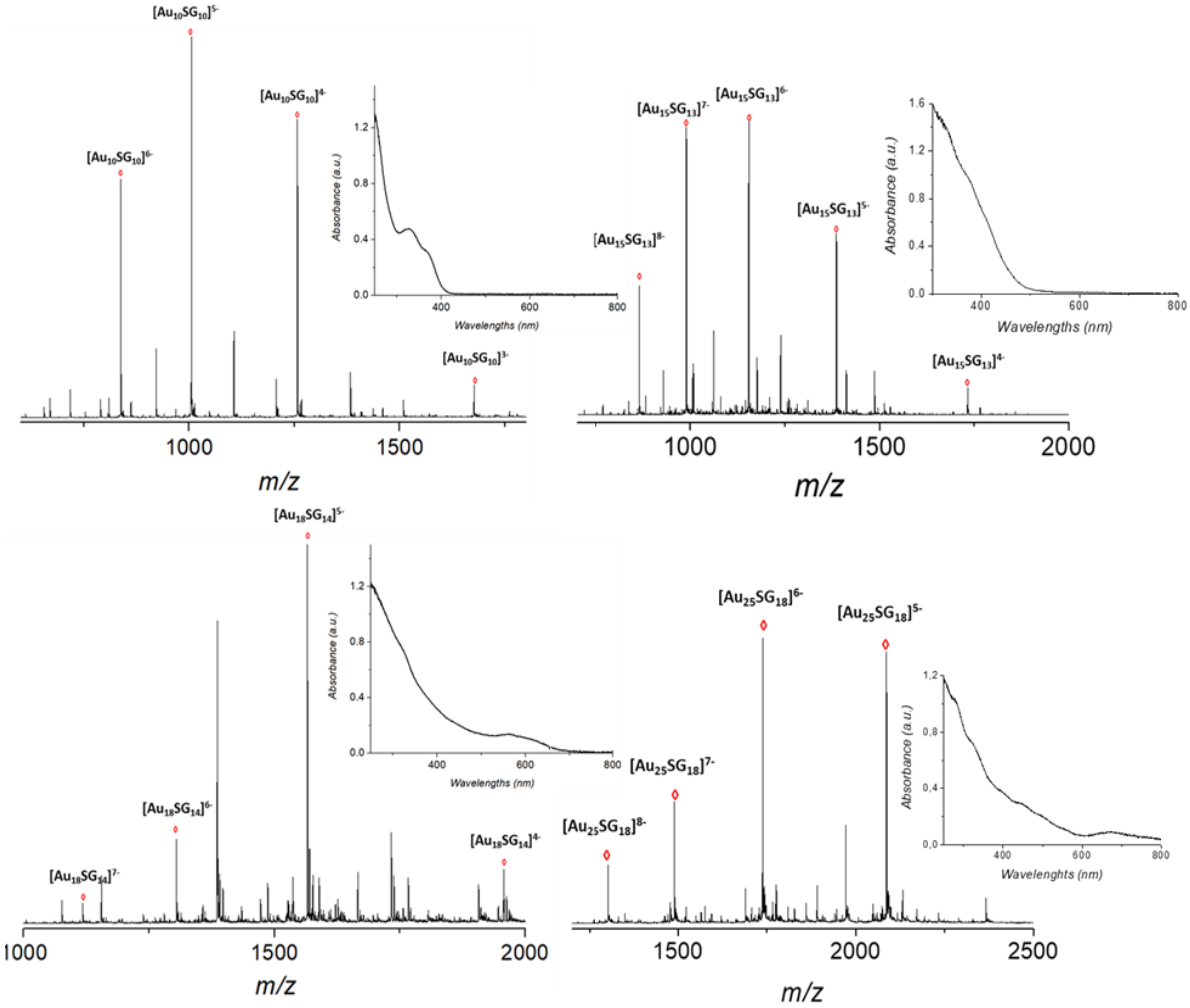

Figure 3.1 : ESI Mass Spectrum and UV-visible absorption spectra of different glutathione capped gold NCs ($Au_{10}SG_{10}$, $Au_{15}SG_{13}$, $Au_{18}SG_{14}$ and $Au_{25}SG_{18}$), other peaks was observed in MS spectrum are due to some impurities, gold NCs are mostly presented as anions in the solution, the ESI-MS will provide spectrum of the samples with different charge state, for example $Au_{15}SG_{13}$ have 5 charge state 4-,5-,6-,7-and 8- and so 5 spectra will appear in the graph.

$Au_{15}SG_{13}$ and $Au_{25}SG_{18}$ present also a very weak fluorescence in water (with QYs in the order of 10^{-4} – 10^{-3}). On the other hand, Au18SG14 also present a strong fluorescence in water (with

QY about 1.6%). We though that $Au_{18}SG_{14}$ will be the best candidate. However, as a main drawback, this NC presents a poor stability and quickly deteriorate (about 1 hour) in the room condition. Doping gold nanoclusters with heteroatoms (in particular with silver) has been demonstrated as a versatile approach to tune their physicochemical performances. Generally, doping atom(s) into parent nanoclusters will enhance their thermal stability, catalytic activity, and more importantly for us their photoluminescence. In addition, many recent work has shown that silver doping strategy will also enhance l nonlinear optical properties[4]. It can also modify the emission towards the near infrared window, improving their two photon bioimaging

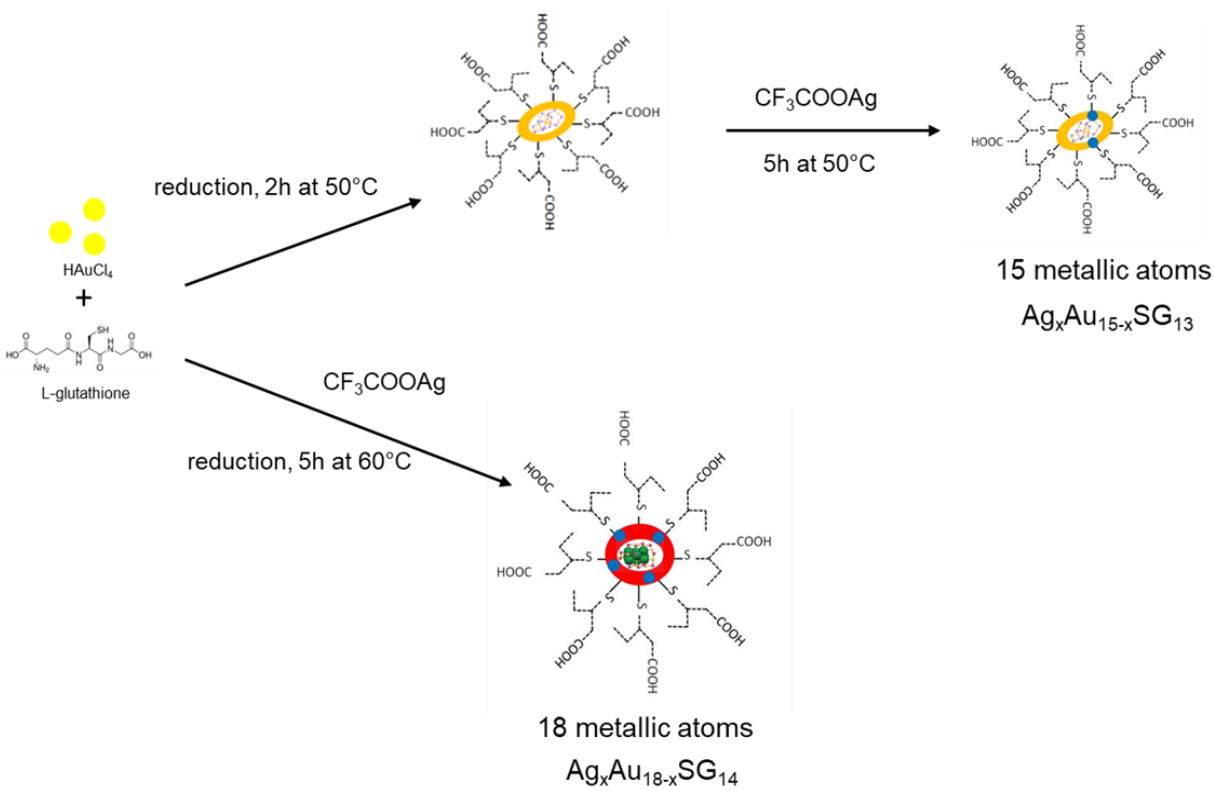

Figure 3.2 : Two strategies of silver doping for gold nanoclusters. (top) silver doping of $Au_{15}SG_{13}$, where metal exchange is produced after prepared $Au_{15}SG_{13}$,(bottom)one pot synthesis silver doping for gold nanoclusters for $Au_{18}SG_{14}$ where we added silver salt directly in the synthesis. Both strategies will lead to 0,1,2 and even more substitution depending on the ratio of silver to gold in the synthesis.

applications and interest[5]. The silver doping strategy was explored on gold nanoclusters for Au10SG10, and $Au_{15}SG_{13}$ NCs to improve their optical properties (in particular their photoluminescence), and for $Au_{18}SG_{14}$ NCs to enhance the stability and increase their photoluminescence. There are basically two strategies to dope nanoclusters. First depending on the ratio of silver salt added with the gold salt in the gold NCs synthesis , the silver atoms will substitute gold atoms in the metallic core, leading to one or more doping in the NC. This strategy was explored for silver doping Au18SG14 NCs (see **Figure 3.2)**. A second strategy consists in doing silver exchange directly on the preformed gold nanoclusters. depending on the amount of silver salt added, the silver atoms will substitute gold atoms in the metallic core of the preformed gold nanoclusters, leading to one or more doping in the NCs. This strategy was explored for silver doping Au15SG13 NCs (see **Figure 3.2).**

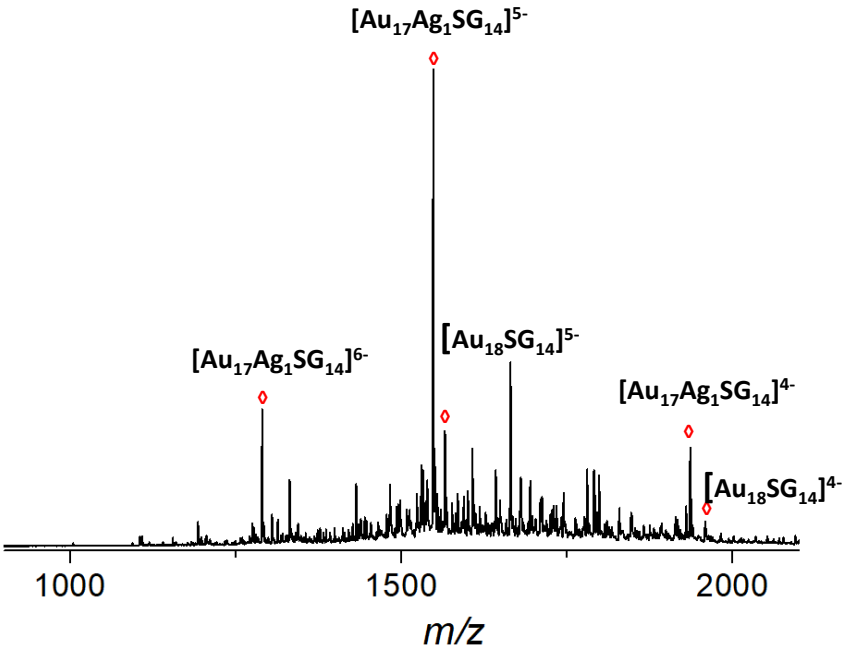

Figure 3.3 : ESI MS spectra for silver doped $Au_{18}SG_{14}$ NCs. Doping silver strategy produce a mixture of $Au_{18}SG_{14}$ and $Au_{17}AgSG_{14}$, this nanocluster solution was stable after dissolution in water.

We performed ESI MS measurement showed that silver doping with atomic precision **Figure 3.3**. The $Au_{18}SG_{14}$ NC was always presented in the solution and there was one silver doping, the results were two products in the solution, $Au_{18-x}Ag_xSG_{14}$ with x=0,1, with about 30% and 70% ratio in the solution, respectively. We tried hard to replace only one atom and get a pure Au17AgSG14 solution, but it was impossible. Once we tried to ride on from $Au_{18}SG_{14}$ and increase the ratio of silver to gold in the synthesis, we realized that the doping of silver was increased, leading to more silver atom replacing gold atom with x=0,1,2 (number of silver atom in the core) and even more silver doping and more impurities, in this case the source of the optical property will be unknown (which cluster will give this optical properties) and so we stayed on 1 silver doping ratio strategy. We did not observe any enhancement of optical properties after silver doping, we used DCM in methanol (QY 60%) as reference to calculate the quantum yield, $Au_{18-x}Ag_xSG_{14}$ QY was slightly lower (1.25 %) than $Au_{18}SG_{14}$ with a QY of 1.5%. We noticed a slight modification of fluorescence lifetime after silver doping (see **Figure 3.4**). Also a slight blue- shift in one photon emission for silver doped Au18SG14 NCs is observed and in addition UV-vis spectra showed that the band at 600nm for $Au_{18}SG_{14}$ was not anymore present after silver doping **Figure 3.6**. Such modifications in absorption spectra may suggest that the structure and electronic states of the NC was changed upon silver doping silver[6].

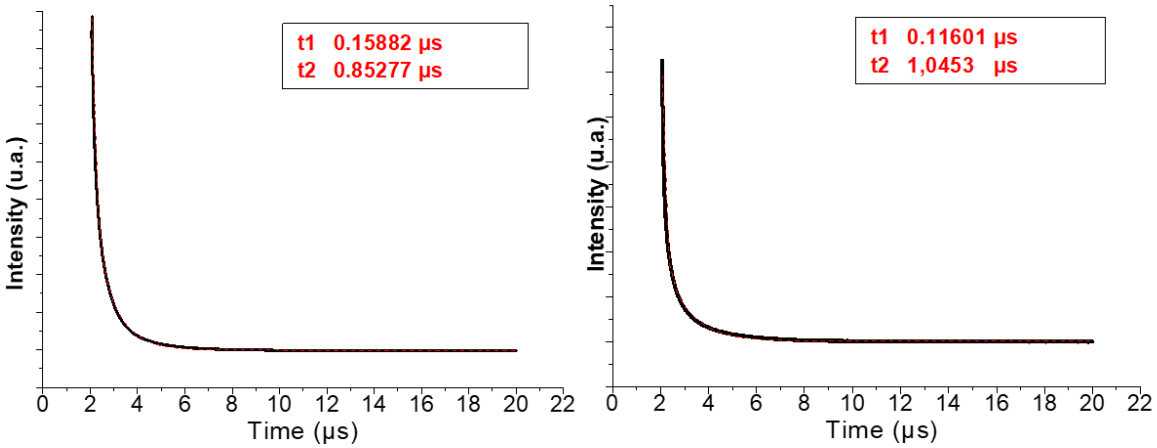

Figure 3.4 : (In black) Fluorescence lifetime of $Au_{18}SG_{14}$ (left) and dopped silver (right) with their fitting with double exponential (in red), clearly doping silver has changed the relaxation time of the original.

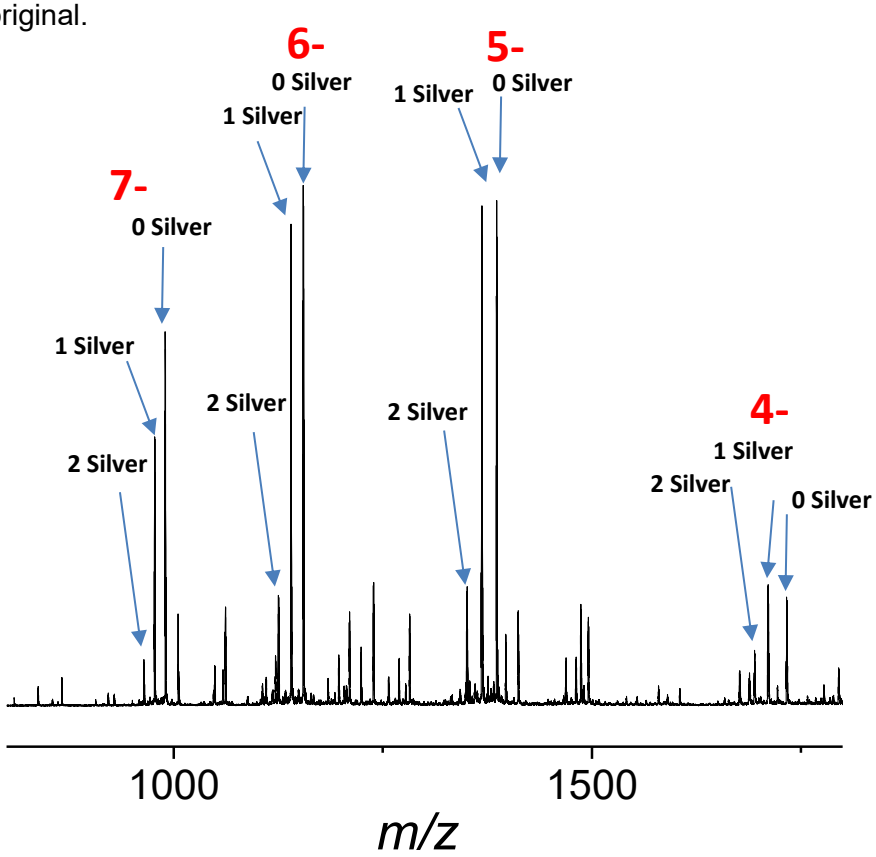

Figure 3.5: ESI MS spectra for $Au_{15}SG_{13}$ dopped silver, in red the charge state of $[Au_{15-x}Ag_xSG_{13}]^{z-}$, it was complicated to control silver doping in the synthesis.

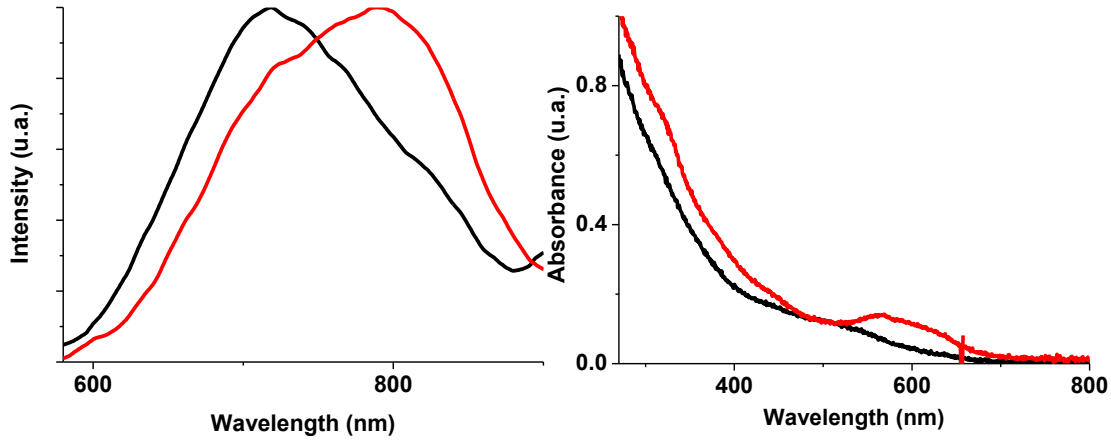

Figure 3.6: In red $Au_{18}SG_{14,}$ black solver doped-$Au_{18}SG_{14}$. Normalized one photon emission fluorescence after excitation at 500nm, doping this NC with silver leads to significant bleu shift (about 50nm), on the left UV-vis spectra where the shoulder at 600nm was deceased significantly after silver doping.

Doping silver was more complicated for $Au_{15}SG_{13}$ **Figure 3.5**. It was possible to produce silver-doped $Au_{15}SG_{13}$ NCs using this strategy described for $Au_{18}SG_{14}$. Silver doping was performed on the $Au_{15}SG_{13}$ clusters but the ratio was too sensitive to the number of silver atoms doping, the minimum silver ratio will give up to 2 silver doping, which lead us to the same problem of the synthesis purity (not possible to produce a single metal atom doping nanoclusters, but more a collection of silver doped and pure $Au_{15}SG_{13}$). In addition, no luminescence enhancement was observed. Of note, we also explored the possible enhancement effect of silver doping on the 2-photon excited fluorescence signals. **Figure 3.7** shows TPEF spectra recorded for $Au_{15}SG_{13}$, $Au_{18}SG_{14}$ and the corresponding silver doped NCs in water under 780 nm excitation. No TPEF luminescence enhancement was observed by using the silver doping strategy.

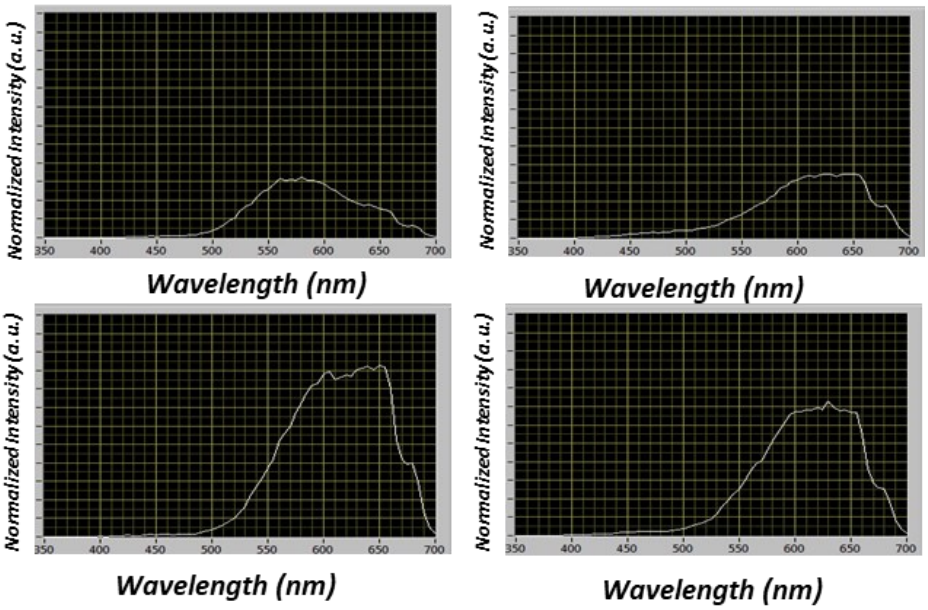

Figure 3.7: TPEF spectra recorded for $Au_{15}SG_{13}$, $Au_{18}SG_{14}$ and the corresponding silver doped NCs in water under 780 nm excitation.

Finally, we aimed at evaluating the impact of silver doping for $Au_{10}SG_{10}$ in terms of optical properties with the heteroatom substitution, with structurally resolved nanoclusters. This work was conducted with Srestha Basu [7]. Indeed, we showed by powder X-ray diffraction XRD measurements (and comparison with simulated XRD pattern for trial structures)[7] that the "unique" catenane structure was preserved by silver doping on Au10 nanoclusters motifs. Thus, for this Au10 nanoclusters, a direct structure-optical properties relations can be drawn, since catenane structures are preserved upon silver doping.

We showed that the ratio of silver to gold in the synthesis play a large factor in the number of silver doping on Au10 nanoclusters (see **Figure 3.8**, it was also impossible for us to get a solution with only one species, the results was always one or more silver-doped NCs in the same solution whatever strategies that we tried.

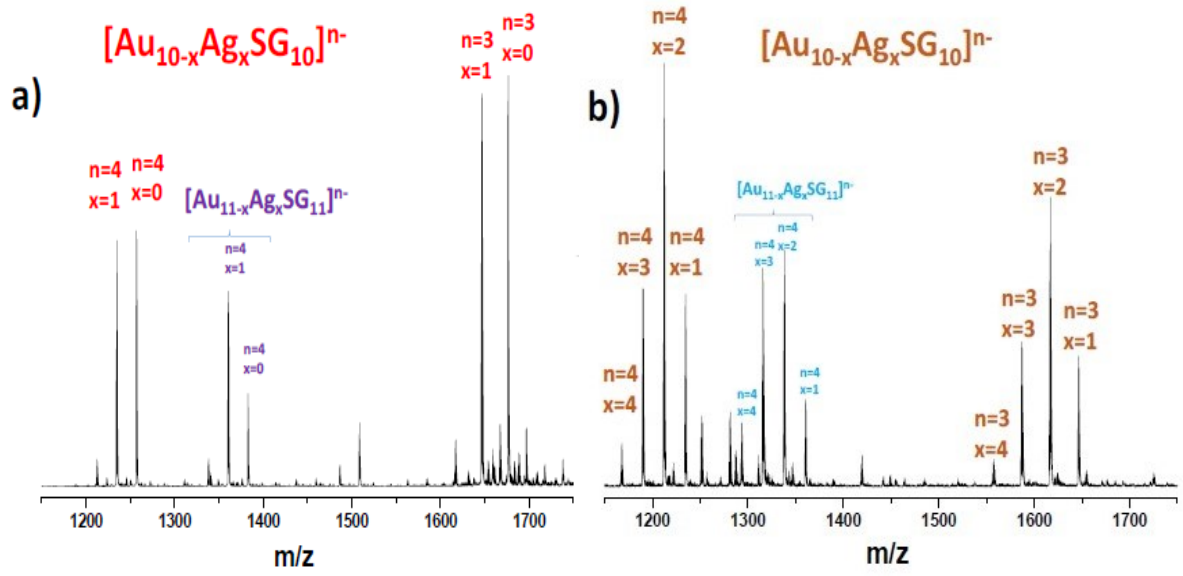

Figure 3.8 : ESI-MS spectrum of a) $Au_{10-x}Ag_xSG_{10}$ with x= 0-2 and b) $Au_{10-x}Ag_xSG_{10}$ with x= 1-4. More silver dopped atoms will appear if the ration of gold to silver is increased during the synthesis.

Concerning optical properties, such Au10 nanoclusters present no photoluminescence in water (and extremely weak luminescence in powder). However, in the NLO regime, TPEF signal is observe (although TPEF cross sections remain quite modest, ~0.002 GM). Interestingly, a significant red shift in TPEF emission spectra of about 50 nm was observed for $Au_{10-x}Ag_xSG_{10}$ with x=1-4 as compared to pure Au10SG10 NCs. the normalized TPEF spectra for $Au_{10}SG_{10}$ shows a maximum band at 555nm, while for $Au_{10-x}Ag_xSG_{10}$ with x=1-4 was at 660 nm **Figure 3.9**. This effect main be explained by the fact that silver doping upon $Au_{10}SG_{10}$ change the

relaxation in the S1 state and cause the red shift. The changes in relaxation in the S1 state induce a lowering of S1 energies and was accounted for the breaking of the silver–gold bonds in the first excited state of the silver atom-doped clusters.

Silver doping is an important method to manipulate optical properties, and for fundamental investigation of the NCs to understand the relation between the structure and the optical properties. It is important to mention that $Au_{10}SG_{10}$ do not display any photoluminescence in water , and we recorded the TPEF emission spectra in dried gel. Wet environment will quench the optical properties of NCs and exposed the core of the NC to the solvent and the glutathione will not protect it from the interaction with the solvent, and the energy of the excited state is lost in vibration effect in degenerated energy levels.

In conclusion, we spent a considerable number of months to exploring silver-doping strategies. Optical properties (photoluminescence) of glutathione-protected gold nanoclusters were not significantly improved by silver doping. Interestingly, a red shift in TPEF spectra was observed for silver doped Au10 NCs. Such silver doping strategy might be useful to produce NC-based target to reach the NIR window important for bio-imaging applications. Also, silver doping was able to increase the stability of the high-luminescent Au18SG14 nanoclusters. However, whatever the strategy used to do silver doping, we failed to produce silver doped NCs at the atomic precision. Thus, we have abandoned this strategy.

Of note, Au25SG13 NCs were also investigated but their optical properties were similar and even a bit smaller in terms of photoluminescence (as compared to Au15SG13). Thus, we choose to use $Au_{15}SG_{13}$ NC, although it was not the best candidate in linear and nonlinear optical properties, but it was the most stable and the most efficient target for functionalization for detection of protein carbonylation in dried gel.

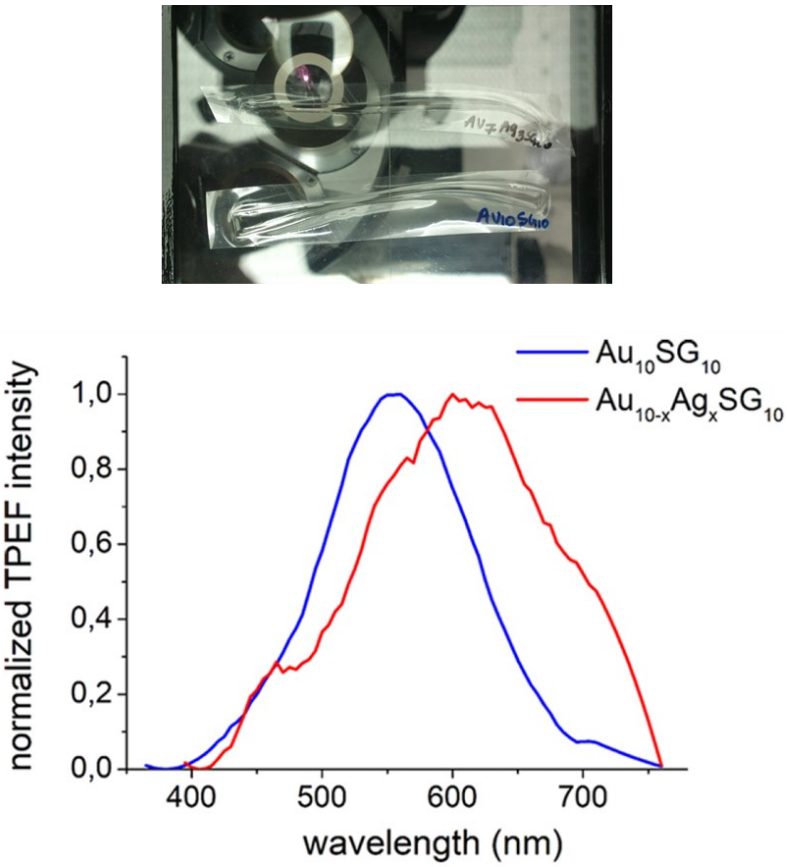

Figure 3.9 : (Down) Normalized two-photon excited fluorescence spectra at excitation wavelength 780 nm of $Au_{10}SG_{10}$ compared to that of silver doped $Au_{10-x}Ag_xSG_{10}$ (x = 1−4) in gels with the same concentration ~750 µM. TPEF measurements were performed on nanocluster containing gels with a customized confocal microscope (top).

3.2 Sensitivity test for using gold nanoclusters as optical probe

In order to show that NCs can be applied in bio-imaging domain to detect proteins in dried gel, we conducted, in parallel to these nanoclusters synthesis strategies described above, a sensitivity tests on gels with nanoclusters alone. To assess the efficiency of using nanoclusters as optical probes and compare it with ordinary methods (using organic dyes), we start by scanning the gels under multiphoton confocal microscopy and compared it with one linear gel scanning technic. We evaluated whether our NCs is detectable with both instruments. As I mentioned before, NCs present low quantum yield in aqueous medium like water, so we performed our experiments with dried the gels. We did random tests for different NCs at the beginning, at the point where we were still choosing between the different NCs **Figure 3.10**.

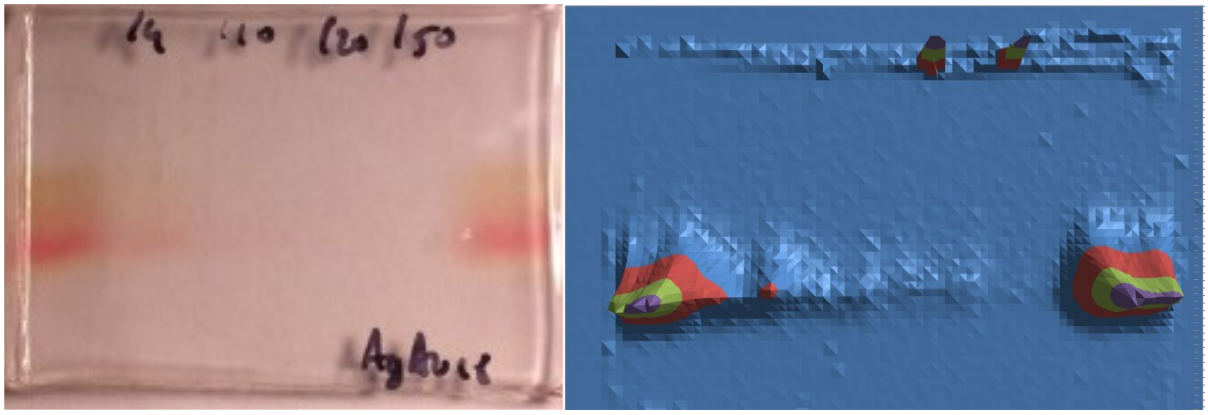

Figure 3.10 : Gel scanning performed with multiphoton confocal microscopy for dried gel for $(AuAg)_{18}SG_{14}$, 10mM, using 0.1µg of solution (the most colored on left) and decreasing concentration to 0.0002 µg and then back to the max concentration.

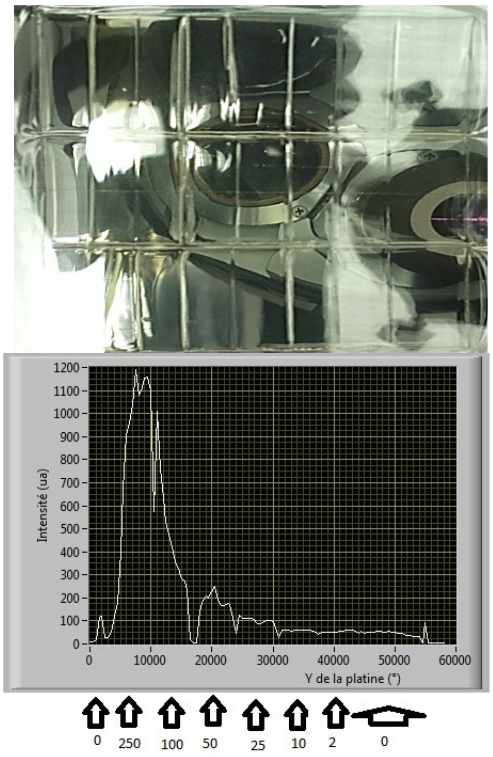

Figure 3.11 : Sensitivity test on dried gel with an excitation wavelength at 780nm, we insert $Au_{15}SG_{13}$ using different concentration (in µM), the system showed good detection for NCs.

The optimization of the parameters was difficult, gels scanning takes long time (sometimes one whole night), and we were not the only team using the system. **Figure 3.11** shows a test of sensitivity on dried gel of $Au_{15}SG_{13}$ NCs, note that even for low concentration (2 and 10 µM), we could increase the gain of the photon-multiplayer to increase the intensity of the pic, but we couldn't do that because it will saturate the signal for high concentration (250µM), at this point we realized that we won't have a problem to visualize low concentration of carbonylated protein with NC. We compared the linear system with non-linear system, **Figure 3.12** shows a comparison of sensitivity of $Au_{25}SG_{18}$ in gel between Typhoon™ FLA 9500 biomolecular imager gel scanning system and multiphoton confocal microscopy. The two system showed a good ability to visualize low concentration of gold NCs in dried gels with a linear dependency

on the concentration, so we started to immigrate protein with functionalized NCs and evaluate them with the two systems.

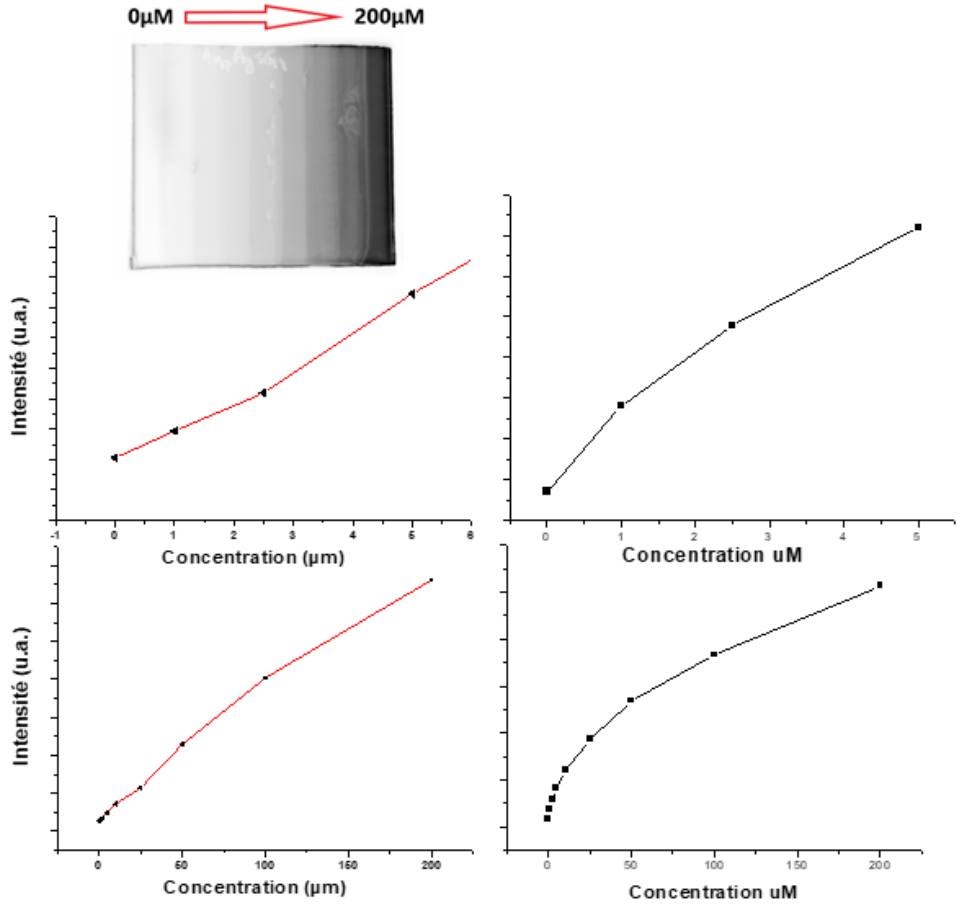

Figure 3.12 : Sensitivity test on dried gel of $Au_{25}SG_{18}$ NC collected by multiphoton confocal microscopy (in Red) and by Typhoon™ FLA 9500 biomolecular imager gel scanning system (in black), above shows the data at low concentration to show that both system are sensitive to low concentration of NCs.

3.3 Functionalization of gold nanoclusters

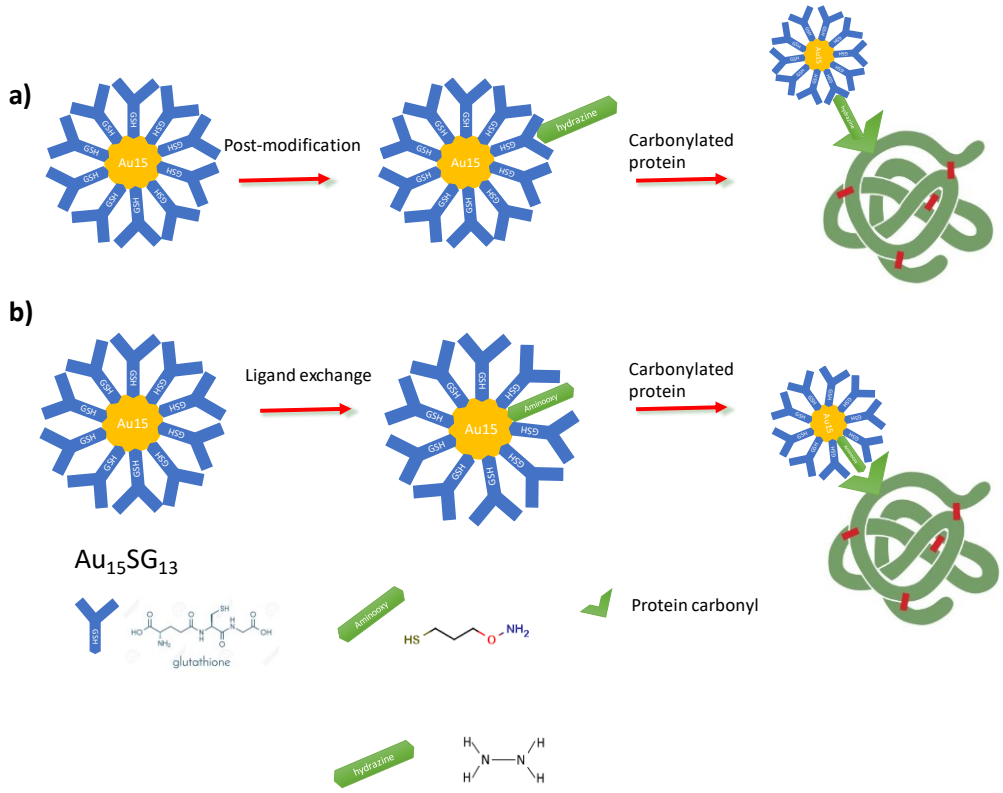

Scheme 3-1 : Strategies used in this thesis to functionalize nanoclusters to detect carbonylated proteins. (a) by post-modification and (b) by ligand exchange.

In this section, I will explain how we addressed challenges associated to the development of the first nanocluster based-imaging system for protein carbonylation detection. The nanoclusters, we finally choose, are liganded by glutathione (SG) and are produced at the atomic precision with the exact formula Au15SG13. After a ligand exchange procedure, the clusters are targeted with a carbonyl sensitive probe and are used to detect the protein carbonyls (see scheme 1). Two strategies were used in this thesis to functionalize nanoclusters to detect

carbonylated proteins. (See scheme 1a) by post-modification and (see scheme 1b) by ligand exchange.

Indeed, $Au_{15}SG_{13}$ will not allow the detection of carbonyl group alone, while the glutathione holds either amine or carboxylic acid groups at the end, these group present no specific interactions and no direct binding with carbonyl groups, hence a need for functionalization of gold NCs is necessary. As illustrated in scheme 1a), we started by adding hydrazine NH_2NH_2 to the $Au_{15}SG_{13}$, the first amine group will bind to the carboxylic acid of the NC, and the second amine will be used to react with carbonyl groups forming a hydrazone bond. Thus, we

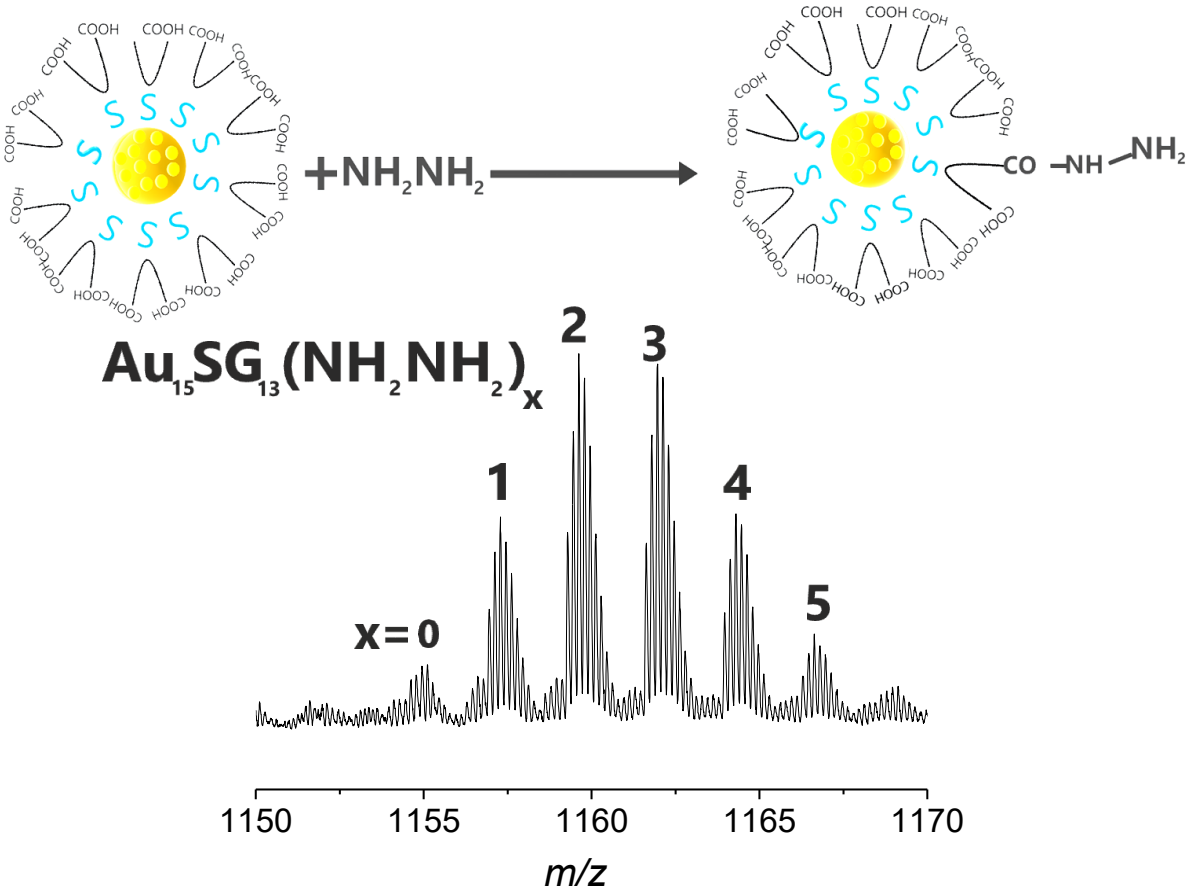

Figure 3.13 : (Top) Illustration image about the strategy of adding hydrazine to $Au_{15}SG_{13}$ where the goal was to obtain only one hydrazine for each NC, (down) ESI MS results for this strategy where we can see that nanoclusters with 0 to 6 hydrazide groups can be produced.

expect to replace one of the accessible carboxylic groups of glutathione (-COOH) by the functional (-CO-NH-NH2) reactive group. Even using low centration of hydrazine, unfortunately we failed to control the number of hydrazine attached to $Au_{15}SG_{13}$, an in particular to have only one hydrazine attached to $Au_{15}SG_{13}$ (see **Figure 3.13** for ESI-MS results showing that up to 6 hydrazide can bind carboxylic groups of Au15SG13). In fact, as it is commonly used with organic dyes, nanoclusters should be produced with only one functional group to keep a one-to-one correspondence between the number of nanoclusters and the number of carbonylated proteins, especially if we want to go further like quantification. Clearly, with up to 5 hydrazine on a single nanocluster, several carbonylated proteins can bind the nanoclusters and if we want to compare our strategy of detection with dyes, it will be insufficient to have more than one carbonyl detection functional group for one NC, so this method was abandoned and we explored the strategy, e.g. ligand exchange strategy (see scheme 1b).

Ligand exchange has found to be a powerful strategy to controlling gold atoms in gold NCs [8,9]. The goal of this method is to give the NCs the appropriate functional groups for carbonyl detection, we showed that ligand exchange with (3-Aminooxy)-1-propanethiol ligand noted as Ao (or aminooxy) is the adapted strategy to functionalized $Au_{15}SG_{13}$ into $Au_{15}SG_{12}Ao$ who binds to carbonyl group and enabling the detection of this phenomena in dried gel. **Figure 3.14**

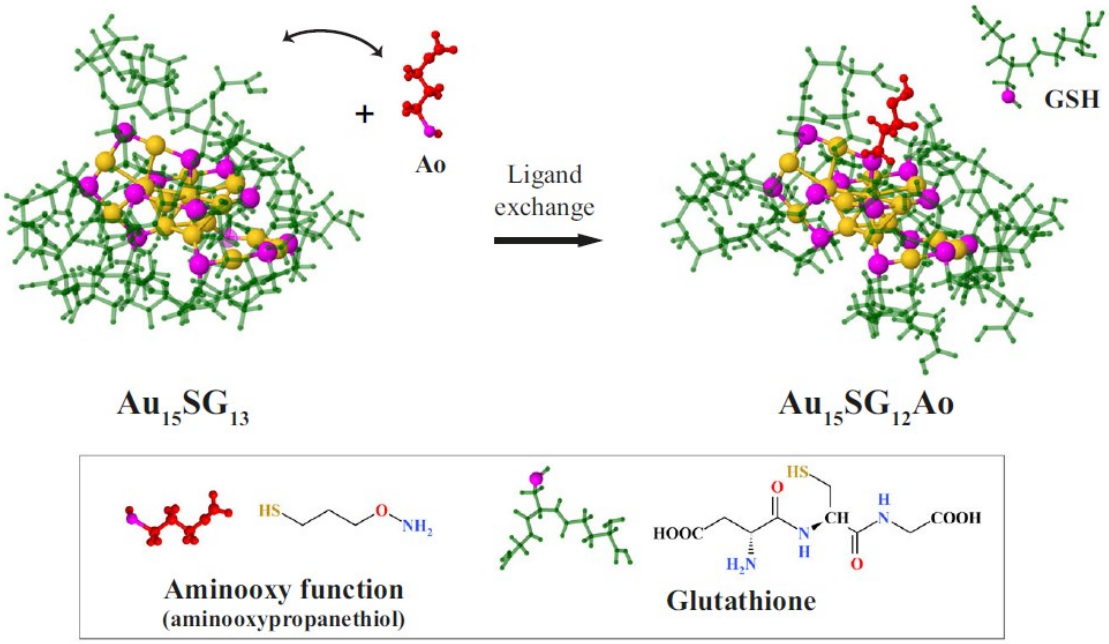

Figure 3.14 : DFT structures illustrate the ligand-exchange strategy to functionalize the NCs with an aminooxy (Ao) function ($Au_{15}SG_{12}$-Ao). We labeled sulfur atoms with magenta, Au-gold, glutathione-green, and aminooxypropanethiol with red.

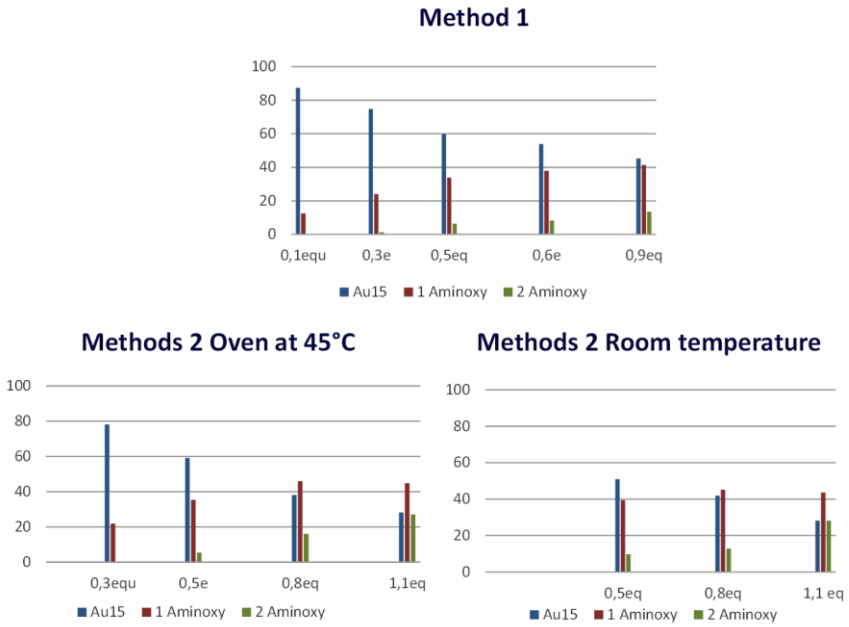

Figure 3.15 : Graphs showing the percentage of different compounds after adding AO using the different ligand exchange methods.

shows a more quantitative picture of the new strategy (with DFT calculations of structures of Au15SG13 with and without ligand exchange), where the goal is to replace one glutathione (in green in the figure) with one aminooxy function (in red). $Au_{15}SG_{13}$ NCs were post functionalized via ligand exchange reaction with (3-aminooxy)-1-propanethiol as functional ligand using two methods. We used $Au_{15}SG_{13}$ as mother solution for both methods. We tried all those method with different ratio of Ao ligand to obtain the optimized ratio that gives the best ligand exchange in term of number ligand numbers and ratio, this study is shown in graphs in **Figure 3.15** . In the first method, we added a solution of Aminooxy (0.1 to 1 equivalent relative to $Au_{15}SG_{13}$) to $Au_{15}SG_{13}$ in water (1 mg/ ml, pH ~ 8.5). We stirred the solution at room temperature for 3 hours, we tried 0.1 to 0.9 equivalent of Ao. For the second method, we used the same protocol, except that we added aminooxy fractionally (0.1 equivalent of Aminooxy every 30 min) at ambient temperature (0.5 to 0.9 equivalent) or at 45 °C (0.3 to 0.9 equivalent). It is worth to mention that we cannot separate the products with varying numbers

of Ao and once we purify and precipitate the final solution with methanol/acetic acid solution, all the NCs with different number of aminooxy replaced the GSH will be in the final powder.

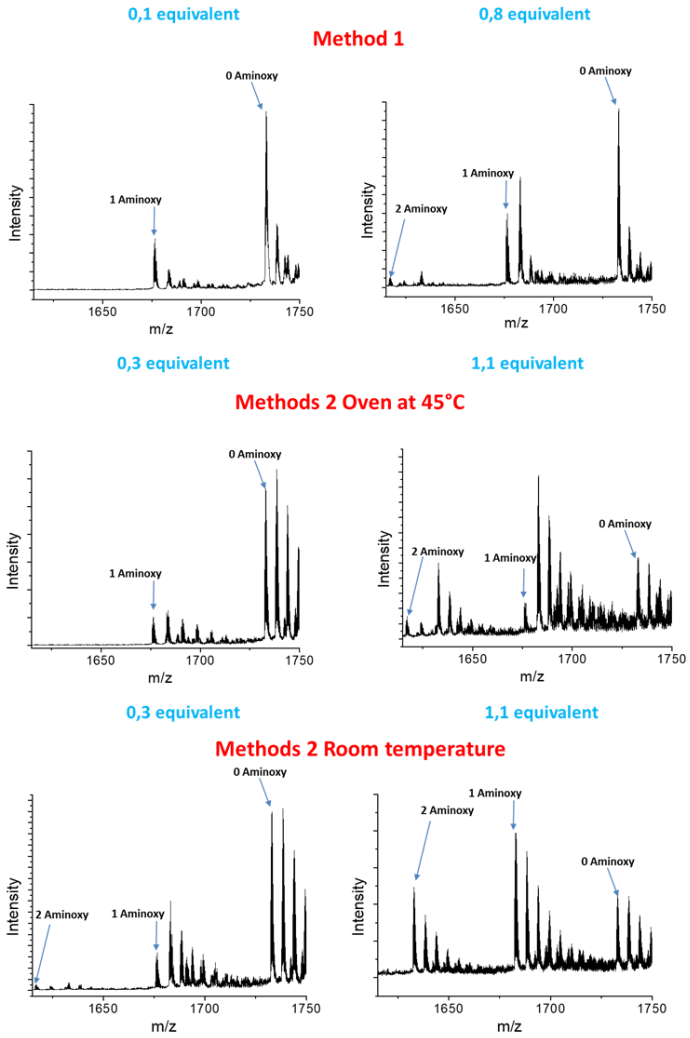

Figure 3.16 : ESI-MS spectrum of the test on ligand exchange, the pics beside the original are due to pollution by salt that we suffered at that time by the tube on the lab, the problem was fixed but those was only essay to test the ratio.

To check and characterize the formation of $Au_{15}SG_{12}$-Ao (by single ligand exchange by glutathione and aminooxypropanethiol) the reaction mix was analyzed using negative-mode ESI-MS and a new peak corresponding to $Au_{15}SG_{12}$-Ao for the charge state 4- was observed

Figure 3.17. Adding 0.1-0.3 equivalent of Ao control ligand exchange to just one. But to be more efficient for detection, and to add more quantity of functionalized NCs in the solution, we decided to use method 2 at room temperature with 0.8 eq where we got the optimal quantity of single ligand exchange (in other words, the ratio 1:0 between single and no ligand exchange is better with method 2 than method 1,see **Figure 3.17**),. The simulated ESI-MS pattern with the exact formula $\mathbf{Au_{15}(C_{10}H_{16}N_3O_6S)_{12}(C_3H_8NOS)_1}$ was in perfect agreement with their experimentally determent isotopic pattern **Figure 3.18**.

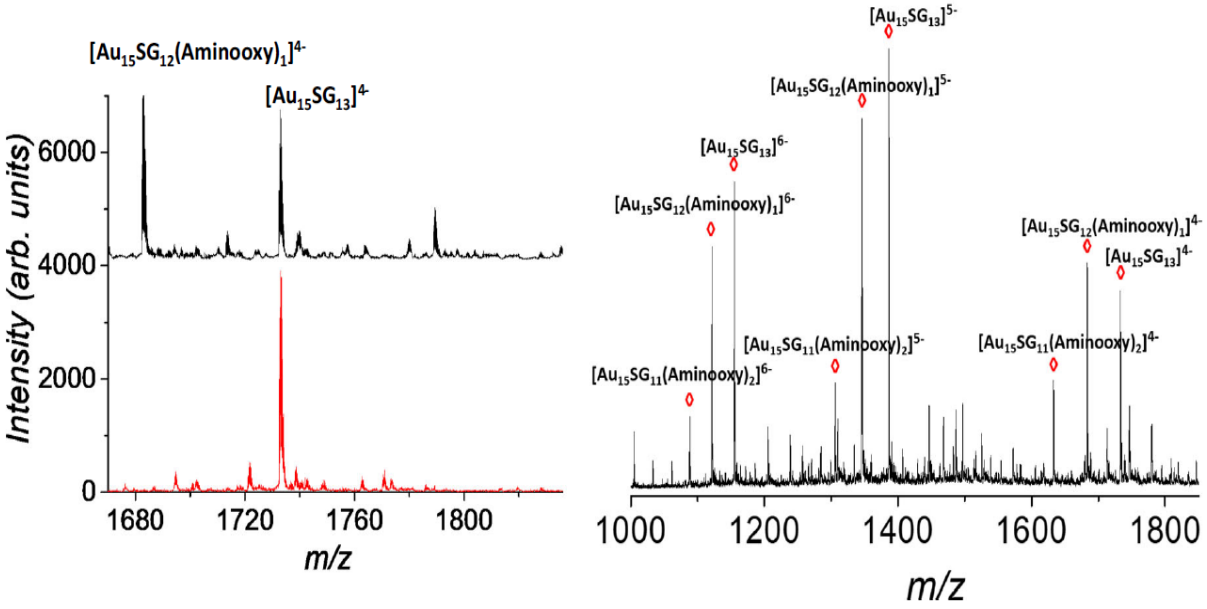

Figure 3.17 : (Left) Zoom of the ESI mass spectrum of $Au_{15}SG_{13}$ and $Au_{15}SG_{12}Ao$ NCs corresponding to the m/z region of the fourth state of deprotonation of the NCs, we visualize a new peak that correspond to $Au_{15}SG_{12}$-Ao after the ligand-exchange reaction. (Right) Mass spectra showing exchange of more than one SG ligand.

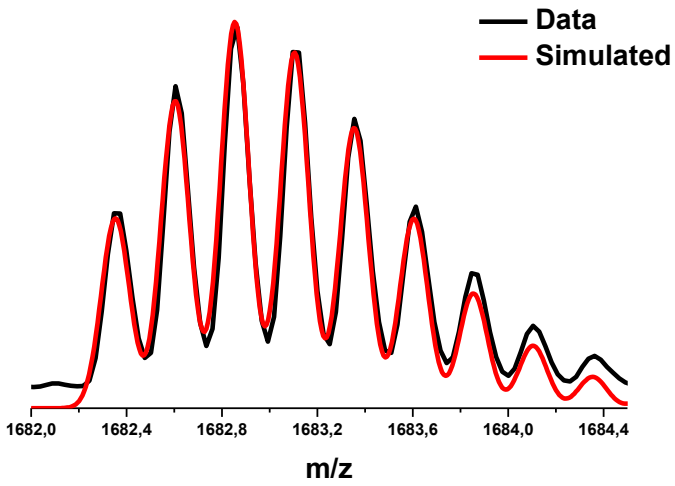

Figure 3.18 : Isotopic patterns of the 4-charge states of $Au_{15}SG_{12}$-Ao is in perfect agreement with the simulated one, using the formula $Au_{15}(C_{10}H_{16}N_3O_6S)_{12}(C_3H_8NOS)_1$.

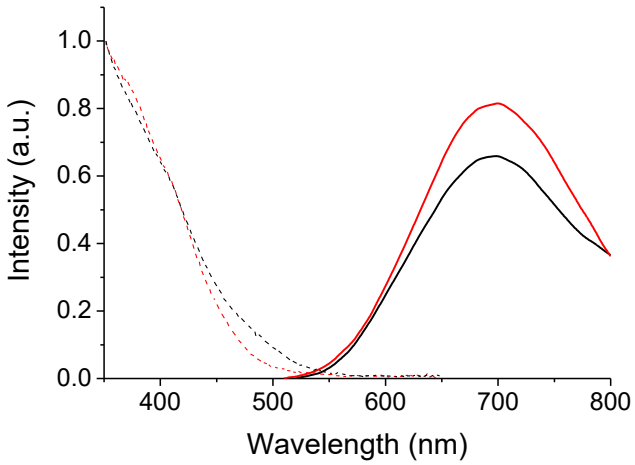

Figure 3.19 : Normalized UV-vis absorption spectra (dashed lines) and fluorescence spectra (straight lines) (with excitation at 473 nm) of $Au_{15}SG_{12}$-Ao (in black) and $Au_{15}SG_{13}$ (in red).

As mentioned, we choose $Au_{15}SG_{13}$ for our next experiments with the ratio of ligand exchange found in method 2 (at room temperature with 0.8 equivalent of Ao). We wanted to know if the optical properties changed after ligand exchange. **Figure 3.19** shows UV-vis absorption and emission spectra of $Au_{15}SG_{13}$ and $Au_{15}SG_{12}$-Ao. They display similar primary features of the spectra. The linear optical absorption spectra were composed of a monotonous increase of

absorption below 500–550 nm. Photoluminescence spectra displayed a broad band extending in the NIR region and centered around 650−700 nm.

3.4 Ability of functionalized $Au_{15}SG_{12}Ao$ to probe carbonylated species.

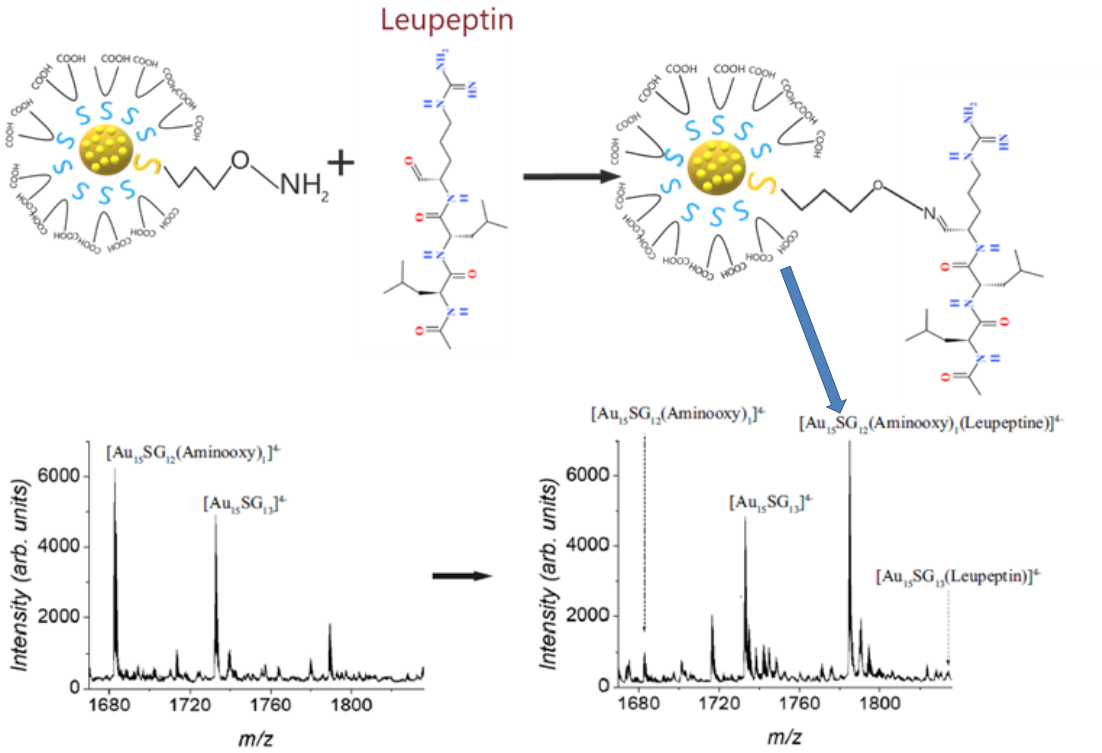

Figure 3.20 : (Top) Illustration of the reaction of the Ao group of the functionalized NC forming an oxime linkage with the aldehyde of leupeptin. (below) ESI-MS spectrum following the formation of the stable oxime linkages: we detected a new peak corresponding to $Au_{15}SG_{12}$-Ao bonded to leupeptin.

Aminooxy function ligand will form an extremely stable oxime bond with carbonyl groups. We did not start directly with carbonylated protein, we though that small model will be a good beginning. We predicted that $Au_{15}SG_{12}$-Ao will react to leupeptin (N acetyl- L-leucyl-L-leucyl-L-argininal), a natural tripeptide inhibitor of serine proteases containing a carbonyl group. In particular, since both $Au_{15}SG_{12}$-Ao and leupeptin have moderate molecular weights, the ability of $Au_{15}SG_{12}$-Ao to react with leupeptin could be checked and followed by MS analysis.

If $Au_{15}SG_{12}$-Ao can bind protein carbonyls, we would expect the formation of a stable

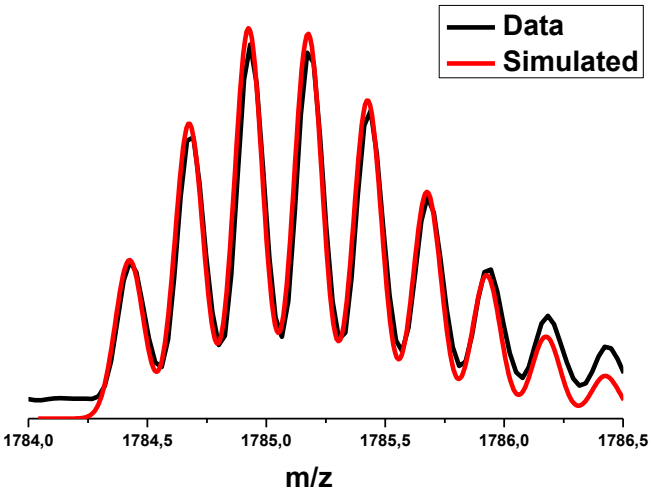

Figure 3.21: Isotopic patterns of the 4-charge states of Au15SG12-Ao-Leupeptin is in perfect agreement with the simulated one, using the formula $Au_{15}(C_{10}H_{16}N_3O_6S)_{12}(C_3H_7NS)_1(C_{20}H_{37}N_6O_4)$.

[$Au_{15}SG_{12}$-Ao–leupeptin] complex upon mixing of the $Au_{15}SG_{12}$- Ao with leupeptin **Figure 3.20**. To get insight into the formation of such complex and test specificity of $Au_{15}SG_{12}$-Ao for a carbonyl on leupeptin, we analyzed a mixture of $Au_{15}SG_{13}$ and $Au_{15}SG_{12}$-Ao by negative-mode ESI-MS before and after addition of leupeptin peptide . As expected, after the addition of leupeptin a new peak was detected under the charge state 4-, which corresponded to the newly formed [$Au_{15}SG_{12}$-Ao-leupeptin] complex, this peak was in total agreement with the simulation pattern **Figure 3.21**. Note that the precursor $Au_{15}SG_{12}$-Ao has almost disappeared demonstrating its high reaction rate with leupeptin. Importantly, the $Au_{15}SG_{13}$ peak was

unchanged, indicating that the non-functionalized NC does not react un-specifically with leupeptin under indicated conditions.

We then tried to increase the size of carbonylated species and perform similar MS analysis (as we did with leupeptin). For this purpose, we used the carbonylated lysozyme (using the MCO oxidation described below) with functionalized NCs and try to detect them with MS-TOF. The problem with MCO oxidation is that it causes pollution for detection, still we did not detect anything via ESI-MS-TOF. We then tried MALDI-TOF mass spectrometry. MALDI-TOF use another soft ionization technique using laser ablation assisted by matrix to ionize molecules. Since the carbonylation ratio was less than 1%, the MS instrument was not enough sensitive, and we failed to observe any proof of formation of NCs-Ao with oxidized lysozyme by any MS techniques. The proof of binding was finally indirectly demonstrated by proteomics analysis.

We also analyzed the mix of functionalized NC's with carbonylated lysozyme, to have an indirect proof of the grafting of $Au_{15}SG_{12}$-thiominooxy on the carbonylated site of the lysozyme, we analyzed the MCO protein derivatized with $Au_{15}SG_{12}$-thioaminooxy after degradation of the cluster. Indeed, we cannot analyze the cluster bonded to carbonylated lysozyme with LC-MS/MS after trypsin digestion and therefore the cysteine will deteriorate the cluster. The oxime bond is strong and should be stable after the degradation of NCs. The grafted carbonylated sites should be an aminooxy-C3-thiol group. As the IAM can react with the free thiols remaining on the carbonylated sites, we implemented the forty-three know modifications derivatized with aminooxy-C3-thiol-IAM for the database search. We identify seven peptides with these modifications were using Protein prospector **Figure 3.22**. We found the modifications on W^{28}, W^{123} and I^{94}, as already observed after derivatization with DNPH. These results indicate that the $Au_{15}SG_{12}$-Aminooxy cluster is grafted on the carbonylated site of the lysozyme.

m/z	z	Peptide + Oxi-AminooxyThiol(IAM) modification	Error ppm	Score	Expect	Area in FMS
399.8528	3	CELAAAMKR^{14}[+148.0307]	-8.2	30.2	7.50E-04	4.15E+05
961.7669	3	GYSLGNW^{28}[+148.0307]VCAAKFESNFNTQATNR	-2.6	41.2	7.50E-10	5.96E+05
961.7669	3	GYSLGNWVCA^{31}[+148.0307]AKFESNFNTQATNR	-2.6	40.9	1.70E-09	5.44E+06
952.7581	3	GYSLGNW^{28}[+121.0098]VCAAKFESNFNTQATNR	-8.1	46.2	2.50E-08	4.23E+05
952.0914	3	GYSLGNW^{28}[+119.0041]VCAAKFESNFNTQATNR	-8.6	45	1.20E-07	2.21E+05
651.3103	3	KI^{98}[+148.0307]VSDGNGMNAWVAWR	-8	25.9	1.30E-04	9.10E+05
388.1763	3	GTDVQAW^{123}[+119.0041]IR	-14	30.2	7.50E-04	1.37E+04

Figure 3.22 : List of oxidized peptides identified in MCO lysozyme sample labelled with $Au_{15}SG_{12}$-thioaminooxy after degradation of the cluster, using Protein Prospector.

3.5 Quantification of protein carbonylation with proteomics and biotin-aminooxy assays

The first proof of our concept is the detection of the protein carbonyls in a native 1D gel, the idea is to mix and incubate aminooxy-Au15 NCs with oxidized and non-oxidized lysozyme recombinant protein.

Lysozyme is a single chain polypeptide of 129 amino acids that our group used previously in systematic protein carbonylation studies[10]. To induce carbonylation of the lysozyme we chose the metal-catalyzed oxidation (MCO) method. This method was preferred to the other ones (Sodium hypochlorite (Bleach) and UV irradiation) because less harsh. We developed a reproducible protocol for MCO oxidation. The MCO occurs in vitro by Fenton reaction whereby ascorbic acid and iron-chloride generate highly reactive oxygen species (ROS such as hydroxyls) that react with proteins and generate carbonyl groups on susceptible amino acids[11].

It is crucial to quantify and determine the carbonylation levels and sites in lysozyme. We discovered 8 carbonylated amino acids with MCO oxidation doses described in **Figure 3.30**. **Figure 3.23** show LC-MS/MS results for the different doses used, where we can see under the table the sequence of amino acids that build lysozyme, and in purple the amino acids that has been found with the carbonylation modification. This will allow us to mark in red the carbonylated amino acids in a 3D structure of the lysozyme, this will give us an idea of the accessibility of the carbonylated sites of the protein **Figure 3.24**.

MCO doses						
0.001	0.005	0.01	0.05	0.1	0.5	1
116 K	116 K	116 K	116 K	116 K	116 K	116 K
	52 K	52 K	52 K	52 K	52 K	52 K
		32 K	32 K	32 K	32 K	32 K
		135 K	135 K	135 K	135 K	135 K
		70 T	70 T	70 T	70 T	70 T
		89 P	89 P	89 P	89 P	89 P
				137 T	137 T	137 T
					62 T	62 T

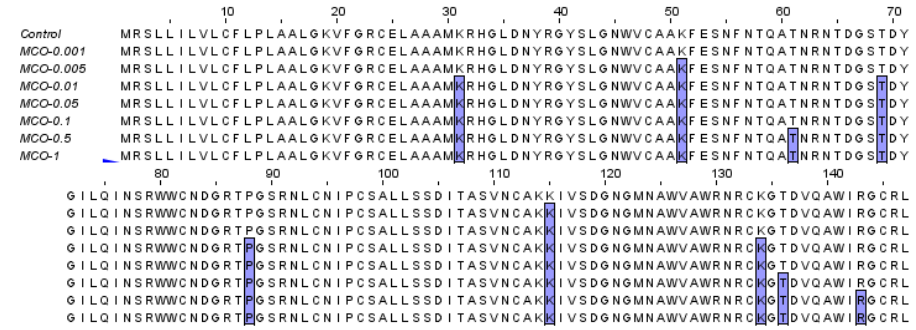

Figure 3.23 : LC-MS/MS proteomic results of different doses of MCO where 8 sites was identified in total, no carbonylation site was observed for control, as expected sites found at lower doses are found at higher doses.

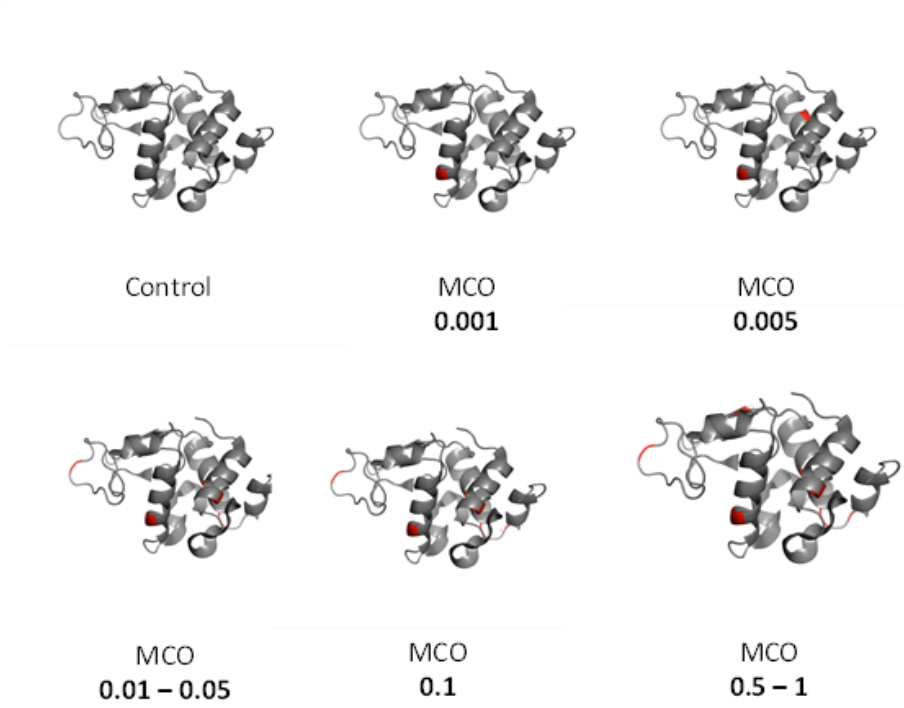

Figure 3.24 : 3D structures of oxidized protein at different doses of MCO oxidation, the carbonylation sites are mostly positioned on the surface of the protein and accessible to functionalized NCs.

To confirm the efficiency of the MCO, we measured carbonylation of the lysozyme by a Western Blot-based method **Figure 3.25 (a)** and quantify the carbonylation of lysozyme using 2,4-Dinitrophenylhydrazine (DNPH) colorimetric assay as described before **Figure 3.25 (b)** [12]. Both approaches revealed a significant increase in carbonylation in oxidized lysozyme as compared to non-oxidized control under indicated conditions.

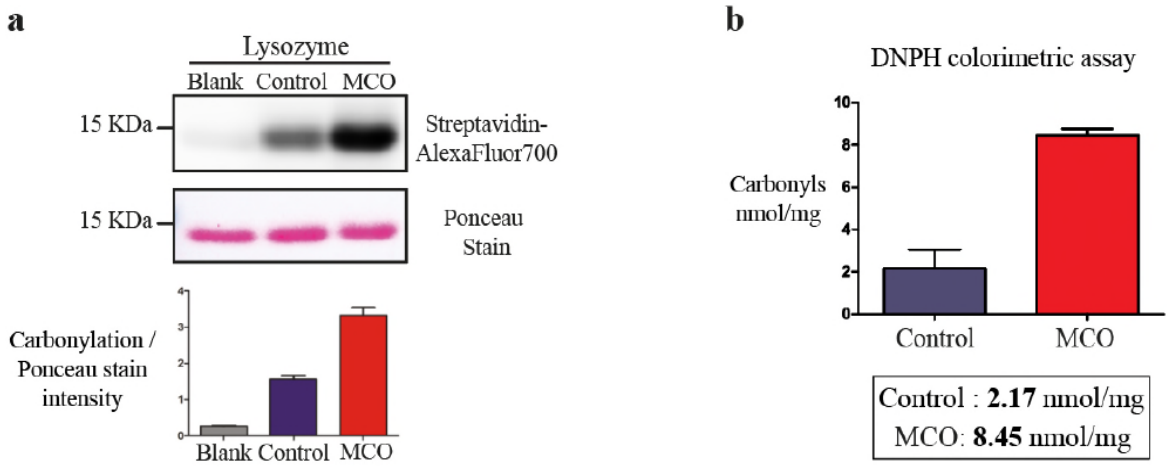

Figure 3.25 : a. Carbonyl detection of lysozyme protein by 1D-WB. We evaluated non-oxidized protein as control. We used biotin-Aminooxy to derivatize the carbonyls as described in the Experimental Chapter. Protein loading was determined by Ponceau staining b. Protein carbonyl content was determined using DNPH colorimetric assay.

We quantify and identify carbonylated amino acids of the lysozyme using a sequence of database search and tandem mass spectrometry MS/MS. The MS procedure is described in **Figure 3.26**.

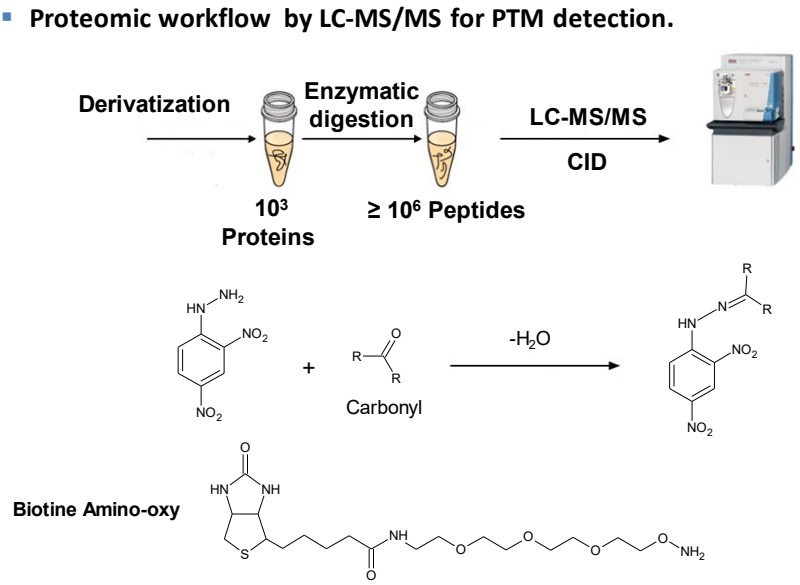

Figure 3.26 : Experimental procedure to describe experimental method to quantify carbonylated amino acids using LC-MS/MS mass spectrometry.

We used a list know carbonyl modification derivatized with DNPH from the literature to identify these modifications. We identify nineteen Oxi-DNP modified peptides with confidence in the derivatized MCO-lysozyme **Figure 3.28**. Among the identified carbonylation sites, tryptophan (W) appeared as the most frequently oxidized amino acids. We did not detect any modification of the peptides for control protein. We performed the quantification of detected oxidized peptides at the MS1 level **Figure 3.28**. To estimate the amount of oxidized versus the non-oxidized protein peak areas for each oxidized peptide we normalize to the areas of the corresponding non-oxidized peptides in the control samples **Figure 3.28**. Approximately 1.3 % of the total protein amount is oxidized, with W108, K13, andW62 as the most intense carbonylated sites. The 3D structure of oxidized lysozyme with identified carbonylation sites is given in **Figure 3.27**.

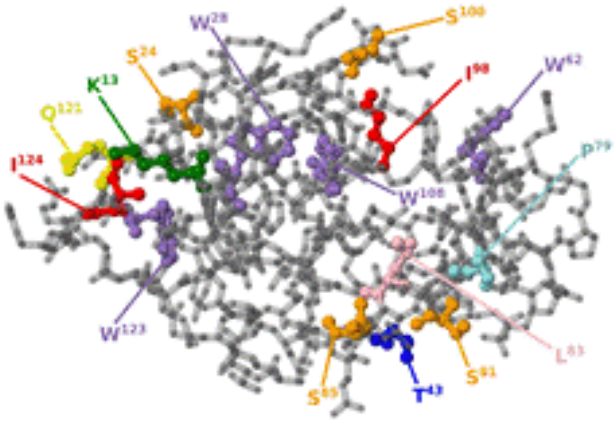

Figure 3.27 : 3D structure of oxidized lysozyme with the carbonylated site identified using protein prospector.

a)

m/z	z	Peptide + Oxi-DNP modification	Error ppm	Score	Expect	Area in FMS
614.7578	2	CELAAAMK[13][+178.0127]R	-9.4	28.9	1.10E-04	1.47E+06
752.3223	2	GYS[24][+178.0127]LGNWVCAAK	-4.1	17	1.70E-03	2.89E+05
768.3348	2	GYSLGNW[28][+210.0025]VCAAK	19	17.1	2.30E-03	2.80E+06
769.3386	2	GYSLGNW[28][+212.0182]VCAAK	14	31.2	2.20E-04	3.69E+05
803.8241	2	FESNFNTQAT[43][+178.0127]NR	-14	22.7	1.90E-06	3.34E+05
602.2157	2	W[62][+210.0025]WCNDGR	18	19.7	7.10E-05	1.32E+07
886.7518	3	NLCNIP[79][+150.0178]CSALLSSDITASVNCAK	13	24.2	1.50E-03	6.71E+05
901.4000	3	NLCNIPCS[81][+194.0076]ALLSSDITASVNCAK	-4.2	28.4	4.10E-05	3.62E+05
901.4000	3	NLCNIPCSAL[83][+194.0076]LSSDITASVNCAK	-4.2	31.1	1.10E-06	3.62E+05
896.0682	3	NLCNIPCSALLS[85][+178.0127]SDITASVNCAK	-4.3	26	8.50E-07	2.87E+05
943.4082	2	I[98][+194.0076]VSDGNGM[+16]NAWVAWR	3	16.1	1.60E-04	1.63E+05
943.4082	2	IVS[100][+194.0076]DGNGM[+16]NAWVAWR	3	17.9	1.30E-04	2.85E+05
943.3994	2	IVSDGNGM[+16]NAW[108][+194.0076]VAWR	-6.4	23.3	3.30E-04	3.21E+06
943.3994	2	IVSDGNGMNAW[108][+210.0025]VAWR	-6.4	23.3	2.20E-04	3.21E+06
951.3895	2	IVSDGNGM[+16]NAW[108][+210.0025]VAWR	-14	21.6	3.10E-04	5.89E+05
620.2711	2	GTDVQ[121][+194.0076]AWIR	-12	18	6.00E-04	3.43E+05
628.2641	2	GTDVQAW[123][+210.0025]IR	-19	17.7	5.60E-05	2.08E+06
620.2728	2	GTDVQAW[123][+194.0076]IR	-9.5	24.2	6.00E-04	2.11E+05
620.2728	2	GTDVQAWI[124][+194.0076]R	-9.5	27.4	4.40E-05	1.42E+05

b)

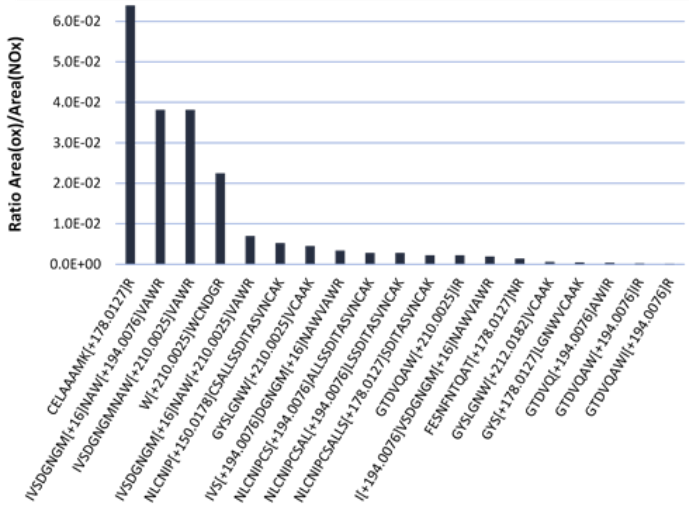

Figure 3.28 : a) List of oxidized peptides identified in MCO Lysozyme sample using Protein Prospector. b) Ratio of oxidation of each peptide for Lysozyme. Peak area of the modified peptide in MCO sample, Area (Ox), divided by peak area of the corresponding non-modified peptide in the control sample, Area(NOx).

3.6 The quest for the best 1D gel migration conditions

While protocols for protein and oxidized protein migration in 1D gel were quite robust, a huge amount of time was devoted to find optimal conditions to have protein, oxidized protein and protein bound with nanoclusters migration in 1D gels.

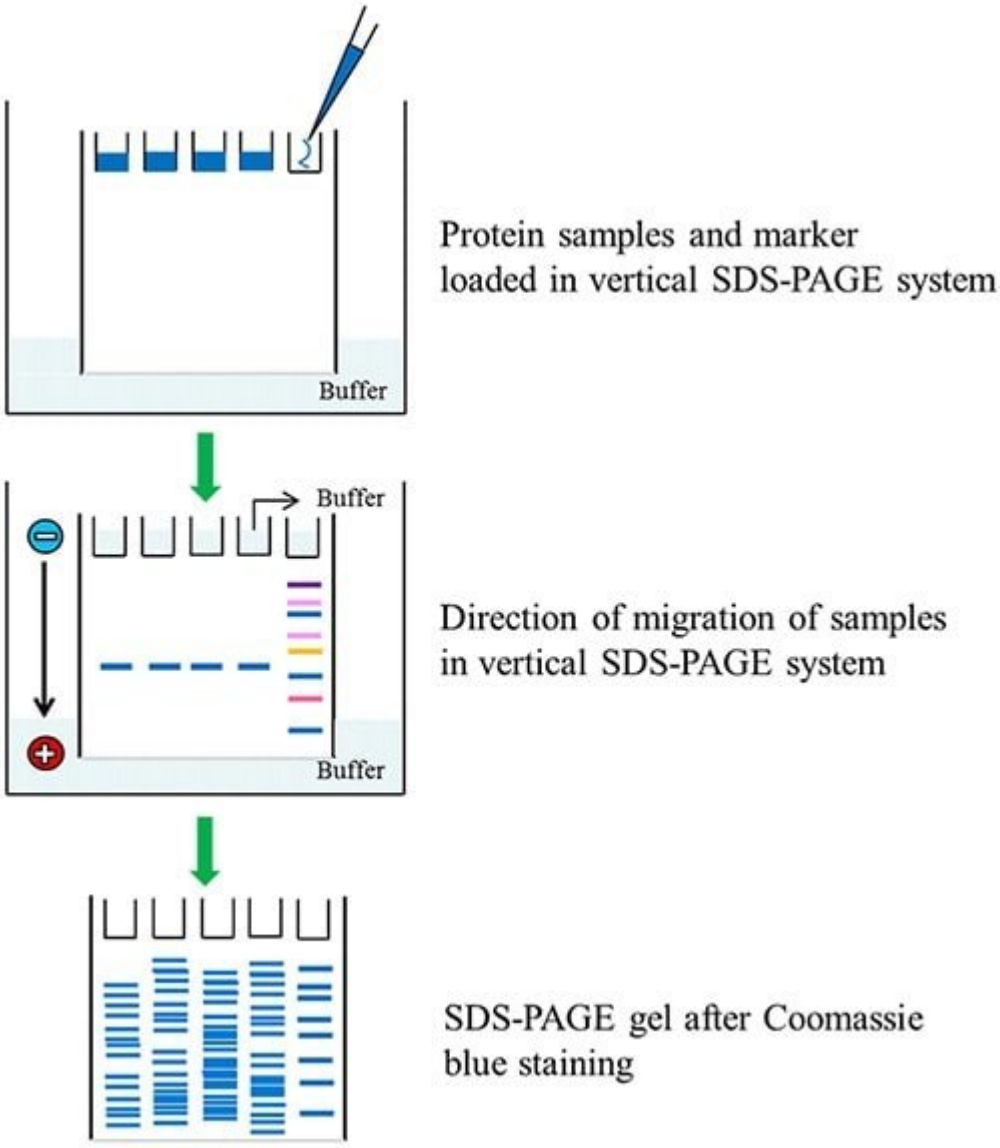

Figure 3.29 : SDS-PAGE of protein samples and color burst protein marker.

Polyacrylamide gels are formed by the reaction of acrylamide and bis-acrylamide (N,N'-methylenebisacrylamide) that results in highly cross-linked gel matrix. The gel acts as a sieve

through which the proteins move in response to the electric field. Proteins contain an overall positive or negative charge; this enables the movement of a protein molecule towards the isoelectric point at which the molecule has no net charge. By denaturing the proteins and giving them a uniform negative charge, it is possible to separate them based on the size as they migrate towards the positive electrode.

We started by evaluating the migration of the protein and NC in the same condition and define the oxidation protocol of the Lysozyme **Figure 3.30**. We did not observe any specific signal which could correspond to the protein bound to the NC **Figure 3.31**. The separation with this type of gel is not strong enough. Due to high charge of NCs, they will migrate faster in the gels, so we increased the resolution of the gel by either increasing the percentage of acrylamide or the crosslinker percentage (or both). We prepared 25% polyacrylamide gel with 29:1 Acrylamide/Bisacrylamide ratio (3.4% Crosslinker). Even after we increased the percentage of acrylamide, we did not notice any enhancement. This was due to that NC and the lysozyme

Sample	*Lysozyme in Oxidation buffer*	*H_2O*	*Volume of Asc/$FeCl_3$*	*Ascorbic acid [400mM]*	*$FeCl_3$ [1.6mM]*
1	***750 µl***	***0 µl***	***50 µl***	*25 mM*	*100 µM*
0.5	***750 µl***	***25 µl***	***25 µl***	*12.5 mM*	*50 µM*
0.1	***750 µl***	***45 µl***	***5 µl***	*2.5 mM*	*10 µM*
0.05	***750 µl***	***47.5 µl***	***2.5 µl***	*1.25 mM*	*5 µM*
0.01	***750 µl***	***49.5 µl***	***0.5 µl***	*0.25 mM*	*1 µM*
Make 1:10 solution (1µl Asc/FeCl3 + 9 µl H_2O)					
0.005	***750 µl***	***47.5 µl***	***2.5 µl***	*0.125 mM*	*0.5 µM*
0.001	***750 µl***	***49.5 µl***	***0.5 µl***	*0.025 mM*	*0.1 µM*

Figure 3.30 : Oxidation protocol by metal catalyze oxidation MCO with different doses of oxidation 0.0001 lowest to 1 highest.

displayed opposing migration properties: while NC was detectable in the gel exposed to the conventional polarity, the lysozyme was detectable in the inverted polarity.

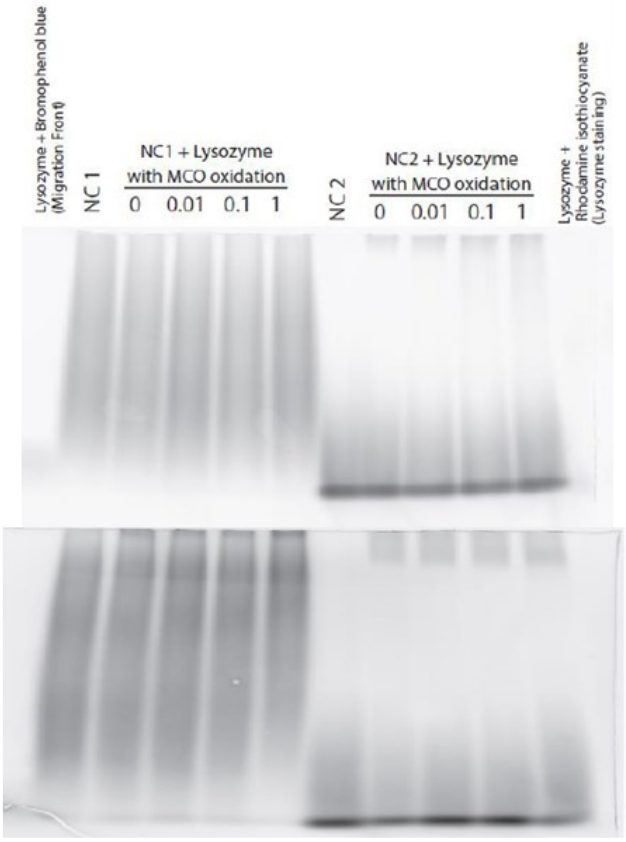

Figure 3.31 : Two different gel ratio of (Top) 20% acrylamide (37.5:1 Acry:BicAcry ratio) and (Below) 25% acrylamide (29:1 Acry:BicAcry ratio) with lysozyme and NCs+ Lysozyme at different dose of oxidation see Figure 3.30.

The story of protein migration in gels does not end at polarity selection, another problem appears during the gel's essays, is the non-specific binding of non-functionalized NCs with carbonylated lysozyme. This problem will delete the proof of the ability of targeting the carbonylation, but we need to change the condition of gels, migration voltage and composition. We saw that that after testing the gels in MEDILS institute in Split, we were trying to reproduce the same gels in the lab in Lyon, but we added non-functionalized NCs with oxidized lysozyme,

and we detected this problem, we also noticed that the non-oxidized lysozyme doesn't migrate in the gel, the isoelectric point of lysozyme is 11.83, the buffer used in our lab in Lyon have a PH of 8.3, but once the functionalized NC will bind to it, it will cause a total negative charge, but non-oxidized lysozyme is positively charged at this condition, so it will not enter in the gel.

We moved next to modify the gel condition to immigrate all components. We start by using acetate buffer where the PH is 4, in this case lysozyme (both state) will enter the gel easily see **Figure 3.32**. We change the migration direction of the gels from positive to negative (suitable for the lysozyme both oxidized and non-oxidized) and from negative to positive (suitable for

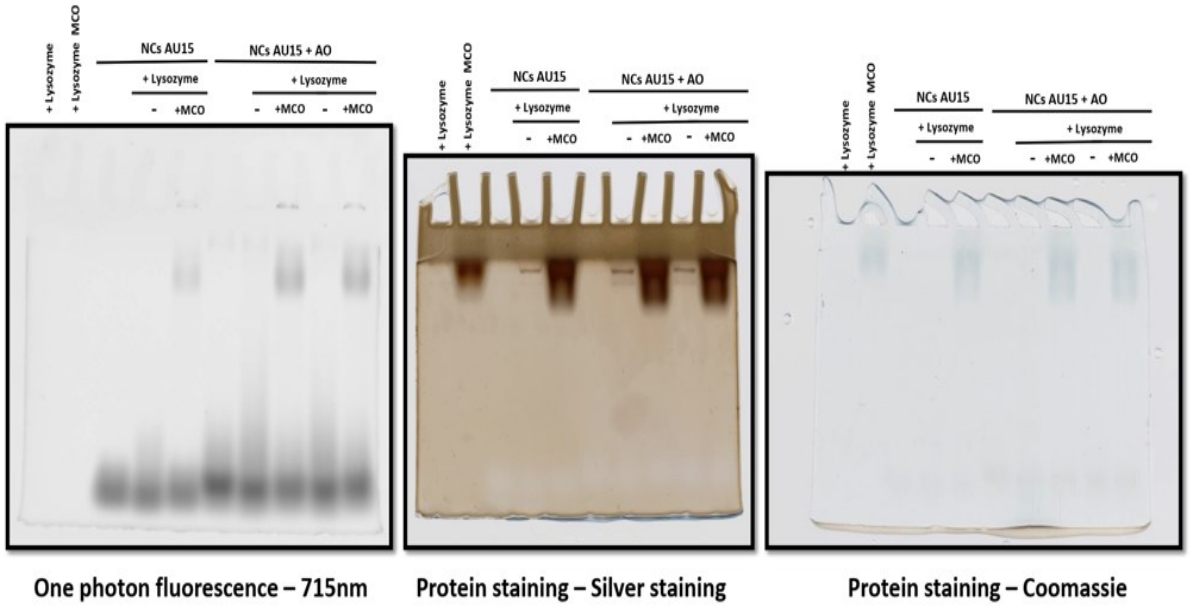

Figure 3.32: New gel composition with acetate buffer, where we can see that both state of lysozyme is migrated in the gel (Positive to negative migration direction) and NCs as well (Negative to positive migration direction).

NCs, and NCs bind with lysozyme), non-specific binding is still appearing, with the percentage of 95% in signal compared to specific binding, quite high.

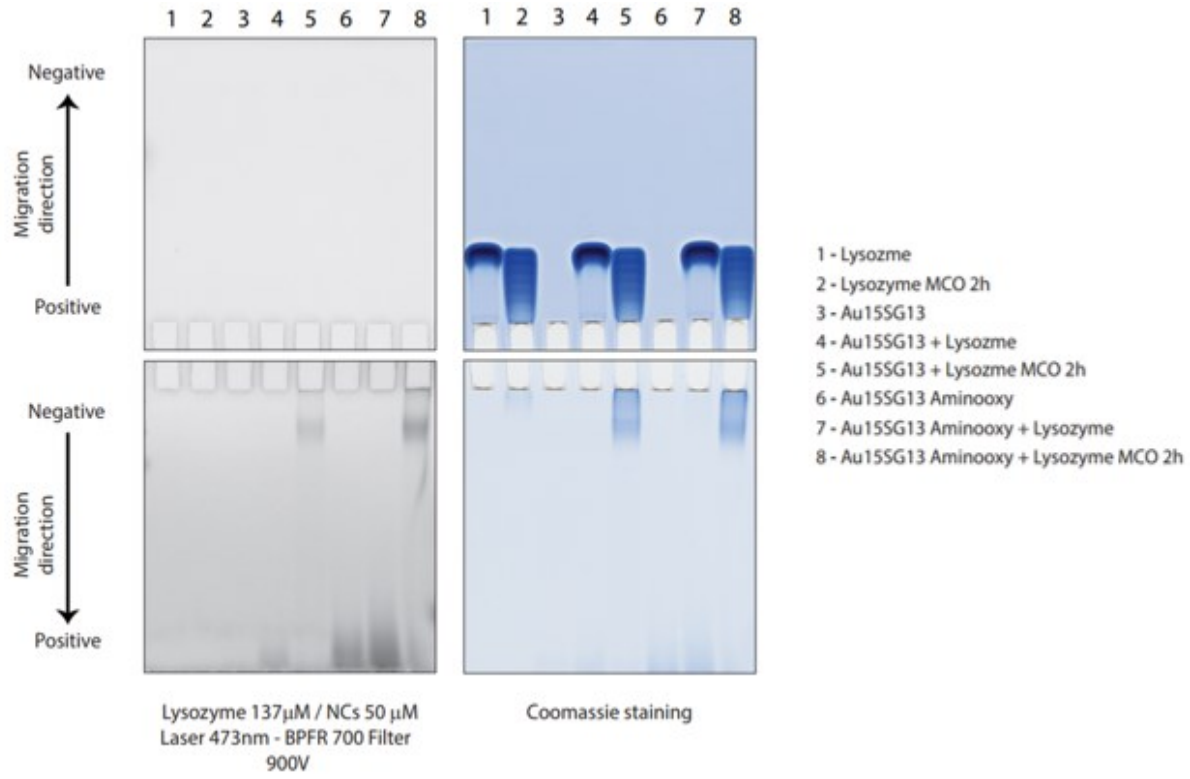

Figure 3.33: New gel composition with acetate buffer, where we can see that both state of lysozyme is migrated in the gel (Positive to negative migration direction) and NCs as well (Negative to positive migration direction).

The non-specific binding still, but bot non-oxidized and oxidized lysozyme is entering the gel with the new buffer, and NCs are migrating with opposite polarity direction. We tried to alkylate the cysteine in oxidized lysozyme by adding iodoacetamide and acrylamide but did not solve the problem **Figure 3.34**.

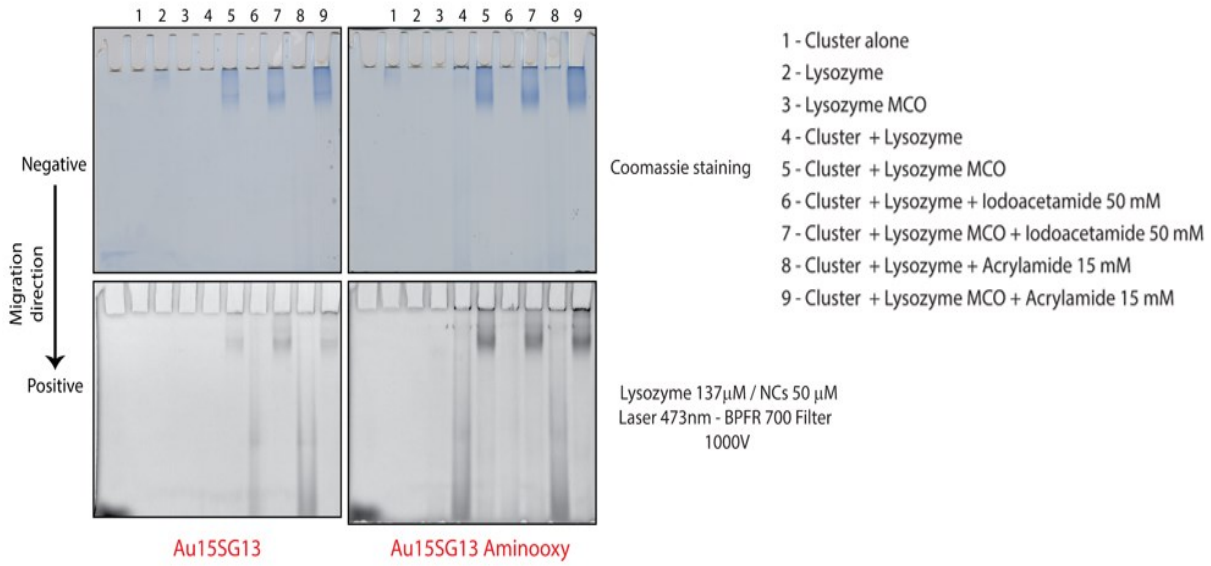

Figure 3.34 : Adding iodoacetamide and acrylamide to the samples to check if alkylating the cysteine will decrease non-specific binding with non-functionalized NC.

Cysteine in oxidized lysozyme is not the cause of non-specific binding, hence it should be electrostatic interaction. Since the charge of the lysozyme is positive and NC are negatively charged, it could be the cause, but clearly it will only be possible for oxidized lysozyme, since we did not see any interaction with NC, both states, with non-oxidized lysozyme. Next step is to decrease protein concentration in the gels, from 137uM to around 68uM, since it a low concentration, we added also pPDA (p-Phenylenediamine) to the reaction and incubated (protein + NC+ pPDA) overnight at 10°C , we also added stacking (to improve protein separation and gel resolution) and resolving (separate protein based on their molecular weight) to the gel condition and decreased the voltage in the migration (50V to 80V instead of 120V in previous gels) for a longer time of migration, all this condition could decrease the non-specific interaction.

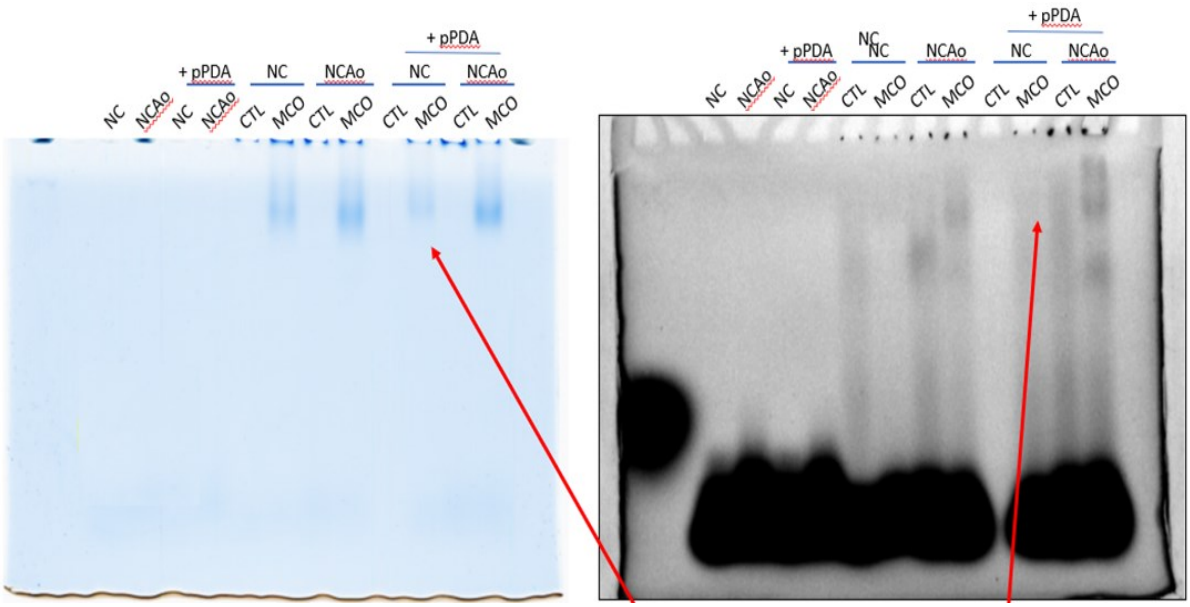

Figure 3.35 : Adding pPDA catalyze to the mix of lysozyme and nanoclusters, with 5% stacking, 15% resolving, 60V for 30 minute and then 80V for 1 hour and half and incubation overnight at 10°C.

Adding pPDA decreased the signal of non-specific binding, it decreases the electrostatic interaction, the question is whether the concentration of lysozyme is high, and it is causing electrostatic binding. We moved next to longer incubation, 22h instead of overnight, decreasing the voltage to 50 V decreased non-specific binding, but we can see that even lower concentration of lysozyme 68uM that a weak signal of the problem. We moved next to the same gels, incubation, and reagent condition but we decreased further lysozyme concentration. And as we can see in **Figure 3.36** that the last conditions is the right one for our next experiment and essays, to proof the targeting of the carbonylation of lysozyme, without any signal of non-specific binding.

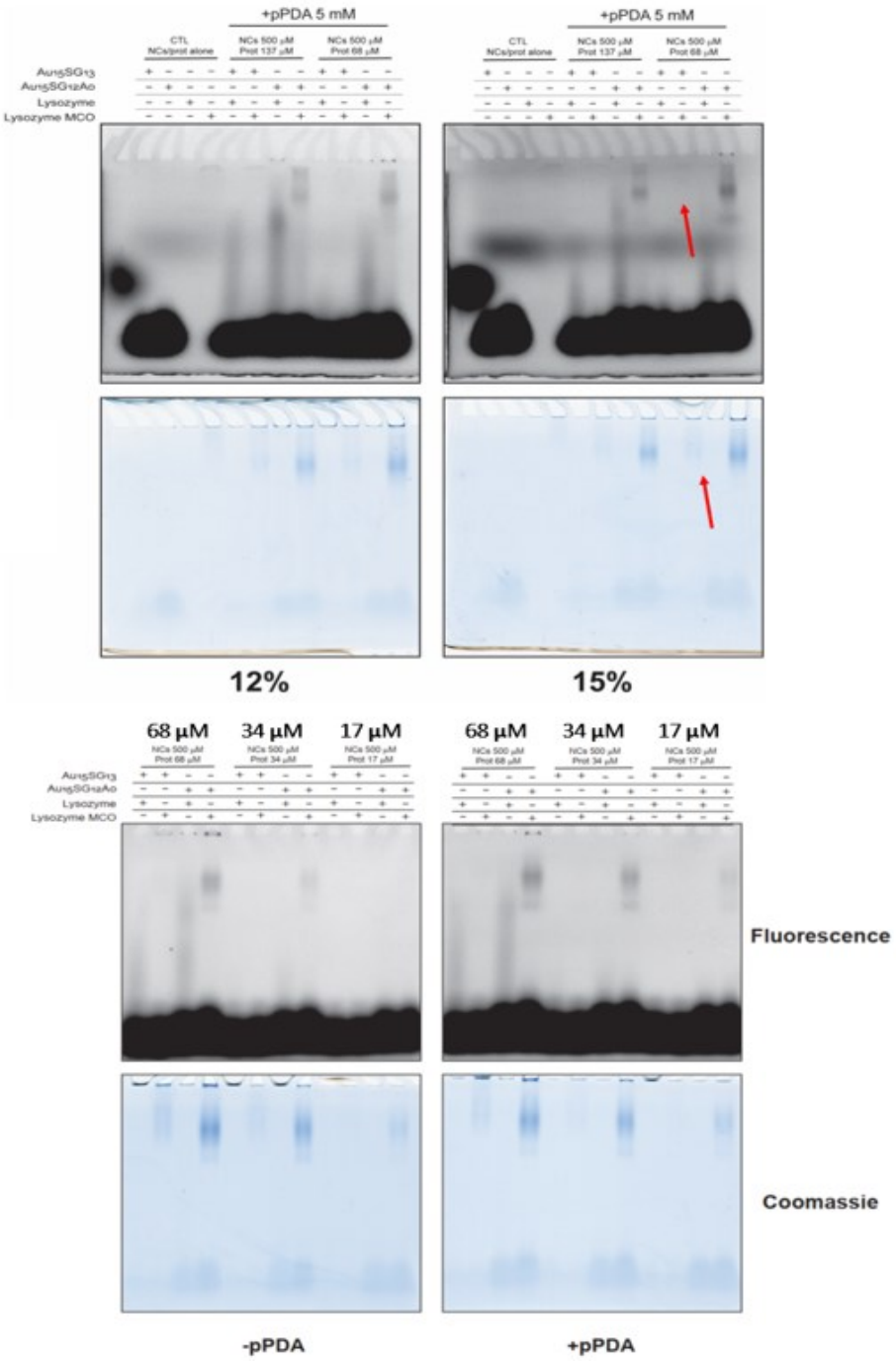

Figure 3.36 : (Top) Longer incubation time with lower voltage, different resolving (12% on the left and 15% on the right), (below) 15% resolving, different lysozyme concentration. Adding pPDA decreases the non-specific binding, but not for high concentration, the major factor is to decrease the concentration of the lysozyme.

3.7 Detection of the carbonylation in 2D gels

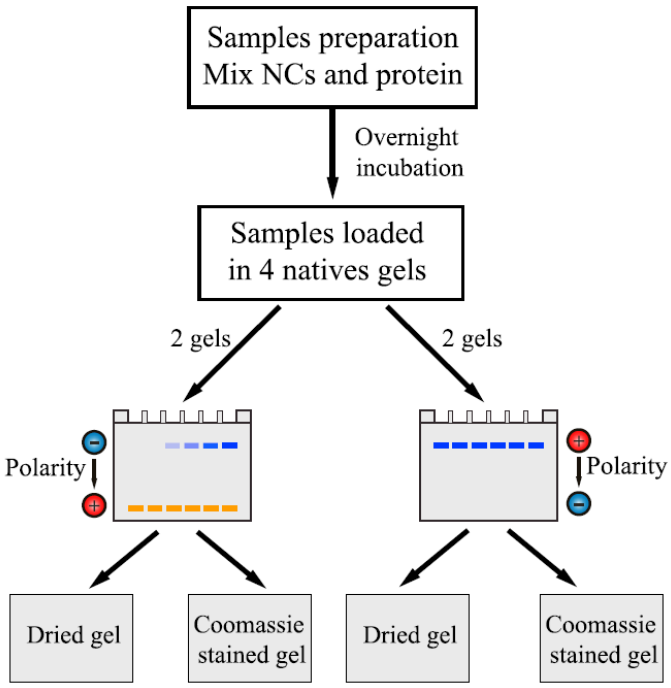

Figure 3.37 : Schematic representation of the experimental setup for NCs migration in gels.

Detecting protein-NC complexes seemed impossible to visualize with mass spectrometry, so we moved next to evaluate whether labeling of carbonylated proteins with $Au_{15}SG_{12}$-Ao is applicable for the detection of the protein–NC complexes in polyacrylamide gels. As the NCs are sensitive to detergents and can react with free thiols commonly present in the buffers used in sodium-dodecyl sulfate polyacrylamide gel electrophoresis (SDS-PAGE), native PAGE was applied in these experiments both with the conventional (migration direction from anode to cathode) and with the inverted polarity **Figure 3.37** (migration direction from cathode to anode), we can see clearly in **Figure 3.38** that NC and the lysozyme displayed opposing migration properties: while NC was detectable in the gel exposed to the conventional polarity,

the lysozyme (both oxidized and non-oxidized) that has isoelectric point of 11.35 under given conditions migrated into the gel only upon inversion of the polarity.

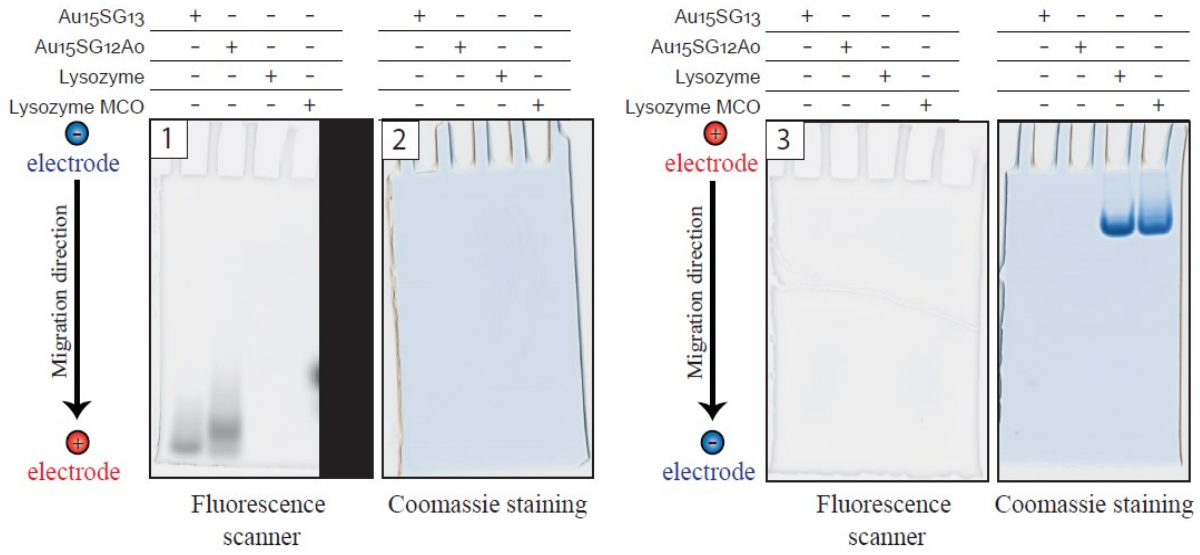

Figure 3.38 : Demonstration of the NCs and protein migration in this experimental setup. Scans of the four native gels. We dried gels 1 and 3 and stained gels 2 and 4 with Coomassie staining. Migration patterns of NCs with and lysozyme in the gel is clear in this essay.

So now after we optimized everything, from gel composition to NCs functionalization, we moved to visualize the mixture of $Au_{15}SG_{12}$-Ao with the oxidized lysozyme along with corresponding controls to native PAGE **Figure 3.39**, expecting to detect the stable complex formed between the protein and the NC in one of the two gels. In fact, we observed co-migration of the $Au_{15}SG_{12}$-Ao and the oxidized protein, which is coherent with our result that the NCs are grafted on the carbonyl sites of the protein (**Figure 3.39**, gels 1 and 2, lane 8). The complex was globally negatively charged since it migrated from anode to cathode (**Figure 3.39**, gels 1 and 2) and no fluorescence was observed in the gel upon migration from cathode to anode (**Figure 3.39**, gels 3 and 4). Furthermore, there was no detectable complex of $Au_{15}SG_{12}$-Ao with the non-oxidized protein (**Figure 3.39**, gels 1 and 2, lane 7), indicating that there were no unspecific, carbonyl unrelated interactions between the protein and the NC.

Importantly, little to no fluorescence was observed upon native PAGE of the $Au_{15}SG_{13}$ oxidized lysozyme mixture (**Figure 3.39**, lane 5), further supporting the absence of unspecific interactions between the NC and the protein .

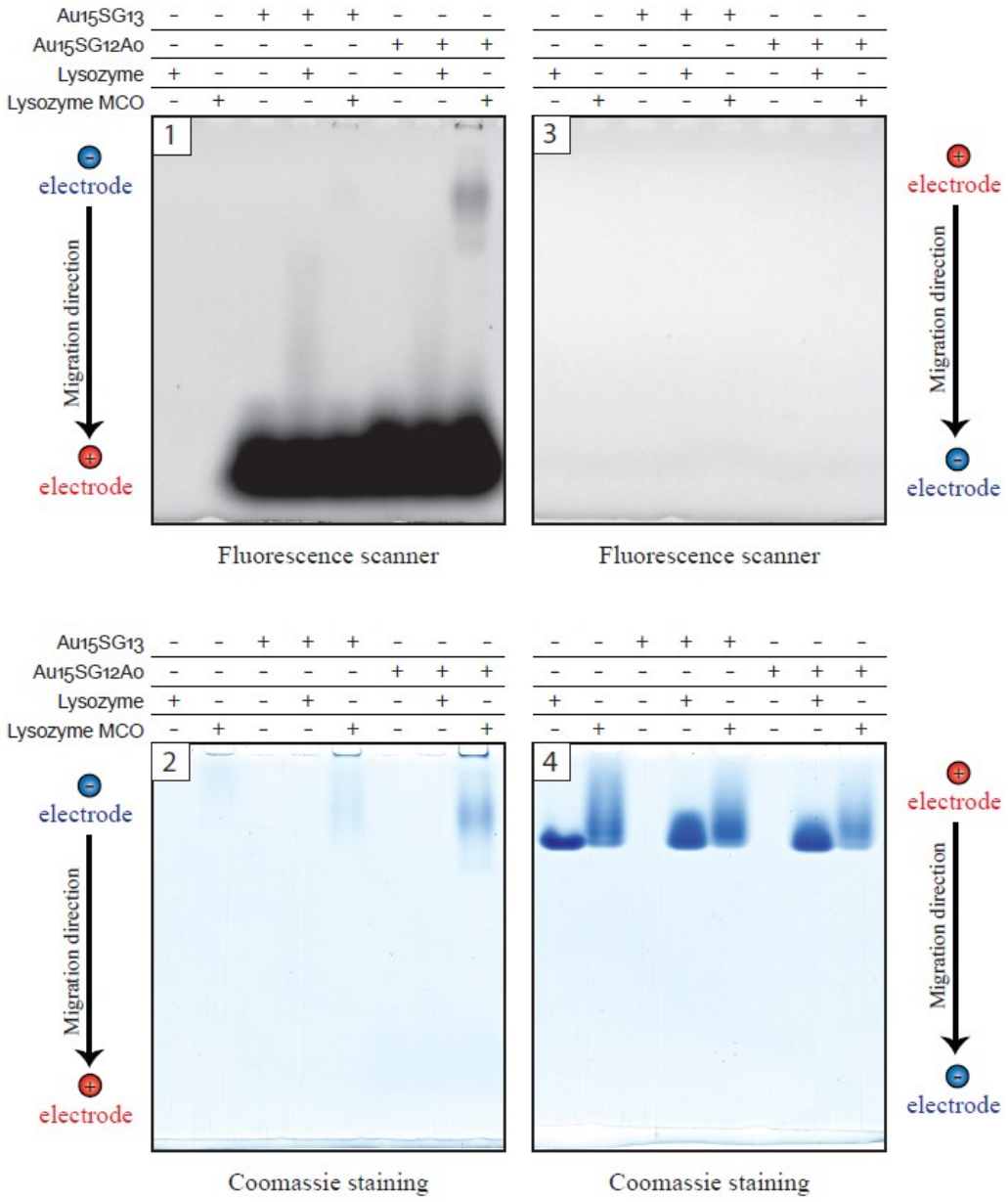

Figure 3.39 : Four identical sets of samples were simultaneously migrated on native polyacrylamide gels with electricity direction from anode to cathode (gels 1 and 2) or from cathode to anode (gels 3 and 4). We dried gels 1 and 3 and stain gels 2 and 4 with Coomassie and scan them under gel scanner.

We next evaluated the potential of the NC for quantitative analysis of protein carbonyls. Fixed concentration of 500 µM Au15SG12-Ao was incubated with a decreasing range of concentrations of the lysozyme (50–1 µM corresponding to 5–0.1 µg protein loaded in the gel) and the reaction products were migrated on native PAGE **Figure 3.40**. An obvious decrease in the fluorescent signal corresponding to NC correlated with decreasing amounts of oxidized

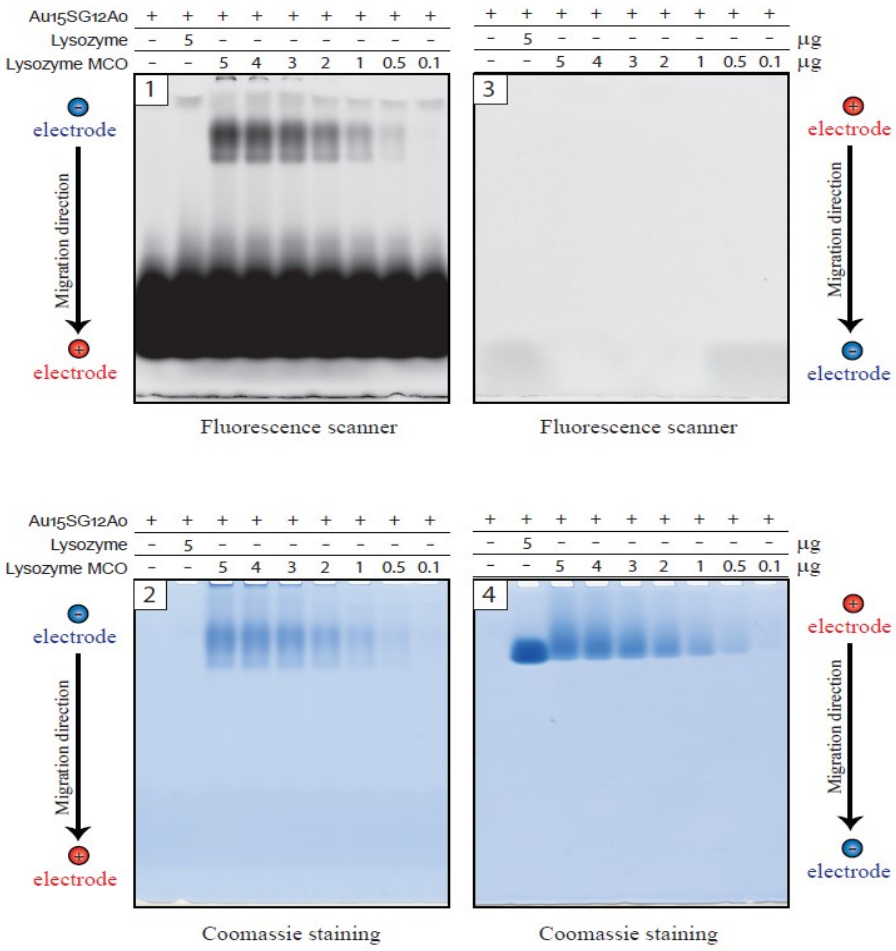

Figure 3.40 : The in-gel signal of $Au_{15}SG_{12}$-Ao decreases with the lowering of the oxidized lysozyme amounts. Gels 1 and 3 were dried and imaged using a fluorescence scanner. Gels 2 and 4 were stained using Coomassie staining, and images were obtained using a gel scanner. The displayed images are representative of three replicates.

lysozyme, indicating that NC-based assays can be for quantifying the carbonylation of the protein.

Finally, we evaluated the applicability of NCs in protein carbonylation detection in polyacrylamide gels using biphotonic confocal microscopy and observed an intense two-photon excited fluorescent signal for higher protein quantities. We tried also to see if we can detect signal in the infrared region, to see the possibility of application in the bio-imaging domain **Figure 3.41**.

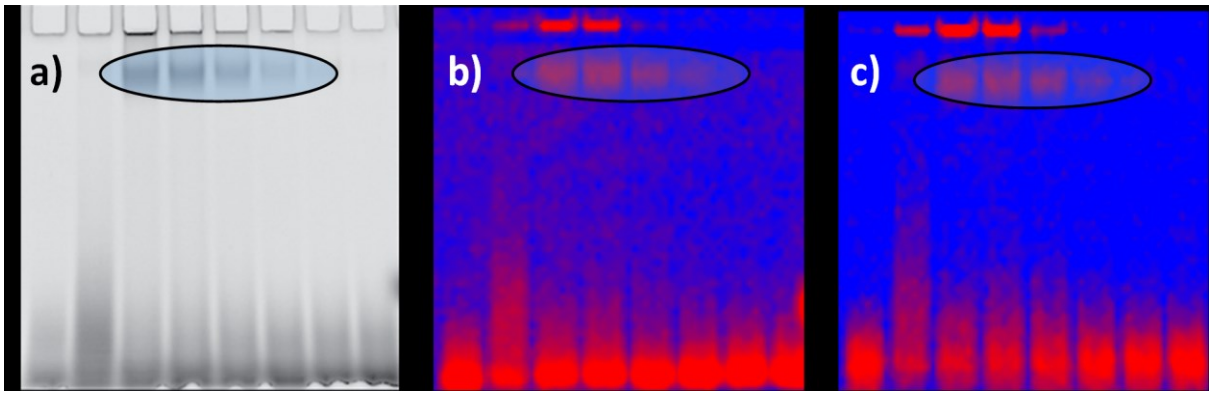

Figure 3.41 : $Au_{15}SG_{12}$-Ao targeted carbonylated proteins detected on gels by fluorescence scanner (a) and multiphoton confocal imaging (b and c). Laser excitation was at 780 nm and emitted photons were detected with b) visible range (350-700 nm) and c) IR range (>850 nm). Fixed concentration of 500 µM $Au_{15}SG_{12}$-Ao was incubated with a decreasing range of concentrations of the lysozyme (50-1 µM corresponding to 5-0.1 µg protein loaded in the gel).

We tested $Au_{15}SG_{12}$-Ao with other type of proteins to test the efficiency of targeting **Figure 3.42** .Together, these data establish a novel NC, $Au_{15}SG_{12}$-Ao, as suitable for specific detection of protein carbonyls by PAGE while offering photostability and biocompatible optical properties. The approaches do not end here, we should assess the NCs inside the cells, another story and new challenges is on the way.

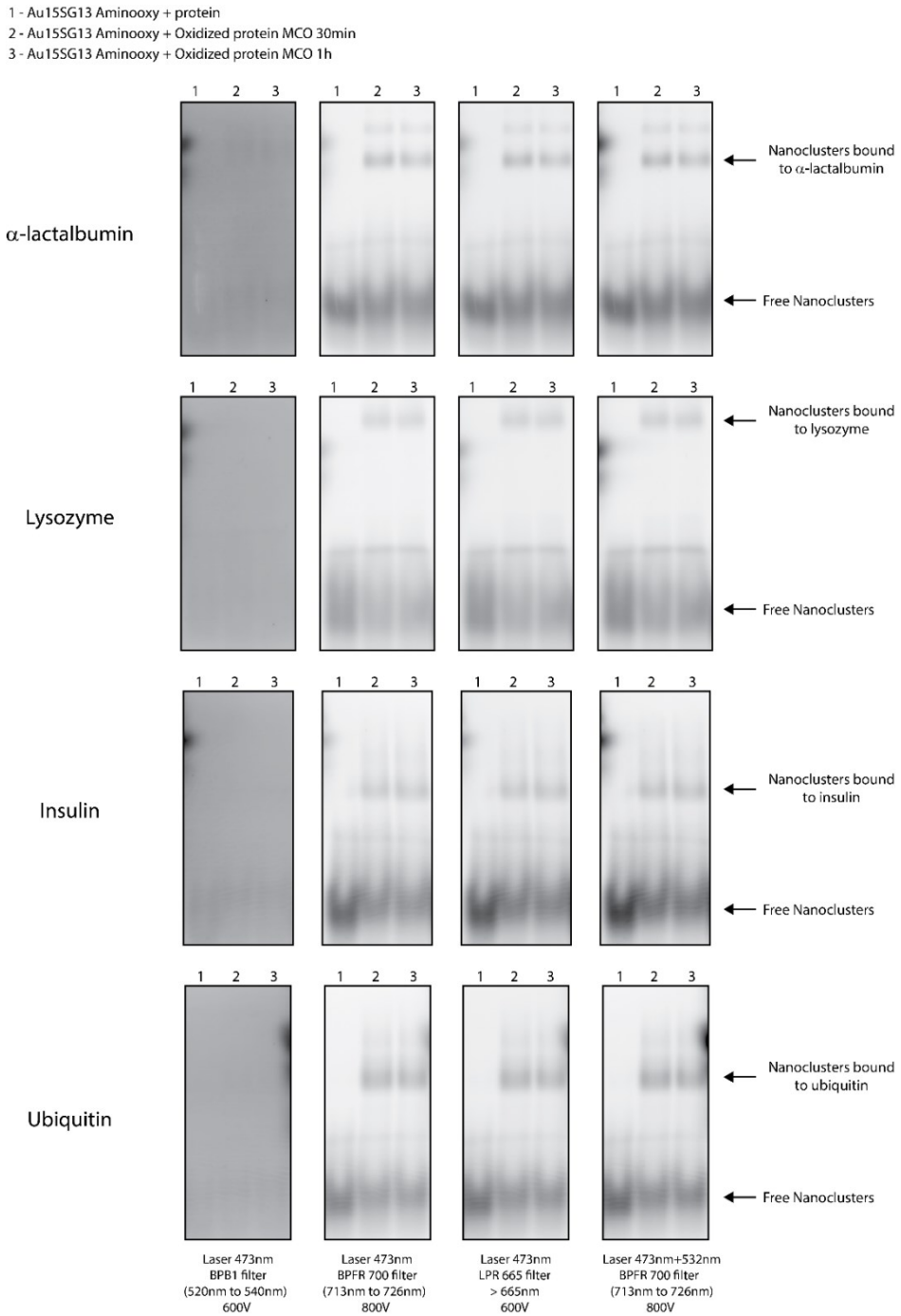

Figure 3.42 : Other test on other type of proteins with the same NCs and oxidation process.

Conclusion

Our team have been investigating structure and optical properties of gold NCs in the last 10 years. Since gold NCs present remarkable optical properties, detecting carbonylation of the proteins by optical methods using nanoclusters as optical targets seems to be a good option to go towards bio-applications. We synthesized a palette of NCs at the atomic precision. To be applicable in bio-imaging domain, we tried to manipulate linear optical properties by silver doping strategies on various gold NCs. However, the added value of metal doping on optical properties of gold nanoclusters was not at the level of our expectations. Thus, we move towards the most stable gold nanoclusters that was easy to synthesize (e.g., Au15SG13).

To target carbonylation, carboxylic acid groups exposed at the surface of glutathione surface protecting ligands was not able to bind to aldehyde groups (specific to carbonylation). Ligand exchange is an effective way to modify the NC surface, and Au15SG13 showed a facile surface modification with aminooxy ligand, and we proceed the experiments with it. We successfully achieve the first proof of targeting the carbonylation with functionalized gold NCs under ESI Q-TOF mass spectrometry after mixing the functionalized NC with aminooxy with Leupeptin, a natural carbonylated peptide (with marginal (carbonylated arginine) residue as carbonylation site).

After efficiently functionalizing Au15 NCs suitable for carbonylation targeting, we chose lysozyme as the model system due to the large amount of data available regarding carbonylation of this protein. To mimic biological approaches in this manner, we used and developed electrophoresis to demonstrate our technique. We faced to major challenges concerning migration of protein and NCs. After gel protocols optimization, in terms of immigration voltage and time, composition, chemical reagents added was established, we conducted gel imaging with a two-photon confocal microscope (two-photon excited fluorescence, TPEF). Laser excitation was at 780 nm and emitted photons were detected with

two ranges of detection. TPEF Images of gels are similar to the one recorded by fluorescence scanner. If applied *in vivo*, this strategy could offer definitive advantages over visible-range fluorescence, particularly the lack of interfering autofluorescence typical for biological molecules. Another advantage of using metal clusters as opposed to commonly used dyes is that they are biocompatible, soluble, photostable and likely to pass through the cellular membranes due to their small size. The noble AuNCs composed of a small number of atoms stabilized by a peptide ligand might thus be further developed as efficient contrast agents for post-translational modification detection.

References

[1] Combes GF, Fakhouri H, Moulin C, et al. Functionalized Au15 nanoclusters as luminescent probes for protein carbonylation detection. Commun Chem. 2021;4(1):1-11. doi:10.1038/s42004-021-00497-z

[2] Jin R. Atomically precise metal nanoclusters: stable sizes and optical properties. Nanoscale. 2015;7(5):1549-1565. doi:10.1039/C4NR05794E

[3] Bertorelle F, Russier-Antoine I, Calin N, et al. Au10(SG)10: A Chiral Gold Catenane Nanocluster with Zero Confined Electrons. Optical Properties and First-Principles Theoretical Analysis. J Phys Chem Lett. 2017;8(9):1979-1985. doi:10.1021/acs.jpclett.7b00611

[4] Fakhouri H, Perić M, Bertorelle F, et al. Sub-100 nanometer silver doped gold–cysteine supramolecular assemblies with enhanced nonlinear optical properties. Phys Chem Chem Phys. 2019;21(23):12091-12099. doi:10.1039/C9CP00829B

[5] Olesiak-Banska J, Waszkielewicz M, Obstarczyk P, Samoc M. Two-photon absorption and photoluminescence of colloidal gold nanoparticles and nanoclusters. Chem Soc Rev. 2019;48(15):4087-4117. doi:10.1039/C8CS00849C

[6] Kang X, Zhu M. Tailoring the photoluminescence of atomically precise nanoclusters. Chem Soc Rev. 2019;48(8):2422-2457. doi:10.1039/C8CS00800K

[7] Rationale Strategy to Tune the Optical Properties of Gold Catenane Nanoclusters by Doping with Silver Atoms | The Journal of Physical Chemistry C. Accessed August 6, 2021. https://pubs.acs.org/doi/10.1021/acs.jpcc.0c05402

[8] Templeton AC, Wuelfing WP, Murray RW. Monolayer-Protected Cluster Molecules. Acc Chem Res. 2000;33(1):27-36. doi:10.1021/ar9602664

[9] Cao Y, Fung V, Yao Q, et al. Control of single-ligand chemistry on thiolated Au25 nanoclusters. Nat Commun. 2020;11(1):5498. doi:10.1038/s41467-020-19327-2

[10] Girod M, Enjalbert Q, Brunet C, et al. Structural Basis of Protein Oxidation Resistance: A Lysozyme Study. PLOS ONE. 2014;9(7):e101642. doi:10.1371/journal.pone.0101642

[11] Hawkins CL, Davies MJ. Detection, identification, and quantification of oxidative protein modifications. J Biol Chem. 2019;294(51):19683-19708. doi:10.1074/jbc.REV119.006217

[12] Augustyniak E, Adam A, Wojdyla K, et al. Validation of protein carbonyl measurement: A multi-centre study. Redox Biology. 2015;4:149-157. doi:10.1016/j.redox.2014.12.014

Chapter 4: In situ visualization of carbonylation: Towards in vitro imaging.

Introduction

The previous chapter described how functionalized gold nanoclusters can be used contrast agents for detection of protein carbonylation separated by SDS-*PAGE* according to standard techniques. This first proof of concept was demonstrated using a model lysozyme protein. Lysozyme is present in many biological tissues. And clearly in the previous demonstration, this protein was taken out of its biological context. One more global approach would consist in measuring carbonylated proteins in the context of its biological tissues. Two methods for measuring carbonylation have been developed so far. The first method allows the enumeration and identification of carbonylated proteins in the sample of several individuals having undergone the same treatment. This method is based on the extraction and chemical separation of proteins, the carbonyls of which are specifically marked. The chemical separation of proteins can be SDS-*PAGE* as shown in the previous chapter. However, most of the employed procedures included extraction and purification steps likely to cause loss of carbonylated proteins. These problems revealed the need for complementary carbonylation measurements without protein. Such new measurements would for instance rely on optical analysis with the opportunity to study several parameters at the same time. Thus such method would consist in measuring the level of carbonylation of biomolecules (proteins, DNA, RNA and lipids) in the whole organism (as pioneered by Radman, Frelon and coworkers[1]). It uses confocal imaging, and multiple labeling of biomolecules (carbonyl labeling and specific labeling identifying each biomolecule). It is with this in mind that we built this second project, aiming at in situ visualizing carbonylation inside the cells with metal NCs.

A lot of research show that NCs could be a promising fluorescent agents in different bioapplications[2–5] especially using gold NCs. However, there are many issues that need to be addressed for applying NCs (instead of dyes) in the bio-imaging domain. First, biocompatibility and toxicity issues need to be addressed. In this size regime, where each atom (and each ligand) counts, toxicological effects might be highly size-dependent. For this purpose, during my PhD work, a related project was conducted in collaboration with Prof.

Dusica Maysinger (McGill University, Montreal, Canada) aiming at exploring size and ligand effects of gold nanoclusters incubated in cells (human non-tumor brain cells, astrocytes). In the first part of this chapter (even if not related to carbonylation detection), I will show that AuNCs can interact with compartments of cells and are not inert in primary human astrocytes, and that their sizes play a critical role in cell behavior. The aim of this part is to show that even if nanoclusters are found to be non-toxic (by classical cell viability kit measurements), they have subtle interactions within the cell compartments.

Second, biocompatible NCs should be highly luminescent targets. As mentioned in the previous chapter, we performed all experiments in dried gels. The reason for this is that glutathione protected gold nanoclusters present very low QY ($<10^{-4}$-10^{-3}) in water. The reason behind this is that glutathione is a floppy ligand and could not fully protect the gold core from interaction with the solvent, leading to huge quenching of the fluorescence signal and causing non-radiative relaxation[6,7]. To solve this, we need to develop ligand engineering strategies to better protect gold NCs for this purpose. This part took me a lot of energy, many NCs synthesis were explored during the third year of my PhD work, and for most of them leading to disappointing results, because in addition of highly luminescent targets, NCs should be stable in complex biological media, and this was the main issue to bridge the gap for in vitro imaging. For us, the three most crucial factors for these in vitro applications are biocompatibility, high QY and stability. In the second part of this chapter, I will aim at presenting the different ligand engineering strategies, e.g., protein templating, multi-shell ligand protection and finally metal doping of the NC core (that led to the best compromise for in vitro applications).

4.1 Gold nanoclusters interacting with compartments of cells.

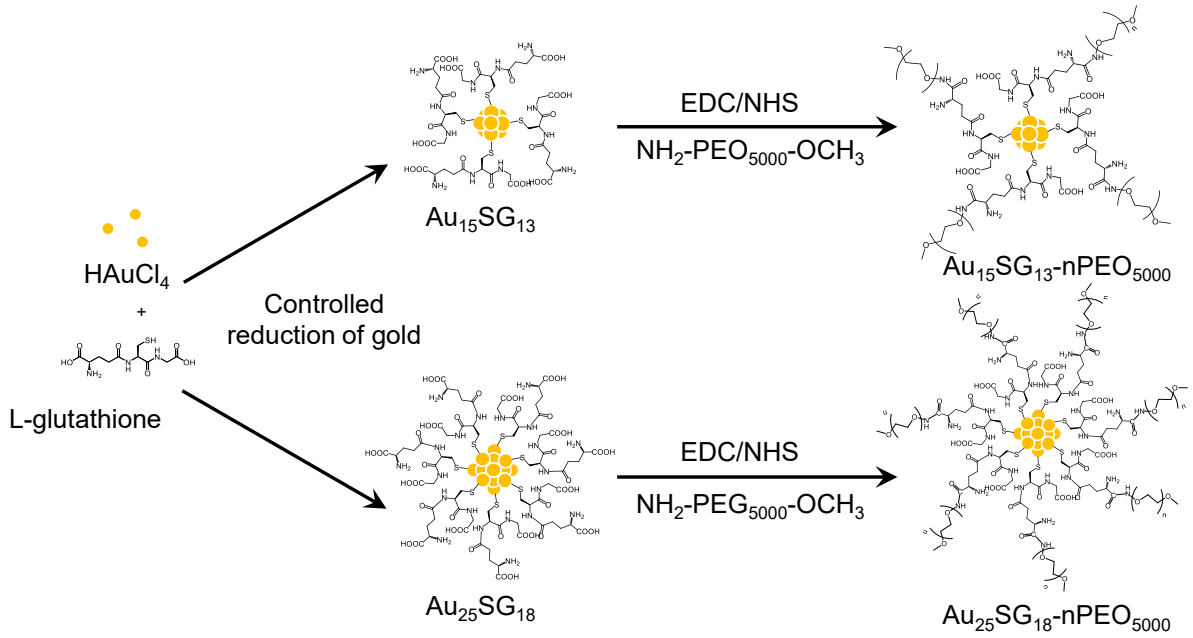

Figure 4.1: Illustration of glutathione gold NCs synthesis following by surface functionalization with PEG polymers using EDC for linking carboxylic acid of the glutathione.

Today, only a few research works have been devoted to the in-depth exploration of the interaction of gold NCs with biomolecules within cells, which leaves us room to attempt an approach in this field. As mentioned in the previous paragraph, as a side-project, I was involved in the collaboration between ILM and McGill University (Maysinger's group at Montreal). I was co-author of two papers published in Nanoscale[8] and Theranostics [9]. My contribution to this work was mainly on the synthesis and characterization of tailor-made atomically precise gold nanoclusters. Since TEM and DLS analysis are quite tricky for the cluster size range <5 nm, I used time-resolved fluorescence anisotropy technique (described in experimental

chapter) to accurately evaluate size modification upon surface functionalization with PEG polymers.

As an illustration on how tricky the effects of nanoclusters on the toxicology of cells may be, I have decided to focus on the effect of surface modification for a given cluster size. From a nanotoxicological interest, the physiological responses of living human glioblastoma cells to nanoclusters were currently unknown. To address this point, we examined how atomically precise gold NCs affect U251N glioblastoma cell viability, lysosomal properties, and functions relevant to homeostatic and cytoskeletal biomarkers. We focused on the activity of the lysosome (organelles) inside the cell, due to the particularly important role of this organelles in sensing stress and nutrient inside the cell, it is also known by its crucial position inside the cell to determine the lysosomal pH and activity. Cell stress can also alter nuclear translocation of the transcription factor Nrf2 (nuclear factor erythroid 2–related factor 2 NFE2L2).

We synthesized and fully characterized different two well-known atomically precise gold NCs for this study, $Au_{15}SG_{13}$, $Au_{25}SG_{18}$ with the pegylated form $Au_{15}SG_{13}$-$nPEO_{5000}$ and $Au_{25}SG_{18}$-$nPEO_{5000}$. Synthesis and surface functionalization with PEG polymers using EDC for linking carboxylic acid of the glutathione is shown in **Figure 4.1**. No change on UV-vis was noticed after this modification (see **Figure 4.2**). Of note, NIR luminescence is observed for such nanoclusters (when they are pegylated) but the QYs were too low to use these nanoclusters as luminescent probe for bio-imaging.

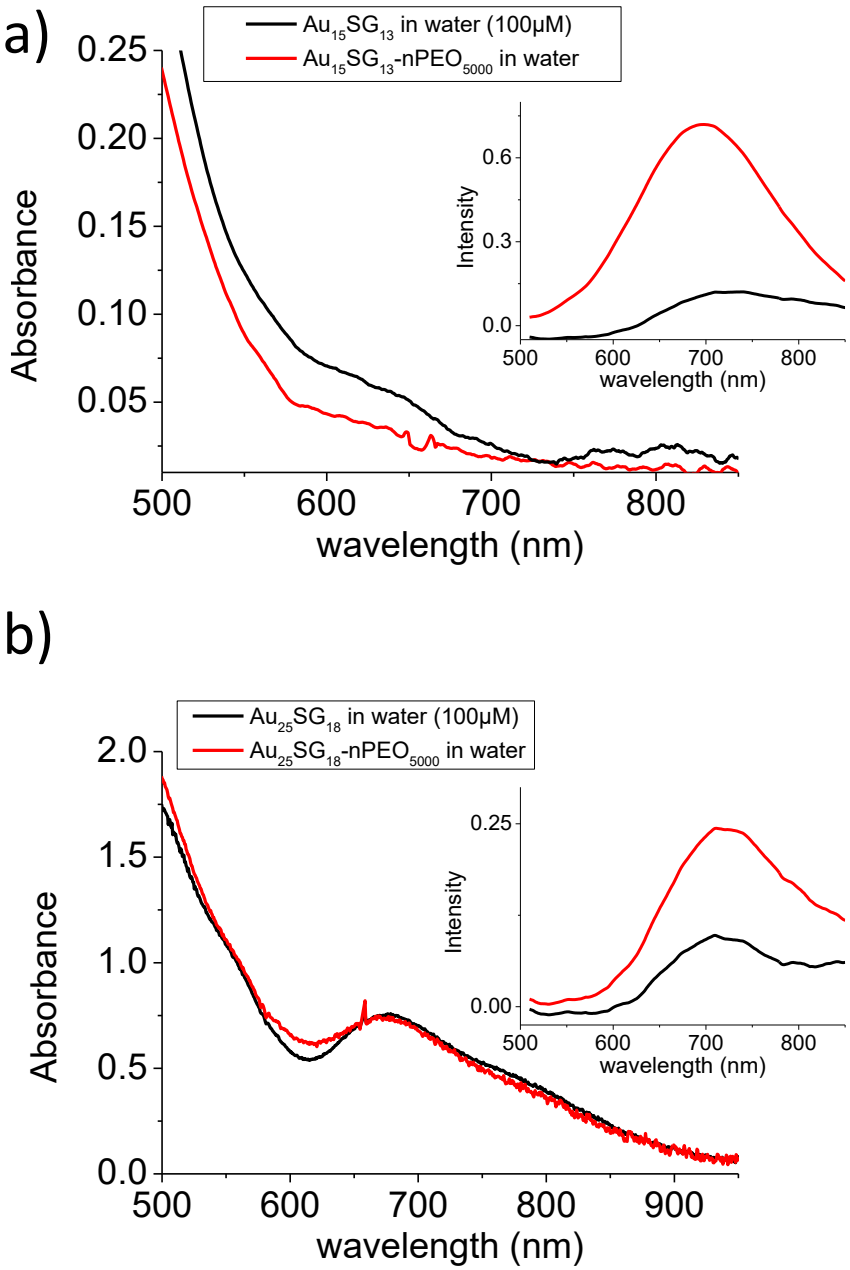

Figure 4.2 : Absorbance and (insets) emission spectra (excitation at 500 nm) of AuSG NCs and PEGylated AuSG NCs in water. a) Au_{15} and b) Au_{25}. Maysinger, D., Gran, E.R., Bertorelle, F., Fakhouri, H., Antoine, R., Kaul, E.S., Samhadaneh, D.M., Stochaj, U. (2020). Gold nanoclusters elicit homeostatic perturbations in glioblastoma cells and adaptive changes of lysosomes. Theranostics, 10(4), 1633-1648. https://doi.org/10.7150/thno.37674.

We also studied their hydrodynamic diameters size using time-resolved fluorescence anisotropy technique, an increase of size is observed, and this can be explained by the polymeric layer of the PEG. Beside we measured the zeta potential with Malvern Zetasizer Nano Zs and we found that all NCs are negatively charged. We also tried to extract the hydrodynamic size using dynamic light scattering (DLS), but we found a large uncertainty due to the limitations of DLS technique to size such ultra-small nanoclusters, see **Table 4-1**. Cell compartment is an extremely complicated system, and to understand parts of this system we choose lysosome due to it intervene in many cellular functions (see **Figure 4.3**). We concentrated on lysosomes, because they are the intracellular destination for many nanoparticles, regulate cellular homeostasis and control cell survival.

Gold NCs	*Hydrodynamic diameter (nm)*	*Zeta (mV)*
$Au_{15}SG_{13}$	**2.9**	**-3.86**
$Au_{15}SG_{13}$-$nPEO_{5000}$	**6**	**-2.14**
$Au_{25}SG_{18}$	**3.3**	**-7.46**
$Au_{25}SG_{18}$-$nPEO_{5000}$	**4.5**	**-15.4**

Table 4-1 : Hydrodynamic size (measured by TRFA technique) and Zeta potential (measured by zettameter, MALVERN zeta-sizer) of different NCs in the experiment.

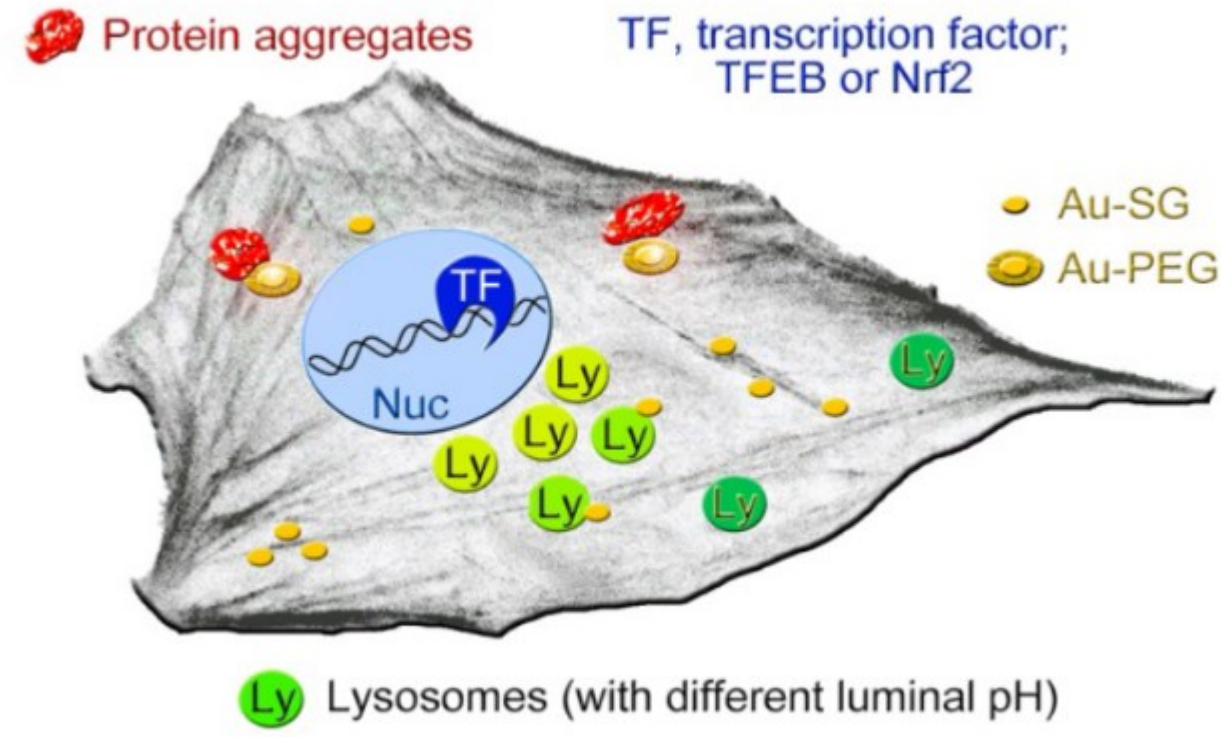

Figure 4.3 : Simplified model depicting the cellular components that are affected, at least transiently, by AuNCs. AuNCs in this study were surface-modified with GSH (Au-SG) or PEGylated (Au-PEG). Lysosomes with more acidic pH (light green) are perinuclear, whereas peripheral lysosomes are less acidic (dark green). AuNCs stimulate the transient nuclear accumulation of transcription factors TFEB and Nrf2. PEGylated AuNCs may increase protein aggregation. *Maysinger, et al, Gold nanoclusters elicit homeostatic perturbations in glioblastoma cells and adaptive changes of lysosomes. Theranostics, 10(4), 1633-1648. https://doi.org/10.7150/thno.37674.*

Our experiments focused on lysosomes and stress responses because they are essential for overall cellular homeostasis and cell fate. Lysosomes are particularly relevant to tumor biology, as they are required to remove damaged proteins and organelles through autophagy. Before starting lysosome approaches, it is very important to study cell viability after adding different

concentrations of NCs, because we need the good condition to prevent cell death and sense whether we have a modification on cell activity. Indeed, with a too high NCs concentration, the cells will be in a high stress and the toxicity will be the driving process inhibiting the interaction of NCs with different compartments of the cells.

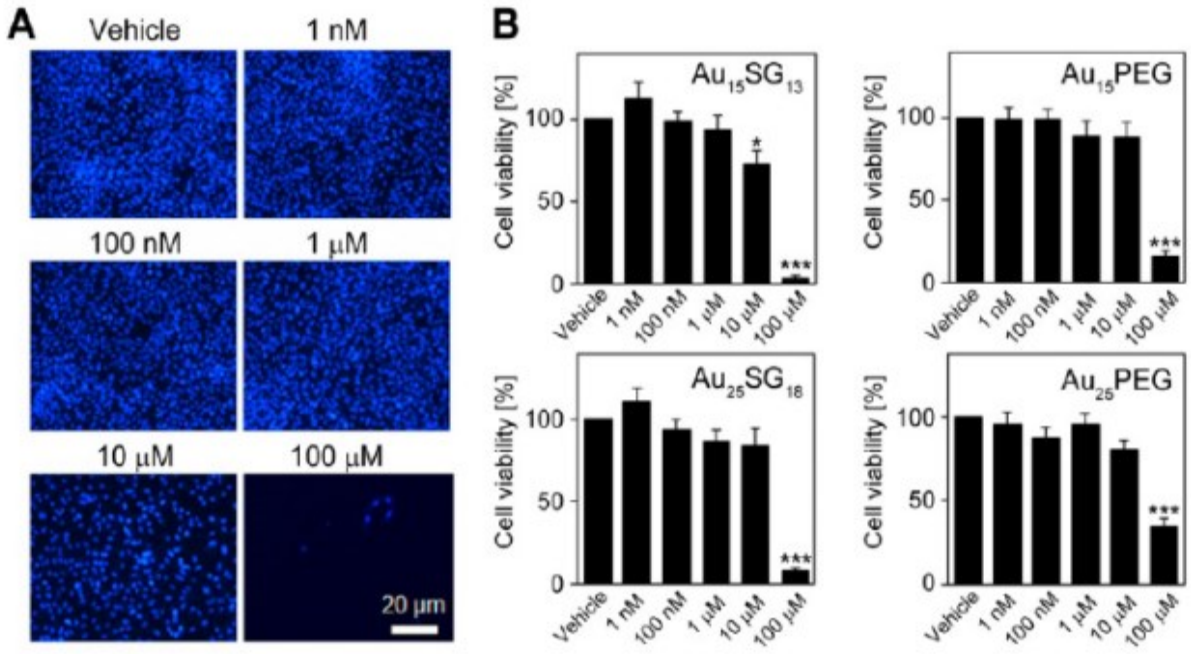

Figure 4.4: (A) U251N human cell treated with different concentration of Au15SG13 for 72 hours, nucleus is stained with Hoechst 33342 to identify cells and (B) Cell number counting compared to vehicle after incubation with the different gold NCs, significant change after treatment with NCs are marked. *Maysinger, et al, Gold nanoclusters elicit homeostatic perturbations in glioblastoma cells and adaptive changes of lysosomes. Theranostics, 10(4), 1633-1648. https://doi.org/10.7150/thno.37674.*

Cell counting and metabolic activity of the cells are the two assess that will lead us to the good concentration of NCs for cell viability and homeostatic. NCs concentration were varied between 1nM and 100µM, and for cell counting the nucleus was stained with Hoechst 33342 to identify the cells, after that a statistical study of cell viability is establish referring to the vehicle control cells (normal cells without adding NCs) see **Figure 4.4**. At low concentration

<10μM gold NCs do not seem to have a massive impact on cell viability, except for $Au_{15}SG_{13}$ where they impact 25% of live cells compared to vehicle control cells and it was the only NCs that affect the cell viability at this concentration. $Au_{25}SG_{18}$ and pegylated NCs (15 and 25) do not affect cell viability at this concentration. After cell metabolic activity test **Figure 4.5** using MTT essays, we can say that gold NCs with concentration lower than 10 μM was not harmful for cell viability and activity, leaving us to proceed the experiment following this concentration. In summary, our quantitative analysis presented here show that gold nanoclusters (with 15 and 25-gold-atoms),

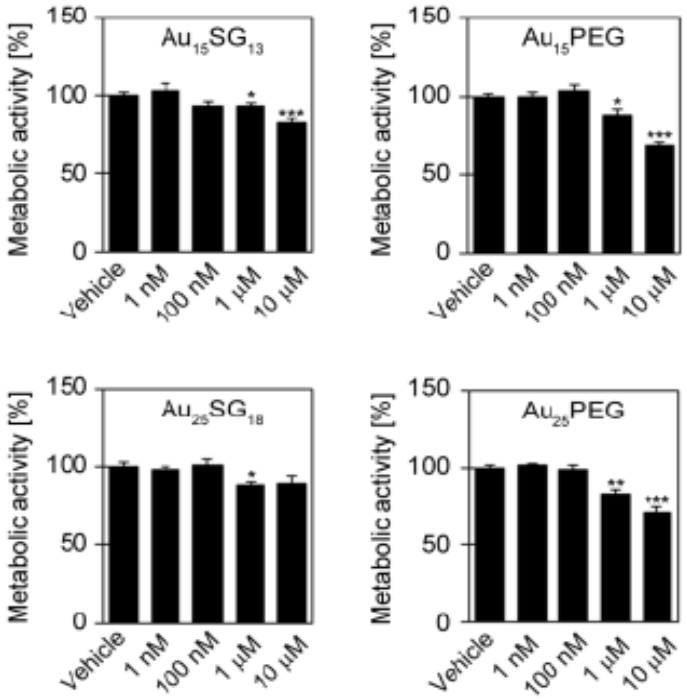

Figure 4.5 Effect of AuNCs on the metabolic activity of U251N cells. U251N cells incubated for 72 hours with AuNCs at the final concentrations indicated. The MTT assay assessed metabolic activities for at least two independent experiments, with triplicate samples for each data set. Results are shown as average + SEM; *, p<0.05; **, p<0.01; ***, p<0.001. *Maysinger, et al, Gold nanoclusters elicit homeostatic perturbations in glioblastoma cells and adaptive changes of lysosomes. Theranostics, 10(4), 1633-1648. https://doi.org/10.7150/thno.37674.*

surface-modified with glutathione or PEG, did not diminish cell viability at concentrations ≤1 μM.

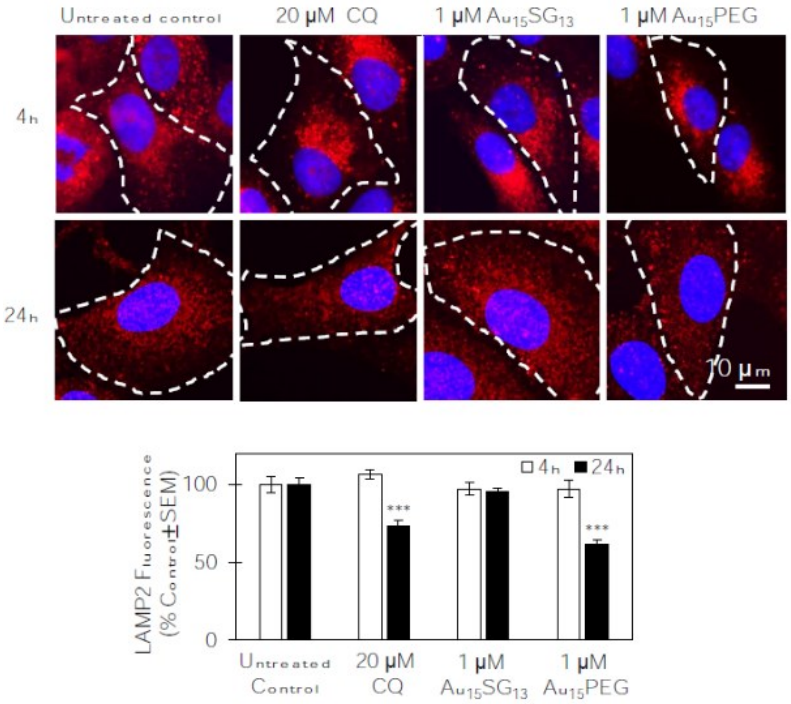

Figure 4.6: Immunofluorescence of lysosome-associated membrane protein 2 (LAMP2) in U251N glioblastoma cells. Cells were treated with 20 μM of CQ, 1 μM of Au15SG13 or 1 μM of Au15PEG in DMEM for 4 or 24 hours. Cells were stained with anti-LAMP2 (red) and Hoechst 33342 (blue). . Shown are averages of fluorescence intensity normalized to control with standard errors of the mean. *p<0.05, **p<0.01, ***p<0.001. *Maysinger, et al, Gold nanoclusters elicit homeostatic perturbations in glioblastoma cells and adaptive changes of lysosomes. Theranostics, 10(4), 1633-1648. https://doi.org/10.7150/thno.37674.*

However, even at sublethal concentrations, gold nanoclusters modulated the abundance, positioning, pH and enzymatic activities of lysosomes. More importantly, the size and surface properties of gold NCs that will accumulate inside will affect different organellar properties. For instance, among all investigated AuNCs, only Au15PEG decreased lysosomal abundance in glioblastoma cells (as shown in **Figure 4.6**). Membrane protein LAMP-2 was used as a marker for lysosome and late endosomes[10], this protein is found in lysosomal compartment and

can tell us about general changes in lysosomes (size and numbers). On the other hand, Only Au15SG13 decreased protein aggregation abundance in glioblastoma cells (as shown in **Figure 4.7**). Here, the Proteostat assay examined how AuNCs impinge on protein aggregation in the cytoplasm.

In addition, gold nanoclusters also affected other aspects of cellular homeostasis (not presented here). Specifically, they stimulated the transient nuclear accumulation of TFEB and Nrf2, transcription factors that promote lysosome biogenesis and stress responses.

Even if not specialist in cell biology, I have decided to present some important parts of this study done in collaboration with Maysinger's group, because it permits to highlight the complexity and richness of gold nanoclusters interacting with compartments of cells. Taken together, this study has explored the subcellular and molecular effects induced by gold nanoclusters and shows their effectiveness to regulate lysosome biology. Our results indicate that, even at very low concentration (that do not diminish cell viability), gold nanoclusters cause homeostatic perturbations (as summarized in Figure 3). Of note, unfortunately, the produced gold nanoclusters were not enough luminescent to use them as contrast agents for localizing them in different cell compartments (instead, specific and functionalized fluorescent dyes were used). Glutathione (and even Pegylated glutathione surface) is not a pertinent ligand

to produce highly luminescent probes in cells, and other strategies must be explored. This is the aim of the next part of this chapter.

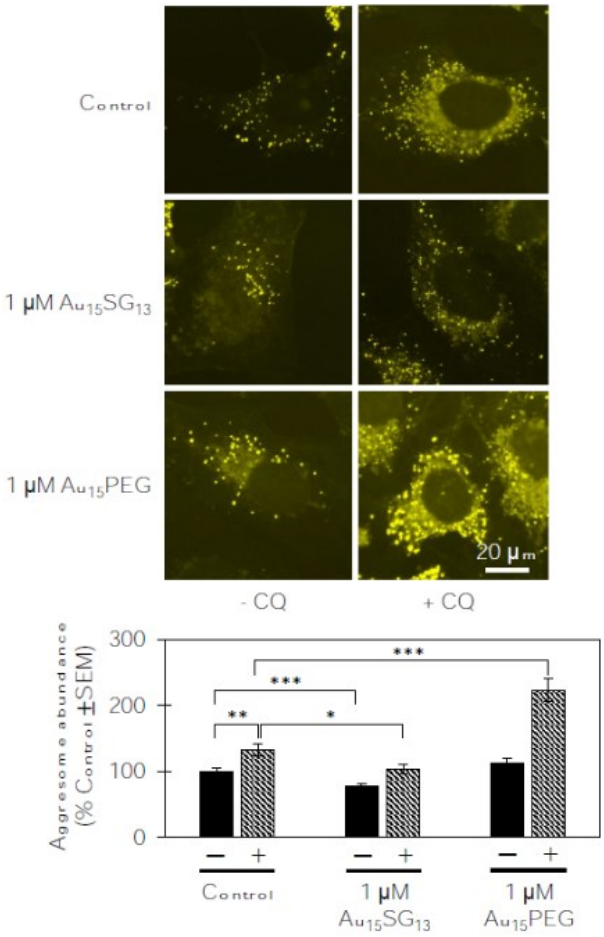

Figure 4.7 : Assessment of aggresomal abundance using Proteostat®reagent. Shown are images of untreated control, cells treated with 1 μM of Au15SG13 or Au15PEG with (+) or without (-) 20 μM of CQ in DMEM for 24 hours. Cells were fixed with 4% paraformaldehyde incubated with Proteostat®reagent (λex/λem=500/600 nm) and anti-LAMP2 for 2 hours. Shown are averages of fluorescence intensity normalized to control with standard errors of the mean. *p<0.05, **p<0.01, ***p<0.001. *Maysinger, et al, Gold nanoclusters elicit homeostatic perturbations in glioblastoma cells and adaptive changes of lysosomes. Theranostics, 10(4), 1633-1648. https://doi.org/10.7150/thno.37674.*

4.2 Advanced strategies to render metal NCs enough luminescent for in vitro imaging.

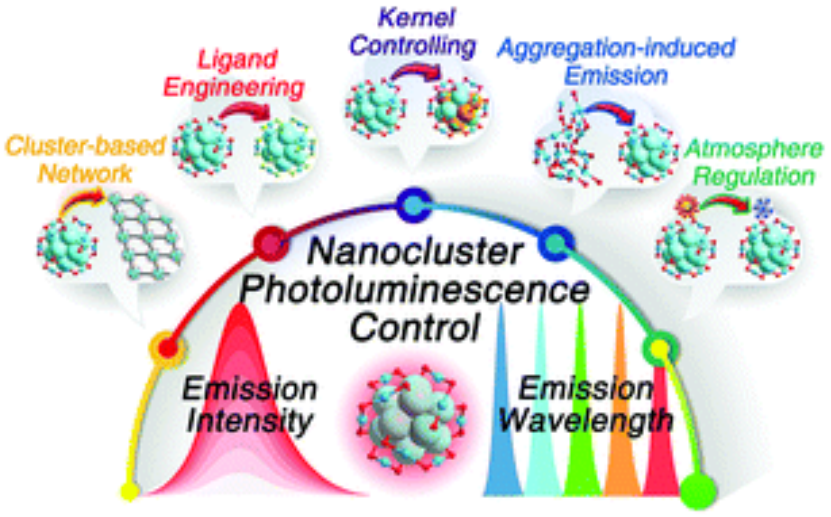

Figure 4.8 : Strategies to control the photoluminescence of nanoclusters. It's clear that this nano-objects can be manipulated to control the QY or the emission wavelength[6].

As already mentioned, for bridging the gap of in vitro imaging with nanoclusters, three essential aspects must be fulfilled : (i) strong luminescence, (ii) biocompatibility and (iii) high NCs stability towards cell environments. The PL of the synthesized nanoclusters (presented in this manuscript) is still unsatisfactory—the PL quantum yield (QY) is relatively low (lower than fraction of %). To address these shortcomings, several strategies have been adopted (see **Figure 4.8**[6]), and have been reviewed by Zhou and colleagues[6] : capped-ligand engineering, metallic kernel alloying, aggregation-induced emission, self-assembly of nanocluster building blocks into cluster-based networks, and adjustments on external environment factors. For in vitro imaging applications, aggregation, self-assembly or networks of nanoclusters may induce drastic problems of biocompatibility (due to uncontrolled size change upon external cellular environment factors). Thus, we decided to focus our strategy to enhance (PL) properties of NCs using either (i) capped-ligand engineering and (ii) metallic kernel alloying.

The first capped-ligand engineering strategy we explored, has consisted in using protein templates as capping ligand for enhancing properties of gold nanoclusters. Such bio-templates (natural proteins) may present easiness of functionalization (due to numerous carboxylic and amine surface groups), biocompatibility and usually present high QY (in the order of 10%). At the beginning, we choose to use BSA gold NCs (Bovine serum albumin). This green synthesis route of gold NCs was pioneered by Jianping Xie opened the route for protein-directed synthesis of highly fluorescent gold nanoclusters[11]. Due to the numerous sulfur atoms (present in 35 cysteine residues), the gold atoms may aggregate and be hosted inside the protein. This strategy will not only give high fluorescent NCs (~6% of QY) but will also protect the gold core from the solvent, enhancing cluster stability. Many studies suggest a core of 25 atoms of gold inside of the BSA[3], other suggest a dispersive distribution of different cluster size 3-13 atoms around the protein[12], but this kind of information's remains un-clear nowadays. Using an alternative ligand-exchange strategy, we also successfully incorporated Au_{25} inside BSA and prove it with MALDI-TOF and ESI-TOF mass spectrometry[13].

For us, visualizing BSA-directed gold NCs inside the cell will be the first goal before going to target carbonylation by post-functionalization. After NCs synthesis, we first sent the BSA gold NCs to MEDILS institute in Split Croatia where they studied the cellular uptake of the NCs. I would like to outline that this period was quite difficult due to COVID crisis (where travels to Croatia were not possible). And sending samples were not the most useful way to do collaborations !

We tested two type of cells on the first experiment, A549 (epithelial carcinoma derived from a 58 year old male patient) and V79 (Chinese hamster lung fibroblast) cell lines, the cells was treated for 24h with different concentration of BSA-Au NCs, no fluorescent signal was detected after adding BSA-Au NCs see **Figure 4.9**, we doubted first about microscope sensitivity, and that conventional microscope used is not sensitive enough.

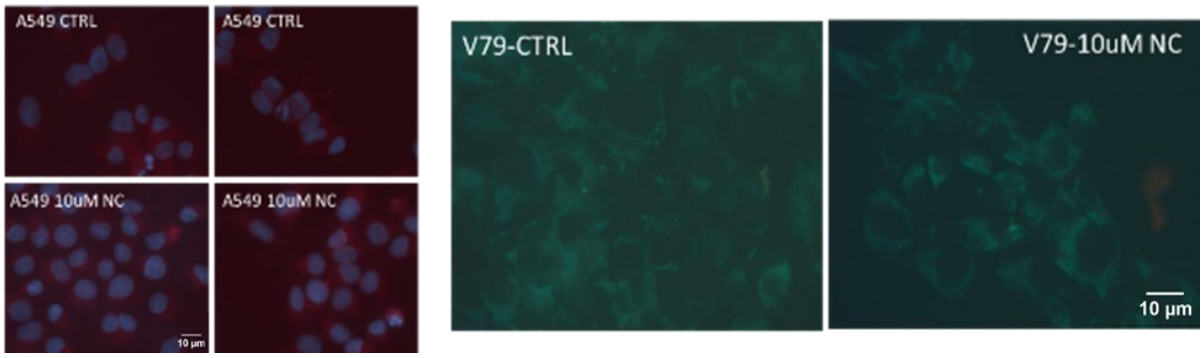

Figure 4.9: Microscope images after incubation with BSA-Au NCs, we stained the nucleus with DAPI to visualize the cell, red and green signal is due to auto-fluorescence of membrane, no signal of nanoclusters was found, this was the first result of using gold nanoclusters in vitro, which encourage us to find other systems of nanoclusters to proceed in vitro experiments.

We tried also flow cytometer technique to study cellular uptake of BSA-Au NCs, cell where incubated for 24h at different concentration of NCs see **Figure 4.10**, a slight shift in median fluorescence signal is detected for a concentration of 10µM of NCs (15% increase), but still very week signal compared to the control (from the point of view of cytometry experts). Note that a small shift is observe in serum-free medium (without FBS). BSA-Au NCs do not internalize inside the cells efficiently; it was a disappointment for us because it worked fine for other reported published studies. We were quite optimistic with BSA-Au NCs because we were able to develop a strategy to functionalize it for carbonylation issues. Indeed, we were able to reduce the surface groups of BSA with formaldehyde and glutaraldehyde and then with hydrazine, to proof the surface functionalization and carbonyl targeting at the same time, we mixed the F-BSA-Au NCs with 3-pyridinecarboxaldeyde (aldehyde molecule). We measured first the UV-Vis absorption spectra for aldehydes only, and then mix the solution with F-BSA-

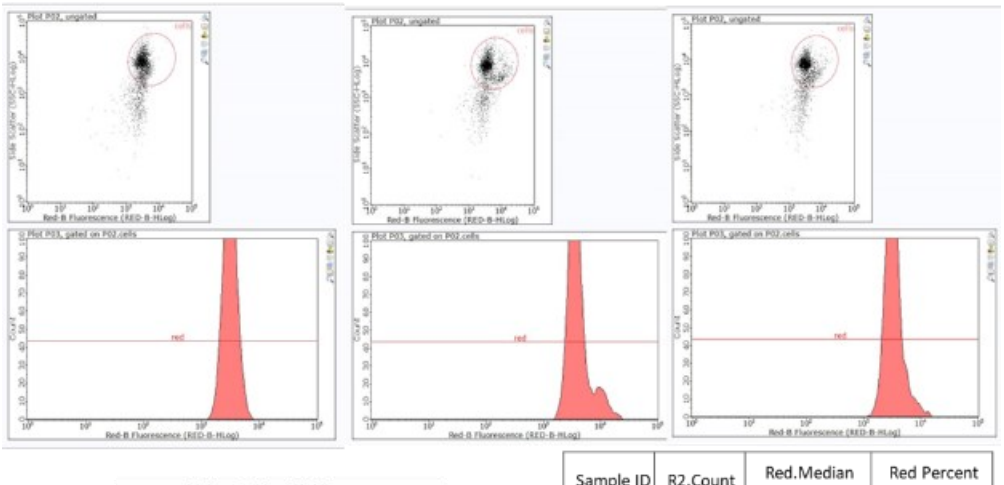

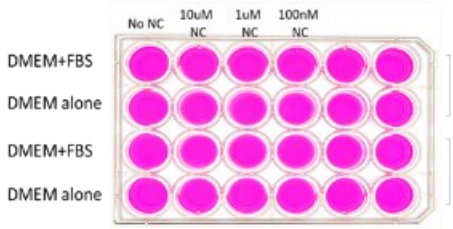

Sample ID	R2.Count	Red.Median	Red Percent
ctrl	2385	3190	29
ctrl	2384	3170	30
ctrl	2412	3195	29
1uM	2486	3268	48
1uM	2453	3258	42
1uM	2425	3267	46
10uM	2473	3755	63
10uM	2438	3729	63
10uM	2499	3705	63

Figure 4.10: Measurement of cellular uptake of BSA-Au NCs using flow cytometer. No change in signal was found between ctrl and cells incubated with NCs, which confirm the previous results under the microscope.

Au NCs, we then centrifuge the solution with membrane 5000KDa where the BSA will stay on the upper part and only small molecules (aldehyde well pass). The UV-Vis spectra show a decrease of aldehyde absorption with 4 to 5 aldehyde per F-BSA-Au NCs see **Figure 4.11**, which indicate that part of aldehyde where bind to F-BSA-NCs.

Even if quite appealing due to easiness of functionalization and high QYs, BSA-Au NCs was quite disappointing for in vitro imaging issues. In fact two main drawbacks we figured out by Xie and collaborators[14] and could limit their further applications in biological and biomedical fields. One is the susceptibility of BSA-AuNCs towards oxidative decomposition by reactive oxygen species (ROS), and the other is the degradation of BSA-AuNCs by proteases or other enzymes in lysosomes.

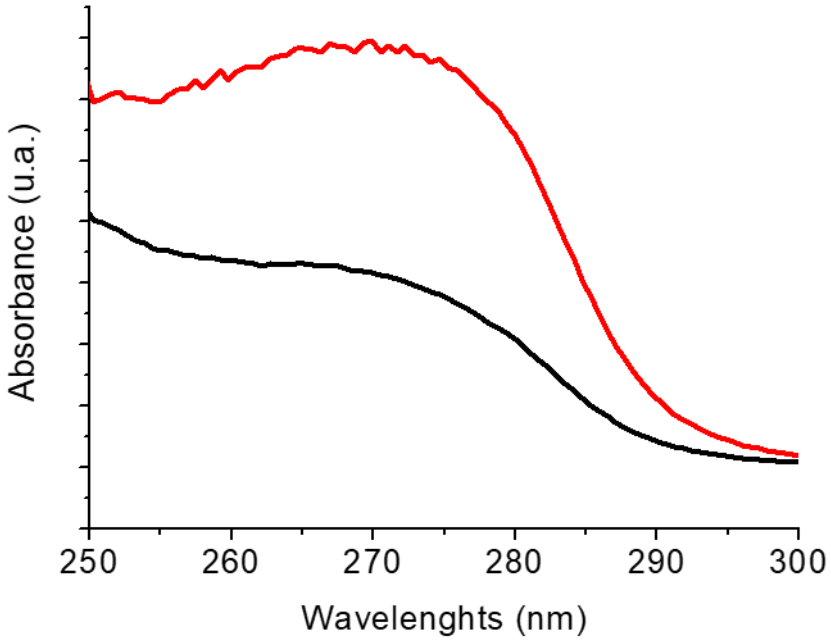

Figure 4.11: UV-Vis's absorption spectra of (red) the 3-pyridinecarboxaldeyde before mixing and (black) after mixing and filtration with F-BSA-Au NCs. This results confirms that functionalized nanoclusters can target carbonylation, but the problem was the ability of this nanoclusters to penetrate the cells.

Thus, we decided to skip BSA-Au NCs and try other proteins (already found to be good templates for producing AuNCs) : Insulin[15], Lysozyme[15], Transferrin gold NCs[5], surface functionalization of BSA-Au NCs with folic acid (FA-BSA-Au)[4] and with glucose (G-BSA-Au). We included Lysozyme and Insulin gold NCs to see the size effect on cell internalization (Insulin 5.8KDa Lysozyme 14.3KDa BSA 66KDa), and their dynamic size after synthesis is also coherent with to their size (respectively 7.4nm, 9.0nm and 9.4nm)[15]. Protein NCs are synthesized very similarly with small changes, briefly proteins is dissolved in water and 10mM of $HAuCl_4$ solution is added, the pH is modified to basic by adding 1M NaOH to reduce gold atoms and oxidize the tryptophane and tyrosine inside the protein also to reduce gold, H-Gly-Trp-OH is added only for Insulin and Lysozyme during synthesis, transferrin was left for 3 hours, BSA for 16h and Insulin, Lysozyme for 24h at 37°C, the solution were then purified by ultrafiltration Millipore using different size depending on the protein size. Post

functionalization BSA-Au NCs showed better cell internalization, some cancer cells overexpress folate receptor α (FRα) for cancer cells[16], to do this we added NHS and EDC to the as-prepared BSA-Au NCs following by folic acid solution and the shacked overnight and then purified 50KDa Millipore membrane. And lastly, we also explored the multi-shell capped ligand strategy for enhancing stability and QYs of gold nanoclusters, using ATT/Arginine as multi-shell ligand system. The gold nanoclusters are first protected by ATT ligands and then a second shell of charged ligands (e.g. Arginine) is added and "stick" electrostatically on the surface of ATT-AuNCs.[17]

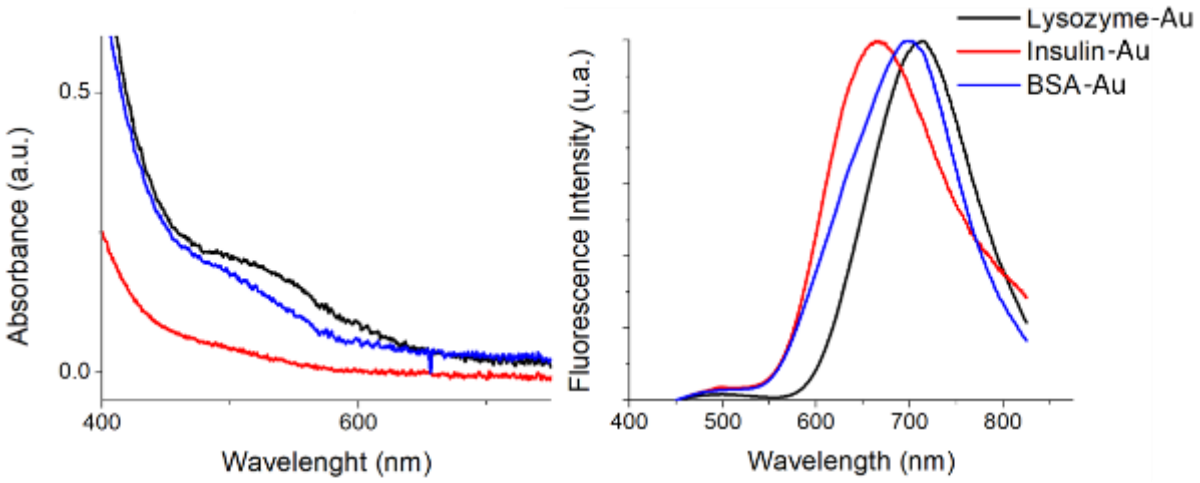

	Absorption at 425nm	Integrate emission	QY	Emission Peak (nm)
BSA-Au	0,39	2,4	7 %	700
G-BSA-Au	0,65	2,2	2,5%	692
Lysozyme-Au	0,42	1,5	2,6%	713
Insulin-Au	0,13	0,64	3,6%	665
FA-BSA-Au	0,12	0,3	3%	690
Transferrin-Au	0.13	0.45	4%	690
AuATT/Arg	0.23	0.43	2.3%	540

Figure 4.12: Linear optical properties of synthesized protein gold NCs, (Top) UV-vis spectra and emission fluorescence (after excitation at 425nm) and (below) table showing parameters to calculate QY using DCM as external reference.

The different synthesis shows high QY, stability and should be biocompatible due to their biocompatible surface ligands (protein for protein NCs and Arginine for AuATT/Arg). We studied their one photon optical properties before doing in vitro application see **Figure 4.12**. We also explored their two photon optical properties (TPEF) before doing in vitro application see **Figure 4.13**. TPEF spectra show a common red band at ~650 nm for all protein templates which might be appealing for multi-photon confocal microscopy. Also, AuATT/Arg NCs present an impressive TPEF cross section with a green band centered at 530 nm.

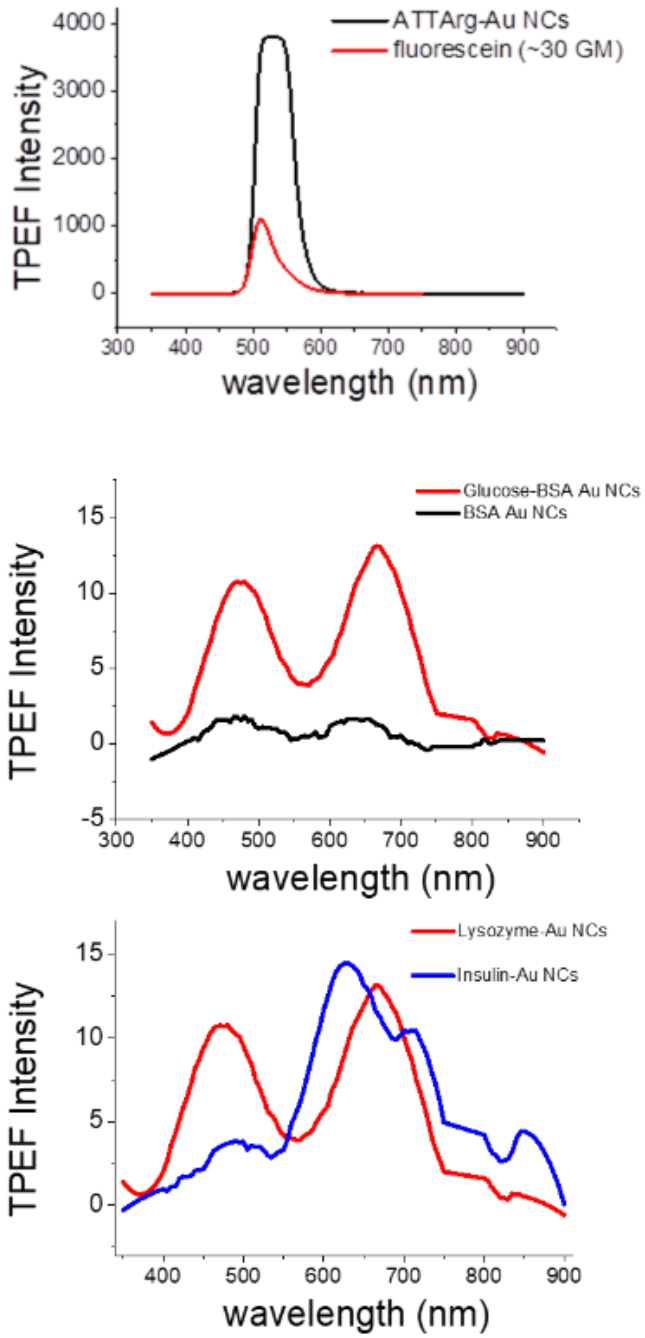

Figure 4.13 : Two photon emission fluorescence spectra of protein-based gold NCs after excitation at 780nm. The aim of this experiments is to see the possibility to visualize the cells under multiphoton confocal microscopy.

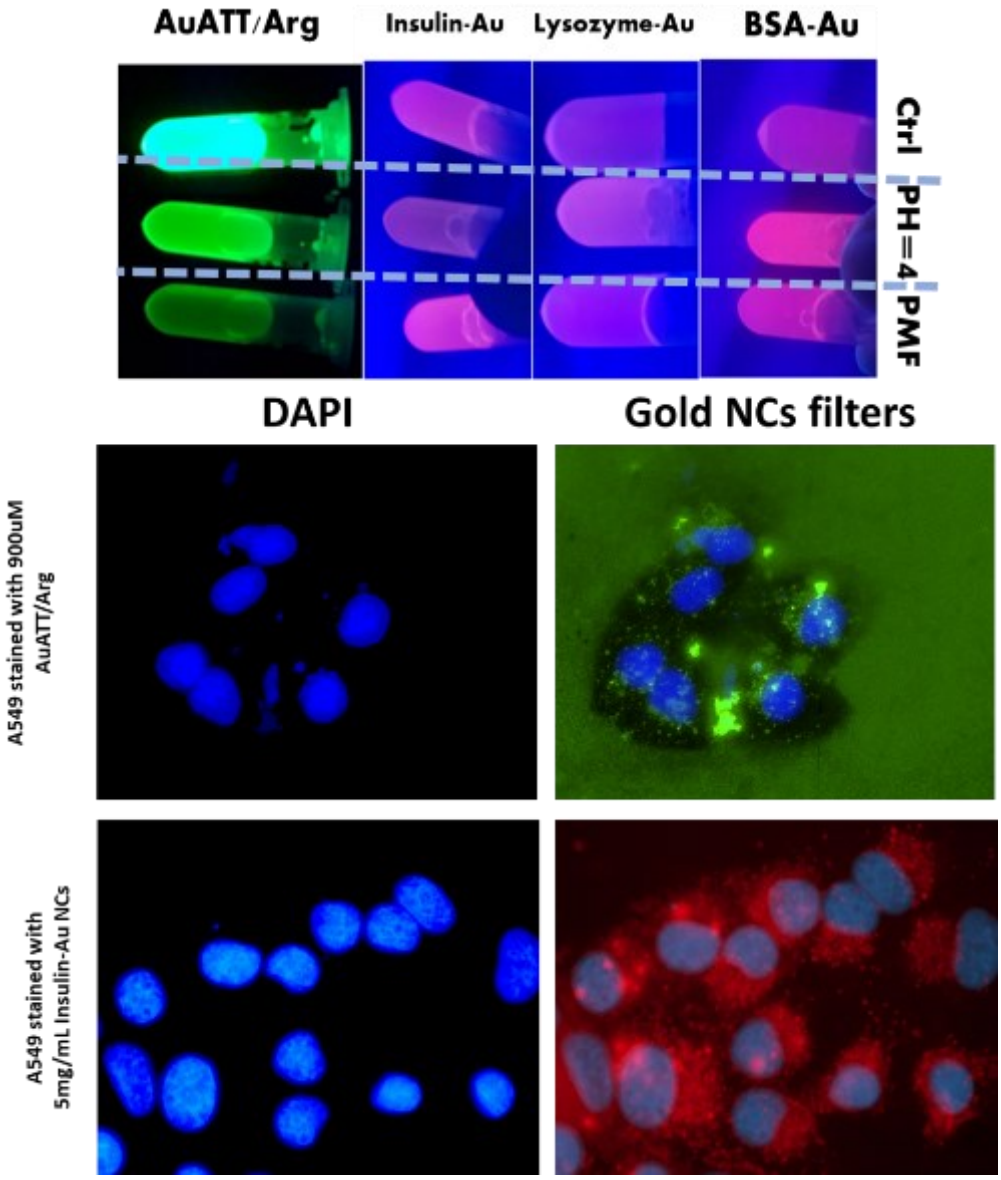

Figure 4.14 : (Top) NCs tested in different conditions, same concentration was used for each NCs and a control to compare the signal (below) Conventional epi-fluorescence microscopy images of A549 cells after incubation with gold NCs, only Insulin-Au NCs (24h) and AuATT/Arg (1h) was able to internalize the cells.

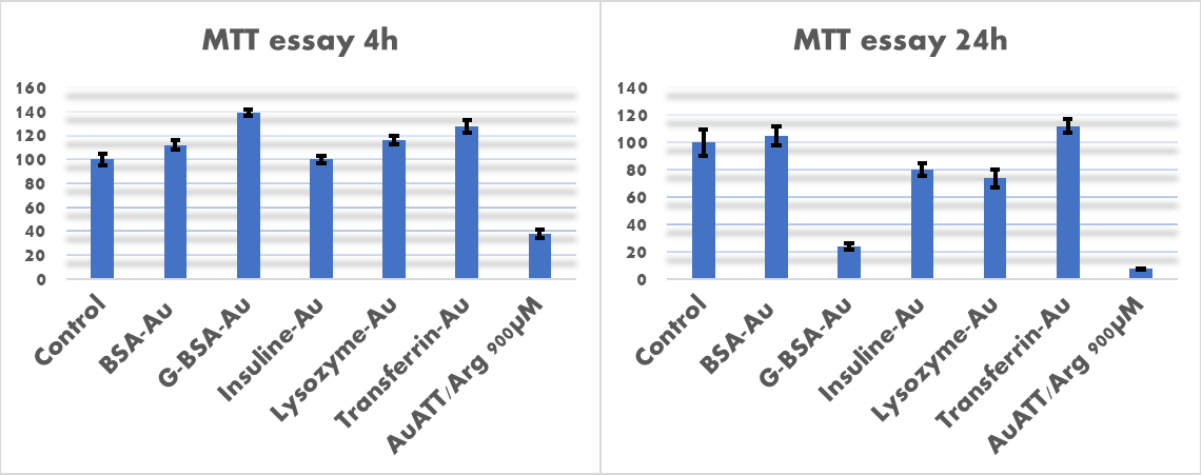

Figure 4.15 : MTT viability assay on A549 cells incubated for 4 h (left side) and 24h (right side) with gold NCs where the concentration is set at 5mg/mL for protein gold NCs and 900µM for AuATT/Arg.

We first tested if the NCs can be robust enough when they are inside the cell, acidic pH and paraformaldehyde (for cell fixation), the more it will migrate towards nucleus, more acidic it will come and as we can see in **Figure 4.14** acidic pH and PMF doesn't seem to affect fluorescence signal, except for AuATT/Arg, because his fluorescence is mainly based of the rigidification effect of Arginine and this harsh conditions can "remove" the arginine shell from the clusters.

We assessed NCs in different condition and concentration, after we follow publication and we did not see signal in cells, when using a high concentration from 5mg/mL for protein NCs to 0.1mg/mL and from 900uM to 1uM for AuATT/Arg NCs. We dissolve the NCs in DMEM only without FBS and incubate them for 4h and 24h. At the end of incubation time, we washed the dishes three times with PBS 1x and after we fixed the cells with 4% PMF and stained with DAPI to identify the cells. First results show that only insulin-Au (24h) and AuATT/Arg (1h) internalized the cells, with only high concentrations. The other problem is the high concentration used compared to publications, and the green layer visualized when staining with AuATT/Arg. Its unusual and not clear how we stop seeing signal for this two NCs when we tried to lower the concentration, even with a factor of five. We evaluated the cell metabolic

activity for all NCs, even if they did not internalize the cell see **Figure 4.15**. We can see that protein gold NCs did not highly affect cell viability, even at high concentration. For all NCs except Insulin-Au, they may have low toxicity, but at the same time the negligible impact is probably because they did not internalize at the first place, or they did enter and deteriorated inside the cells.

We also tried the same coverslips under a more sensitive confocal microscopy in Zagreb. Sample where excited at 425nm (for gold NCs) and 395 (for DAPI) and the signal was collected with photomultiplier tube, different windows is used to differentiate between DAPI and gold NCs signal, we used the same window for all protein gold NCs since there emission peak is quite similar see **Figure 4.12**. As we can in **Figure 4.17** the problem was not the sensitivity of the microscope, and only two NCs was internalizing the cells, Insulin-Au and AuATT/Arg. The conclusion is the following, two gold NCs are suitable for in vitro, we used high concentration, we saw a green layer when incubating with AuATT/Arg which have high toxicity at the same time. Note that the molecular weight for all NCs is unknown, no mass spectrometry data is available, meaning that in future experiment and if we can functionalize them to target protein, it will be a challenging to prove the ratio of surface modification and the modification itself. We tried all the conditions possible, from time incubation to concentration, from different cell lines to different medium (HBSS, DMEM, with and without FBS/antibiotics), even cell numbers per well (30k to 80k of cells per well) especially for AuATT/Arg to get rid of the green layer. We also studied the internalization method of gold NCs, we did it only for AuATT/Arg, it will show if the NCs enter the cell via endosome i.e., endocytic membrane transport pathway, so we used EEA1 dye (early endosome antigen 1), LAMP1 (Lysosomal-associated membrane protein 1). Results shown in **Figure 4.16** exhibits no inter-localization of dyes signal with AuATT/Arg NC, which means that NCs directly penetrate the membrane cells without any intermediate stage. It was important to verify this

because if the enter with endosome phase, they will not be able to react with anything inside the cells, therefore will not target carbonylation.

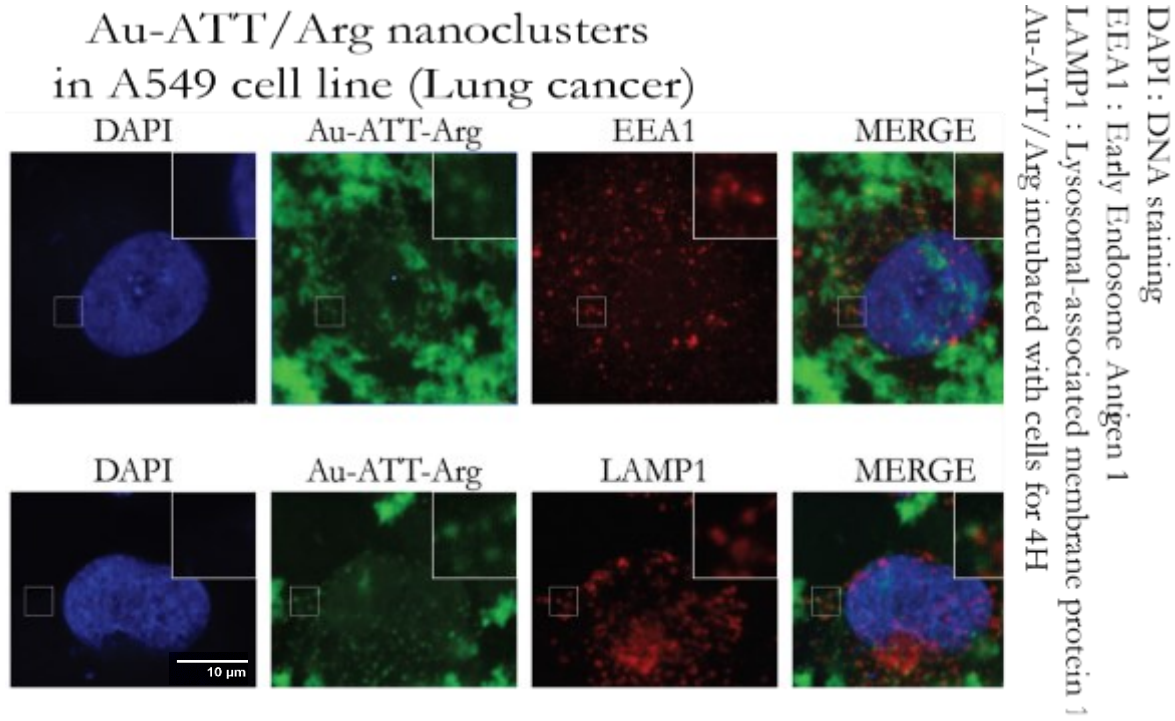

Figure 4.16 : Cell imaging using Leica confocal microscopes of A549 cells incubated with AuATT/Arg NCs for 4h and stained with EEA1 and LAMP1 for 10 minutes. The results show no colocalization of the nanoclusters with dye used, meaning that nanoclusters are penetrating the membrane to reach the cells.

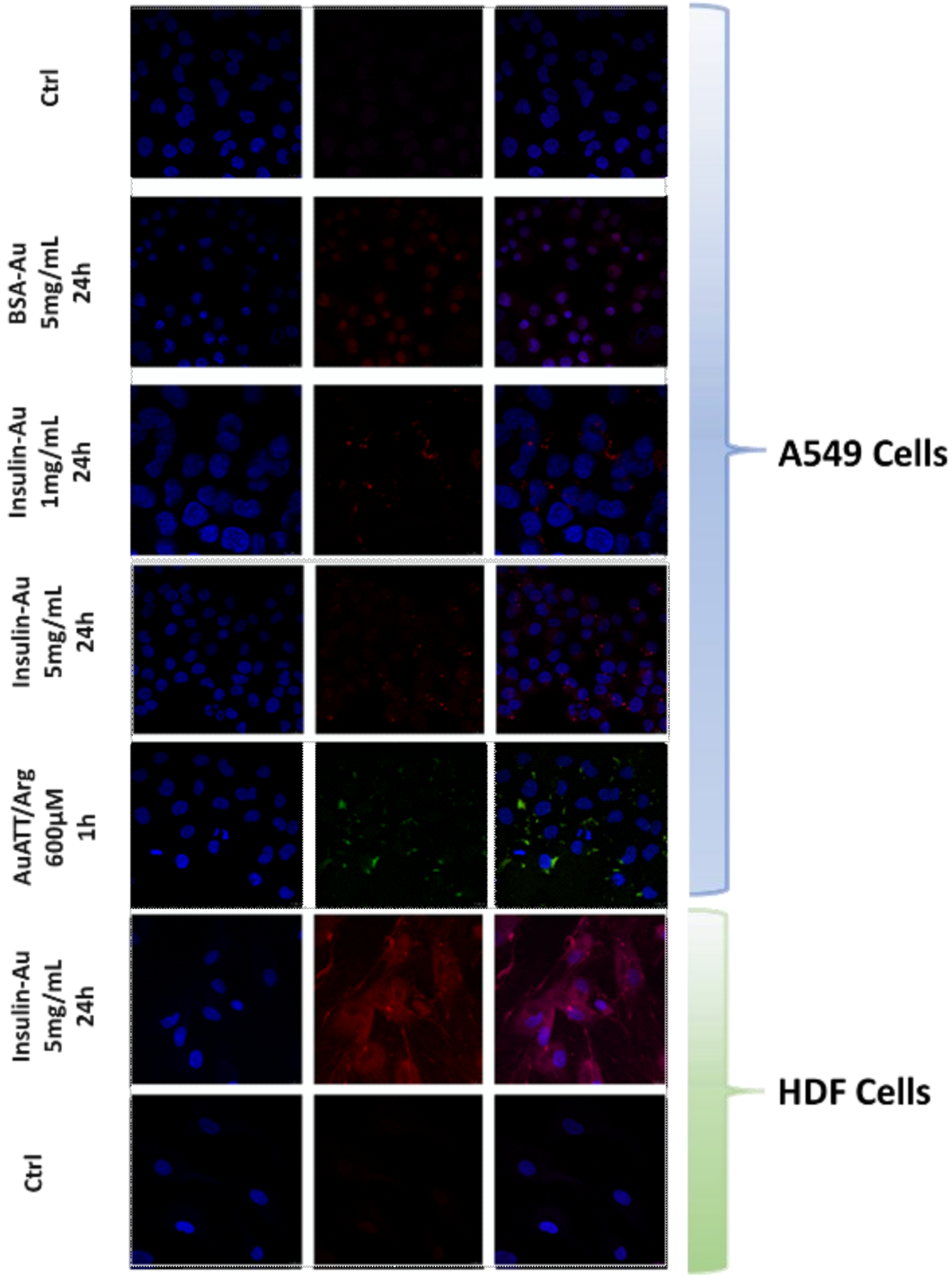

Figure 4.17 : Cell imaging using Leica confocal microscopes for different cells lines and gold NCs, we stained the nucleus with DAPI, first colon is showing DAPI window, second column showing gold NCs window and the third one is the overlay of both windows.

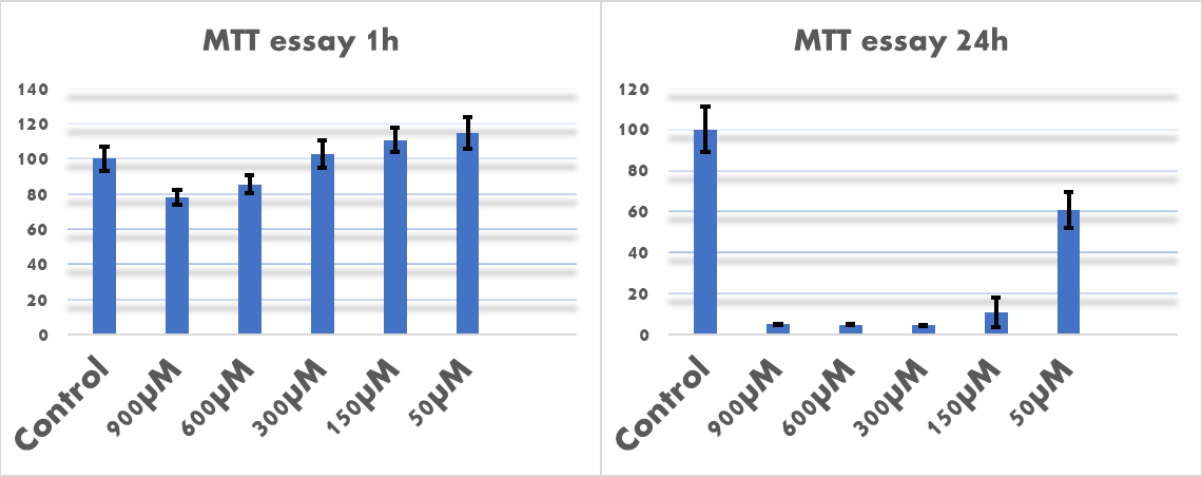

Figure 4.18 : MTT viability assay on A549 cells incubated for 1 h (left side) and 24h (right side) with AuATT/Arg NCs with different concentration, showing the high toxicity of the nanoclusters.

Finally, we can say the ligand engineering strategy to protect gold NCs was not convincing for in vitro experiments, and we were not satisfied with the results, mainly because of the high concentrations used, and we followed exactly the experimental setup for references who visualize normal internalization. The reason behind all that is unknown, but the only difference between us and others is that they used directly their NCs after a fresh synthesis towards in vitro experiments compared to us, because we lyophilized all protein gold NCs to take them via airplane in the baggage, even though they did not change in term of fluorescence, color. So we wondered if lyophilization itself caused some modification, it may lead to the loss of the protein due the freeze and de-freeze process, putting such systems under physical stress[18], partially unfolded and dehydration-induced aggregation due the PH shift[19]. To prove this hypothesis, or explanation, we decided to do all next experiments in Lyon, where I am can do fresh synthesis and do in vitro experiments in my institute ILM, with biophysical group where they have all materials needed.

Beside of doing fresh synthesis, we noticed that AuATT/Arg started to degrade with time, a black precipitation was observed at the bottom of the tube, and the QY found is 3%, wasn't

high as found in the reviews, so a modification is needed to optimize the synthesis, I also bring all the coverslips from Split to view them under two photon confocal microscopy, but they were destroyed during the transportation under humidity (we saw water bubbles for almost all coverslips). Flowing the synthetic method of Wang et al[17], the ratio molar ratio of arginine to ATT was 1 for 30, so I increase the ratio to have 1 for 2, and I managed to have a QY of 21%. We also discovered that what we were using in vitro experiment was more of AuATT alone without arginine and this led to fast degradation and explain the green layer observed on the coverslips. At the same time, I did the synthesis of Insulin-Au to do experiment with fresh synthesis, note that we waited 2 months to have access to the cell culture facility, it gave us time to explore and optimize more systems for in vitro experiments.

Since it is important to explore the composition of the gold NCs investigated in the project, we proceed MALDI-TOF mass spectrometry experiments. Afterward, MALDI-TOF experiments are crucially depending on sample and matrix preparation in order to have optimized results, therefore an exploration of different matrices used and the preparation method (double layer, triple layer) is needed, see **Table 4-2** for experimental preparation following some reviews in this subject[20–23].

We tried the four matrices mentioned in **Table 4-2** for each NCs, wherein we put calibrator in the well centered between the four wells of NCs. We applied reflector and linear mode regarding the size expected, we use mostly the positive mode because all protein-gold NCs are based on positively charged protein used. As we can see in **Figure 4.19,** we did not conclude any promising results from the different runs. Even though these results can afford an idea on the composition such as the Au_2ATT_2 and $Au_{10}ATT_{10}$, and the differences in mass in Au-BSA spectra, it could be accurate or not, because the delta calculated can say the there is a mix off Au_x-BSA after the synthesis, but still not dependable. We visualized a large dispersion of peaks separated buy 125 in mass/charge for AuATT/Arg and Au-Insulin, suggesting that the matrices

Matrix	System	Analyte concentration	Matrix concentration	method	Comments
SA	Protein	Pico mol	1st layer, 6 mg/ml in 60:40 methanol/acetonitrile 2nd mixed with analyte, saturated matrix solution	Mass layer (double layer) Matrix then 1:1 matrix/protein mix	Used in many systems, especially proteins
DHB	$Au_{22}SG_{18}$	3mM	Saturated	Mix	Depends on the isomers used, 2,4- et 3,5- are better in negative mode et 2,6- et 2,5 are more suitable for positive mode
HCCA	Protein	Pico mol	1st layer : 20mg/ml 40% methanol in acetone Second layer: saturated solution in 40/60 methanol/water Third layer: Only analyte	Three layers (sandwich)	Pay attention to the PH of the deposited protein, it must be acidic (the base dissolves in the matrix), better resolution in double layer
NBA-Butadiene (matrix-dye)	Protein	Nano mol	Dye 0,1M and saturated matrix	Mix, and mass layer (matrix, dye then protein)	Glucose or Rhodamine 6G can be used for visible mode (if analyte have low absorption in the visible rang)

Table 4-2 : Sample and matrixes preparation for different method and concentration for MALDI-TOF experiments found in literature.

bind on the surface. We then stopped investigating in mass spectrometry analysis since the priority is in vitro experiments, and the results was not encouraging.

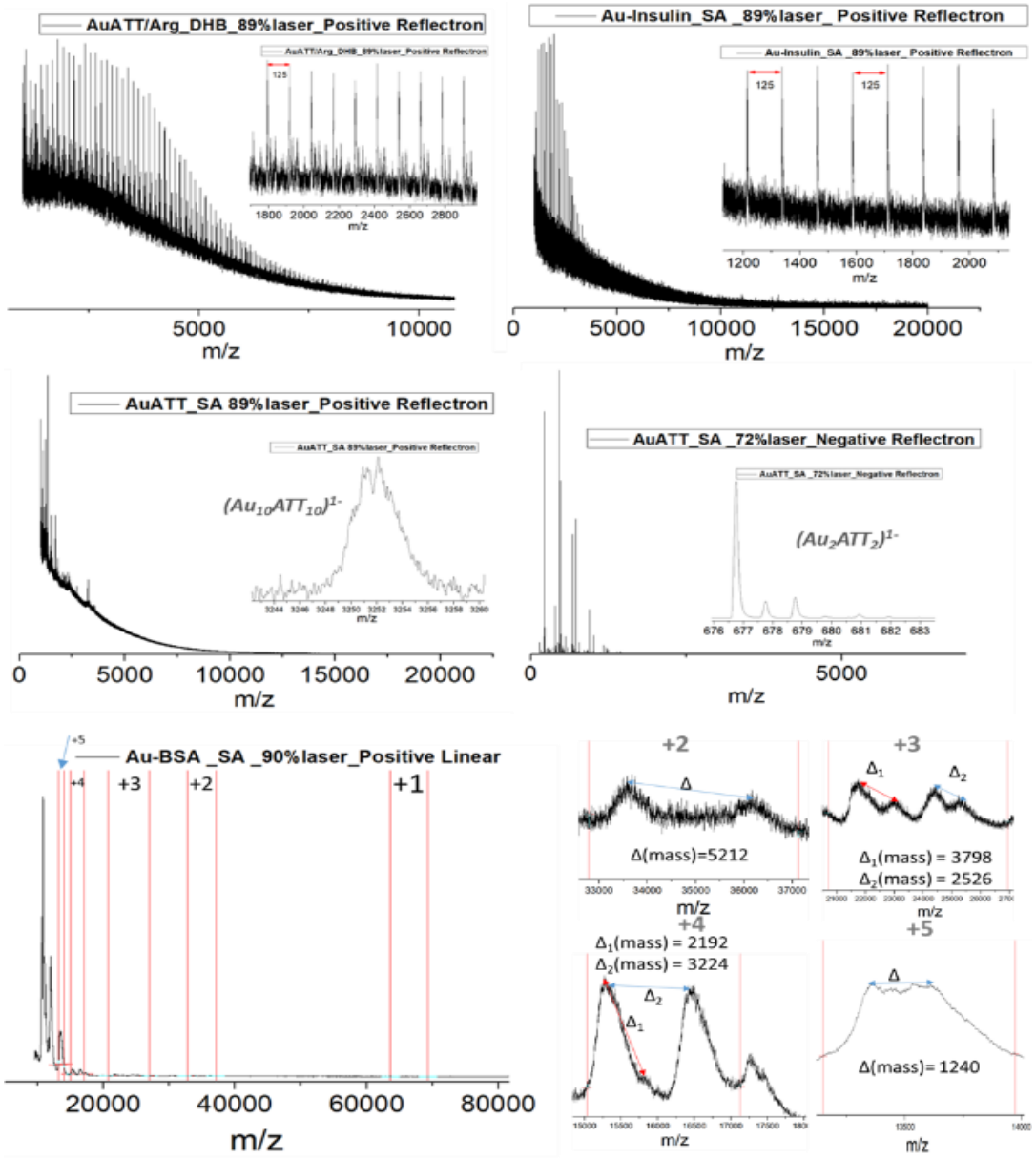

Figure 4.19 : MALDI mass spectra for different gold NCs with different matrices and method of preparation. We only showing few results with interisting spectra, the other didn't show any analatycal spectra.

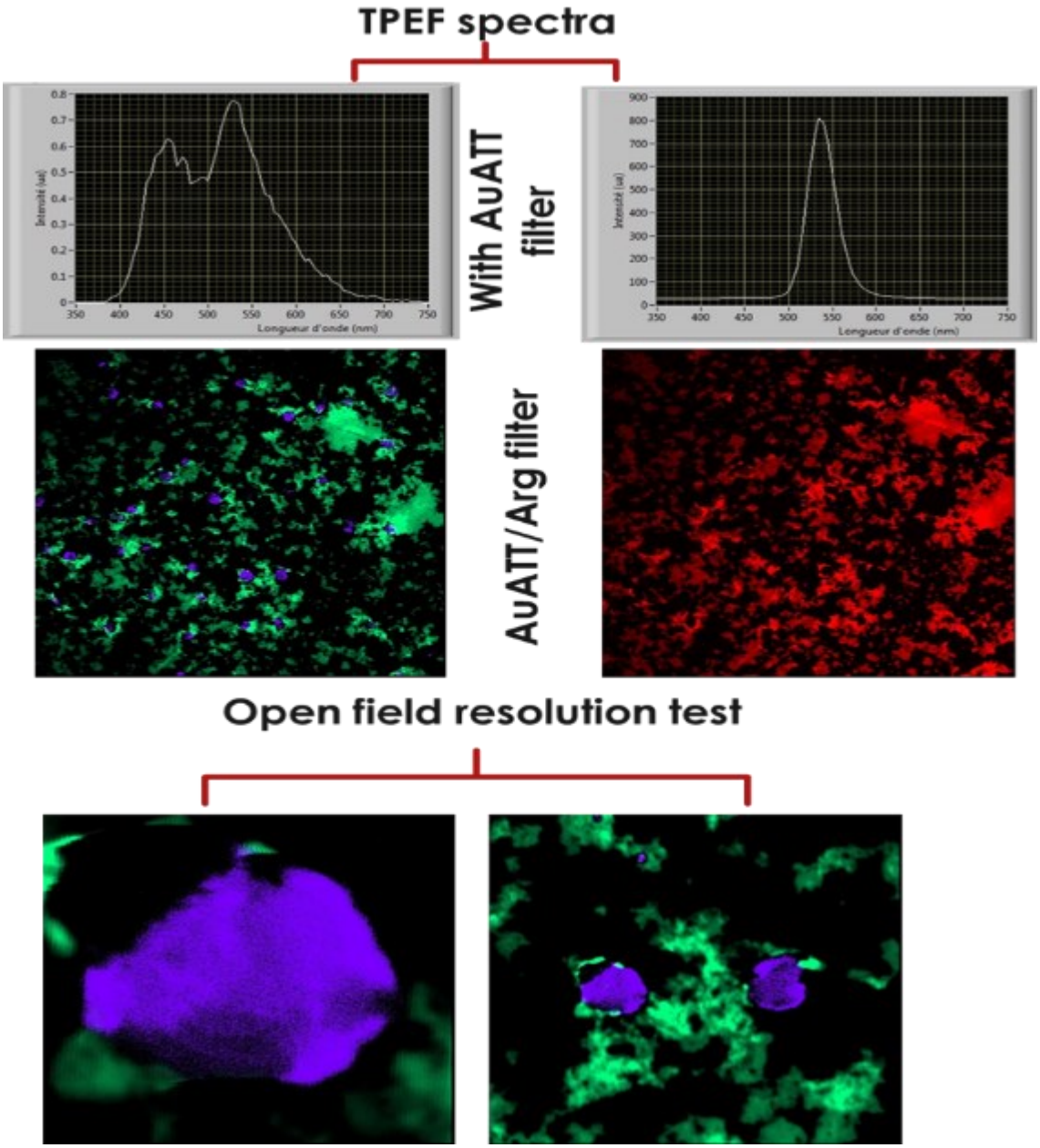

Figure 4.20 : Images of HDF cells incubated with DAPI and AuATT/Arg under multiphoton confocal microscopy with an excitation wavelength at 780nm. This was a primary results to see the sensitivity of the multiphoton confocal microscopy, the image show damaged samples due to the transportation of the prepared samples in Croatia, where this experiments was conducted in Lyon.

We moved next to optimize multi-photon confocal microscopy for bio-imaging, with what we

have left from the experiment done in Split, after transportation of the samples (discussed before). Since DAPI and NCs coexist in the same location, it will be challenging to separate signals, it is equivalent to mixing different fluorophore is the same solution and try to see only one signal, but since DAPI signal is more shifted to blue, with an emission peak centered at 457nm and AuATT/Arg is at 530nm filters can be efficient in this case. As we can see in **Figure 4.20** we succeeded to separate both signal and we were able to register two photon emission fluorescence of gold NCs inside the cells. The advantage of using multiphoton excitation is to prevent photobleaching, autofluorescence of membrane and mostly the importance of this method for bio-imaging.

After we succeeded in synthetic optimization and optical characterization, we did not see any signal of gold NCs inside the cells even after following the same protocol applied in the experiment concluded in Split. Strongly disappointed, we moved towards another strategy using metallic kernel alloying.

Silver nanoclusters are known to be extremely appealing for luminescence (since higher QY can bez obtained). Currently, $Ag_{29}(SSR)_{12}$ (SSR stands for a di-thiolate ligand) is a very famous "magic-size" nanoclusters where multiple approaches to manipulate the system by ligand exchange to rigidify the system and decreases non-radiative emission[24] and by doping the NCs with different metal atoms (gold, platinum)[25,26] have been explored. But the application of such system in vitro is remained unclear, the cytotoxicity of silver NCs seems to be important issue as compared to gold NCs. Thanks to a starting collaboration with the group of Manzhou Zhu in Anhui University in China, who are specialist in metallic kernel alloying of Silver NCs, we explore the possibility to use platinum as doping atom for enhancing stability and properties of silver NCs.

It was challenging to record mass spectrometry for silver NCs with ESI Q-TOF mass spectrometer, we did not visualize any spectra because they may be aggressive during their passing on the system. **Figure 4.21** shows mass spectra for $Ag_{29}DHLA_{12}$ and $Ag_{28}PT_1DHLA_{12}$ mass spectra recorded with ESI LTQ mass spectrometer, system parameter was inspired by the

old work in our lab for the same silver NCs back in 2016[27], the loss of one ligand is also noticed in there study. As we can see that the ratio of doping is 60/40 (without doping/dopped) in $Ag_{28}PT_1DHLA_{12}$. The QY deduced for this system is quite important for small NCs, up to 1.6%, promising for bio-imaging field. We also study two photon emission cross section (see **Table 4-3**) and hyper Rayleigh scattering hyperpolarizability with a $\beta=127(3).10^{-30}$ esu ($(106).10^{-30}$ esu for the work in 2016[27]), reasonably similar.

	Intensity	Concentration	TPEF Cross section (GM)
Fluorescein	56	1 µM	33,3
$Ag_{29}(BDT)_{12}$	62	273 µM	0,13
$Ag_{28}Pt_1(BDT)_{12}$	74	531 µM	0,08
$Ag_{29-x}Au_x(BDT)_{12}$	78	316 µM	0,14
$Ag_{29}DHLA_{12}$	56	970 µM	0,06
$Ag_{28}Pt_1DHLA_{12}$	54	980 µM	0,06

Table 4-3 : Calculated TPEF cross section using fluoresceine as external reference, we can see the effect of ligand rigidification (BDT) compared to floppy ligand (DHLA).

HeLa cells are used in the next step due to the limitation to access to other cell lines in the cell culture facility, we started to incubate the cell with silver NCs dissolved in DMEM complete and as we can see that we succeeded to observe signal of $Ag_{28}PT_1DHLA_{12}$ silver NCs inside

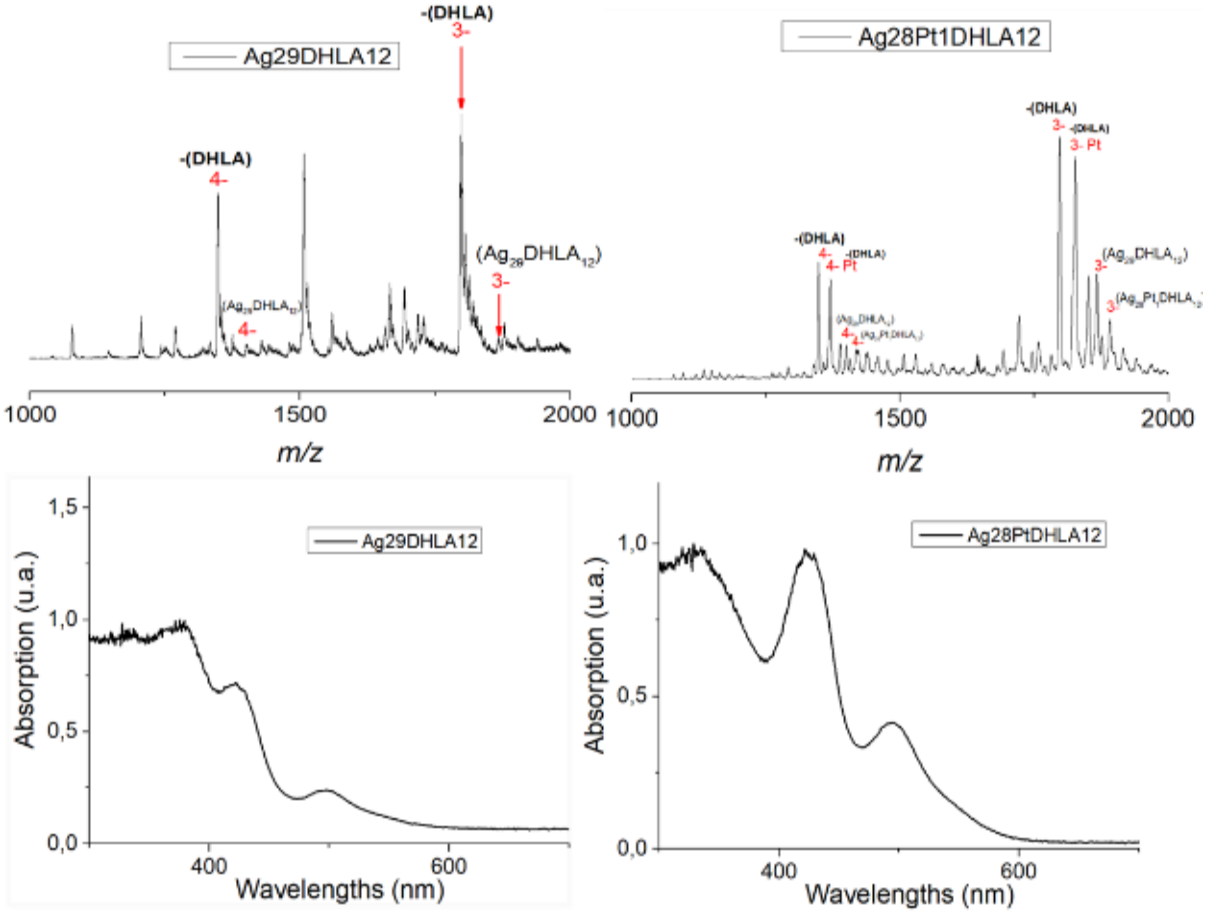

Figure 4.21 : (top) ESI mass spectrum of the synthesized Ag clusters using LTQ mass spectrometer and (below) UV-vis absorption.

the cells, note that $Ag_{29}DHLA_{12}$ didn't internalize the cells or it was already deteriorate, and this was the idea of platinum doping, but we still need to try more experiments in the future. Since we have limited time, we decided to only investigate $Ag_{28}PT_1DHLA_{12}$ in the next experiments. After used DMEM only (without FBS), the signal seems more important for the same concentration used with DMEM complete. At this stage we wanted to ensure the reproducibility of the results due the past experiment in vitro, that did not show repeatability when changing cells lines, non-coherent on terms of concentration study, and high concentration used. In contrast, $Ag_{28}PT_1DHLA_{12}$ shows it can be applicable for vitro application even at small concentration (30µM). After that we picture HeLa cells under

multiphoton confocal microscopy using an excitation wavelength at 780nm see **Figure 4.24**, and it gives a good signal without auto-fluorescence of membrane, and it's considered a soft method due to the low absorption of the NCs at 780nm and it prevent damage and photobleaching. The results can promote $Ag_{28}PT_1DHLA_{12}$ to the next step, but still particularly challenging due to the sensitivity of this NCs to PH and light. We then performed MTT essay for the same cell lines in Split where I took fresh synthesis in my bag, I took both $Ag_{29}DHLA_{12}$ and $Ag_{28}PT_1DHLA_{12}$ in powder, and incubate the cell for 2h and 24h in DMEM only, we tried only $Ag_{28}PT_1DHLA_{12}$ being the silver NCs that interests us, and results shown **Figure 4.25** show high toxicity for silver NCs for high concentrations. We then concluded that $Ag_{28}PT_1DHLA_{12}$ already loses their fluorescence due to travel and this result is not accurate since we evaluated the cell metabolism with deteriorated NCs. $Ag_{29}DHLA_{12}$ kept his fluorescence properties under UV, we try to incubate the cells for 2h with $Ag_{29}DHLA_{12}$ and the results is more promising showing internalization inside the cells for this short duration **Figure 4.26**.

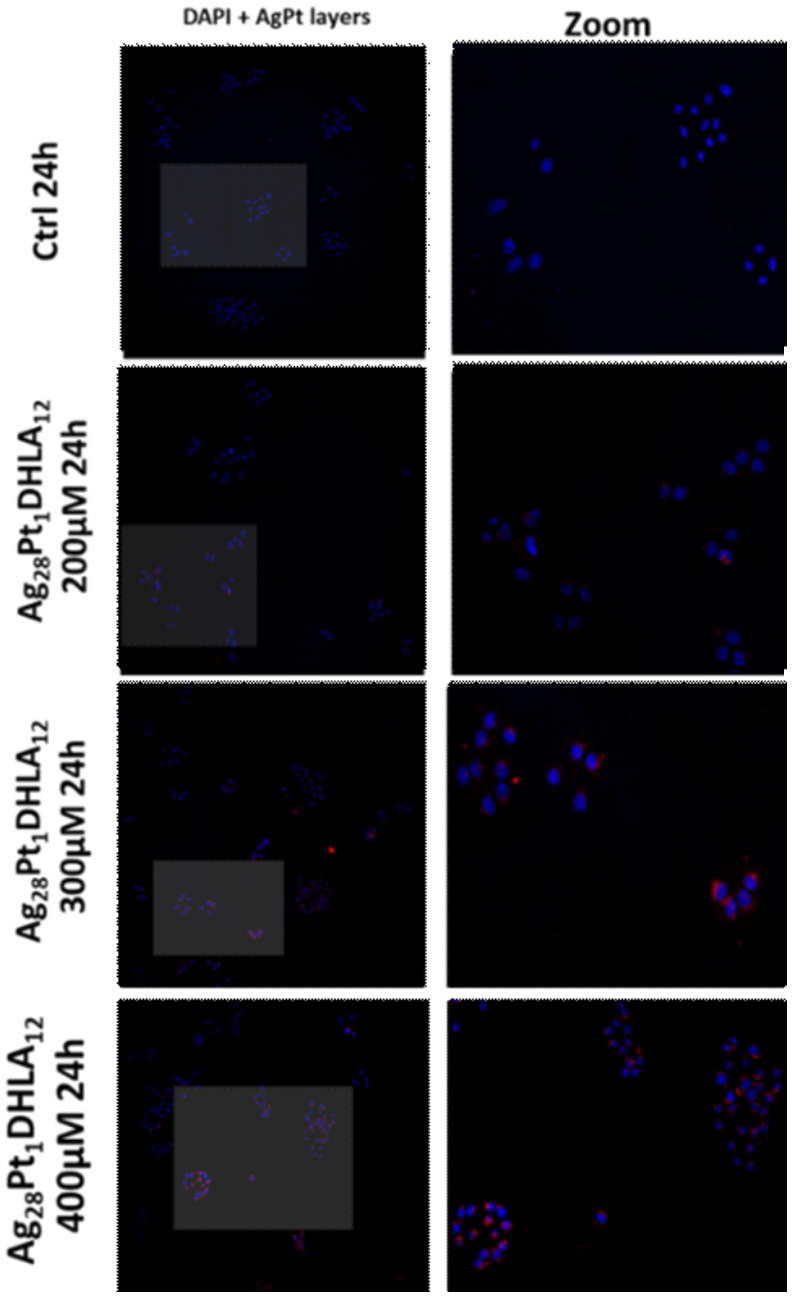

Figure 4.22 : HeLa cells visualized under Nikon spinning disk confocal microscopy incubated with $Ag_{28}PT_1DHLA_{12}$ silver NCs for 24h, we stained the nucleus with DAPI. In this experiment we dissolved silver NCs in DMEM with FBS which shows after that adding FBS to the medium will limit internalization.

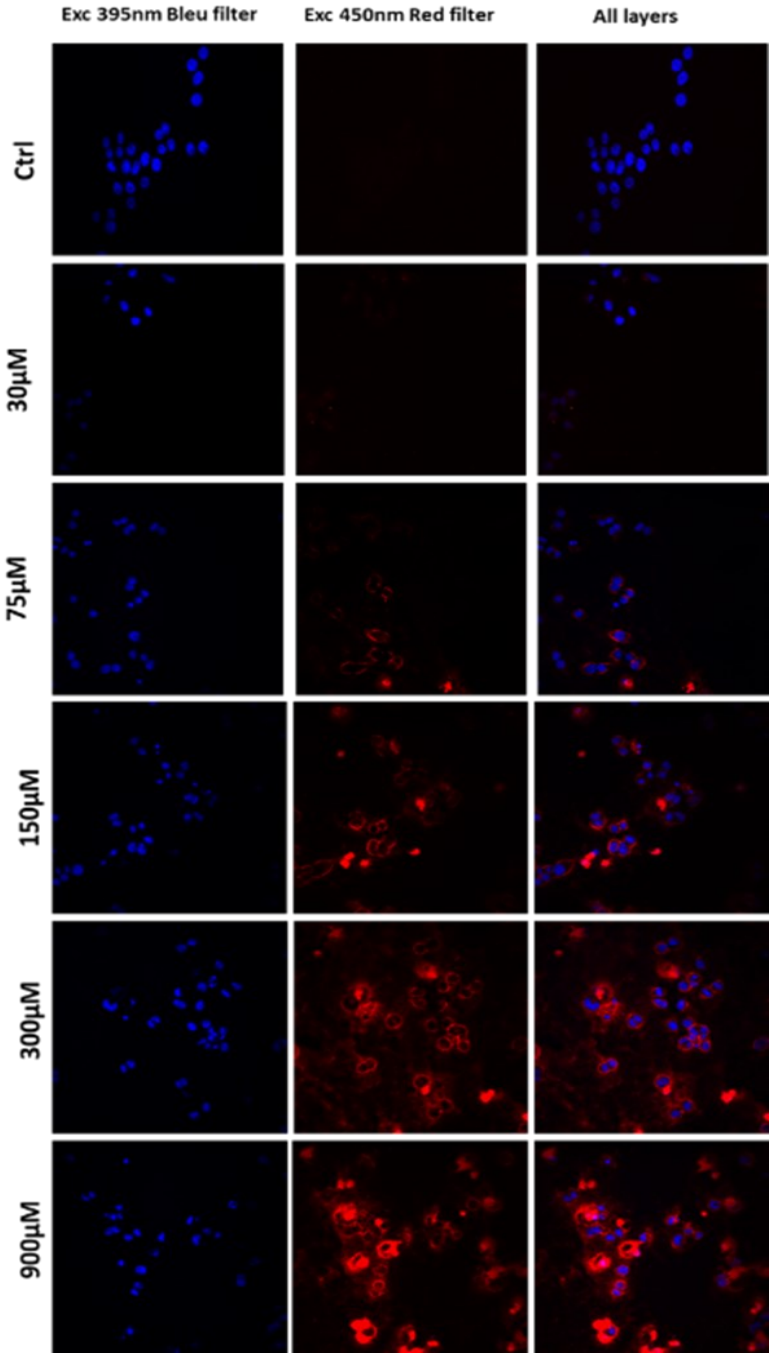

Figure 4.23 : HeLa cells visualized under Nikon spinning disk confocal microscopy incubated with $Ag_{28}PT_1DHLA_{12}$ silver NCs for 24h, we dyed the nucleus with DAPI. Removing FBS is better for the internalization of silver NCs for lower concentration up to 30 µM.

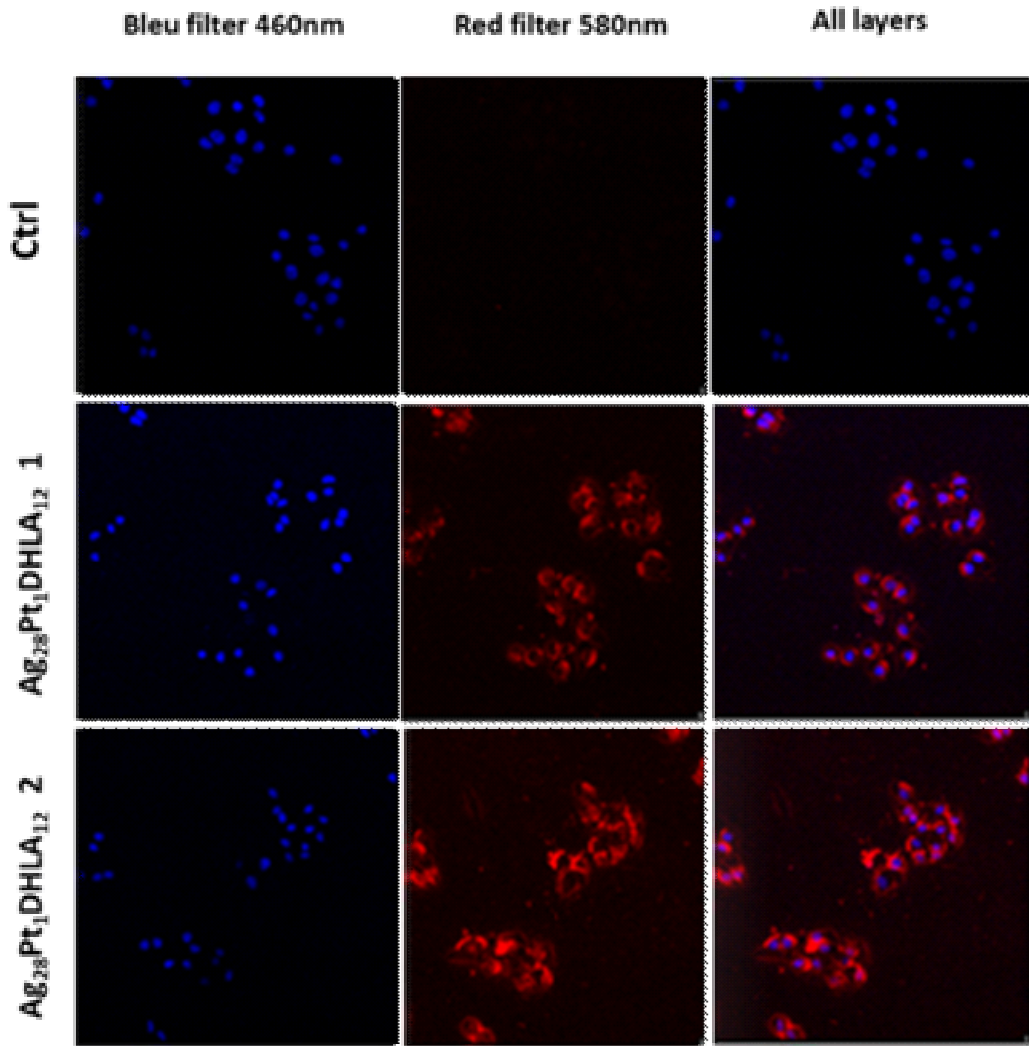

Figure 4.24 : Images taken with multiphoton confocal microscopy for HeLa cells incubated with $Ag_{28}PT_1DHLA_{12}$ with a concentration of 300µM with an excitation wavelength at 780nm, we used the optimized setup with filters to separate DAPI and silver NCs signal. 1 and 2 show only different picture for the same coverslips.

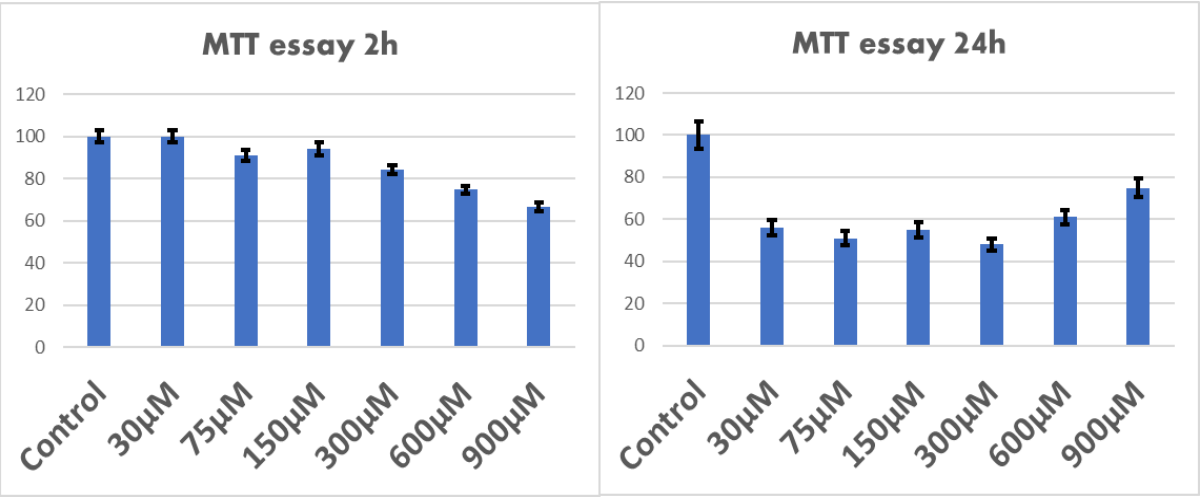

Figure 4.25 : MTT viability assay for HeLa cells incubated for 2 h (left side) and 24h (right side) with $Ag_{28}PT_1DHLA_{12}$ silver NCs with different concentration. The results show high toxicity for silver NCs at high concentrations and longer time of incubation.

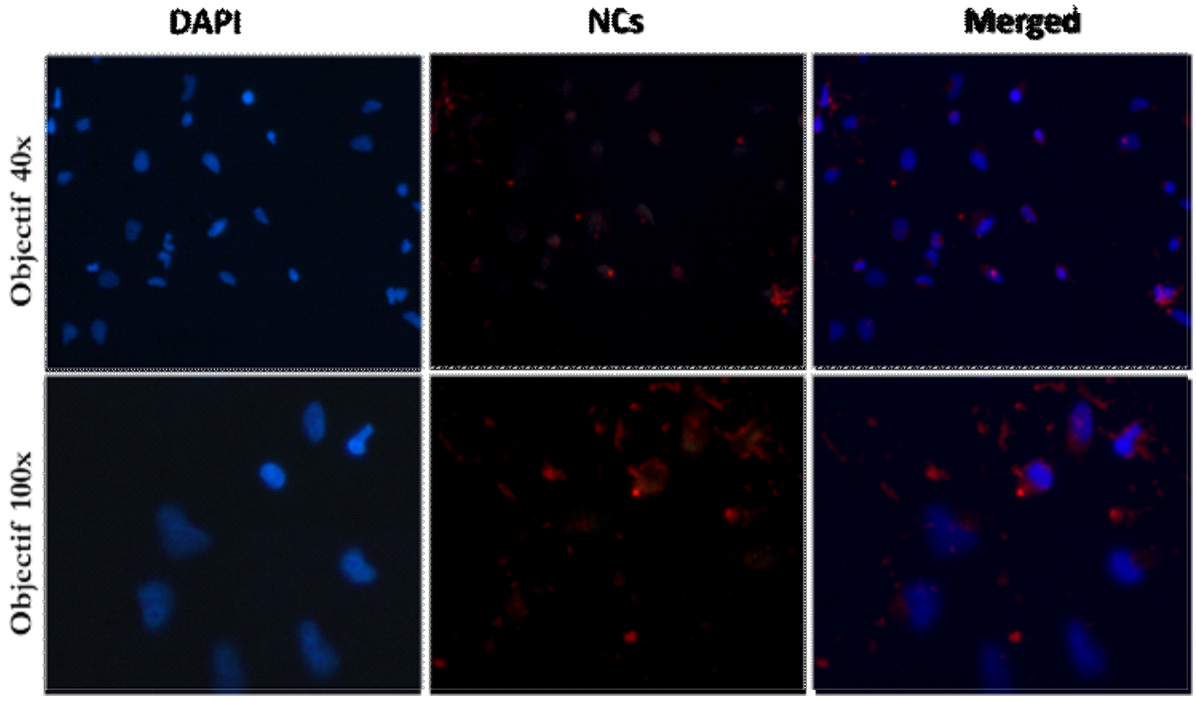

Figure 4.26 : Conventional epi-fluorescence microscopy images of HeLa cells after incubation with silver NCs dissolved in DMEM only for 2h. We observed the same spot of silver NCs outside the cells for the experiments before.

Conclusion

Glutathione protected gold nanoclusters presented low fluorescence (quantum yield are only 10^{-4}-10^{-3}) in water and thus showed no interest for in vitro application, forcing us to explore alternative strategy to produce highly luminescent targets that should be stable in complex biological media. To illustrate how complex and rich may be the interaction of nanoclusters with different compartment of cells, I presented in the first part of this chapter, the interaction of nanoclusters and their influence in the lysosomal activity and metabolic activity in glioblastoma cells. This work was part of an ongoing collaboration with Prof. Dusica Maysinger (McGill University) aiming at exploring the nanotoxicology of nanomaterials composed by ligand protected metal nanoclusters.

To bridge the gap to in vitro imaging with nanoclusters, the three most crucial factors are biocompatibility, high QY and stability. In the second part of this chapter, I presented the different ligand engineering strategies, e.g., protein templating, multi-shell ligand protection and finally metal doping of the NC core, which have led to the best compromise for in vitro applications. We first synthesized different protein-based gold NCs. BSA-Au NCs was the first system to apply due to its easy and reproducible synthesis, biocompatibility and easiness to functionalize to target carbonylation. BSA-Au NCs shows no internalization in A549 and HeLa cells for different concentrations. We examined another set of systems based on different other proteins (insulin, transferrin, lysozyme…) and one multi-shell protected gold NCs with a first shell of ATT as ligand and a second of arginine for rigidification. We went to Split to do cell culture and to test all the system together in vitro. Results show that only Au-Insulin and AuATT/Arg gold NCs were internalized in the cell but only at very high concentration. We also conducted MTT essays to measure the metabolic activity of the cells. We imaged cells incubated with gold NCs under colibri conventional microscope in MEDILS institute and Leica confocal microscopy in Zagreb. We concluded new experiments in Lyon using fresh synthesis,

but unfortunately both protein-protected gold NCs and multi-shell protected gold NCs failed to be used as luminescent target by confocal microscopy.

The last strategy we explored was the metal doping strategy. Thanks to an ongoing project with group of Prof. Manzhou Zhu (Anhui University, China), exploring ligand and platinum doping effects on Ag29 nanoclusters, we started with silver nanoclusters obtained at atomic precision (namely Ag29DHLA12) and some doping strategy with platinum were conducted leading to the production of Ag28Pt1DHLA12. Different images with varied concentration show a good internalization in HeLa cells under confocal microscopy at low cluster concentrations. Lastly, our collaborators in MEDILS have evaluated $Ag_{29}DHLA_{12}$ on HeLa cells that show internalization of silver NC after 2 hours. The effects of single-platinum doping of a class of Ag_{29} nanoclusters (protected either by DHLA) were evaluated on their photoluminescence (both upon one and two photon excitation) and their stability. Pt doping of $Ag_{29}DHLA_{12}$ nanoclusters significantly increases their stability but has low effect on their NLO properties. Similar trends are observed when BDT is used as ligands. Thanks to their strong stability, water-solubility, and due to large two-photon excited luminescence signals, we have successfully demonstrated the application of $PtAg_{28}DHLA_{12}$ in two-photon excitation live cell fluorescence imaging. Pt doping of Ag_{29} preserves their NLO properties (in particular large two-photon brightness) and thanks to their strong stability, water-solubility, $PtAg_{28}$ clusters make them a good alternative for bio-imaging.

Since we successfully bridged the gap to internalize silver-based NC inside the cell, we need to progress in rendering these silver-based nanoclusters functional for detecting carbonylation in cells. For this purpose, some efforts should be paid to find reproducible protocols for cell carbonylation, this part will be handled by the biologists at MEDILS. The second part will concern the functionalization strategies to render silver NC specific to carbonylation, and this is a difficult challenge.

How to render functional these nanoclusters for protein carbonylation detection ?

Two strategies are being explored:

- Post-functionalization : adding hydrazine (or aminooxy) groups on the surface of NCs. This can be proceeded by adding EDC (N-(3-Dimethylaminopropyl)-N′-ethyl carbodiimide hydrochloride) +NHS (NHS :N-Hydroxy succinimide) (catalyzer) plus silver based-NCs, and then adding the desired amine group in the ligand or molecule that contain at the end the proper group to target carbonylation (aminooxy or hydrazine).

- Ligand exchange : transforming DHLA into DHLA-hydrazine and doing ligand exchange.

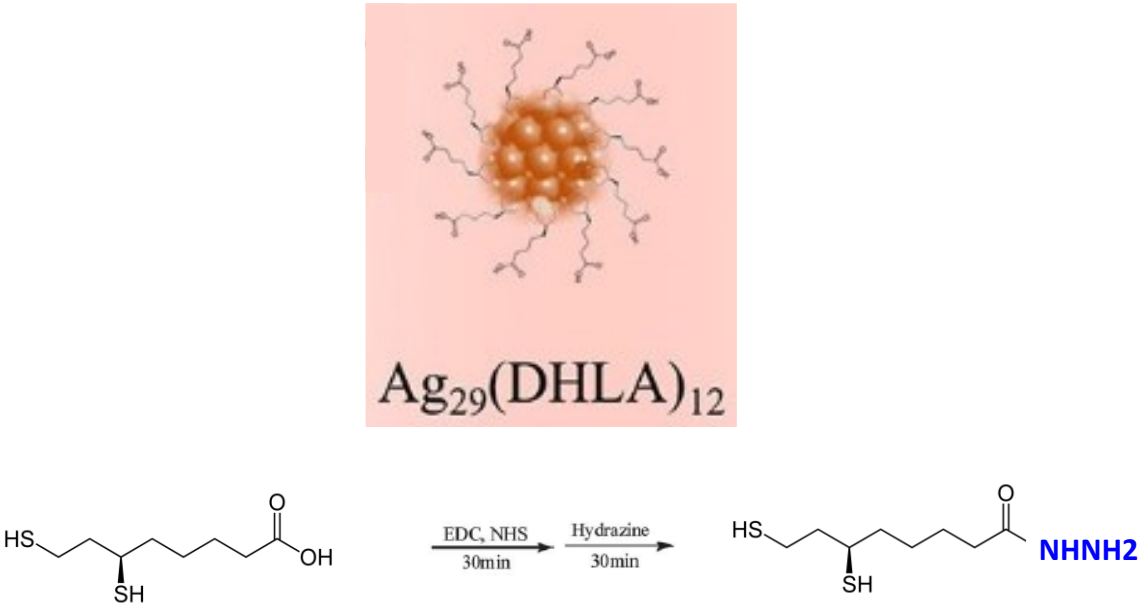

Figure 4.27: Illustration of the synthetic strategy to functionalize DHLA ligand to target carbonylation.

The PhD work of Hao Yuan (funded by the Chinese Scientific Council, CSC-University of Lyon agreement) is starting in October 2022 for 4 years, and these strategies will be explored, keeping in mind that cluster stability is an issue to better evaluate which strategy will be the more appealing for specific targeting of carbonylation.

Of note, no specific method is report nowadays to target only on part of organelles inside the cell, when carbonylation reagents is inserted inside the cells, the macromolecules that will be subjected to carbonylation are proteins, lipids, sugars and nucleic acids even DNA[28–31]. So, one can imagine that any fluorophore that can target carbonylation, and incubated with the cells, the microscope images will give signal of all these macromolecules mentioned.

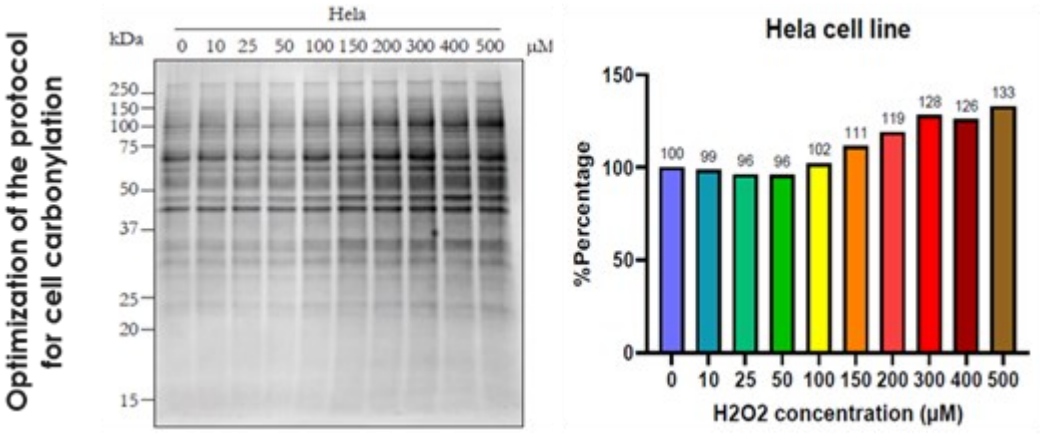

Figure 4.28 : Carbonylation protocol with H_2O_2 on HeLa cells visualized under streptavidin Alexa fluor 700 and quantified with GraphPad software, the signal observed in the non-treated cells is normal since without any reagents carbonylation exist in normal cells.

Concerning reproducible protocols for carbonylation in cells, different methods are being explored : “standard” method using UV radiation where the cells are irradiated in an UV box for certain time and UV intensity, and at the end they can adapt a protocol of UV duration and UV power for their experiments. Another method uses hydrogen peroxide H_2O_2, by mixing a certain amount of H_2O_2 with the cells at a certain time. Since we are interested in imaging the carbonylated cells under multiphoton confocal microscopy (in Lyon), we preferred to use H_2O_2 since it is easy to use this protocol in our institute, since UV irradiation set-up is only available in Split. Recently reproducible protocols were developed at MEDILs, by mixing HeLa cells with different concentration of H_2O_2 for 4 hours in DMEM only, the medium containing H_2O_2 is replaced with a fresh medium and left for 2 hours. Next cells are lysis with lysed buffer and centrifuged at 21000 per g for 15 minutes. Protein extracted with lysis is then derivatize with

1mM biotin-aminooxy probe and 20 mM of pPDA catalyze at 10°C with shaking at 500rpm overnight. Finally, we suspended the derivatized proteins in PBS1x and migrated in the gels and then transferred with semi-dry. Visualized under streptavidin Alexa fluor 700 and signal was quantified with GraphPad software. **Figure 4.28** show a nice increase of the protein carbonylation with increasing the concentration of H_2O_2.

References

[1] Kuzmic M, Javot H, Bonzom JM, et al. In situ visualization of carbonylation and its co-localization with proteins, lipids, DNA and RNA in Caenorhabditis elegans. Free Radical Biology and Medicine. 2016;101:465-474. doi:10.1016/j.freeradbiomed.2016.11.004

[2] Yu Q, Gao P, Zhang KY, et al. Luminescent gold nanocluster-based sensing platform for accurate H2S detection in vitro and in vivo with improved anti-interference. Light Sci Appl. 2017;6(12):e17107-e17107. doi:10.1038/lsa.2017.107

[3] Dong L, Li M, Zhang S, et al. Cytotoxicity of BSA-Stabilized Gold Nanoclusters: In Vitro and In Vivo Study. Small. 2015;11(21):2571-2581. doi:10.1002/smll.201403481

[4] Hada AM, Craciun AM, Focsan M, et al. Folic acid functionalized gold nanoclusters for enabling targeted fluorescence imaging of human ovarian cancer cells. Talanta. 2021;225:121960. doi:10.1016/j.talanta.2020.121960

[5] Guével XL, Daum N, Schneider M. Synthesis and characterization of human transferrin-stabilized gold nanoclusters. Nanotechnology. 2011;22(27):275103. doi:10.1088/0957-4484/22/27/275103

[6] Kang X, Zhu M. Tailoring the photoluminescence of atomically precise nanoclusters. Chem Soc Rev. 2019;48(8):2422-2457. doi:10.1039/C8CS00800K

[7] Li Q, Zhou D, Chai J, et al. Structural distortion and electron redistribution in dual-emitting gold nanoclusters. Nat Commun. 2020;11(1):2897. doi:10.1038/s41467-020-16686-8

[8] Gran ER, Bertorelle F, Fakhouri H, et al. Size and ligand effects of gold nanoclusters in alteration of organellar state and translocation of transcription factors in human primary astrocytes. Nanoscale. 2021;13(5):3173-3183. doi:10.1039/D0NR06401G

[9] Maysinger D, Gran ER, Bertorelle F, et al. Gold nanoclusters elicit homeostatic perturbations in glioblastoma cells and adaptive changes of lysosomes. Theranostics. 2020;10(4):1633-1648. doi:10.7150/thno.37674

[10] Eskelinen EL, Tanaka Y, Saftig P. At the acidic edge: emerging functions for lysosomal membrane proteins. Trends in Cell Biology. 2003;13(3):137-145. doi:10.1016/S0962-8924(03)00005-9

[11] Xie J, Zheng Y, Ying JY. Protein-Directed Synthesis of Highly Fluorescent Gold Nanoclusters. J Am Chem Soc. 2009;131(3):888-889. doi:10.1021/ja806804u

[12] Russell BA, Kubiak-Ossowska K, Mulheran PA, Birch DJS, Chen Y. Locating the nucleation sites for protein encapsulated gold nanoclusters: a molecular dynamics and fluorescence study. Phys Chem Chem Phys. 2015;17(34):21935-21941. doi:10.1039/C5CP02380G

[13] Bertorelle F, Wegner KD, Perić Bakulić M, et al. Tailoring the NIR-II Photoluminescence of Single Thiolated Au25 Nanoclusters by Selective Binding to Proteins**. Chemistry – A European Journal. 2022;28(39):e202200570. doi:10.1002/chem.202200570

[14] Zhou W, Cao Y, Sui D, Guan W, Lu C, Xie J. Ultrastable BSA-capped gold nanoclusters with a polymer-like shielding layer against reactive oxygen species in living cells. Nanoscale. 2016;8(18):9614-9620. doi:10.1039/C6NR02178F

[15] Soleilhac A, Bertorelle F, Antoine R. Sizing protein-templated gold nanoclusters by time resolved fluorescence anisotropy decay measurements. Spectrochimica Acta Part A: Molecular and Biomolecular Spectroscopy. 2018;193:283-288. doi:10.1016/j.saa.2017.12.025

[16] Cheung A, Bax HJ, Josephs DH, et al. Targeting folate receptor alpha for cancer treatment. Oncotarget. 2016;7(32):52553-52574. doi:10.18632/oncotarget.9651

[17] Deng HH, Shi XQ, Wang FF, et al. Fabrication of Water-Soluble, Green-Emitting Gold Nanoclusters with a 65% Photoluminescence Quantum Yield via Host–Guest Recognition. Chem Mater. 2017;29(3):1362-1369. doi:10.1021/acs.chemmater.6b05141

[18] Bhatnagar BS, Bogner RH, Pikal MJ. Protein Stability During Freezing: Separation of Stresses and Mechanisms of Protein Stabilization. Pharmaceutical Development and Technology. 2007;12(5):505-523. doi:10.1080/10837450701481157

[19] Schwegman JJ, Carpenter JF, Nail SL. Evidence of partial unfolding of proteins at the ice/freeze-concentrate interface by infrared microscopy. JPharmSci. 2009;98(9):3239-3246. doi:10.1002/jps.21843

[20] Pyo K, Thanthirige VD, Yoon SY, Ramakrishna G, Lee D. Enhanced luminescence of Au22(SG)18 nanoclusters via rational surface engineering. Nanoscale. 2016;8(48):20008-20016. doi:10.1039/C6NR07660B

[21] Cornett DShannon, Duncan MA, Amster IJonathan. Liquid mixtures for matrix-assisted laser desorption. Anal Chem. 1993;65(19):2608-2613. doi:10.1021/ac00067a011

[22] Keller BO, Li L. Three-Layer Matrix/Sample Preparation Method for MALDI MS Analysis of Low Nanomolar Protein Samples. Journal of the American Society for Mass Spectrometry. 2006;17(6):780-785. doi:10.1016/j.jasms.2006.02.012

[23] Schiller J, Süß R, Fuchs B, et al. The suitability of different DHB isomers as matrices for the MALDI-TOF MS analysis of phospholipids: which isomer for what purpose? Eur Biophys J. 2007;36(4):517-527. doi:10.1007/s00249-006-0090-6

[24] Zeng Y, Havenridge S, Gharib M, et al. Impact of Ligands on Structural and Optical Properties of Ag29 Nanoclusters. J Am Chem Soc. 2021;143(25):9405-9414. doi:10.1021/jacs.1c01799

[25] Soldan G, Aljuhani MA, Bootharaju MS, et al. Gold Doping of Silver Nanoclusters: A 26-Fold Enhancement in the Luminescence Quantum Yield. Angewandte Chemie International Edition. 2016;55(19):5749-5753. doi:10.1002/anie.201600267

[26] Ghosh A, Mohammed OF, Bakr OM. Atomic-Level Doping of Metal Clusters. Acc Chem Res. 2018;51(12):3094-3103. doi:10.1021/acs.accounts.8b00412

[27] Russier-Antoine I, Bertorelle F, Hamouda R, et al. Tuning Ag29 nanocluster light emission from red to blue with one and two-photon excitation. Nanoscale. 2016;8(5):2892-2898. doi:10.1039/C5NR08122J

[28] Luo S, Wehr NB. Protein carbonylation: avoiding pitfalls in the 2,4-dinitrophenylhydrazine assay. Redox Report. 2009;14(4):159-166. doi:10.1179/135100009X392601

[29] Afzal S, Jensen SA, Sørensen JB, Henriksen T, Weimann A, Poulsen HE. Oxidative damage to guanine nucleosides following combination chemotherapy with 5-fluorouracil and oxaliplatin. Cancer Chemother Pharmacol. 2012;69(2):301-307. doi:10.1007/s00280-011-1700-2

[30] Dalle-Donne I, Rossi R, Giustarini D, Milzani A, Colombo R. Protein carbonyl groups as biomarkers of oxidative stress. Clinica Chimica Acta. 2003;329(1):23-38. doi:10.1016/S0009-8981(03)00003-2

[31] Fritz KS, Petersen DR. Exploring the Biology of Lipid Peroxidation-Derived Protein Carbonylation. Chem Res Toxicol. 2011;24(9):1411-1419. doi:10.1021/tx200169n

Conclusion

Thanks to the strong expertise in synthesizing noble metal NCs with atomically precision (in particular using glutathione SG as ligand) and further strategies for their surface modification, the "Lyon-Split consortium" initially established through a CNRS International laboratory – Nanoclusters for biological aging- NCBA, headed by Philippe Dugourd and Vlasta Bonačić-Koutecký, decided to go towards bio-imaging applications and precisely to detect the carbonylation of the proteins. This application-oriented project was rendered possible thanks to the strong fundamental understanding gained on the structure-optical properties relationships of nanoclusters. In the past ten years, we have been implementing a large set of experimental setups to characterize their structure and to study the structure-properties relationships concerning their linear and non-linear optical properties.

Our group has been working in the fundamental study of different gold NCs during a long time giving us a vast set of glutathione protected NCs of different number and ligand number (Au_nSG_m) with different properties and structures in front of our choice. These nanoclusters protected by glutathione represent opportunities for biological applications, indeed they present non-toxicity, small size, atomic precision, good ability to easily enter cells, good biocompatibility, good photo-stability. However, although tunable emission is possible thanks to ligand strategy, such nanoclusters present poor luminescence (as compared to dyes) as shown in **Figure 5.1**[1].

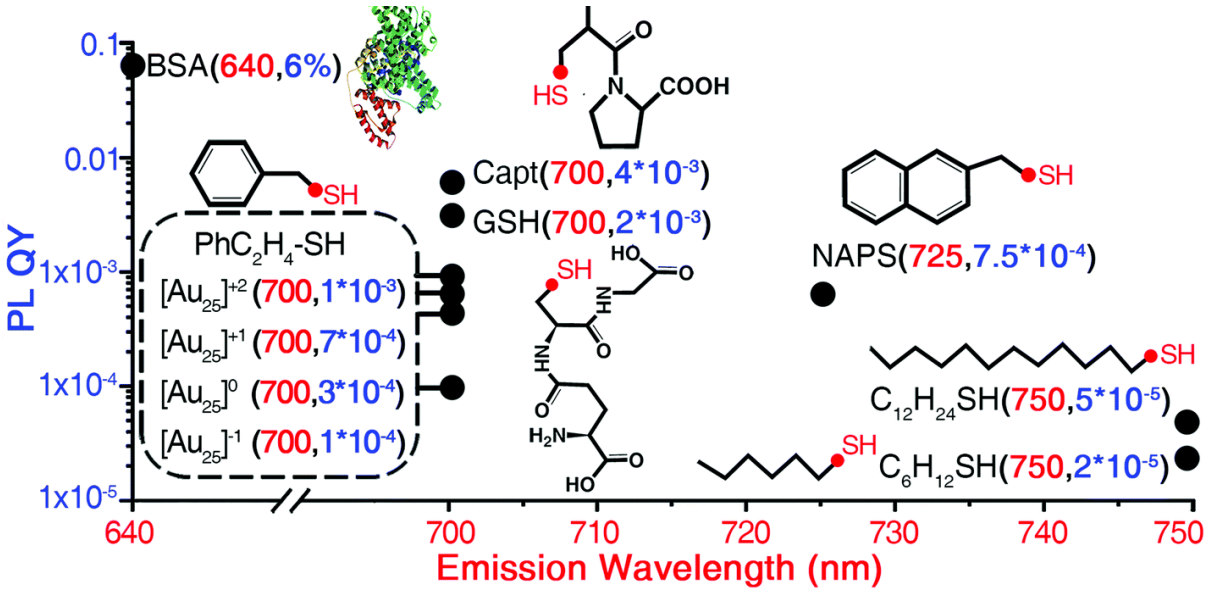

Figure 5.1: Comparison of the emission wavelengths (λ_{em}) and PL QYs of $Au_{25}(SR)_{18}$ nanoclusters with different capped ligands and valence states. The λ_{em} and PL QYs are summarized from Xie kang et al.[1]

In addition, synthetic protocols should be adapted to produce stable nanoclusters bearing functional ligands. During my PhD work, after a long journey of choosing and modifying the optimal gold NCs for carbonylation detection, only $Au_{15}SG_{13}$ has shown good stability after functionalization, e.g., ligand exchange with aminooxy ligand. During the first part of my PhD work, we demonstrated the easy synthesis of atomically precise Au_{15} nanoclusters and their functionalization through the formation of a thiolated aminooxy probe via a simple ligand exchange protocol. These nanoclusters were found to be highly reactive towards carbonyls. Also, with the functionalized Au15 nanoclusters, we demonstrate their ability as one- and two-photon excitation fluorescence contrast agents for protein carbonylation detection in gels.

Compared to existing and established technique using functionalized NIR-dyes used nowadays in this field[2], our approach is still behind and need a lot of improvements for enhancing fluorescence QYs. Quantification of the carbonylation using nanoclusters has also to be evaluated. Indeed, robust protocols should be developed to correlate the level of fluorescence

recorded with NCs and the corresponding number of carbonylated proteins. In fact, during our proof-of-principle work, only a qualitative detection of carbonylation was possible. However, one of the main advantages of ligand protected NCs is the possibility to create NC platform with functional moieties appended onto each surface ligand, that could be appealing in other domains of application in particular for enhancing targeting sensitivity toward cancer materials[3].

However, glutathione protected gold nanoclusters present poor luminescence in water (as illustrated for Au25 in figure 1). Protein-protected gold NCs present an acceptable and applicable QY in water and could be useful for in vitro applications. We synthesized six protein-based gold NCs (BSA-Au, FA-BSA-Au, G-BSA-Au, Transferrin-Au, Insulin-Au, Lysozyme-Au) for in vitro experiments. Unexpectedly, and in contrast with some published papers, such NCs show no (or only for high NCs concentration) internalization and reproducibility in the cells. Other strategies were explored, namely multi-shell rigid nanoclusters and alloyed nanoclusters. Hopefully silver NCs doped with platinum show a good system for in vitro investigations with even low concentration and short incubation, our goal being the detection of carbonylation inside the cells, we developed a protocol for cell carbonylation using H_2O_2.

Producing functional nanoclusters with high quantum yield and with high stability remains a big challenge. The main issue for the future of this work will consist in developing adapted chemical strategies to functionalize platinum doped silver NCs (without degradation). This is a challenging issue, and this will be done under the PhD work of Hao Yuan starting in October 2022. Finally, a strategy that was at the center of my Master internship consisted in producing self-assembled nanoclusters presenting high QYs and high stability[4,5]. This strategy was not too much explored during the course of this PhD work because the main challenging issue here is to be able to control both size and size-dispersion of self-assemblies. However, some assembled structures have been used as biomarkers for cellular imaging and cancer therapy due

to their enhanced physicochemical properties, which are advantageous for biological applications[6]. This route should also be explored more in the future.

References

[1] Kang, X.; Zhu, M. Tailoring the Photoluminescence of Atomically Precise Nanoclusters. Chem. Soc. Rev. 2019, 48 (8), 2422–2457. https://doi.org/10.1039/C8CS00800K.

[2] Luo, S.; Wehr, N. B. Protein Carbonylation: Avoiding Pitfalls in the 2,4-Dinitrophenylhydrazine Assay. Redox Rep. 2009, 14 (4), 159–166. https://doi.org/10.1179/135100009X392601.

[3] Antoine, R.; Maysinger, D.; Sancey, L.; Bonačić-Koutecký, V. Open Questions on Proteins Interacting with Nanoclusters. Commun. Chem. 2022, 5 (1), 1–5. https://doi.org/10.1038/s42004-022-00665-9.

[4] Basu, S.; Fakhouri, H.; Moulin, C.; Dolai, S.; Russier-Antoine, I.; Brevet, P.-F.; Antoine, R.; Paul, A. Four Orders-of-Magnitude Enhancement in the Two-Photon Excited Photoluminescence of Homoleptic Gold Thiolate Nanoclusters Following Zinc Ion-Induced Aggregation. Nanoscale 2021, 13 (8), 4439–4443. https://doi.org/10.1039/D0NR08764E.

[5] Fakhouri, H.; Perić, M.; Bertorelle, F.; Dugourd, P.; Dagany, X.; Russier-Antoine, I.; Brevet, P.-F.; Bonačić-Koutecký, V.; Antoine, R. Sub-100 Nanometer Silver Doped Gold–Cysteine Supramolecular Assemblies with Enhanced Nonlinear Optical Properties. Phys. Chem. Chem. Phys. 2019, 21 (23), 12091–12099. https://doi.org/10.1039/C9CP00829B.

[6] Kolay, S.; Bain, D.; Maity, S.; Devi, A.; Patra, A.; Antoine, R. Self-Assembled Metal Nanoclusters: Driving Forces and Structural Correlation with Optical Properties. Nanomaterials 2022, 12 (3), 544. https://doi.org/10.3390/nano12030544.